12-2008

EXPERIMENTAL AND MODELING STUDIES FOR OPTIMIZING FLOCCULANT-AIDED SEDIMENT RETENTION PONDS

Byung joon Lee
Clemson University, byungjooni@hotmail.com

Recommended Citation

Lee, Byung joon, "EXPERIMENTAL AND MODELING STUDIES FOR OPTIMIZING FLOCCULANT-AIDED SEDIMENT RETENTION PONDS" (2008). *All Dissertations*. 316.
https://tigerprints.clemson.edu/all_dissertations/316

EXPERIMENTAL AND MODELING STUDIES FOR OPTIMIZING FLOCCULANT-AIDED SEDIMENT RETENTION PONDS

A Dissertation
Presented to
the Graduate School of
Clemson University

In Partial Fulfillment
of the Requirements for the Degree
Doctor of Philosophy
Environmental Engineering and Science

---

by
Byung Joon Lee
December 2008

Accepted by:
Chair: Dr. Mark A. Schlautman
Co-Chair: Dr. Fred J. Molz, III
Dr. Igor Luzinov
Dr. John C. Hayes

ABSTRACT

Attempts to control sediment-containing runoff and associated water quality problems have involved the establishment of many small to medium sediment retention ponds and the injection of nonionic and anionic polyacrylamide (PAM) flocculants to enhance colloid removal. However, to date use has been driven more by practicing engineers and trial-and-error approaches than by logical and consistent design approaches. Therefore, the purpose of this research was to optimize colloidal clay removal in PAM-aided sediment retention ponds by applying experimental and theoretical methodologies.

Initially, simple measurement techniques for the molecular weight (MW) and charge density (CD) of various PAMs were tested and their characteristic behaviors in aqueous solution were investigated for use in subsequent optimization tasks. A simple intrinsic viscosity measurement technique and acid-base titration method showed their capabilities as the most plausible substitutes of state-of-the-art techniques in measuring MW and CD, respectively. Also, a cylindrical shape for PAM conformation in aqueous solution was shown to be the best assumption for predicting the characteristic behavior of PAM molecules.

In adsorption and flocculation experiments with nonionic PAMs and negatively-charged kaolinite clay particles, adsorption capacities of PAMs on kaolinite were found to increase with increasing PAM MW up to a certain size (~ 18 M g/mol) but then decrease beyond this size due to entanglements between PAM molecules. Flocculation efficiency with nonionic PAM also increased with increasing MW up to a point due to its nonequilibrium kaolinite flocculation but eventually decreased by entanglements between PAM molecules. In parallel experiments with anionic PAMs and negatively-charged kaolinite particles, adsorption capacities were found to be inversely proportional to the PAM CDs, while flocculation efficiencies were directly proportional to the PAM MWs. Along with the effects of PAM MW and CD, the presence of divalent cations such as Ca^{2+} and Mg^{2+} enhanced adsorption and flocculation due to cationic bridging and/or charge screening between PAM and kaolinite (PAM^{-}–$^{+}M^{+}$–$^{-}$Kaolinite). However, concurring steric stabilization was also found to counteract flocculation due to the conformational compaction of adsorbed PAMs by the cationic bridging between pre-adsorbed PAM molecules (PAM^{-}–$^{+}M^{+}$–^{-}PAM). In short, PAM and solution characteristics, including change density (CD), molecular weight (MW) of PAM, and cationic species in the solution, were found to make critical effects on adsorption and flocculation and thus to be the controlling parameters in optimizing PAM applications as soil stabilizers or flocculants. In a model-based optimization of PAM-aided sediment retention ponds, the applicability of utilizing multi-dimensional Discretized Population Balance Equations combined with a Computational Fluid Dynamics (CFD-DPBE model) was demonstrated in a series of simulation tasks with a model retention pond. The CFD-DPBE model was demonstrated to be a valuable simulation tool for natural and engineering flocculation and sedimentation systems as well as flocculant-aided sediment retention ponds.

DEDICATION

This achievement is dedicated to my parents and grandparents who had and have devoted all their efforts to provide what I am enjoying nowadays.

ACKNOWLEDGMENTS

My doctoral study has been a pilgrimage to an academic sanctuary. I have been frustrated at many obstacles, such as laborious experiments, incomprehensible theories, emotional depression, and so on. Without help from companions, I could never have reached the glorious end.

First of all, I would like to acknowledge my two advisors, Dr. Schlautman and Dr. Molz, for their endless encouragement and helps. Dr. Schlautman has never set any boundaries on my research and helped and encouraged me to try whatever I wanted to do. So, he has provided a great chance for me to have a broad perspective in the academic world. Dr. Molz has always cheered me up, as my parents do. Whenever I have been depressed with the poor outputs from my research work, I have been encouraged with his cordial praises even on my trivial achievements. Also, I appreciate his guidance to get into the new world of multi-dimensional simulation.

I am grateful to other committee members, Dr. Larry Murdoch, Dr. Igor Luzinov, and Dr. John Hayes, for their helpful discussion and guidance. Especially, I was lucky to take Dr. Luzinov’s class, Polymer Science, and to invite him as a committee member. Without Dr. Luzinov’s help and guidance on polymer science, which is an unknown field for many environmental engineers, I could never have finished my doctoral research. Even though Dr. Karanfil is neither an advisor nor a committee member, he has trained me with many TA assignments. His diligence and sincerity gave me an inspiration on how I should live during my future life.

I am also would like to express my gratitude to other Korean colleagues in the EEES department. The doctor couple, Dr. HoCheol Song and Dr. JeongRan Im, have helped me as a brother and a sister. They have been excellent consultants on living and research issues. Dr. Jin Hur and Dr. SeokOh Ko have provided me with momentous guidance and tips. Also, I am thankful to my office mates, James Henderson, Fei Chen, Vijay Elango, Heifung Shan, Jia Hu, Dr. Deniz Inci Demirkanli, Jim Chamberlain, and Saumya Sarkar, for their help and lively chats.

I would like to express my utmost gratitude to my parents, HoYoon Lee and JungNam Park, and also to my brother, Major IkWon Lee, for their endless support and love.

Finally, I would like to acknowledge the EEES department for financial support during my doctoral study, including the TA assistantship and the R.C. Edward Fellowship and also acknowledge Dr. Linvil Rich for the L.G. Rich Fellowship. I am thankful again to Dr. Schlautman for arranging various research funds from the Natural Resources Conservation Service of the U.S. Department of Agriculture through the Changing Land Use and Environment Project at Clemson University and the Cooperative State Research, Education, and Extension Service of the USDA.

TABLE OF CONTENTS

Page

TITLE PAGE i

ABSTRACT ii

DEDICATION iv

ACKNOWLEDGMENTS v

LIST OF TABLES..x

LIST OF FIGURES xi

CHAPTER 1. INTRODUCTION 1
- 1.1 Characterizing the Molecular Weight and Charge Density of PAMs (Chapter 2)...4
- 1.2 Characteristic Behaviors of PAMs in the Aqueous Phase (Chapter 3).............5
- 1.3 Molecular Weight Effects on PAM-induced Adsorption and Flocculation (Chapter 4) 6
- 1.4 Effects of PAM and Solution Properties on Adsorption and Flocculation (Chapter 5) 7
- 1.5 Simulation of Turbulent Flocculation and Sedimentation (Chapter 6).............7
- 1.6 References..8

CHAPTER 2. APPLICABILITY OF SIMPLE MEASUREMENT TECHNIQUES IN ESTIMATING MOLECULAR WEIGHTS AND CHARGE DENSITIES OF POLYACRYLAMIDE SOIL STABILIZERS OR FLOCCULANTS 13
- 2.0 Abstract..13
- 2.1 Introduction..14
- 2.2 Materials and Methods...17
  - 2.2.1 Polyacrylamide sample preparation......................................17
  - 2.2.2 Molecular Weight measurement...18
  - 2.2.3 Charge Density measurement 24
- 2.3 Results and Discussion 27
- 2.4 Conclusion and Recommendation 45
- 2.5 References..46

Table of Contents (Continued)

Page

CHAPTER 3. APPLICABILITY OF SIMPLIFIED ELECTROSTATIC INTERACTION MODELS IN PREDICTING ELECTROSTATIC INTERACTION CHEMISTRY OF POLYACRYLAMIDE-co-ACRYLATE : IMPERMEABLE SPHERE, DONNAN, AND CYLINDRICAL MODEL 49

- 3.0 Abstract 49
- 3.1 Introduction 50
- 3.2 Model Description 55
  - 3.2.1 Electrostatic Acid-Base Chemistry Model 55
  - 3.2.2 Spatial Electrostatic Potential Distribution Models 56
- 3.3 Materials and Methods 60
  - 3.3.1 Polyacrylamide Sample Preparation and Characterization 60
  - 3.3.2 Potentiometric Titration Test and Model-Data Fitting Procedure 62
  - 3.3.3 Specific Viscosity Measurement 64
- 3.4 Results and Discussion 65
- 3.5 Conclusion and Recommendation 79
- 3.6 References 80

CHAPTER 4. INVESTIGATION ON THE EFFECTS OF POLYACRYLAMIDES' MOLECULAR WEIGHTS ON ADSORPTION AND FLOCCULATION PROCESSES IN KAOLINITE AND POLYACRYLAMIDE-CONTAINING SUSPENSIONS 83

- 4.0 Abstract 83
- 4.1 Introduction 84
- 4.2 Materials and Methods 87
  - 4.2.1 Materials 87
  - 4.2.2 Adsorption Test 88
  - 4.2.3 Viscosity Measurement 89
  - 4.2.4 Flocculation (Jar) Test 91
- 4.3 Results and Discussion 92
  - 4.3.1 Adsorption Test 92
  - 4.3.2 Steady-Shear Viscosity 95
  - 4.3.3 Flocculation Test 97
- 4.4 Conclusion and Recommendation 103
- 4.5 References 104

CHAPTER 5. INVESTIGATION ON THE EFFECTS OF PAM AND SOLUTION CHARACTERISTICS ON ADSORPTION AND FLOCCULATION OCCURING IN SIMILARLY CHARGED ANIONIC PAM- AND KAOLINITE-CONTAINING SUSPENSIONS 108

- 5.0 Abstract 108
- 5.1 Introduction 109

Page

5.2 Materials and Methods 113
5.2.1 Polyacrylamide Purification and Characterization with respect to MW and CD 113
5.2.2 Jar Test – Adsorption and Flocculation Test 116
5.2.3 Measurements of Experimental Indices 118
5.3 Results and Discussion 121
5.3.1 Adsorption and Flocculation Behaviors 121
5.3.2 Effect of Molecular Weight and Charge Density on Adsorption and Flocculation 131
5.3.3 Zeta Potential and Ca^{2+}/Mg^{2+} Adsorption 133
5.4 Conclusion and Recommendation 138
5.5 References 139

CHAPTER 6. SIMULATION OF TURBULENT FLOCCULATION AND SEDIMENTATION IN FLOCCULANT-AIDED SEDIMENT RETENTION PONDS 145
6.0 Abstract 145
6.1 Introduction 146
6.2 Background and Mathematical Models 149
6.2.1 Computational Fluid Dynamics (CFD) 149
6.2.2 Multi-dimensional Discretized Population Balance Equations (DPBE) 152
6.2.3 Kinetics of Particle/Floc Aggregation and Breakage 154
6.3 Numerical Simulation 158
6.4 Results and Discussion 163
6.5 Conclusion and Recommendation 170
6.6 References 172

CHAPTER 7. SUMMARY, CONCLUSIONS AND RECOMMENDATIONS 178
7.1 Summary 178
7.2 Conclusions 179
7.3 Recommendations 180
7.4 References 182

APPENDICES 185
A: Molecular Weight Measurement with Multi-Angle Light Scattering Analyzer : Zimm-Berry Plots 186
B: Molecular Weight Estimation with Intrinsic Viscosity Measurement Technique 197
C: Charge Density Measurement with Potentiometric Acid-Base Titration 208

Page

- D: Potentiometric Titration Plots and Fitted Curves with Donnan, Impermeable Sphere, and Cylindrical Models 211
- E: Specific Viscosity (η_{sp}) Plots with respect to pH for anionic PAMs 220
- F: Matlab® Code for Potentiometric Titration Data Fitting with DN, IS, and CY models 223
  - F.1 Code for data fitting with DN model 223
  - F.2 Code for data fitting with IS model 225
  - F.3 Code for data fitting with CY model 227
- G: Finite Difference Approximation of Multi-Dimensional PBEs 229
  - G.1 PBE Differential equations 229
  - G.2 Operator splitting algorithm 230
  - G.3 Finite Difference approximation 230
  - G.4 Numerical strategy for an operator splitting algorithm 233
  - G.5 Boundary conditions 234
  - G.6 References 236
- H: Matlab® Code for the DPBE-CFD Model 237

LIST OF TABLES

Table Page

2.1 Polyacrylamide characteristics provided by manufacturers for CD and MW 18

2.2 Mark–Houwink-Sakurada (MHS) equations to estimate MW with measured intrinsic viscosities ($[\eta] = K \cdot MW^{a}$). All the equations were developed at 25 ^{o}C. 23

2.3 Molecular weight and root-mean-square radius estimated with light scattering analyses for various nonionic and anionic PAM samples. Data represent Mean ± Standard Error, of which error was obtained in the data fitting process to the Zimm-Berry plot. 29

2.4 Molecular weight estimated with the intrinsic viscosity measurement for various nonionic and anionic PAM samples. Data represent Mean ± Error, of which error was set as the difference between the paired MWs obtained from Kreamer and Huggins plots. Numbers in the parentheses represent $k'' - k' = \{slope/[\eta]^2\}_{Huggins} - \{slope/[\eta]^2\}_{Kreamer}$ 32

2.5 Summarized results from MW and CD measurements for nonionic anionic PAMs. Data represent Mean ± Standard Error for triplicate measurements. 34

3.1 Measured molecular weights (MW) and ionizable site densities (ISD) of the pre-cleaned Kimera® PAMs used in electrostatic interaction model applications 62

4.1 Nonlinear data fitting results onto the Langmuir isotherm ($q_e = q_{,max} \times C_e/(K_s+C_e)$) for 1.5K, 10K, 0.6~1M, 5~6M, and 18M PAMs 94

5.1 Measured molecular weights (MW) and charge density (CD) of the pre-cleaned Kimera® PAMs used in adsorption and flocculation tests. Errors of MWs represent the lowest and highest values calculated in the data fitting procedures. Errors of CDs represent the standard deviations of the triplicate samples. 116

List of Tables (Continued)

Table Page

6.1 The simplified numerical algorithm for solving the CFD-DPBE model 160

6.2 Flow field characteristics and flocculation/sedimentation efficiencies for three different turbulent conditions in the mixing zone 170

LIST OF FIGURES

Figure Page

1.1 Molecular structures of the repeating units of (a) nonionic and (b) anionic PAMs. (c) Schematic diagram of a PAM molecule (adopted from Barvenik, 1994) 3

2.1 Schematic diagram of a polymerized anionic PAM molecule (adopted from Barvenik, 1994). 15

2.2 (a) schematic diagram describing the theory of MALS analysis (adopted from *http://www.wyatt.com/theory/rayleighscattering/size.cfm*) and (b) an example of scattered light intensity data measured with 90^o angle detector with tolune (for calibration), polyethyleneglycol (for normalization), and N2 PAM solutions in 1 M NaCl (for sample measurements) 21

2.3 (a) a picture of Cannon-Fenske routine viscometer (adopted from *http://www.cannoninstrument.com/cfr.htm*) and (b) an example of Huggins and Kreamer plots 23

2.4 (a) an example of chromatographic data with CHN elemental analysis and (b) estimated carbon and nitrogen contents and charge densities for various anionic PAM samples. 25

2.5 Acid-base titration curves used to estimate CD of A3 PAM sample in different NaCl concentrations. Symbols, ○, ×, and □, represent experimental data obtained in 0.001, 0.01, and 0.1 M NaCl solutions, respectively 26

2.6 Zimm-Berry plots of the triplicate light scattering analyses to estimate MW of N2 PAM sample 28

2.7 Kreamer and Huggins plots used to estimate MW of N2 PAM sample in different solution conditions with various salt species and concentrations. Dotted lines represent 95% confidence level between the fitted line and experimental data. The estimated MW ± Error is shown in the figure. Error was set as the difference between the paired MWs obtained from Kreamer and Huggins plots 31

List of Figures (Continued)

Figure Page

2.8 Comparison between (a) MWs provided by the manufacturer and MWs measured with a light scattering analysis, (b) MWs provided by the manufacturer and MWs measured with an intrinsic viscosity measurement technique, and (c) MWs between two different measurement techniques, for nonionic PAMs (N1, N2, and, N3). 39

2.9 Comparison between MWs measured with a light scattering analysis and MWs with an intrinsic viscosity measurement technique, for nonionic and anionic PAMs, (a) before and (b) after applying the correction factor (MW_W/MW_V = 1.7129) 40

2.10 Number and weight distributions for a polydisperse PAM sample for an illustration purpose 42

2.11 Comparison between CDs measured with CHN elemental analysis and CDs with acid-base titration for nonionic and anionic PAMs 45

3.1 Schematic diagrams of co- and counter-ion distributions and electrostatic interaction potential distributions around polyelectrolytes in aqueous solutions in IS, DN, and CY models (adopted from Avena *et al.* (1999)) 57

3.2 Experimental and simulated potentiometric titration curve with IS model application for ISD35-1 PAM ($MW_v = 2.18 \times 10^6$ g/mol, ISD = 35%) at 0.0196M ionic strength. Degree of ionization (α) represents the normalized ionized site density of a polyelectrolyte by assuming the maximum ionized density as one. The inner plot represents SRE *versus* S plot in the model-data fitting procedure. 64

3.3 (a) typical experimental and simulated potentiometric titration curves with application of three different electrostatic interaction models. (b) and (c) represent residual plots between experimental and simulated data. ISD35-1 PAM ($MW_v = 2.18 \times 10^6$ g/mol, ISD = 35%) was used. (See Appendix D for all the other PAMs) 67

3.4 (a) specific viscosities (η_{sp}) measured at different ionic strengths and pHs for ISD25-3 PAM ($MW_v = 2.18 \times 10^6$ g/mol, ISD = 35%) (See Appendix E for all the other PAMs) and (b) schematic diagrams of the polymer conformation assumed in DN and IS model and the one measured in specific viscosity tests with increasing pH 69

List of Figures (Continued)

Figure Page

3.5 Comparison between measured specific viscosities at pH 9 and estimated specific surface areas for ISD25 group PAMs which have different molecular weights 71

3.6 (a) comparison between measured specific viscosities (pa-s) and estimated specific volume (m^3/g) with DN model and (b) comparison between measured specific viscosities (pa-s) and estimated specific viscosities (m^2/g) with IS model 72

3.7 (a) experimental and simulated potentiometric titration curves and (b) residual plots between experimental data and best-fit curves for ISD10 PAM in different ionic strengths. All the simulated curves were obtained in application of CY model with constant model parameters (L_{seg} = 0.2 nm and a = 0.66 nm) (Ullner and Jonsson, 1996). 75

3.8 (a) experimental and simulated potentiometric titration curves and (b) residual plots between experimental data and best-fit curves for ISD18 PAM in different ionic strengths. All the simulated curves were obtained in application of CY model with constant model parameters (L_{seg} = 0.2 nm and a = 0.66 nm) (Ullner and Jonsson, 1996). 75

3.9 (a) experimental and simulated potentiometric titration curves and (b) residual plots between experimental data and best-fit curves for ISD20 PAM in different ionic strengths. All the simulated curves were obtained in application of CY model with constant model parameters (L_{seg} = 0.2 nm and a = 0.66 nm) (Ullner and Jonsson, 1996). 76

3.10 (a) experimental and simulated potentiometric titration curves and (b) residual plots between experimental data and best-fit curves for ISD25 PAMs in different ionic strengths. All the simulated curves were obtained in application of CY model with constant model parameters (L_{seg} = 0.2 nm and a = 0.66 nm) (Ullner and Jonsson, 1996). 76

List of Figures (Continued)

Figure Page

3.11 (a) experimental and simulated potentiometric titration curves and (b) residual plots between experimental data and best-fit curves for ISD35 PAMs in different ionic strengths. All the simulated curves were obtained in application of CY model with constant model parameters (L_{seg} = 0.2 nm and a = 0.66 nm) (Ullner and Jonsson, 1996). 77

3.12 Schmatic diagram of conformational transition of polyelectrolytes with respect to degree of ionization (α) and pH.......... 79

4.1 (a) schematic digram of Couttee-type viscometer, (b) an example plot of steady-shear viscosity *versus* shear rate at different PAM concentrations, and (c) an example plot of zero-shear specific viscosity versus PAM concentration.......... 91

4.2 Experimental results of the adsorption tests. (a) Adsorption isotherm curves of 1.5 K, 10 K, 0.6~1 M, 5~6 M, and 18 M PAMs and (b) Maximum adsorption capacity (mgPAM/gKaolite) *versus* PAM MW 94

4.3 Experimental results of the steady-shear viscosity measurements. (a) Steady-shear viscosity *versus* shear rate at different PAM concentrations for 18 M PAM and (b) zero-shear specific viscosity *versus* PAM concentration for 1.5 K, 10 K, 0.6~1 M, 5~6 M, and 18 M PAMs.......... 97

4.4 The experimental results of the flocculation tests with 0.6~1 M and 5~6 M PAMs at different shear conditions. Figures (a) and (b) represent the plots of adsorption capacities *versus* PAM dose concentrations for 0.6~1 M and 5~6 M, respectively. Figures (c) and (d) represent the plots of relative turbidities *versus* PAM dose concentrations (mg/L), for 0.6~1 M and 5~6 M, respectively.......... 102

4.5 Schematic diagram of equilibrium and nonequilibrium flocculation mechanisms occurring in PAM- and kaolinite-containing suspensions. ... 103

5.1 (a) a raw image and (b) a processed image of a fixed floc sample in an agar plates 120

List of Figures (Continued)

Figure Page

5.2 PAM adsorption isotherm (mgPAM/gKaolinite), residual suspended solid concentration (mgKaolinite/L), and volume-averaged floc diameter (μm) with increasing PAM dose concentrations for different PAM species and solution chemistries 128

5.3 (a) maximum adsorption capacity (mgPAM/gKaolinite) and (b) maximum volume-averaged floc size (μm) in the range of applied PAM dose concentrations for different PAM species and solution conditions 129

5.4 Adsorption isotherm curves for different PAM species and solution conditions, A100H in 1 mM NaCl, A100H in 3 mM NaCl, and N300 in 1 mM NaCl... 131

5.5 Trend curves of (a) CD *versus* maximum adsorption capacity and (b) MW *versus* maximum volume-averaged floc size for different solution chemistries, 3 mM NaCl, 1 mM $CaCl_2$, and 1 mM $MgCl_2$.......... 133

5.6 (a) measured zeta potentials with increasing PAM dose concentration and (b) zeta potentials with increasing PAM adsorption capacity for different PAM species in 3 mM NaCl aqueous solution...................... 134

5.7 (a) zeta potential and Ca^{2+} adsorption capacity *versus* PAM dose and (b) Ca^{2+} adsorption capacity *versus* PAM adsorption capacity in 1 mM $CaCl_2$ aqueous solution.
(c) zeta potential and Mg^{2+} adsorption capacity *versus* PAM dose and (d) Mg^{2+} adsorption capacity *versus* PAM adsorption capacity in 1 mM $MgCl_2$ aqueous solution 136

5.8 Schematic diagram of cationic bridging adsorption and flocculation mechanisms in mixed suspensions of divalent cations, PAM, and kaolinites 137

6.1 Diagram of aggregation and break-up processes for the *i* = 3 particle/floc size class in the DPBE 156

6.2 Schematic diagram of a flocculent-aided sediment retention pond with a turbulent mixing zone by a sedimentation basin and discharge drain 161

Figure Page

6.3 Schematic diagram of the computational domain representing a simplified turbulent mixing zone in a sediment retention pond............. 162

6.4 Steady state flow field profiles from CFD simulation for (a) Case 1 : low turbulence, (b) Case 2 : moderate turbulence, and (c) Case 3 : high turbulence. Arrows and colors represent flow velocities and shear rates, respectively... 164

6.5 (a) Mass fractions and balances and (b) mass mean floc diameter (D_{mm}) with respect to dimensionless residence time, which is normalized by dividing real fluid residence time with theoretical mean residence time... 166

6.6 Mass mean floc diameter (D_{43}) distributions in the computational domain. The distributions of Case 1, Case 2, and Case 3 are listed from the top.. 168

6.7 Solid concentration distributions in the computational domain. The distributions of Case 1, Case 2, and Case 3 are listed from the top. 168

6.8 Cumulative mass distribution of particle/floc sizes at the outlet of the model basin.. 170

A.1 Zimm-Berry plots for triplicate N1 PAM samples used to estimate molecular weights. 186

A.2 Zimm-Berry plots for triplicate N2 PAM samples used to estimate molecular weights. 187

A.3 Zimm-Berry plots for triplicate N3 PAM samples used to estimate molecular weights. 188

A.4 Zimm-Berry plots for triplicate A1 PAM samples used to estimate molecular weights. 189

A.5 Zimm-Berry plots for triplicate A2 PAM samples used to estimate molecular weights. 190

A.6 Zimm-Berry plots for triplicate A3 PAM samples used to estimate molecular weights. 191

List of Figures (Continued)

Figure Page

A.7 Zimm-Berry plots for triplicate A4 PAM samples used to estimate molecular weights. 192

A.8 Zimm-Berry plots for triplicate A5 PAM samples used to estimate molecular weights. 193

A.9 Zimm-Berry plots for triplicate A6 PAM samples used to estimate molecular weights. 194

A.10 Zimm-Berry plots for triplicate A7 PAM samples used to estimate molecular weights. 195

A.11 Zimm-Berry plots for triplicate A8 PAM samples used to estimate molecular weights. 196

B.1 Kreamer and Huggins plots of N1 PAM sample in different background salt species and concentrations, used to estimate molecular weights. 197

B.2 Kreamer and Huggins plots of N2 PAM sample in different background salt species and concentrations, used to estimate molecular weights. 198

B.3 Kreamer and Huggins plots of N3 PAM sample in different background salt species and concentrations, used to estimate molecular weights. 199

B.4 Kreamer and Huggins plots for triplicate A1 PAM samples in 0.2 M Na_2SO_4, used to estimate molecular weights. 200

B.5 Kreamer and Huggins plots for triplicate A2 PAM samples in 0.2 M Na_2SO_4, used to estimate molecular weights. 201

B.6 Kreamer and Huggins plots for triplicate A3 PAM samples in 0.2 M Na_2SO_4, used to estimate molecular weights. 202

B.7 Kreamer and Huggins plots for triplicate A4 PAM samples in 0.2 M Na_2SO_4, used to estimate molecular weights. 203

B.8 Kreamer and Huggins plots for triplicate A5 PAM samples in 0.2 M Na_2SO_4, used to estimate molecular weights. 204

B.9 Kreamer and Huggins plots for triplicate A6 PAM samples in 0.2 M Na_2SO_4, used to estimate molecular weights. 205

List of Figures (Continued)

Figure Page

B.10 Kreamer and Huggins plots for triplicate A7 PAM samples in 0.2 M Na_2SO_4, used to estimate molecular weights. 206

B.11 Kreamer and Huggins plots for triplicate A8 PAM samples in 0.2 M Na_2SO_4, used to estimate molecular weights. 207

C.1 Potentiometric titration curves and equations for background subtraction of the deprotonation capacity in 0.001 M, 0.01 M, and 0.1 M NaCl solutions. 208

C.2 Potentiometric titration curves for N1, N2, A1, A2, and A3 PAM samples. 209

C.3 Potentiometric titration curves for A4, A5, A6, A7, and A8 PAM samples. 210

D.1 Potentiometric titration plots for ISD10 PAM in different salt concentrations and fitted curves with DN model. 211

D.2 Potentiometric titration plots for ISD18 PAM in different salt concentrations and fitted curves with DN model. 211

D.3 Potentiometric titration plots for ISD20 PAM in different salt concentrations and fitted curves with DN model. 212

D.4 Potentiometric titration plots for ISD25 PAMs in different salt concentrations and fitted curves with DN model. 212

D.5 Potentiometric titration plots for ISD35 PAMs in different salt concentrations and fitted curves with DN model. 213

D.6 Potentiometric titration plots for ISD10 PAM in different salt concentrations and fitted curves with IS model. 214

D.7 Potentiometric titration plots for ISD18 PAM in different salt concentrations and fitted curves with IS model. 214

D.8 Potentiometric titration plots for ISD20 PAM in different salt concentrations and fitted curves with IS model. 215

List of Figures (Continued)

Figure Page

D.9 Potentiometric titration plots for ISD25 PAMs in different salt concentrations and fitted curves with IS model. 215

D.10 Potentiometric titration plots for ISD35 PAMs in different salt concentrations and fitted curves with IS model. 216

D.11 Potentiometric titration plots for ISD10 PAM in different salt concentrations and fitted curves with CY model. 216

D.12 Potentiometric titration plots for ISD18 PAM in different salt concentrations and fitted curves with CY model. 216

D.13 Potentiometric titration plots for ISD20 PAM in different salt concentrations and fitted curves with CY model. 218

D.14 Potentiometric titration plots for ISD25 PAMs in different salt concentrations and fitted curves with CY model. 218

D.15 Potentiometric titration plots for ISD35 PAMs in different salt concentrations and fitted curves with CY model. 219

E.1 Specific Viscosity (η_{sp}) Plots for ISD10 PAM in different salt concentrations. 220

E.2 Specific Viscosity (η_{sp}) Plots for ISD18 PAM in different salt concentrations. 220

E.3 Specific Viscosity (η_{sp}) Plots for ISD20 PAM in different salt concentrations. 221

E.4 Specific Viscosity (η_{sp}) Plots for ISD25 PAMs in different salt concentrations. 221

E.5 Specific Viscosity (η_{sp}) Plots for ISD35 PAMs in different salt concentrations. 222

G.1 A typical computation cell within the problem domain. F and G represent mass fluxes through the cell boundaries...................... 231

G.2 Flowchart for solving DPBEs with operator splitting algorithm.............. 233

List of Figures (Continued)

Figure Page

G.3 Schematic diagram of the problem domain 234

G.4 Boundary conditions for advection based transport equations 234

G.5. Boundary conditions for dispersion-reaction equations 235

CHAPTER 1. INTRODUCTION

Soil erosion and sediment-laden runoff occur from both urban and rural areas during storm events. In general, the problem increases with increasing land disturbance (*e.g.*, tillage, mining, road grading, rural to urban land conversion, and population density increase). The most problematic sediment particles typically are of colloidal-size, and if not controlled they can end up in various receiving water bodies and contribute to the coating of bottom sediments, algae blooms, oxygen depletion, and food-chain impairments (Stumm and Morgan, 1996; Chapra, 1997; Schwarzenbach *et al.*, 2003). These are considered as all major water quality problems by the Environmental Protection Agency (USEPA), and they are likely to worsen in the future due to population growth, urban sprawl, *etc*. For example, among the major nonpoint source pollutants of concern, the USEPA has identified pathogens and suspended sediment as the first and second most frequent stressors of rivers and streams (USEPA, 2002). Attempts to control sediment-containing runoff have involved the establishment of many small to medium sediment retention ponds. These ponds collect sediment, which can be removed and disposed of in an environmentally acceptable manner when the ponds reach their storage capacity.

Typically, sediment retention ponds are operated in a passive mode. Stormwater containing suspended sediment enters the pond, drops whatever sediment that naturally settles out, and then exits the pond (typically via a standpipe or other flow control structure). This works reasonably well with coarser particles having adequate settling velocities. However, clays, pathogens and other colloidal-sized particles often do not have adequate time to settle completely, so they simply pass through the retention pond along with the flow of water (Pitt *et al.*, 1995; Tuccillo, 2006; Li *et al.*, 2007). To counteract this effect, a few operators are now experimenting with the addition of flocculating agents to the inflow during storm events, which can greatly improve the retention properties of the ponds (Kang *et al.*, 2007; Sojka *et al.*, 2007). Among various flocculants used, nonionic and anionic polyacrylamides (called PAMs) have been reported as the most applicable polymeric flocculants due to their colloid flocculation ability and reported low-toxicity to plants and animals (McCollister *et al.*, 1965; Wallace and Wallace, 1986; Stephens, 1991). A drawback, however, is the relatively high cost of PAM. Aluminum sulfate (alum) and gypsum are also common coagulants. PAMs function well at low concentrations, and they are finding increased applications in irrigation management and soil erosion control (McLaughlin and Bartholomew, 2007). Therefore, nonionic and anionic PAMs have been chosen as target flocculants for study in this research.

PAMs can be polymerized as either linear or cross-linked forms. However, in the field of water treatment or soil erosion control, linear PAMs are mainly used. Based on the functional groups along backbone chains, PAMs can be classified into three types, nonionic, anionic, and cationic PAMs. Nonionic PAMs can be formed simply by the polymerization of monomeric acrylamide, whereas cationic and anionic PAMs can be manufactured by copolymerization of acrylamide and cationic or anionic monomers. The molecular weights of PAMs span from a few thousand up to 20 million g/mol (Barvenik, 1994). Figure 1.1 shows the typical repeating units of nonionic and anionic PAMs and the schematic diagram of a polymerized PAM molecule. The fully anionic PAM is named as polyacrylate (PAA).

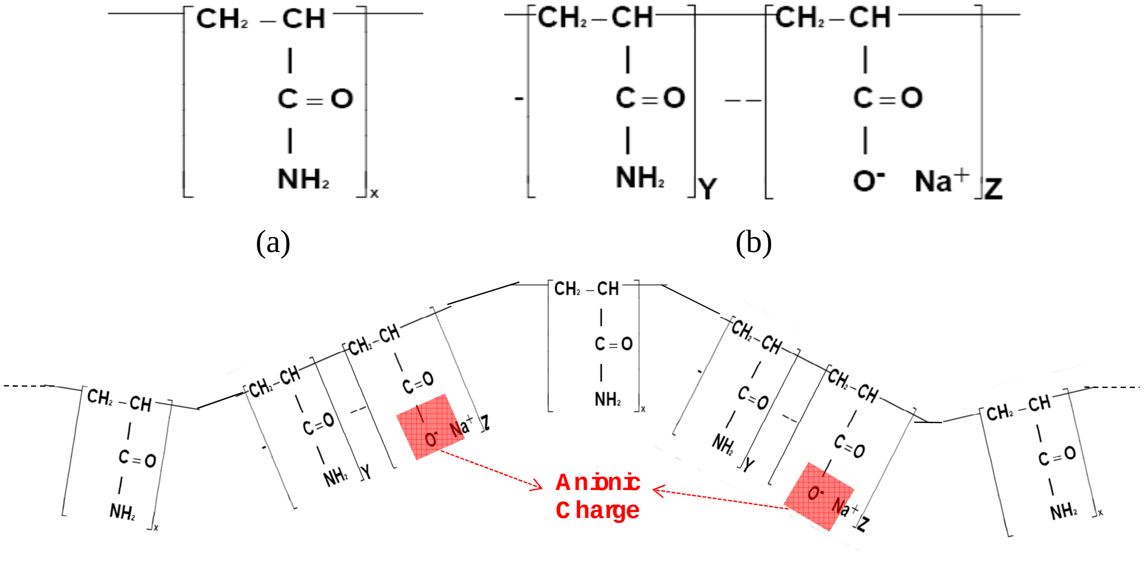

(a) (b)

(c)

Figure 1.1. Molecular structures of the repeating units of (a) nonionic and (b) anionic PAMs. (c) Schematic diagram of a PAM molecule (adopted from Barvenik, 1994).

Reading contemporary literature and talking to sediment pond operators supports the conclusion that automated flocculant-aided sediment retention ponds are going to become increasingly important in future years as a means to minimize the detrimental effects of erosion and non-point-source water pollution on people and the environment (Gowdy and Iwinski, 2007; Harper, 2007). To date, use has been driven more by practicing engineers and trial-and-error approaches than by logical and consistent design approaches (Harper, 2007). However, the operation of such ponds is complicated, involving various physicochemical processes, such as adsorption and flocculation processes, and fluid mechanic and mass transport problems, such as particle transport and sedimentation in a turbulent fluid field. Most existing pond systems are not designed and operated in a consistent manner based on fundamental principles. For example, many designs are based simply on an ad-hoc rule such as a set pond volume per hectare of drained area (Akan and Houghtalen, 2003). So the entire field would benefit from a better understanding of the fundamental physicochemical processes occurring in a flocculant-aided sedimentation pond and the development of a realistic, physically-based model for designing and optimizing sediment retention ponds. In the main chapters of this dissertation, both experimental and modeling studies are presented, including characterization of PAMs (Chapter 2), application of electrostatic interaction models in predicting acid-base chemistry of PAMs (Chapter 3), investigation on physicochemical processes occurring in PAM- and clay-containing suspensions (Chapter 4 and 5), and development of a flocculant-aided pond simulation model (Chapter 6). The combined product will be a tool for the optimum design and operation of a PAM-aided sediment retention pond. The research objectives of the individual research tasks will be briefly introduced in the following paragraphs.

1.1 Characterizing the Molecular Weight and Charge Density of PAMs (Chapter 2)

Among the various properties of PAMs, molecular weight (MW, g/mol) and anionic charge density (CD, $\frac{\text{No. of Charged Units}}{\text{No. of Repeating Units}} \times 100$ %) have been reported as the key characteristics in determining physicochemical processes in PAM- and clay-containing suspensions. For example, many previous physicochemical experiments in PAM- and clay-containing suspensions have proven to be the decisive characteristics of MW and CD with respect to adsorption capacities and flocculation efficiencies (Levy and Agassi, 1995; Green *et al.*, 2000; Chibowski and Wisniewska, 2002; Heller and Keren, 2002; Heller and Keren, 2003; Farrokhpay *et al.*, 2004). The MW and CD of PAM stabilizers or flocculants can be measured with various state-of-the-art techniques such as multi-angle light scattering analysis (MALS) or gel permeation chromatography (GPC) for MWs and Carbon-Hydrogen-Nitrogen (CHN) elemental analysis for CDs (Francois *et al.*, 1979; Klein and Westerkamp, 1981; Griebel *et al.*, 1991; Hunkeler *et al.*, 1992; Scott *et al.*, 1996; Sperling, 2006). However, lack of accessibility and the difficulty of these elaborate measurement techniques are limiting factors for on-site measurements by soil/environmental scientists or engineers who are inexperienced in polymer sciences. Thus, in this research, we chose two simple measurement techniques, an intrinsic viscosity measurement technique and an acid-base titration method, and estimated their applicability and validity as simple and easy alternative techniques for MW and CD measurements (Klein and Conrad, 1978; McCarthy *et al.*, 1987; Griebel *et al.*, 1991; Wu *et al.*, 1991). In Chapter 2, the potential and limitation of these simple measurement techniques will be discussed in comparison with more elaborate techniques.

1.2 Characteristic Behaviors of PAMs in the Aqueous Phase (Chapter 3)

In Chapter 3, simplified analytical models (impermeable sphere (IS), Donnan (DN), and cylindrical (CY) models) were evaluated for their validity and applicability in predicting the electrostatic interaction acid-base chemistry of anionic PAMs. Though these simplified models do not represent all the physicochemical phenomena occurring at PAM-solution interfaces, they were demonstrated to be practical tools for predicting the electrostatic interaction chemistry of polyelectrolytes with their simplified hypothetical shapes for polyelectrolyte molecules (Hill, 1955; Ullner and Jonsson, 1996; Avena *et al.*, 1999; Koopal *et al.*, 2005; Saito *et al.*, 2005). In a comparative study of experimental results and model theories, with a series of weakly charged linear polyacrylamide-co-acyliates (anionic PAM), we tried to speculate on the rationality of the models with respect to the hypothetical conformations of a PAM and to study on the reciprocal effects between a polyelectrolyte's conformation and electrostatic interaction chemistry.

1.3 Molecular Weight Effects on PAM-induced Adsorption and Flocculation (Chapter 4)

Adsorption and flocculation processes in PAM- and clay-containing suspensions are known to be affected by various PAM and solution characteristics, such as PAM molecular weight (MW) and charge density (CD), and the pH, ionic strength, and salt species of an aqueous solution. In Chapter 4, MW has been chosen among various factors as a key factor in adsorption and flocculation tests, because it may be customized in the manufacturing process and used as the controlling factor in field applications involving adsorption and flocculation. In adsorption tests, the hypothesis that the adsorption capacity of a PAM increases with increasing MW (Levy and Agassi, 1995; Green *et al.*, 2000; Heller and Keren, 2002) was tested again in the present study, and in flocculation tests, nonequilibrium flocculation was investigated with PAMs having different MWs under various fluid shear conditions (Pelssers *et al.*, 1989; Pelssers *et al.*, 1990; Lu and Pelton, 2001). The high-MW PAM and the strong fluid shear rate were hypothesized to give rise to a transient and elongated conformation of the adsorbed polymeric chains and consequently to enhance the flocculation efficiency. In Chapter 4, the conformity to and the deviation from the MW-related hypotheses are discussed closely with the observed experimental results from the adsorption and flocculation tests.

1.4 Effects of PAM and Solution Properties on Adsorption and Flocculation (Chapter 5)

In addition to MW described above, other PAM and solution characteristics were investigated with respect to their effects on adsorption and flocculation processes. Firstly, the characteristics of anionic PAMs, molecular weight (MW) and charge density (CD) were chosen as the experimental parameters in adsorption and flocculation tests (Levy and Miller, 1999; Green *et al.*, 2000; Heller and Keren, 2002; Heller and Keren, 2003). Secondly, the effects of solution properties on adsorption and flocculation, such as the constituent cation species, were investigated in the presence of different monovalent or divalent cations (Na^+, Ca^{2+}, and Mg^{2+}). Chapter 5 elucidates the effects of PAM and solution properties on adsorption and flocculation processes.

1.5 Simulation of Turbulent Flocculation and Sedimentation (Chapter 6)

For the optimal design and operation of PAM-aided sediment retention ponds, what is needed beyond the experimental findings in the previous chapters is a realistic and mechanistic theory describing flocculation and non-homogeneous turbulent sedimentation in retention ponds and a mathematical tool for solving the rather complex governing equations of flocculation and sedimentation. This chapter deals primarily with the mathematical formulation and computation underlying flocculation and sedimentation processes in flocculant-aided sediment retention ponds. One of the most realistic ways to simulate flocculation and non-homogeneous turbulent sedimentation in retention ponds is by applying the Population Balance Equations (PBE) within a Computational Fluid Dynamics (CFD) framework for solving the Navier-Stokes equations. Thus, discretized population balance equations combined with a fluid dynamics model (CFD-DPBE model) was set up and the applicability of the combined model was tested in the turbulent mixing zone of sediment retention ponds. The mathematical formulation and application strategy of the CFD-DPBE model were studied in a two-dimensional computational domain representing the vertical cross-section of the turbulent mixing zone of a flocculant-aided sediment retention pond.

1.6 References

Akan, A. O., and R. J. Houghtalen, 2003, *Urban Hydrology, Hydraulics and Stormwater Quality,* John Wiley & Sons, Hoboken, NJ

Avena, M. J., L. Koopal, and W. H. v. Riemsdijk, 1999, Proton binding to humic acids: electrostatic and intrinsic interactions, *Journal of Colloid and Interface Science,* **217**, 37-48

Chapra, S. C., 1997, *Surface Quality Modeling*, McGraw-Hill,

Chibowski, S., and M. Wisniewska, 2002, Study of electrokinetic properties and structure of adsorbed layers of polyacrylic acid and polyacrylamide at Fe_2O_3-polymer solution interface, *Colloids and Surfaces A: Physicochem. Eng. Aspects*, **208**, 131-145

Farrokhpay, S., G.E. Morris, D. Fornasiero, and P. Self, 2004, Effects of chemical functional groups on the polymer adsorption behavior onto titania pigment particles, *Journal of Colloid and Interface Science*, **274**, 33-40

Francois, J., D. Sarazin, T. Schwartz, and G. Weill, 1979, Polyacrylamide in water: molecular weight dependence of $<R^2>$ and $[\eta]$ and the problem of the excluded volume exponent, *Polymer*, **20**, 969-975

Gowdy, W., and S. R. Iwinski, 2007, Removal efficiencies of polymer enhanced dewatering systems. *In Proceedings of the 9th Biennial Conference on Stormwater Research & Watershed Management*, Orlando, FL, May 2 - 3, 2007.

Green, V. S., D. E. Stott, L. D. Norton, and J. G. Graveel, 2000, Polyacrylamide Molecular Weight and Charge Effects on Infiltration under Simulated Rainfall, *Soil Sci. Soc. Am. J.*, **64**, 1786-1791

Griebel, T., W.M. Kulicke, and A. Hashemzadeh, 1991, Characterization of water-soluble, cationic polyelectrolytes as exemplified by poly(acrylamide-co-trimethylammoniumethylethacryate chloride) and the establishment of structure-property relationships, *Colloid & Polymer Science*, **269**, 113-120

Harper, H. H., 2007, Current research and trends in alum treatment of stormwater runoff. *In Proceedings of the 9th Biennial Conference on Stormwater Research & Watershed Management*, Orlando, FL, May 2 - 3, 2007.

Heller, H., and R. Keren, 2002, Anionic Polyacrylamide Polymers Effect on Rheological Behavior of Sodium-Montmorillonite Suspensions, *Soil Sci. Soc. Am. J.*, **66**, 19-25

Heller, H., and R. Keren, 2003, Anionic polyacrylaide polymer adsorption by pyrophyllite and montmorillonite, *Clays and Clay Minerals*, **51**(3), 334-330

Hill, T. L., 1955, Approximate calculation of the electrostatic free energy of nucleic acids and other cylindrical macromolecules, *Arch. Biochem. Biophys.*, **57**, 229-239

Hunkeler, D., X.Y. Wu, and A. E. Hamielec, 1992, Molecular weight characterization of polyacrylamide-co-sodium acrylate. II. Light scattering, *Journal of Applied Polymer Science*, **46**, 649-657

Kang, J. H., Y. X. Li, S. L. Lau, M. Kayhanian, and M. K. Stenstrom, 2007, Particle destabilization in highway runoff to optimize pollutant removal, *Jounal of Environmental Engineering - ASCE*, **133**, 426-434

Klein, J., and K. D. Conrad, 1978, Molecular-weight determination of poly(acrylamide) and poly(acrylamide-co-sodium acrylate), *Macromolekulare Chemie - Macromolecular Chemistry and Physics*, **179**(6), 1635-1638

Klein, J., and A. Westerkamp, 1981, Peculiarities of polyacrylamide analysis by aqueous GPC, *Journal of Polymer Science: Polymer Chemistry Edition*, **19**, 707-718

Koopal, L. K., T. Saito, J. P. Pinheiro, and W. H. v. Riemsdijk, 2005, Ion binding to natural organic matter: general considerations and the NICA-Donnan model, *Colloids and Surfaces A: Physicochem. Eng. Aspects*, **265**, 40-54

Levy, G. J., and M. Agassi, 1995, Polymer molelcular weight and degree of drying effects on infiltration and erosion of three different soils, *Aust. J. Soil Res.*, **33**, 1007-1018

Levy, G. J., and W. P. Miller, 1999, Polyacrylamide adsorption and aggregate stability, *Soil & Tillage Research*, **51**, 121-128

Li, Y., A. Deletic, and T. D. Fletcher, 2007, Modelling wet weather sediment removal by stormwater constructed wetlands: Insights from a laboratory study, *Journal of Hydrology*, **338**, 385-396

Lu, C., and R. Pelton, 2001, PEO Flocculation of polystyrene-core poly(vinylphenol)-shell latex: an example of ideal bridging, *Langmuir*, **17**, 7770-7776

McCarthy, K. J., C.W. Burkhardt, and D. P. Parazak, 1987, Mark-Houwink-Sakurada constants and dilute solution behavior of heterodisperse poly(acrylamide-co-sodium acrylate) in 0.5M and 1M NaCl, *Journal of Applied Polymer Science*, **33**, 1699-1714

McCollister, D. D., C. L. Hake, S. E. Sadek, and V. K. Rowe, 1965, Toxicologic investigations of polyacrylamides, *Toxicol. Appl. Pharmacol.*, **7**, 639-651

McLaughlin, R. A., and N. Bartholomew, 2007, Soil factors influencing suspended sediment flocculation by polyacrylamide, *Soil Sci. Soc. Am. J.*, **71**, 537-544

Pelssers, E. G. M., M.A. Cohen Stuart, and G. J. Fleer, 1989, Kinetic aspects of polymer bridging: equilibrium flocculation and nonequilibrium flocculation, *Colloids and Surfaces,* **38**, 15-25

Pelssers, E. G. M., M.A. Cohen Stuart, and G. J. Fleer, 1990, Kinetics of bridging flocculation, *J. CHEM. SOC. FARADAY TRANS.*, **86**(9), 1355-1361

Pitt, R., R. Field, M. Lalor, and M. Brown, 1995, Urban stormwater toxic pollutant, assessment, sources, and treatability, *Water Environment Research*, **67**, 260-275

Saito, T., S. Nagasaki, S. Tanaka, and L. Koopal, 2005, Electrostatic interaction models for ion binding to humic substances, *Colloids and Surfaces A: Physicochem. Eng. Aspects,* **265**, 104-113

Schwarzenbach, R. P., P.M.Gschwend, and D. M. Imboden, 2003, *Environmental Organic Chemistry, 2nd ed,* Johns Wiley & Sons, Inc., Hoboken, New Jersey.

Scott, J. P., P.D. Fawell, D.E. Ralph, and J. B. Farrow, 1996, The shear degradation of high-molecular-weight flocculant solutions, *Journal of Applied Polymer Science,* **62**, 2097-2106

Sojka, R. E., D. L. Bjorneberg, J. A. Entry, R. D. Lentz, and W. J. Orts, 2007, Polyacrylamide in agriculture and environmental land management, *Advances in Agronomy,* **92**, 75

Sperling, L. H., 2006, *Introduction to Physical Polymer Science, 4th Edition,* John Wiley & Sons, Inc., Hoboken, NJ

Stephens, S. H., 1991, Final report on the safety assessment of polyacrylamide, *J. Am. Coll. Toxicol.*, **10**, 193-202

Stumm, W., and J. J. Morgan, 1996, *Aquatic Chemistry, 3rd ed*, Johns Wiley & Sons, Inc., Canada.

Tuccillo, M. E., 2006, Size fractionation of metals in runoff from residential and highway storm sewers, *Science of the Total Environment*, **355**, 388-300

Ullner, M., and B. Jonsson, 1996, A Monte Carlo study of titrating polyelectrolytes in the presence of salt, *Macromolecules*, **29**, 6645-6655

USEPA, 2002, *National Water Quality Inventory: 2000 Report*, EPA-841-R-02-001, Office of Water, U.S. Environmental Protection Agency, Washington, DC

Wallace, A., and G. A. Wallace, 1986, Effects of soil conditioners on emergence and growth of tomato, cotton, and lettuce seedlings, *Soil Science*, **141**, 313-316

Wu, X. Y., D. Hunkeler, A.E. Hamielec, R.H. Pelton, and D. R. Woods, 1991, Molecular weight characterization of poly(acrylamide-co-sodium acrylate). I. Viscometry, *Journal of Applied Polymer Science*, **42**, 2081-2093

CHAPTER 2. APPLICABILITY OF SIMPLE MEASUREMENT TECHNIQUES IN ESTIMATING MOLECULAR WEIGHTS AND CHARGE DENSITIES OF POLYACRYLAMIDE SOIL STABILIZERS OR FLOCCULANTS

2.0 Abstract

Nonionic and anionic polyacrylamides have been used as soil stabilizers and flocculants for several decades due to their stabilization and flocculation capabilities and their reported non-toxicity. Among various characteristics of polyacrylamides, molecular weight and charge density have been reported as decisive characteristics on soil stabilization and flocculation in many soil/environmental researches. Nevertheless, they have been rarely measured in-house by soil/environmental scientists or engineers in the previous researches due to the difficulty or absence of feasible measuring techniques. Thus, in this research, simple and easy characterization techniques, an intrinsic viscosity measurement technique for molecular weight and an acid-base titration for charge density, were tested for their applicability in comparison with state-of-the-art techniques. Molecular weights estimated with simple intrinsic viscosity technique generally were lower by a constant ratio compared to those measured using a state-of-the-art light scattering analysis. Thus, the empirical ratio between viscosity-based molecular weight and weight-average molecular weight ($MW_W/MW_V = 1.7129$) may be used as a provisional correction factor to estimate polyacrylamide molecular weights with simple intrinsic viscosity technique. However, for more accurate and theoretical measurements of polyacrylamides' molecular weights, a new intrinsic viscosity measurement technique

with a proper Mark-Houwink-Sakurada equation, which covers a broad molecular weight range and has a standardized experimental protocol, is required to be developed. In contrast to the discrepancy between molecular weight measurement techniques, acid-base titration method proved its applicability as an easier substitute of state-of-the-art Carbon-Hydrogen-Nitrogen elemental analysis because of the observed consistency between two measurement techniques.

2.1 Introduction

Soil erosion occurs in both urban and rural areas during storm events and increases with increasing land disturbance (*e.g.*, tillage, mining, road grading and rural to urban land conversion). If not controlled, eroded soils can end up in various receiving water bodies and can contribute to the coating of bottom sediments, algae blooms, oxygen depletion and food-chain problems (Stumm and Morgan, 1996; Chapra, 1997; Schwartzenbach *et al.*, 2003). To minimize soil erosion and resulting sediment contamination in aquatic environments, polyacrylamides (PAM) have been used as stabilizers to trap top-soil erosion or as flocculants to precipitate eroded soil particles/flocs in sediment retention ponds (Myagchenkov and Kurenkov, 1991; Barvenik, 1994; Seybold, 1994; Shainberg and Levy, 1994).

Polyacrylamides are defined as water-soluble synthetic organic polymers having high molecular weights. Due to the characteristics of high solubility, viscosity and molecular weight, PAMs have been used as inter-particle bridging agents (like glues) to agglomerate erodible or nonsettleable soil particles. Polyacrylamides are classified into three types, nonionic, anionic, and cationic PAMs with respect to their charges induced by the different functional groups along their backbone chains. Anionic PAMs are negatively charged with hydrolysable carboxylic groups on their backbone chains, while cationic PAMs are charged positively with ammonium functional groups, in ambient aquatic conditions (*e.g.* pH, ionic strengths, *etc.*) (Myagchenkov and Kurenkov, 1991; Barvenik, 1994). As soil stabilizers or flocculants, nonionic and anionic PAMs have been mostly used because of their reported non-toxicities. Contrarily, cationic PAMs are known to have toxic effects on aquatic creatures by blocking membranes and thus are rarely used in soil stabilization and flocculation (Virginia Department of Recreation and Conservation, 2002). Considering the fact that the optimum dose of PAM is rarely achieved in on-site applications and thus residual PAMs exceeding the optimum dose possibly flow into downstream water bodies and end up with the detrimental effects on aquatic creatures, cationic PAMs are not recommendable as soil stabilizers or flocculants and excluded from our consideration in this paper. Figure 2.1 shows the schematic diagram of an anionic PAM molecule. The fully anionic PAM is named as polyacrylate (PAA).

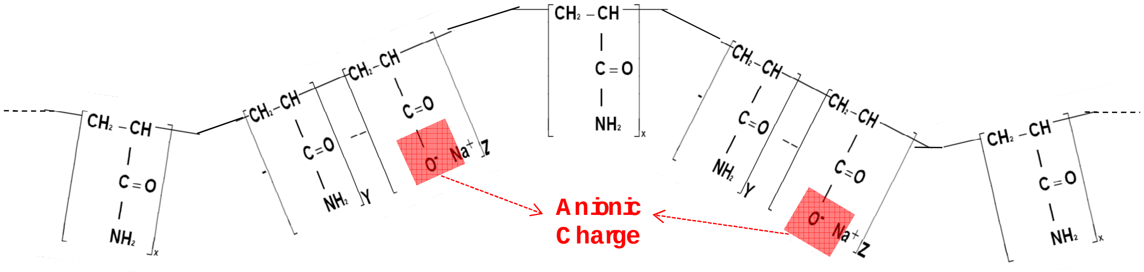

Figure 2.1. Schematic diagram of a polymerized anionic PAM molecule (adopted from Barvenik, 1994).

Among various properties of PAMs, molecular weight (MW, g/mol) and anionic charge density (CD, $\frac{\text{No. of Charged Units}}{\text{No. of Repeating Units}}$ %) have been reported as the key characteristics determining the efficiencies of soil stabilization and flocculation. For example, many previous physicochemical experiments in clay- and PAM-containing suspensions have proven the decisive characteristics of MW and CD on adsorption and flocculation efficiencies (Levy and Agassi, 1995; Green *et al.*, 2000; Chibowski and Wisniewska, 2002; Heller and Keren, 2002; Heller and Keren, 2003; Farrokhpay *et al.*, 2004). However, MW and CD of PAMs rarely have been measured in their experiments by researchers. Instead, generally only manufacturer provided values have been cited. Unfortunately, MW and CD provided by the manufacturers can be very different from those of actual PAMs used in the experiments due to the heterogeneity resulting from bulk manufacturing and storage processes. Due to the importance and possible alteration of MW and CD, the lack of MW and CD measurements by researchers in their experiments may be the evidence of the difficulty or absence of feasible measurement techniques and furthermore the proof of the large gap between two research territories of polymer and soil environmental sciences.

Molecular weight and charge density of PAM stabilizers or flocculants can be measured with various state-of-the-art techniques such as a multi-angle light scattering analysis (MALS) or a gel permeation chromatography (GPC) for MWs and carbon-hydrogen-nitrogen (CHN) elemental analysis for CDs (Francois *et al.*, 1979; Klein and Westerkamp, 1981; Griebel *et al.*, 1991; Hunkeler *et al.*, 1992; Scott *et al.*, 1996;

Sperling, 2006). However, the low accessibility and difficulty of these elaborate measurement techniques are the limiting factors for on-site measurements by soil/environmental scientists or engineers who are inexperienced in polymer sciences. Thus, in this research, we chose two simple measurement techniques, an intrinsic viscosity measurement technique and an acid-base titration method, and estimated their applicability and validity as simple and easy alternative techniques for MW and CD measurements (Klein and Conrad, 1978; McCarthy *et al.*, 1987; Griebel *et al.*, 1991; Wu *et al.*, 1991). In this paper, the potentiality and limitation of these simple measurement techniques will be discussed in comparison with elaborate techniques.

2.2 Materials and Methods

2.2.1 Polyacrylamide Sample Preparation

A series of nonionic and anionic PAMs with different MWs and CDs were obtained from Polysciences Inc. (Warrington, PA) and Kemira Water Solutions Inc. (Lakeland, FL) (see Table 2.1). To remove salts and other impurities (mostly NaCl), PAMs were purified by the serial steps of dissolution, acidification, and precipitation in water-methanol mixtures (Francois *et al.*, 1979). Commercial PAM powders were firstly dissolved in distilled deionized water (DDW) and gently stirred on a Thermolyne® Bigger Bill orbital shaker (Thermo Fisher Scientific Inc., PA) for one to two days. After complete dissolution, PAM solutions were acidified to pH 3 with hydrochloric acid to protonate all carboxyl groups and simultaneously dissociate metal cations from PAM the molecules. Polyacrylamide solids were collected by precipitation induced by addition of methanol and placement in a 4°C cold room. The serial steps of dissolution, acidification, and precipitation were repeated four to five times to collect pure PAM solids without salts or other contaminants on PAM molecules. Finally, purified PAM solids were lyophilized with a VirTis® bench top freeze dryer (SP Industries Inc., NY) and preserved as powder forms for uses in the subsequent experiments. Before MW and CD measuring experiments, 5 g/L aqueous stock solutions were prepared by dissolving purified PAM powders in DDW and then stored in the dark during the experiments.

Table 2.1. Polyacrylamide characteristics provided by manufacturers for CD and MW

Classified Number		Charge Density (%)	Molecular Weight (10^6 g/mol)
Nonionic (Polyscience)	N1	0	0.6 ~ 1
	N2	0	5 ~ 6
	N3	0	18
Anionic (Kemira)	A1	10	High
	A2	15	Ultra-High
	A3	20	Medium
	A4	20	High
	A5	25	Ultra-High
	A6	30	High
	A7	50	Low
	A8	50	Medium

2.2.2 Molecular Weight measurement

Weight-averaged molecular weights (MW_W) and viscosity-based molecular weights (MW_V) of PAMs were measured using a state-of-the-art light scattering analysis and a simple intrinsic viscosity measurement technique, respectively. Firstly, MWs of PAMs were measured with multi-angle laser light-scattering (MALS) technique with Dawn-DSP analyzer (Wyatt Technology Corp., CA) which was equipped with an argonion laser (wave length 488 nm), scattered light intensity detectors at different angles, and scintillating vial sample holder (SV mode) (see Figure 2.2). Dawn-DSP analyzer was calibrated with HPLC-grade toluene (Fisher Scientific Inc., PA) filtered through 0.02 μm Anotop® 25 Plus syringe filters (Whatman Inc., NJ) and normalized with a standard polymer (Polyethylene glycol, MW 5000 g/mol, Mw/Mn~1.10, Polysciences Inc., PA) filtered through 0.2 μm Anotop® 25 Plus syringe filters (Whatman Inc., NJ). After calibration and normalization of the Dawn-DSP system, for MW measurement of a specific PAM sample, a series of PAM solutions with different concentrations of 2.5×10^{-5}, 5.0×10^{-5}, 7.5×10^{-5}, and 1.0×10^{-4} g/mL were prepared in 1 M NaCl background salt concentration by diluting a PAM stock solution. The pH of PAM solutions was set at 9 to standardize all PAM molecules as fully ionized forms. These serial PAM solutions were filtered through 5 μm Acrodisc® syringe filter with Versapor® membrane (Pall Corp., NY) to remove large particles or agglomerates, which are able to make noises during light scattering data collection, transferred into vials, and loaded in the scintillating vial holder of Dawn-DSP analyzer. Refractive indices for different PAM solutions were referred from the previous literature (McCarthy *et al.*, 1987; Hunkeler *et al.*, 1992). Scattered light scattering intensities were collected with multi-angle light detectors of Dawn-DSP analyzer for the serial PAM solutions having different concentrations (see Figure 2.2). With collected scattered light intensity data, MW of a PAM was estimated with Zimm plot method which is formulated to represent the dependency of light scattering magnitudes on MW, solute concentration (c), and detection angle (θ). In this research, the Zimm-Berry plot method in DAWN® software (Wyatt Technology Corp., CA) which is modified from the conventional Zimm method specifically for very large molecules (over 10^6 g/mol) was applied to analyze collected light scattering data. Equations (2.1), (2.2), and (2.3) represent the mathematical formula, which are used in Zimm-Berry plot method for plotting data, estimating MW, and calculating mean square radius, respectively (Wyatt Technology Corp, 1998).

$$\sqrt{\frac{K^{*}c}{R_{\theta}}}=\frac{1}{\sqrt{MP\left(\theta\right)}}+A_{2}c\sqrt{MP\left(\theta\right)} \tag{2.1}$$

$$M=\frac{4}{\left(\sqrt{K^{*}c/R_{\theta}}+\sqrt{K^{*}c/R_{\theta}-4A_{2}c}\right)^{2}} \tag{2.2}$$

$$\left\langle r^{2}\right\rangle=\frac{3\lambda^{2}m_{0}}{8\pi^{2}\sqrt{M}\left(1/M-A_{2}c\right)} \tag{2.3}$$

In Equations (2.1), (2.2), and (2.3), c represents the mass concentration of the solute molecules in the solvent (g/mL), and M is the weight average molar mass (g/mol), A_2 is the second virial coefficient (mol·mL/g^2). K^* is an optical constant ($=4\pi^2 n_0{}^2 (dn/dc)^2 \lambda_0{}^{-4} N_A{}^{-1}$), n_0 is the refractive index of the solvent at the incident radiation (vacuum) wavelength, λ_0 is the incident radiation (vacuum) wavelength, expressed in nanometers, N_A is Avogadro's number (= 6.022×10^{23} mol^{-1}), and dn/dc is the differential refractive index increment of the solvent-solute solution with respect to a change in solute concentration (mL/g). $P(\theta)$ is the theoretically-derived form factor, approximately equal to $1-2\mu^2\langle r^2\rangle/3!+\ldots$, where $\mu=(4\pi/\lambda)\sin(\theta/2)$, and $\langle r^2\rangle$ is the mean square radius. R_θ represents the excess Rayleigh ratio (cm^{-1}) and m_0 is equal to $d\left[K^{*}c/R_\theta\right]/d\left[\sin^2(\theta/2)\right]_{\theta\to 0}$.

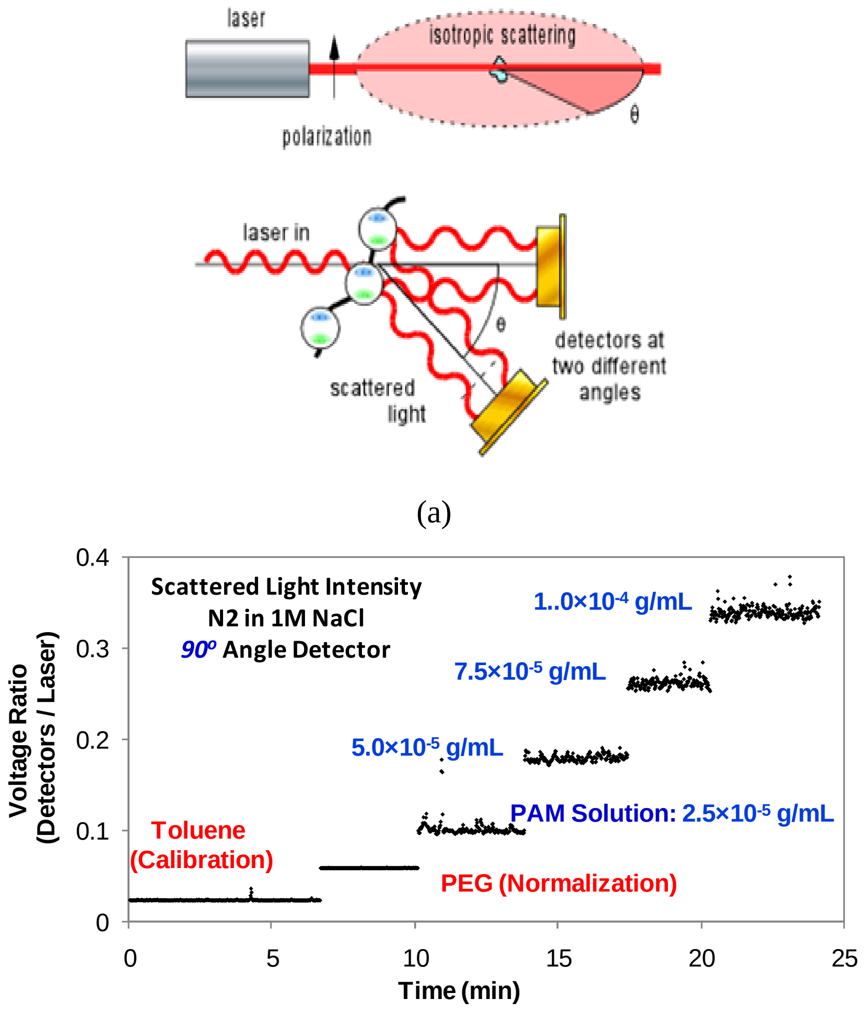

(a)

(b)

Figure 2.2. (a) schematic diagram describing the theory of MALS analysis (adopted from *http://www.wyatt.com/theory/rayleighscattering/size.cfm*) and (b) an example of scattered light intensity data measured with 90^{o} angle detector with tolune (for calibration), polyethyleneglycol (for normalization), and N2 PAM solutions in 1 M NaCl (for sample measurements).

Secondly, MWs of PAMs were estimated from a simple intrinsic viscosity measurement technique with a capillary viscometer (Sperling, 2006). A series of PAM solutions with different concentrations of 2.5×10^{-5}, 5.0×10^{-5} , 7.5×10^{-5}, and 1.0×10^{-4} g/mL were prepared at a specific background salt concentration (see Table 2.2) and pH 9 from a PAM stock solution. The traveling time of the pure solvent and serial PAM solutions through a capillary tube (t_s and t_c) was measured with #50 Cannon-Fenske routine viscometer (Cannon Instrument Company Inc., PA) at 25 ^{o}C in a constant temperature water bath (PolyScience, IL) and were used to estimate relative viscosity ($\eta_{rel} = t_c/t_s$) and specific viscosity ($\eta_{sp} = \eta_{rel} -1$) (see Figure 2.3). Then, following Huggins and Kramer equations, η_{sp} /c *versus* c and $ln(\eta_{rel})/c$ *versus* c (c = PAM concentration) were plotted to estimate the intrinsic viscosity ($[\eta]$) of a certain PAM sample, which is found at zero concentration on the plots (see Figure 2.3) (Sperling, 2006). Finally, Mark-Houwink-Sakurada equation (MHS equation, $[\eta] = K\cdot MW^{a}$) was used to determine MW of a PAM with a measured intrinsic viscosity (Klein and Conrad, 1978; McCarthy *et al.*, 1987; Griebel *et al.*, 1991; Wu *et al.*, 1991). In this research, several MHS equations which had been developed in different solvent conditions *i.e.* different background salt types or concentrations were applied to estimate MWs of nonionic PAMs with measured intrinsic viscosities (see Table 2.2). Noteworthily, Wu's MHS equation which has continuous functions to obtain constants (K and a) with respect to CDs was used as a unique equation to estimate MWs of anionic PAMs having various CDs.

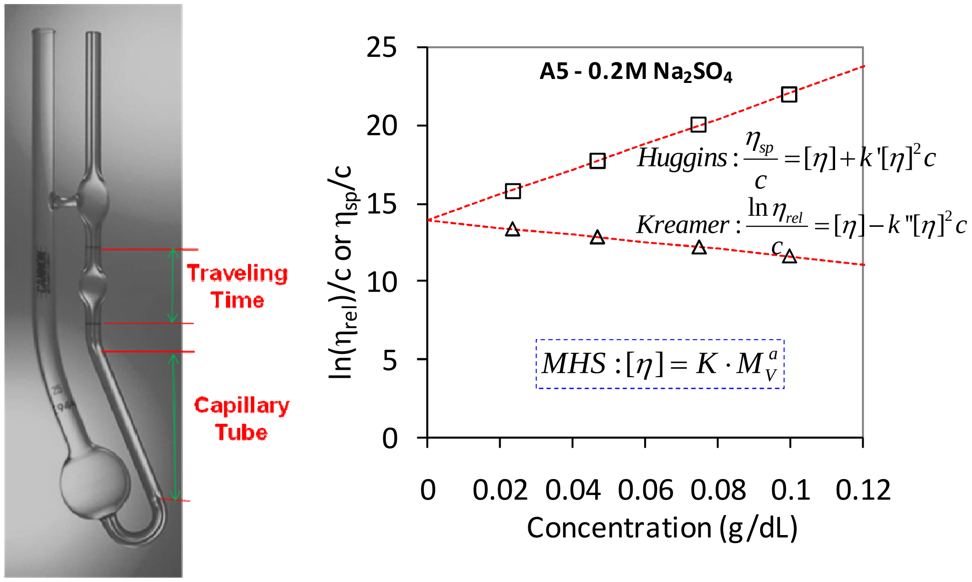

(a) (b)

Figure 2.3. (a) a picture of Cannon-Fenske routine viscometer (adopted from *http://www.cannoninstrument.com/cfr.htm*) and (b) an example of Huggins and Kreamer plots.

Table 2.2. Mark–Houwink-Sakurada (MHS) equations to estimate MW with measured intrinsic viscosities ($[\eta] = K \cdot MW^{a}$). All the equations were developed at 25 ^{o}C.

Reference	Solvent	PAM CD (%)	MW range (10^6 g/mol)	10^2 *K* (cm^3/g)	*a*
Wu *et al.** (1991)	0.2 M Na_2SO_4	Nonionic	0.01~2.0	2.43	0.690
		6~40	0.01~1.2	2.12~3.31*	0.67~0.75*
McCarthy *et al.* (1987)**	0.5 M NaCl	Nonionic	0.09~3.2	1.14	0.746
	1 M NaCl	Nonionic	0.09~3.2	1.912	0.711
Klein and Conrad (1978)	0.5 M NaCl	Nonionic	0.5~5.5	0.719	0.77
Griebel *et al.* (1991)	1 M NaCl	Nonionic	1.1~14.6	2.57	0.670

* For anionic PAMs, continuous functions were developed to estimate *K* and *a wrt.* CDs.

$$\log K = -3.36 - 2.39\times10^{-2}(CD) - 6.96\times10^{-4}(CD^2) - 7.37\times10^{-6}(CD^3)$$

$$a = 0.625 + 8.86\times10^{-3}(CD) - 2.40\times10^{-4}(CD^2) + 2.48\times10^{-6}(CD^3)$$

** Coefficients without heterodispersity corrections were used in this research.

2.2.3 Charge Density measurement

A state-of-the-art CHN elemental analysis and a simple acid-base titration were used to estimate CDs of PAMs. In CHN elemental analysis, FlashEA 1112 CHN-O elemental analyzer (Thermo Scientific Inc., PA) was calibrated with a standard chemical (Sulfanilammide, $C_6H_8N_2O_2S$) of which elemental contents are specified by the manufacturer (C: 41.84, H: 4.68, N: 16.27, S: 18.62, O: 18.58 %). Then, dried PAM samples were prepared in tin boats, weighed carefully with MX5 microbalance (Mettler-Toledo Inc., OH), and introduced into the elemental analyzer. The contents of C, H, and N were estimated by comparing the peak areas of PAM samples with those of the standard chemical (see Figure 2.4(a)). Finally, from the estimated N/C ratio, the content of carboxylic functional groups of a PAM molecule (CD %) was found by applying the equation, $CD = \left(1 - \left(N/C\right) \cdot 36/14\right)(\%)$, where 36 and 14 represent total MWs of three carbon atoms and one nitrogen atom in a repeating unit of a nonionic PAM chain (see Figure 2.4(b)).

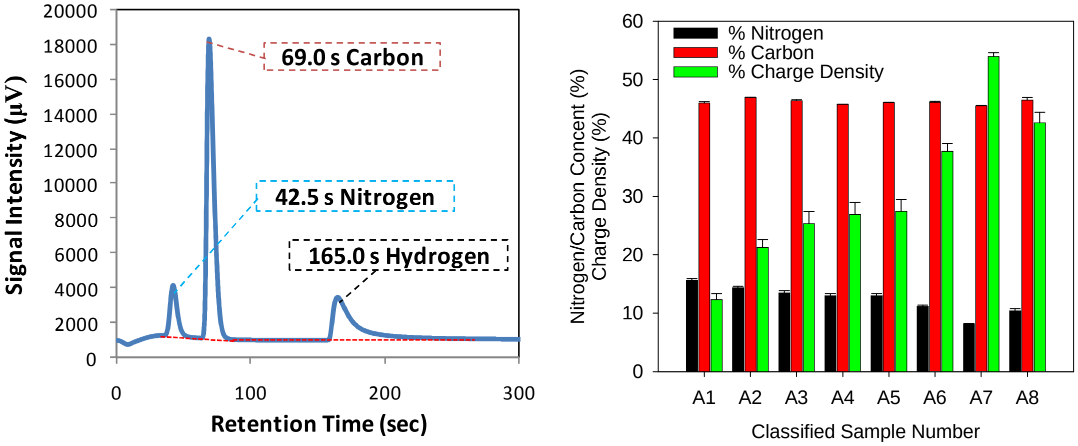

(a) (b)

Figure 2.4. (a) an example of chromatographic data with CHN elemental analysis and (b) estimated carbon and nitrogen contents and charge densities for various anionic PAM samples.

CDs of PAMs were also measured with acid-base titration methods. Three 50 mL PAM solutions with 1 g/L PAM concentration were prepared at 0.001, 0.01, and 0.1 M NaCl background salt concentrations from a PAM stock solution. Titration was done upward to pH 10 with 0.5 M NaOH dose and then downward to pH 3 with 0.5 M HCl dose and pH was monitored continuously with Orion 420A pH meter (Thermo Scientific Inc., PA). During titration, PAM solution was continuously purged with pure nitrogen gas (National Welders Supply Co., NC) to prevent CO_2 dissolution. All the experiments produced identical results for both forward and backward titrations, which consequently endowed the credibility on our experimental methodology. The *S*-shaped titration curves (pH *versus* specific charge density) were plotted after processing the measured data such as acid or base doses and pHs and they were adjusted with subtracting background acid or base consumptions by the NaCl solutions and with activity corrections using Guntelberg equation (Stumm and Morgan, 1996). Eventually, CD of a PAM sample was estimated with the maximum specific charge density on the upper plateau of the *S*-shaped titration curve, where all the carboxyl groups contained in the PAM molecules become fully deprotonated *i.e.* ionized (see Figure 2.5). Figure 2.5 represents acid-base titration plots of A3 PAM sample for an illustration purpose. With the obtained maximum deprotonation capacity, which was found at the plateau of an acid-base titration curve, CD of a PAM was estimated with the simple arithmetic equation shown in Figure 2.5 and compared to the counterpart CD estimated with CHN elemental analysis.

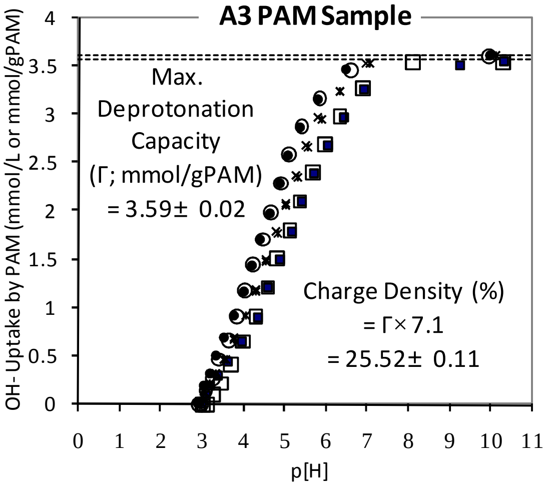

Figure 2.5. Acid-base titration curves used to estimate CD of A3 PAM sample in different NaCl concentrations. Symbols, ○, ×, and □, represent experimental data obtained in 0.001, 0.01, and 0.1 M NaCl solutions, respectively.

2.3 Results and Discussion

Zimm-Berry plots obtained from triplicate light scattering analyses for the N2 PAM are shown in Figure 2.6 for illustration. Molecular weights and root-mean-square (RMS) radii were calculated with the Zimm-Berry plot method, which is the built-in function of DAWN® software (Wyatt Technology Corp., CA) to process the raw scattered light intensities at different angles. Molecular weights and RMS radii of all nonionic and anionic PAM samples estimated with a light scattering analysis and the Zimm-Berry plot method were summarized in Table 2.3.

As shown in Figure 2.6 and Appendix A3, all of the measured light scattering signals were well fitted with the Zimm-Berry plots. However, in spite of the individual well-fitted Zimm-Berry plot for a single measurement, deviation between triplicate measurements was observed. For example, in Figure 2.6 the estimated MWs with the triplicate light scattering analyses for N2 sample were 4.426, 4.066, and 6.713×10^6 g/mol, which produced a standard error of 0.83×10^6 g/mol. These relatively large standard errors were commonly observed in the other nonionic or anionic PAM samples (see Tables 2.3 and 2.5). The possible reasons of these large standard errors between the replicated light scattering measurements will be discussed in a later section with respect to the heterogeneous nature of commercial PAMs and the sensitivity of a light scattering analyzer.

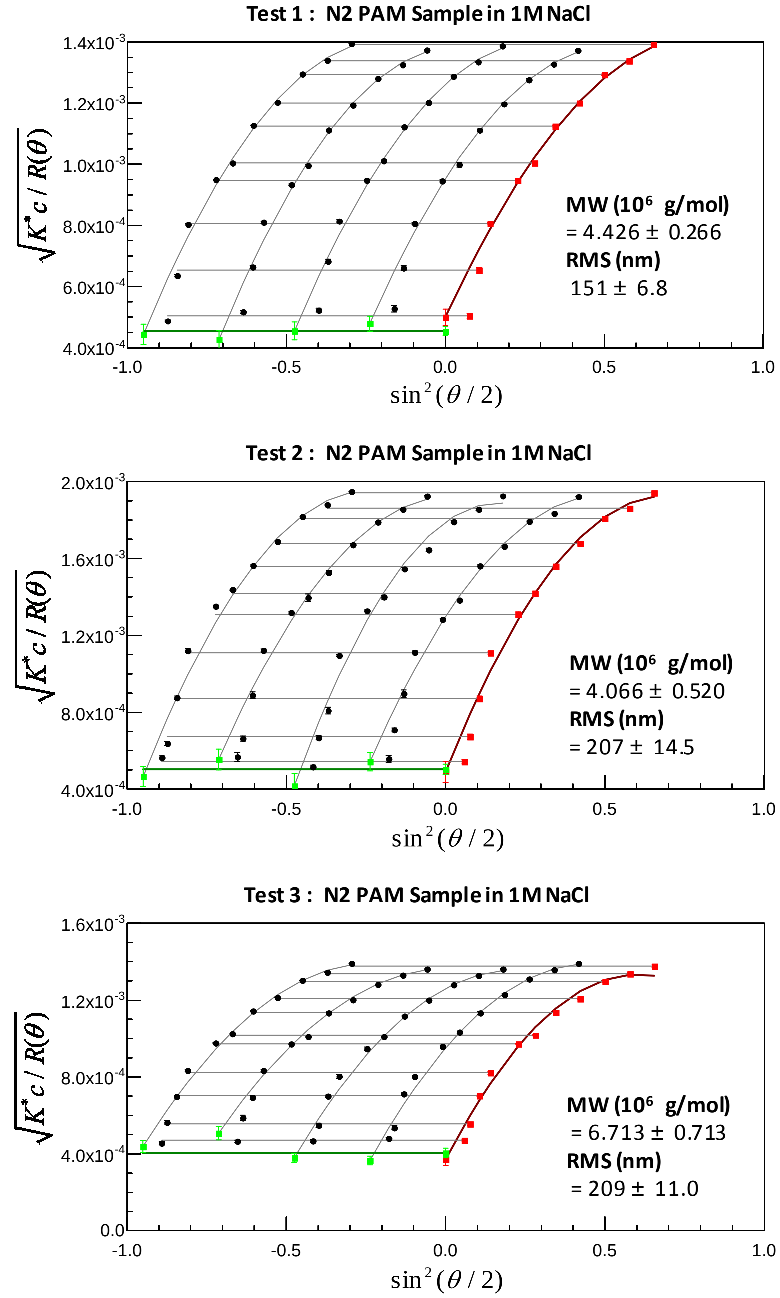

Figure 2.6. Zimm-Berry plots of the triplicate light scattering analyses to estimate MW of N2 PAM sample.

Table 2.3. Molecular weight and root-mean-square radius estimated with light scattering analyses for various nonionic and anionic PAM samples. Data represent Mean ± Standard Error, of which error was obtained in the data fitting process to the Zimm-Berry plot.

Classified Number		Test 1		Test 2		Test 3	
		MW (10^6 g/mol)	RMS Radi (nm)	MW (10^6 g/mol)	RMS Radi (nm)	MW (10^6 g/mol)	RMS Radi (nm)
Non-ionic	N1	1.48 ± 0.04	106.9 ± 4.0	1.28 ± 0.03	89.8 ± 3.2	1.24 ± 0.03	89.7 ± 2.0
	N2	4.43 ± 0.27	151.0 ± 6.8	4.07 ± 0.52	207.6 ± 14.5	6.71 ± 0.71	209.1 ± 11.0
	N3	10.07 ± 1.69	234.4 ± 10.1	10.81 ± 1.53	273.1 ± 17.1	10.45 ± 0.99	262.5 ± 11.2
An-ionic	A1	8.30 ± 0.78	200.4 ± 11.0	6.35 ± 0.37	190.8 ± 7.1	8.51 ± 1.21	223.4 ± 15.7
	A2	10.77 ± 1.14	205.9 ± 10.4	9.21 ± 2.20	276.1 ± 29.0	5.04 ± 0.36	181.3 ± 7.8
	A3	8.40 ± 0.86	209.5 ± 10.3	6.57 ± 0.44	192.0 ± 7.2	8.17 ± 0.42	194.3 ± 5.7
	A4	4.31 ± 0.28	156.8 ± 7.5	4.01 ± 0.24	147.7 ± 5.0	5.37 ± 0.35	169.8 ± 4.1
	A5	5.11 ± 0.31	170.9 ± 6.4	5.00 ± 0.27	176.1 ± 6.3	5.21 ± 0.15	160.0 ± 3.4
	A6	4.06 ± 0.21	162.7 ± 6.5	4.12 ± 0.23	159.8 ± 7.4	4.24 ± 0.21	152.6 ± 5.2
	A7	3.29 ± 0.18	132.9 ± 4.5	3.04 ± 0.14	136.2 ± 4.4	3.02 ± 0.09	110.3 ± 3.3
	A8	5.53 ± 0.36	155.5 ± 5.3	5.89 ± 0.29	173.0 ± 5.5	5.29 ± 0.45	171.6 ± 5.8

Figure 2.7 shows Kreamer and Huggins plots for N2 PAM in different salt species and concentrations. These plots were eventually used to estimate intrinsic viscosities and MWs with the associated MHS equations. In Figure 2.7, the Huggins plot is the upper line with positive slope, while the Kreamer plot is the lower line with negative slope. Thus, two different MWs can be estimated with Kreamer and Huggins plots for a single intrinsic viscosity test. The average value and the difference of the paired MWs estimated with both the Kreamer and Huggins plots were summarized for all nonionic and anionic PAMs in Table 2.4.

At the beginning of this research, three salt conditions, 0.2 M Na_2SO_4, 0.5 M NaCl, and 1 M NaCl, along with their MHS equations (see Table 2.2), were tested with nonionic PAMs (N1, N2, and N3), to check their appropriateness in estimating intrinsic viscosities and MWs. To check the validity of the salt solutions and their MHS equations, two parameters were monitored during the entire intrinsic viscosity measurement and data interpretation. Firstly, the difference between the paired MWs from Kreamer and Huggins plots was used to monitor the appropriateness of the given salt condition and its Kreamer and Huggins plots. The differences between the paired MWs are shown as ± error terms in Figure 2.7 and Table 2.4. The paired MWs should be identical for an ideal case satisfying all the supporting theories, such as Einstein viscosity theorem (Sperling, 2006). However, differences between the paired MWs were observed and the salt condition with 0.2 M Na_2SO_4 was found to make smaller differences between the paired MWs than those with 0.5 M NaCl and 1 M NaCl. For example, the differences between the two estimated MWs (± errors in Figure 2.7 and Table 2.4), were 0.01 ~ 0.02 for 0.2 M Na_2SO_4, while they were 0.05 ~ 0.33 for 0.5 M NaCl and 1 M NaCl.

Secondly, the parameter, *k"-k'* ($\{slope/[\eta]^2\}_{Huggins}$ - $\{slope/[\eta]^2\}_{Kreamer}$), which is known as 0.5 for an ideal polymer solution, was also monitored to identify the appropriateness of the salt conditions and their Kreamer and Huggins plots (Sperling, 2006). The estimated *k"-k'* parameters with 0.2 M Na_2SO_4 solutions were closer to the ideal value than those with 0.5 M NaCl and 1 M NaCl (see Table 2.4). For both nonionic and anionic PAM solutions, the *k"-k'* parameters were 0.51 ± 0.01 (mean ± standard error) with 0.2 M Na_2SO_4, which are very consistent and close to the ideal value of 0.5. Thus, considering that the smaller difference between the paired MWs obtained with Kreamer and Huggin plots and the more proximity and consistency of *k"-k'* parameter to the ideal value, the salt solution with 0.2 M Na_2SO_4 was found to be more suitable for an intrinsic viscosity measurement technique in estimating MWs of PAMs than the solutions with 0.5 M NaCl and 1 M NaCl.

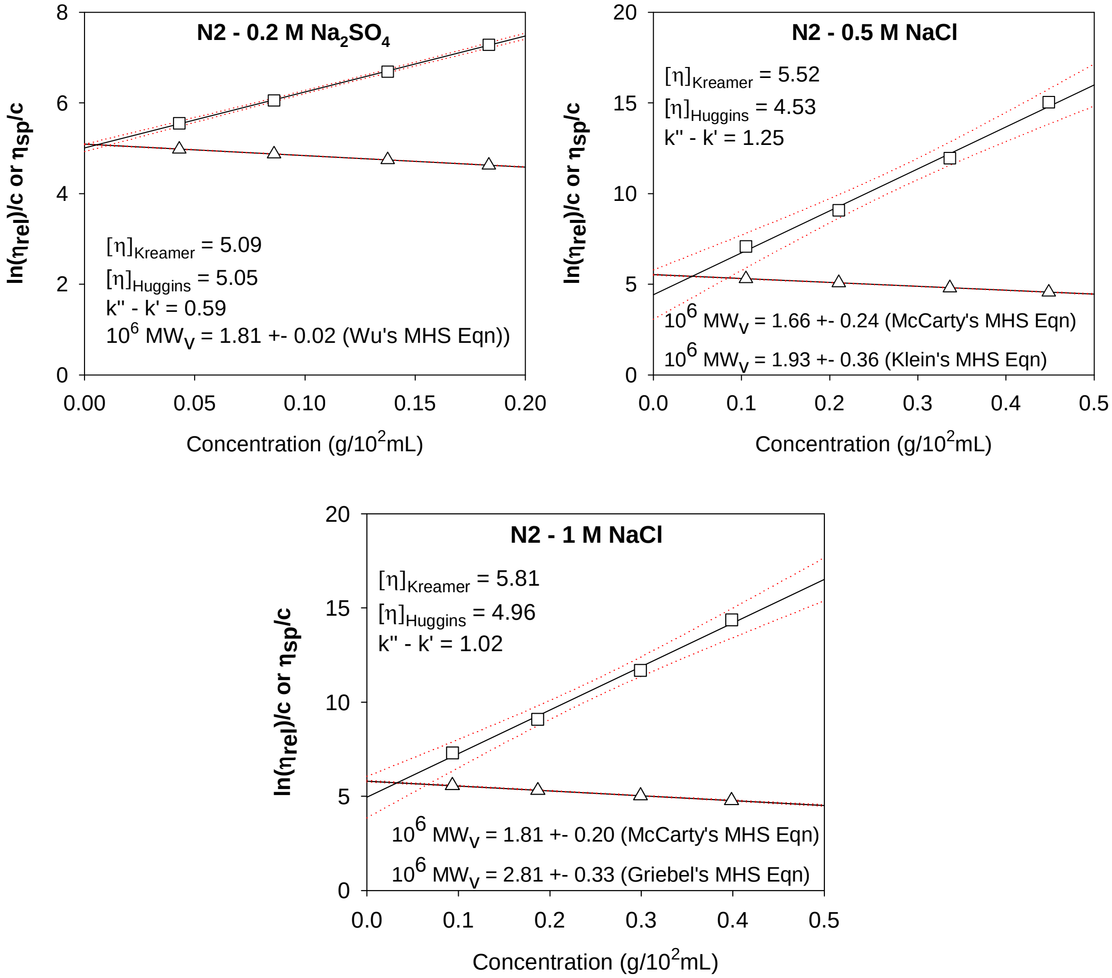

Figure 2.7. Kreamer and Huggins plots used to estimate MW of N2 PAM sample in different solution conditions with various salt species and concentrations. Dotted lines represent 95% confidence level between the fitted line and experimental data. The estimated MW ± Error is shown in the figure. Error was set as the difference between the paired MWs obtained from Kreamer and Huggins plots.

Table 2.4. Molecular weight estimated with the intrinsic viscosity measurement for various nonionic and anionic PAM samples. Data represent Mean ± Error, of which error was set as the difference between the paired MWs obtained from Kreamer and Huggins plots. Numbers in the parentheses represent $k''-k'=\{slope/[\eta]^2\}_{Huggins}-\{slope/[\eta]^2\}_{Kreamer}$.

Classified Number		Wu *et al.* (1991)	McCarty *et al.* (1997)		Klein and Conrad (1978)	Griebel *et al.* (1991)
		0.2M Na_2SO_4	0.5M NaCl	1M NaCl	0.5M NaCl	1M NaCl
Non-ionic	N1	1.00 ± 0.01 (0.56)	0.85 ± 0.07 (0.86)	0.91 ± 0.05 (0.74)	1.02 ± 0.07 (0.86)	1.36 ± 0.08 (0.74)
	N2	1.81 ± 0.02 (0.59)	1.66 ± 0.24 (1.25)	1.81 ± 0.20 (1.02)	1.93 ± 0.28 (1.25)	2.81 ± 0.33 (1.02)
	N3	7.03 ± 0.02 (0.48)	7.45 ± 0.18 (0.61)	7.37 ± 0.08 (0.49)	8.28 ± 0.19 (0.61)	12.48±0.15 (0.49)

Classified Number		Wu *et al.* (1991) 0.2M Na_2SO_4		
		Test 1	Test 2	Test3
An-ionic	A1	4.58 ± 0.06 (0.44)	4.29 ± 0.01 (0.49)	4.31 ± 0.01 (0.48)
	A2	5.28 ± 0.18 (0.43)	5.04 ± 0.07 (0.49)	5.20 ± 0.13 (0.45)
	A3	4.05 ± 0.08 (0.47)	3.91 ± 0.04 (0.49)	3.76 ± 0.01 (0.51)
	A4	2.88 ± 0.02 (0.48)	2.79 ± 0.01 (0.54)	2.79 ± 0.01 (0.54)
	A5	3.29 ± 0.03 (0.49)	3.13 ± 0.02 (0.54)	3.24 ± 0.02 (0.54)
	A6	2.30 ± 0.01 (0.49)	2.19 ± 0.01 (0.52)	2.18 ± 0.01 (0.53)
	A7	1.80 ± 0.07 (0.53)	1.66 ± 0.01 (0.51)	1.68 ± 0.01 (0.50)
	A8	2.58 ± 0.01 (0.53)	2.53 ± 0.01 (0.53)	2.48 ± 0.01 (0.53)

All the measured MWs and CDs are summarized in Table 2.5 for three nonionic and eight anionic PAMs. Molecular weights and charge densities measured with simple measurement techniques, intrinsic viscosity and acid-base titration methods, were compared with those with complex techniques, light scattering and CHN elemental analyses.

In Table 2.5, it is noteworthy that standard errors of MWs measured with a light scattering analysis were much higher than those with an intrinsic viscosity measurement. Even though an individual light scattering analysis was well fit to the Zimm-Berry plot as shown in Figure 2.6 and Appendix A3, the standard error between the triplicate measurements was substantial. With respect to this precision issue of a light scattering analysis, we thought of two possible causes which are amplifying the standard errors. Firstly, in this research, commercial PAM stabilizers or flocculants, which have broad MW distributions occurring in their bulk manufacturing processes, were used as experimental materials instead of well characterized mono-dispersed PAMs. Thus, the poly-dispersity of commercial PAM stabilizers or flocculants might induce significant signal fluctuations during light scattering data collection and eventually produced high standard errors of measured MWs. Secondly, the sensitive nature of a light scattering analysis is prone to amplify erratic signals, which are caused by even traces of contaminants or incompletely dissolved aggregates in commercial PAM stabilizers or flocculants, and thus ready to produce large standard deviations of measured MWs (Berth *et al.*, 1996). In contrast, intrinsic viscosity technique showed very small standard deviations of measured MWs because it estimates MW as a single integrated parameter without considering the poly-dispersity effect of commercial PAMs.

Table 2.5. Summarized results from MW and CD measurements for nonionic and anionic PAMs. Data represent Mean ± Standard Error for triplicate measurements.

Classified Number		Charge Density (%)			Molecular Weight (10^6 g/mol)						
							Intrinsic Viscosity Measurement				
		Company Provided Value	Elemental Analysis	Acid-Base Titration	Company Provided Value	Light Scattering Analysis	Wu *et al.* (1991)	McCarty *et al.* (1997)		Klein and Conrad (1978)	Griebel *et al.* (1991)
							0.2M Na_2SO_4	0.5M NaCl	1M NaCl	0.5M NaCl	1M NaCl
Non-ionic	N1	0	-0.31 ± 1.61†	1.90 ± 0.11†	0.6 ~ 1	1.33 ± 0.07	1.00	0.85	0.91	1.02	1.36
	N2	0	0.16 ± 1.49†	2.10 ± 0.07†	5 ~ 6	5.07 ± 0.83	1.81	1.66	1.81	1.93	2.81
	N3				18	10.44 ± 0.21	7.03	7.45	7.37	8.28	12.48
An-ionic	A1	10	12.34 ± 1.05	11.4 ± 0.02	High	7.72 ± 0.68	4.39 ± 0.16‡				
	A2	15	21.28 ± 1.29	20.6 ± 0.05	Ultra-High	8.34 ± 1.71	5.17 ± 0.12‡				
	A3	20	25.32 ± 2.07	25.5 ± 0.11	Medium	7.71 ± 0.57	3.91 ± 0.14‡				
	A4	20	26.93 ± 2.04	25.2 ± 0.03	High	4.56 ± 0.41	2.81 ± 0.05‡				
	A5	25	27.47 ± 1.97	25.9 ± 0.27	Ultra-High	5.11 ± 0.06	3.18 ± 0.09‡				
	A6	30	37.69 ± 1.35	35.4 ± 0.12	High	4.14 ± 0.05	2.22 ± 0.07‡				
	A7	50	53.98 ± 0.66	51.1 ± 0.04	Low	3.12 ± 0.09	1.71 ± 0.08‡				
	A8	50	42.60 ± 1.79	45.8 ± 0.19	Medium	5.57 ± 0.17	2.53 ± 0.05‡				

† N1 and N2 samples were measured as zero-CD references.

‡ represent Mean ± Std. Error of triplicate measurements done in 0.2 M Na_2SO_4 solution.

In the subsequent discussions of this research paper, MWs and CDs measured with complex techniques such as light scattering and CHN elemental analyses will be assumed as absolute or standard values and thus used as reference values to estimate the applicability of the simple counterparts such as intrinsic viscosity and acid-base titration methods. Considering that MWs measured with a light scattering analysis had been assumed as absolute values in developing MHS equations in many previous researches, MWs measured with a light scattering analysis were deservedly chosen as reference values in this comparative research (Klein and Conrad, 1978; McCarthy *et al.*, 1987; Griebel *et al.*, 1991; Wu *et al.*, 1991). Also, CHN elemental analysis had proven its credibility in estimating CDs of many PAM samples with measured CHN elemental contents and thus was assumed as the absolute measurement technique in this research (Francois *et al.*, 1979; McCarthy *et al.*, 1987; Wu *et al.*, 1991).

Figure 2.8 shows comparisons between (a) MWs provided by the manufacturer and MWs measured with a light scattering analysis, (b) MWs provided by the manufacturer and MWs measured with an intrinsic viscosity measurement technique, and (c) MWs between two different measurement techniques, for nonionic PAMs (N1, N2, and N3). In Figure 2.8, *x*-data and *y*-data of a single data point represent a pair of provided or measured MWs for a PAM sample (10^6 g/mol). Thus, if both the paired MWs in the different domains are consistent, the data point should fall onto 1-to-1 line.

Firstly, in Figure 2.8 (a), the data points of two smaller PAMs (N1 and N2) were close to 1-to-1 line. Thus, MWs measured with a light scattering analysis were proven to be very similar to MWs provided by the manufacturer. However, for the largest PAM

(N3), the data point was below 1-to-1 line, representing that measured MWs with a light scattering technique is smaller than the MW provided by the manufacturer. This discrepancy may be ascribed to various causes such as heterogeneous nature of the commercial PAM, entanglement between extremely large PAM molecules, and cutoff problem of PAM molecules or agglomerates through the filter paper. Such behaviors of extremely large PAMs should be examined closely in future studies. Secondly, Figure 2.8 (b) shows the comparison between MWs provided by the manufacturer (*x*-axis) and MWs measured with an intrinsic viscosity measurement (*y*-axis). In addition, different MHS equations, which were used to estimate MWs with measured intrinsic viscosities, were compared one another. The data points of N2 and N3 samples were consistently below 1-to-1 line. This means that the measured MWs of N2 and N3 samples were smaller than the manufacturer-provided MWs. Also, the inconsistency between different MHS equations of Wu *et al.* (1991), McCarthy *et al.* (1991), Klein and Conrad (1978), and Griebel *et al.* (1997) was observed with different trend lines in Figure 2.8 (b). This will be closely examined in the following section with the comparison between two MW measurement techniques, a light scattering analysis and an intrinsic viscosity measurement technique

In Figure 2.8 (c), a specific data point represents both MWs measured with a light scattering analysis (*x*-axis) and with an intrinsic viscosity measurement (*y*-axis). Again, the inconsistency between two MW measurement techniques was identified for N2 and N3 PAM samples with the data points falling away from 1-to-1 line and also the inconsistency between different MHS equations of Wu *et al.* (1991), McCarthy *et al.*

(1991), Klein and Conrad (1978), and Griebel *et al.* (1997) was identified. Thus, nevertheless the ability of intrinsic viscosity technique in estimating the relative magnitude of MWs between different PAM samples, its accuracy and applicability is still very questionable because of the observed inconsistencies between different MW measurement techniques and between different MHS equations.

To explain these observed inconsistencies, the backgrounds in developing intrinsic viscosity techniques and MHS equations should be revisited. In the previous researches, most of MHS equations had been developed in comparative studies between a light scattering analysis and an intrinsic viscosity measurement technique (Klein and Conrad, 1978; McCarthy *et al.*, 1987; Griebel *et al.*, 1991; Wu *et al.*, 1991). Generally, a light scattering analysis had been assumed to produce absolute and standard MWs and used as reference data to build up MHS equations. In other words, MHS equations have been formulated by correlating intrinsic viscosities measured with a capillary viscometer to MWs obtained from a light scattering analysis ($[\eta] = K \cdot (MW_{MALS})^a$). Thus, the accuracy and applicability of developed MHS equations rely on the numbers and ranges of PAM samples which are used in the correlating procedure. For example, MHS equations developed with large numbers and broad ranges of MWs are more accurate and applicable with covering broader MW ranges than those developed with small numbers and narrow ranges of MWs.

As an evidence of the above argument, the dissimilarity of estimated MWs and their trend lines were observed in application of different MHS equations which had been developed in different MW ranges (see Table 2.2 and Figure 2.8). In Figure 2.8 (c), measured MWs and their trend lines are plotted with application of different MHS equations proposed by Wu *et al.* (1991) and McCarty *et al.* (1991) developed in similar MW ranges of 0.01~3 million (dotted line), Klein and Conrad (1978) in a MW range of 0.5~5.5 million (long dash line), and Griebel *et al.* (1991) in a MW range of 1.1~14.6 million (dash-dot-dot line). Coincidently, as the upper limit of MW ranges of MHS equations increases, for example, from 3 million of MHS equations of Wu *et al.* (1991) and McCarty *et al.* (1991) to 14.6 million of MHS equation of Griebel *et al.* (1991), estimated MWs and their trend lines moved from the points far below 1-to-1 line to those near or even beyond 1-to-1 line. In other words, MWs estimated with intrinsic viscosity techniques become similar or superior to MWs measured with a light scattering analysis with increase of the upper limit of MW range. Especially, larger PAMs with MWs above 1 million (N2 and N3, see Table 2.5) showed significant changes of estimated MWs in application of different MHS equations. For N2 and N3 samples, in application of MHS equations of Wu *et al.* (1991) and McCarty *et al.* (1991) whose upper limit of MW range does not cover MWs of the samples, estimated MWs were far below 1-to-1 line *i.e.* MWs estimated with intrinsic viscosity technique were lower than MWs with a light scattering analysis. However, with MHS equation of Griebel *et al.* (1997) whose upper limit of MW range is high enough to cover MWs of N2 and N3 samples, estimated MWs were near or even above 1-to-1 line *i.e.* MWs estimated with intrinsic viscosity technique were similar or superior to MWs with a light scattering analysis. With MHS equations of Klein and Conrad (1978) having an intermediate MW range, estimated MWs were located between the above two extreme cases. Thus, this observation leads us to the conclusion that measured MWs with intrinsic viscosity technique can be very different in accordance with the MW ranges used in developing MHS equations.

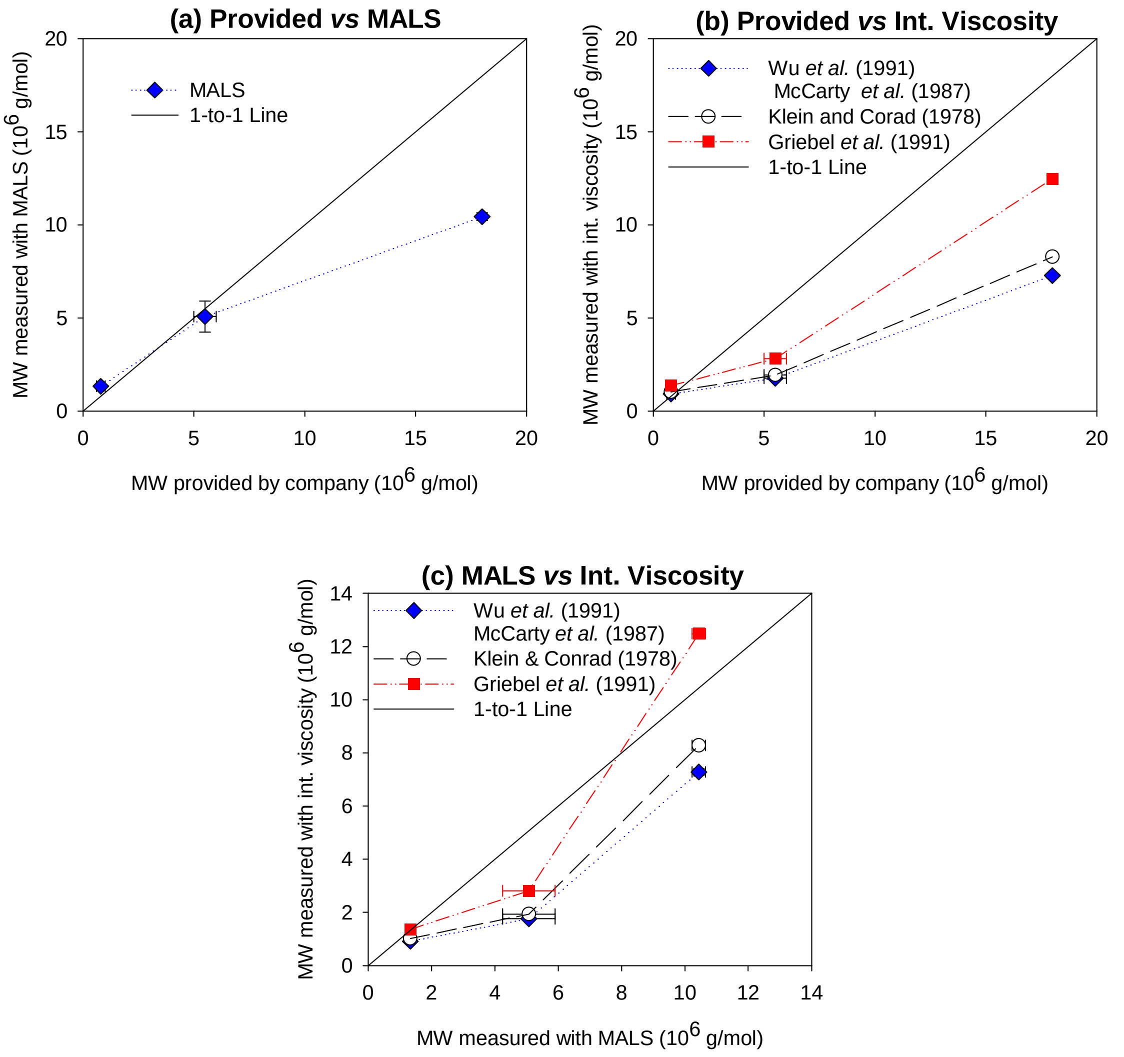

Figure 2.8. Comparison between (a) MWs provided by the manufacturer and MWs measured with a light scattering analysis, (b) MWs provided by the manufacturer and MWs measured with an intrinsic viscosity measurement technique, and (c) MWs between two different measurement techniques, for nonionic PAMs (N1, N2, and, N3).

For anionic PAMs, MHS equation of Wu *et al.* (1991) was used as a unique equation to estimate MWs of anionic PAMs from the measured intrinsic viscosities due to the absence of other available MHS equations covering various CDs. Similar to nonionic PAMs, the inconsistency between intrinsic viscosity and light scattering techniques was observed with the data points falling below 1-to-1 line (see Figure 2.9). This inconsistency might be caused by extrapolation of the MHS equation above its MW range, in the same manner as the observed for nonionic PAMs. Considering these inconsistencies observed with both nonionic and anionic PAMs in Figures 2.8 and 2.9, the application of MHS equations to estimate MWs of PAMs out of their MW ranges may not be recommendable.

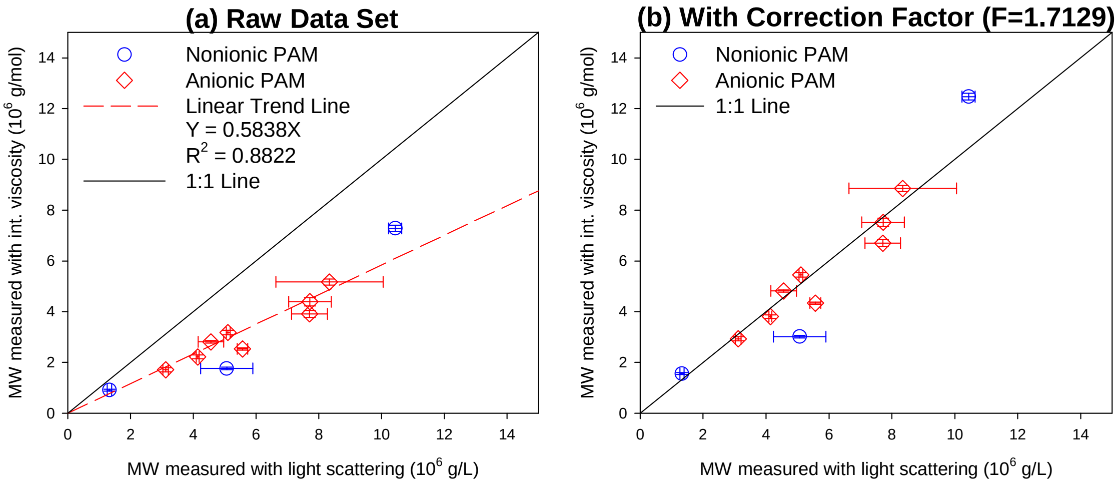

Figure 2.9. Comparison between MWs measured with a light scattering analysis and MWs with an intrinsic viscosity measurement technique, for nonionic and anionic PAMs, (a) before and (b) after applying the correction factor ($MW_W/MW_V = 1.7129$).

In addition to extrapolation of the MHS equation above its MW range, the polydispersity of commercial PAMs, which are generally not strictly characterized and thus have highly polydisperse MW distributions, may be the other possible reason for the inconsistency between intrinsic viscosity and light scattering techniques. With a MW distribution of a highly-polydisperse commercial PAM shown in Figure 2.10 for a illustration purpose, the number-average MW_N, the weight-average MW_W, and the viscosity-average MW_V can be estimated with Equations (2.4), (2.5), and (2.6), respectively. In Equations (2.4), (2.5), and (2.6), MW_i is the molecular weight of i-th slice in a MW distribution curve, N_i is the number of moles with a molecular weight of MW_i, and W_i is the weight with a molecular weight of MW_i. If a PAM is very well characterized and thus has a mono-disperse MW distribution, MW_N, MW_W, and MW_V should be identical. However, considering that commercial PAM stabilizers or flocculants are manufactured in bulk, they necessarily have polydisperse MW distributions. For polydisperse commercial PAMs, we can easily speculate that the weight-average MW_W is higher than the number-average MW_N and the viscosity average MW_V is in the middle way between MW_W and MW_N due to the constant a (0.5 ~ 1) (Fried, 1995). Thus, considering this theoretical relation between MW_W, MW_N, and MW_V, the polydispersity of commercial PAMs might be one of the possible reasons for the lower viscosity-average MW_V measured with an intrinsic viscosity technique than the weight average MW_W measured with a MALS analysis.

$$\mathbf{MW_N} = \left(\sum_{i=1}^{i\max} N_i \cdot M_i \right) / \left(\sum_{i=1}^{i\max} N_i \right) \tag{2.4}$$

$$\mathbf{MW_W} = \left(\sum_{i=1}^{i\max} N_i \cdot M_i^{\,2} \right) / \left(\sum_{i=1}^{i\max} N_i \cdot M_i \right) \tag{2.5}$$

$$\mathbf{MW_V} = \left(\sum_{i=1}^{i\max} N_i \cdot M_i^{\,(1+a)} \right) / \left(\sum_{i=1}^{i\max} N_i \cdot M_i \right) \tag{2.6}$$

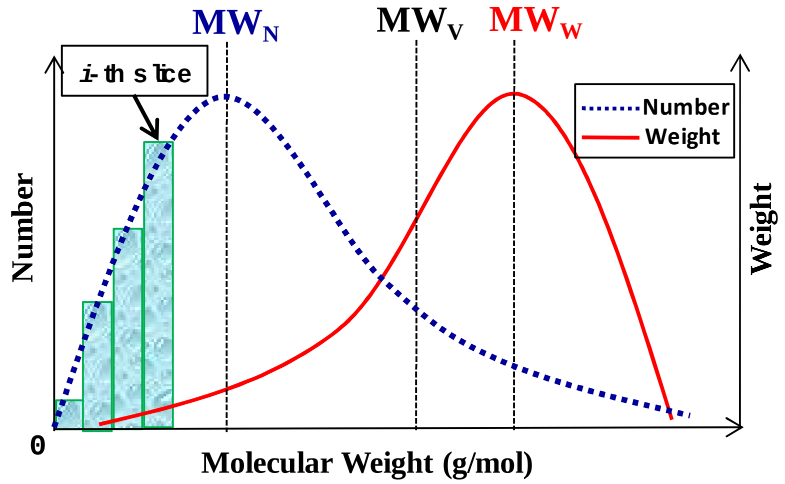

Figure 2.10. Number and weight distributions for a polydisperse PAM sample for an illustration purpose.

However, the data points come off from 1-to-1 line in a very consistent manner and they are well fit onto a linear trend line ($MW_V = 0.5838\ MW_W$). Thus, with incorporating a simple correction factor ($F = MW_W/MW_V = 1.7129$) to compensate MW underestimation of Wu's MHS equation, the actual weight-average MWs of nonionic and anionic PAMs can be estimated. In Figure 2.9 (b), all the data points were found to be on or near 1-to-1 line after applying the correction factor. However, incorporating this correction factor should be an interim and provisional method because the correction factor is developed with the empirical approach but not the theoretical base.

Generally, MWs of most PAM stabilizers and flocculants range from 1 to 20 million, which is a lot higher than the MW range of Wu's MHS equation. Thus, a new MHS equation that is weighted on higher MW ranges should be developed to estimate MWs of PAM stabilizers and flocculants having high MWs and various CDs. In comparison with other MHS equations, Wu's equation is unique in that it is applicable for PAMs having various CDs with its continuous functions to obtain constants (K and a) with respect to CDs (see Table 2.2). Thus, a new MHS equation for PAM stabilizers and flocculants that have various CDs is recommended to be developed from Wu's equation as a prototype. Also, the fact that numerous difficulties in developing MHS equations may be aroused from heterogeneous and dynamic behaviors of commercial PAMs having high MWs should be taken into account. For example, the morphological changes and also aging or aggregation processes of polymeric molecules have been reported to make critical effects in measuring MWs of large polymers such as PAM stabilizers or flocculants (Gardner *et al.*, 1978; Klein and Westerkamp, 1981; Owen *et al.*, 2002). Furthermore, due to polymers' invisible nature, MWs of polymers cannot be measured straightforward with well-defined rulers but should be estimated indirectly with measuring other physicochemical characteristics such as scattered light intensities or intrinsic viscosities. Thus, without controlling or standardizing heterogeneous and dynamic behaviors of large PAMs, which make effects on the key physicochemical characteristics, the indirect MW measurement techniques will be very erratic. With this reason, the standardized protocol in measuring MWs will be required to eliminate all the adverse effects caused by heterogeneous and dynamic natures of large PAMs and eventually to get consistent results.

Figure 2.11 shows the comparison between CDs of anionic PAMs which were measured with both acid-base titration and CHN elemental analysis. In Figure 2.11, a specific data point represents CDs measured with the elemental analysis (*x*-axis) and with acid-base titration (*y*-axis). Nonionic PAMs were first tested as control references. CDs of nonionic PAMs (N1 and N2, see Table 2.5) were estimated as -0.15 % and 2% with elemental analysis and acid-base titration, respectively. The small errors might be caused by sample preparation or data processing. In Figure 2.11, all the data points of anionic PAMs are falling onto or near 1-to-1 line *i.e.* two different measurement techniques were found to be consistent in measuring CDs. Thus, the acid-base titration was proven as an easier alternative technique of complex CHN elemental analysis in measuring CDs of PAMs. For on-site measurements, acid-base titration method will be used simply with pH meter and tube-type titrator which require low costs.

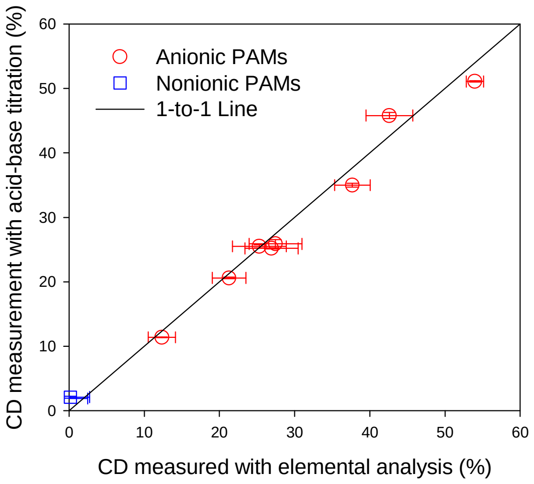

Figure 2.11. Comparison between CDs measured with CHN elemental analysis and CDs with acid-base titration for nonionic and anionic PAMs.

2.4 Conclusion and Recommendation

PAM characterization was performed with respect to MW and CD which are the key characteristics in PAM-induced soil stabilization and flocculation. Also, the applicability of simple MW and CD measurement techniques were investigated in a comparative study with state-of-the-art techniques.

In MW measurements, the consistent difference between MWs measured with two different measurement techniques was found with the ratio of 1.7129 (MW_W / MW_V), which may be used as an interim and empirical correction factor to estimate MWs for various nonionic and anionic PAMs. However, to overcome the observed inconsistencies, which are caused not only by the extrapolation of MHS equations out of the applicable MW ranges, further investigation will be required to set up an adequate intrinsic viscosity measurement technique with proper MHS equation covering a broad

MW range for larger PAM stabilizers or flocculants. In addition, to overcome the difficulties caused by the heterogeneous and dynamic nature of large polymers, the standardized measurement protocols will be required in developing MHS equations.

In CD measurement, the simple acid-base titration method was well correlated with elaborate CHN elemental analysis. Thus, the acid-base titration method was found as an easier on-site measurement technique for CDs of PAM stabilizers or flocculants.

2.5 REFERENCES

Virginia Department of Recreation and Conservation, 2002, Erosion & sediment control technical bulletin #2: Application of anionic polyacrylamide for soil stabilization and stormwater management, from *http://www.dcr.virginia.gov/soil_&_water/documents/anoinic.pdf*

Barvenik, F. W., 1994, Polyacrylamide characteristics related to soil applications, *Soil Science*, 158(4), 235-243

Berth, G., H. Dautzenberg, B.E. Christensen, S.E. Harding, G. Rother, and O. Smidsrod, 1996, Static light scattering studies on Xanthan in aqueous solutions, *Macromolecules*, 29, 3491-3498

Chapra, S. C., 1997, *Surface Quality Modeling*, McGraw-Hill, New York, NY

Chibowski, S., and M. Wisniewska, 2002, Study of electrokinetic properties and structure of adsorbed layers of polyacrylic acid and polyacrylamide at Fe_2O_3-polymer solution interface, *Colloids and Surfaces A: Physicochem. Eng. Aspects*, 208, 131-145

Farrokhpay, S., G.E. Morris, D. Fornasiero, and P. Self, 2004, Effects of chemical functional groups on the polymer adsorption behavior onto titania pigment particles, *Journal of Colloid and Interface Science*, 274, 33-40

Francois, J., D. Sarazin, T. Schwartz, and G. Weill, 1979, Polyacrylamide in water: molecular weight dependence of $<R^2>$ and $[\eta]$ and the problem of the excluded volume exponent, *Polymer*, 20, 969-975

Fried, J. R. , 1995, *Polymer Science and Technology*, Prentice Hall

Gardner, K. L., W.R. Murphy, and T. G. Geehan, 1978, Polyacrylamide solution aging, *Journal of Applied Polymer Science*, 22, 881-882

Green, V. S., D.E. Stott, L.D. Norton, and J. G. Graveel, 2000, Polyacrylamide molecular weight and charge effects on infiltration under simulated rainfall, *Soil Sci. Soc. Am. J.*, 64, 1786-1791

Griebel, T., W.M. Kulicke, and A. Hashemzadeh, 1991, Characterization of water-soluble, cationic polyelectrolytes as exemplified by poly(acrylamide-co-trimethylammoniumethylethacryate chloride) and the establishment of structure-property relationships, *Colloid & Polymer Science*, 269, 113-120

Heller, H., and R. Keren, 2002, Anionic polyacrylamide polymers effects on rheological behavior of sodium-montmorillonite suspension, *Soil Sci. Soc. Am. J.*, 66, 19-25

Heller, H., and R. Keren, 2003, Anionic polyacryamide polymer adsorption by pyrophyllite and montmorillonite, *Clays and Clay Minerals*, 51(3), 334-339

Hunkeler, D., X.Y. Wu, and A. E. Hamielec, 1992, Molecular weight characterization of polyacrylamide-co-sodium acrylate. II. Light scattering, *Journal of Applied Polymer Science*, 46, 649-657

Klein, J., and K. D. Conrad, 1978, Molecular-weight determination of poly(acrylamide) and poly(acrylamide-co-sodium acrylate), *Macromolekulare Chemie - Macromolecular Chemistry and Physics*, 179(6), 1635-1638

Klein, J., and A. Westerkamp, 1981, Peculiarities of polyacrylamide analysis by aqueous GPC, *Journal of Polymer Science: Polymer Chemistry Edition*, 19, 707-718

Levy, G. J., and M. Agassi, 1995, Polymer molelcular weight and degree of drying effects on infiltration and erosion of three different soils, *Aust. J. Soil Res.*, 33, 1007-1018

McCarthy, K. J., C.W. Burkhardt, and D. P. Parazak, 1987, Mark-Houwink-Sakurada constants and dilute solution behavior of heterodisperse poly(acrylamide-co-sodium acrylate) in 0.5M and 1M NaCl, *Journal of Applied Polymer Science*, 33, 1699-1714

Myagchenkov, V. A., and V. F. Kurenkov, 1991, Applications of acrylamide polymers and copolymers: a review, *Polym.-Plast. Technol. Eng.*, 30(2-3), 109-135

Owen, A. T., P.D. Fawell, J.D. Swift, and J. B. Farrow, 2002, The impact of polyacrylamide flocculant solution age on flocculation performance, *Int. J. Miner. Process.*, 67, 123-144

Schwartzenbach, R. P., P.M. Gschwend, and D. M. Imboden, 2003, *Environmental Organic Chemistry, 2nd edition*, John Wiley & Sons, Hoboken, NJ

Scott, J. P., P.D. Fawell, D.E. Ralph, and J. B. Farrow, 1996, The shear degradation of high-molecular-weight flocculant solutions, *Journal of Applied Polymer Science*, 62, 2097-2106

Seybold, C. A., 1994, Polyacylamide review: soil conditioning and environmental fate, *Commun*, *Soil Sci. Plant Anal.*, 25(11-12), 2171-2185

Shainberg, I., and G. J. Levy, 1994, Organic polymers and soil sealing in cultivated soils, *Soil Science*, 158(4),

Sperling, L. H., 2006, *Introduction to physical polymer science, 4th Edition*, John Wiley & Sons, Inc., Hoboken, NJ

Stumm, W., and J. J. Morgan, 1996, *Aquatic chemistry, 3rd ed*, Johns Wiley & Sons, Inc., Canada

Wu, X. Y., D. Hunkeler, A.E. Hamielec, R.H. Pelton, and D. R. Woods, 1991, Molecular weight characterization of poly(acrylamide-co-sodium acrylate). I. Viscometry, *Journal of Applied Polymer Science*, 42, 2081-2093

Wyatt Technology Corp, 1998, *ASTRA for Window's User's Guide*, Wyatt Technology Corp, Santa Barbara, CA, USA.

CHAPTER 3. APPLICABILITY OF SIMPLIFIED ELECTROSTATIC INTERACTION MODELS IN PREDICTING ELECTROSTATIC INTERACTION CHEMISTRY OF POLYACRYLAMIDE-co-ACRYLATE : IMPERMEABLE SPHERE, DONNAN, AND CYLINDRICAL MODEL

3.0 Abstract

The intriguing question on polyelectrolyte's size, shape, conformational alteration, and their reciprocal effects on electrostatic interaction chemistry was investigated in the comparative study between experiments and simulations, with applying three simplified electrostatic interaction models, impermeable sphere (IS), Donnan (DN), and cylindrical (CY) models. Potentiometric acid-base titration experiments were done with linear polyacrylamide-co-acrylates (anionic PAM) having different ionizable site densities and in aqueous solutions having various ionic strengths, both of which are determining factors for electrostatic interaction chemistry. Specific viscosities were measured as polyelectrolyte's size indices and compared with the estimated sizes which are obtained from model-data fitting procedures between experimental and simulated potentiometric titration curves. The observed physicochemical behaviors of linear polyelectrolytes in potentiometric titration and specific viscosity tests were used to estimate the validity of electrostatic interaction models and their underlying hypotheses. In this comparative study, IS and DN models and their hypothetical spheres for polyelectrolyte molecules were proven to be unrealistic with the conflicts between experimental results and model hypotheses. However, CY model and its hypothetical cylinder proved their validity with the close fits between

measured and simulated potentiometric titration curves. Furthermore, the close fits in the CY model application were obtained without the iterative model-data fitting procedures but simply with constant cylindrical dimensions, which are compatible for all the experimental conditions. Thus, irrespective of the reported coiled and spherical shapes for linear polyelectrolyte molecules in the previous research, in the domain of electrostatic interaction chemistry, cylindrical shapes are more reasonable than spherical shapes, with the assumption that coiled polyelectrolytes have large void spaces for counter-balancing ions to travel freely inside the coiled structures without the effects of site-site electrostatic interactions.

3.1 Introduction

Polyelectrolytes are defined as polymers with ionizable functional groups on their backbone chains (Molyneux, 1983). Excluding several unusual structures such as branched or dendritic structures, polyelectrolytes have linear chain structures in general. Thus, in the context of this research paper, polyelectrolyte means rather the linear polyelectrolyte. In aqueous solutions, polyelectrolytes can be charged negatively or positively, depending on their backbone functional groups, and thus have important characteristics such as high solubility, counter-ion binding capacity, conformational alteration. Polyelectrolytes are ubiquitous on the Earth as the natural polyelectrolytes (*e.g.* proteins, nucleic acids, polysaccharides, humic substances), as the modified natural polyelectrolytes (*e.g.* carboxymethylcellulose), and the synthetic polyelectrolytes (*e.g.* polyacrylic acid, polymethacrylic acid). Furthermore, all the polyelectrolytes play their indispensable roles in the environments or industries as the constituent elements in living creatures, the participants in bio- and geo-chemical cycles, the functional materials in many industrial fields, and so on (Rice and Nagasawa, 1961; Molyneux, 1983; Stumm and Morgan, 1996; Tipping, 2002). Thus, for the better understanding and application of the ubiquitous and indispensible polyelectrolytes, many researchers have studied on the characteristic behaviors of polyelectrolytes in aqueous solutions and set up mathematical models to predict those behaviors.

In understanding and predicting the behaviors of polyelectrolytes in aqueous solutions, two key characteristics are (1) electrostatic interaction chemistry which represents acid-base chemistry in cooperation with electrostatic interactions around polyelectrolytes and (2) polyelectrolyte's conformation which includes shapes, sizes and their alterations. The most important aspect of these two key characteristics lies on their reciprocal interactions. For example, anionic polyelectrolytes become fully ionized at high pH and subsequently develop expanded structures due to the electrostatic repulsion between ionized sites. In contrast, at low pH, anionic polyelectrolytes become neutral by counter-ion binding on ionized sites and thus are expected to develop rather coiled and contracted structures with neutralizing electrostatic repulsion. Likewise, polyelectrolyte's electrostatic interaction chemistry in aqueous solutions is able to cause the conformational alteration of polyelectrolytes. Needless to say, the conformational alteration of polyelectrolyte also make critical effects on polyelectrolyte's electrostatic chemistry by enhancing or deteriorating the mobility of counter-ions in expanded or contracted structures of polyelectrolytes (Rice and Nagasawa, 1961; Nagasawa *et al.*, 1965; Olander and Holtzer, 1968; Kawaguchi and Nagasawa, 1969; Oosawa, 1971; Muroga *et al.*, 1972; Cleland, 1984; Ullner and Jonsson, 1996; Matijevic, 2001). In addition to conformational alteration, the geometry of the hypothetical shape of a polyelectrolyte molecule as a charge container (*e.g.* sphere *versus* cylinder) is important in modeling or simulation, with determining the density of charged sites and thus altering electrostatic interaction chemistry and potentiometric titration curves (Hill, 1955; Kotin and Nagasawa, 1962). Thus, as well as the electrostatic interaction chemistry of polyelectrolytes, the conformational shapes and alterations of polyelectrolytes, such as sphericity/linearity and expansibility, should be carefully considered and incorporated into electrostatic interaction models to predict better the physicochemical behaviors of polyelectrolytes in aqueous solutions.

Numerous electrostatic interaction models have been developed to predict electrostatic interaction chemistry with the conformational consideration of polyelectrolytes in aqueous solutions. In general, electrostatic interaction models are the combined equations of the two constituent parts, which are (1) electrostatic acid-base chemistry model to predict association or dissociation of counter-ions on ionizable sites of polyelectrolytes and (2) spatial electrostatic potential distribution model to simulate counter-balancing ion distribution on or near charged surfaces (imagine a buffer zone between the solid and aqueous phases to counter-balance the charged surface). Especially, the spatial electrostatic potential distribution model is the key component to incorporate the conformational characteristics of polyelectrolytes.

Until now, most of electrostatic interaction models have been developed on the basis of the Poisson-Boltzman (PB) equation, in which counter-balancing ions are assumed to be concentrated on the charged surface and diffused away toward the aqueous phase. The Poisson-Boltzman equation is formulated as a form of diffusion equations through the solid-liquid interface, incorporating electrostatic potential as an independent variable. However, the second-order nonlinear PB equation with the variable source term, which is tightly connected to the complex acid-base chemistry model, is not easy to be solved. Thus, to overcome the computational difficulties of the PB equation and to incorporate the conformational characteristics of polyelectrolytes, many approximate analytical electrostatic interaction models have been developed, including Debye-Huckel theory which assumes polyelectrolytes as impermeable spheres or cylinders, Gouy-Chapman theory as flat plates, Donnan model as gel-like permeable spheres, and so on (Stumm and Morgan, 1996; Hansen and Lowen, 2000; Tipping, 2002). However, the hypothetical shapes of various electrostatic interaction models are still debatable due to the absence of the straightforward tools in observing or measuring polyelectrolytes' structures. For example, Nagasawa *et al.* (1965) and Kawaguchi *et al*. (1969) treated the molecules of polymathacrylic acid as rod-like cylinders, while Pohlmeier and Harber-Pohlmeier (2004) assumed as permeable spheres with their argument on "over-coiling" of polyelectrolytes, in which electrostatic repulsion between charged sites is not strong enough to stretch polyelectrolyte chains. Thus, one of the research initiatives in this study was set to identify the realistic hypothetical shape of polyelectrolytes and the related electrostatic interaction model.

In this research, for easiness in computation and applicability into complex aquatic systems, the most simplified analytical models, impermeable sphere (IS), Donnan (DN), and cylindrical (CY) models, were evaluated for the validity of the models and their unique hypothetical shapes for polyelectrolyte molecules. Though these simplified models do not represent all the physicochemical phenomena occurring at PAM-solution interfaces, they were demonstrated to be practical tools for predicting the electrostatic interaction chemistry of polyelectrolytes with their simplified hypothetical shapes for polyelectrolyte molecules (Hill, 1955; Ullner and Jonsson, 1996; Avena *et al.*, 1999; Koopal *et al.*, 2005; Saito *et al.*, 2005). Impermeable sphere and Donnan models assume polyelectrolyte molecules as rigid and gel-like spheres, respectively. Thus, counter-balancing ions are assumed to reside on or near the charged surface of impermeable spheres in IS model, while they smear inside the permeable sphere in DN model (Avena *et al.*, 1999; Koopal *et al.*, 2005; Saito *et al.*, 2005). Cylindrical model, which is the analytical derivation of the PB equation with Debye-Hückel approximation, assumes polyelectrolyte molecules as very long rod-like cylinders on which counter-balancing ions are concentrated and diffused away into the bulk solution (Hill, 1955; Ullner and Jonsson, 1996; Matijevic, 2001). In Cylindrical model, against the argument of Pohlmeier and Haber-Pohlmeier (2004) on the over-coiling structure of polyelectrolytes, we set up the hypothesis that void spaces between chain segments are large enough for counter-balancing ions to access or escape freely in or out of polyelectrolyte structures without the effects of site-site interactions.

A series of weakly charged linear polyacrylamide-co-acyliates (anionic PAM) were selected and tested in experimental and simulation works. Those PAMs have different ionizable site densities (ISD) on their backbone chains *i.e.* have similar chain structures but different electrostatic characteristics, to be used in estimating the model applicability for a wide range of polyelectrolytes' electrostatic characteristics. In a comparative study of experimental results and model theories, we tried to speculate on the rationality of the polyelectrolyte's hypothetical conformations of the models and to research on the reciprocal effects between polyelectrolyte's conformation and electrostatic interaction chemistry.

3.2 Model Description

3.2.1 Electrostatic Acid-Base Chemistry Model

Anionic polyelectrolytes contain ionizable sites on their backbone chains, such as carboxylic groups on anionic PAM ($RCOOH \leftrightarrow RCOO^- + H^+$), and thus develop their surface charges by ionization of functional sites with increasing pH. Degree of ionization (α) of polyelectrolytes can be simulated with acid-base chemistry model (see Equation (3.1)) (Pohlmeier and Haber-Pohlmeier, 2004). In contrast to the acid-base chemistry model for monomeric acids, the electrostatic acid-base chemistry model for polyelectrolytes contains the correction factor (χ), which represents the effects of electrostatic interaction caused by ionized sites and connects two separate domains of the acid-base chemistry model and the spatial electrostatic potential distribution model. The backbone charge (Q) obtained with acid-base chemistry model should be balanced with the counterpart backbone charge calculated with spatial electrostatic potential distribution model, which will be shown in the following section.

$$Q = \frac{\{L^{-}\}}{C_{Poly}} = \frac{\{L^{-}\}_{TOT} \times \exp(-\chi)}{\left(K_0^H [H^+]_b + \exp(-\chi)\right) \times C_{Poly}} \tag{3.1}$$

In Equation (3.1), Q represents the backbone charge of polyelectrolyte (mol/gPolyelectrolyte), $\{L^{-}\}$ is the local concentration of ionized sites of polyelectrolytes (mol/L), and $\{L^{-}\}_{TOT}$ is the total concentration of all the ionizable sites of polyelectrolytes (mol/L). K_0^H is the intrinsic protonation constant of a carboxylic acid group and selected as $10^{-4.25}$ (the protonation constant of a monomeric acrylic acid), which had been proven to be valid in the previous potentiometric titration experiments with polyacrylate-containing solutions (Kotin and Nagasawa, 1962). C_{Poly} is the mass concentration of polyelectrolyte (gPolyelectrolyte/L), χ is the dimensionless electric potential ($-\frac{z_i \cdot F \cdot \psi}{R \cdot T}$), z_i is the charge number of ion i (with sign), F is Faraday's constant (96485 C/mol), ψ is the electrostatic potential (V), R is the ideal gas constant (8.314 J/mol/K), and T is temperature (K). In Equation (3.1), if all the functional sites of polyelectrolytes are fully ionized, Q becomes equivalent to Q_{max} ($Q_{max} = \{L^{-}\}_{TOT} / C_{Poly} = 71 \cdot \mathbf{ISD}(\%)/100$), where 71 is MW of one repeating unit of a PAM molecule (g/mol). ISD represents ionizable charge density of a PAM molecule (%), which is often called as charge density (CD) by soil scientists or engineers.

3.2.2 Spatial Electrostatic Potential Distribution Models

Backbone charge of ionized polyelectrolytes (*Q*) obtained from electrostatic acid-base chemistry model (Equation (3.1)) should be balanced with the counterpart from spatial electrostatic potential distribution models, which are IS, DN, and CY models in this research.

In impermeable sphere model, polyelectrolytes are assumed to be impermeable spheres and their ionized sites to be located on the surface of impermeable spheres (see Figure 3.1). Thus, counter-balancing electrostatic potential develops on or near the surface of the spheres and diffuses away into the solution phase. Equation (3.2) and (3.3) shows the mathematical formula of IS model, which is the simplified analytical solution of the PB equation with the Debye-Hückel approximation in the spherical coordinate (Avena *et al.*, 1999; Saito *et al.*, 2005).

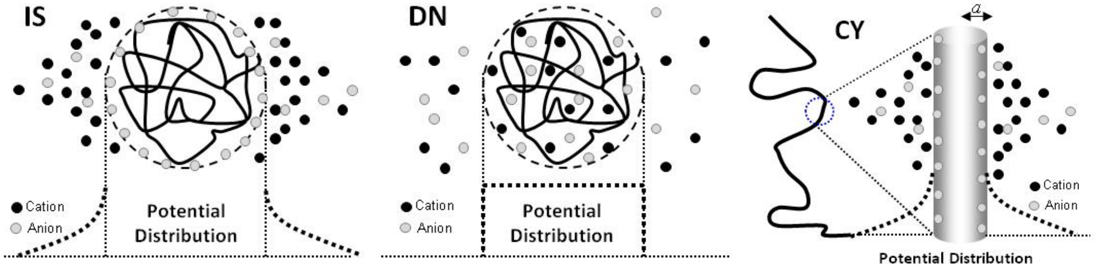

Figure 3.1. Schematic diagrams of co- and counter-ion distributions and electrostatic interaction potential distributions around polyelectrolytes in aqueous solutions in IS, DN, and CY models (adopted from Avena *et al.* (1999)).

In Equation (3.2) and (3.3), *S* represents the specific surface area (m^2/g) which is proportional to the hydrodynamic volume or the specific viscosity of a polyelectrolyte

($V_H \propto S^{3/2}$ where, $\eta_{sp} \propto V_H$), σ_{IS} is the charge density on the surface of the impermeable sphere (C/m^2), χ_{IS} is the dimensionless electrostatic potential in the diffuse domain, R_H is hydrodynamic radius of a PAM molecule ($R_H = \sqrt{S \cdot M_W / \left(4\pi \cdot N_A\right)}$, m), M_W is molecular weight of a PAM molecule (g/mol), N_A is Avogadro's number (6.022 × 10^{23} /mol), κ is defined as the Debye constant (/m), c_{salt} is the background salt concentration in the solution phase (mol/L), z_{salt} is the charge number of the background salt, ε_0 is the permittivity of free space (8.854×10^{-12} C/m/J), and ε is the relative dielectric constant of water (78.5 at 25 ^{o}C) (Stumm and Morgan, 1996).

$$Q = \frac{S \cdot \sigma_{IS}}{F} = S \cdot \frac{2 \cdot c_{salt} \cdot z_{salt}}{\kappa}\left[2 \cdot \sinh\left(-\frac{\chi_{IS}}{2}\right) + \frac{4}{\kappa \cdot R_H}\tanh\left(-\frac{\chi_{IS}}{4}\right)\right] \tag{3.2}$$

$$\kappa = \left(\frac{2 \cdot F^2 \cdot c_{salt} \cdot z_{salt}^2}{R \cdot T \cdot \varepsilon_0 \cdot \varepsilon}\right)^{\frac{1}{2}} \tag{3.3}$$

In Donnan model, polyelectrolytes are assumed as permeable spheres in which counter-balancing ions smear without any hindrance. Thus, counter-balancing ions reside inside polyelectrolyte spheres and thus the electrostatic potential remains constant throughout the sphere (see Figure 3.1). Equation (3.4) represents the mathematical equation of DN model (Avena *et al.*, 1999; Saito *et al.*, 2005). In Equation (3.4), V_D is defined as the Donnan volume (L/g; m^3/kg) which is assumed to be equivalent to the hydrodynamic volume or the specific viscosity of a polyelectrolyte ($V_D = V_H$ where,

$\eta_{sp} \propto V_H$), ρ_D is the charge density in the Donnan volume (C/m^3), ψ_D is the electrostatic potential in the Donnan volume (V), and χ_D is the dimensionless electrostatic potential in the Donnan domain.

$$Q = -\frac{V_D \times \rho_D}{F} = V_D \times 2 \times c_{salt} \times z_{salt} \times \sinh\left(-\chi_D\right) \tag{3.4}$$

In cylindrical model, polyelectrolyte molecules are assumed to be rod-like long cylinders and ionized sites to be located on the surface of cylinders. The potential caused by ionized sites on polyelectrolyte molecules is counter-balanced with the spatial electrostatic potential diffusion on or near cylindrical surfaces. The mathematical equation of CY model is the simplified analytical solution of the PB equation with the Debye-Hückel approximation in the cylindrical coordinate (Hill, 1955; Ullner and Jonsson, 1996; Matijevic, 2001). In Equation (3.5) and (3.6), L represents the specific length (m/g), M_{seg} is the molecular weight of an individual segment of a polyelectrolyte molecule (g/mol), L_{seg} is the length of an individual segment (m), a is the radius of a polyelectrolyte cylinder (m), and $K_n(x)$ is the modified Bessel function of the second kind.

$$Q = \frac{L \times \sigma_{CY}}{F} = \frac{L}{F} \times \varepsilon \times \varepsilon_0 \times \kappa \times \frac{K_1(\kappa a)}{K_0(\kappa a)} \times \left(-\frac{\chi \times R \times T}{F}\right) \times 2\pi \times a \tag{3.5}$$

$$L = \frac{N_A}{M_{seg}} \cdot L_{seg} \tag{3.6}$$

3.3 Materials and Methods

3.3.1 Polyacrylamide Sample Preparation and Characterization

A series of anionic PAMs with different molecular weights (MW, g/mol) and ionizable site densities (ISD = $\frac{\text{No. of hydrolyzable Units}}{\text{No. of Repeating Units}}$ %) were obtained from and Kemira Water Solutions Inc. (Lakeland, FL). To remove salts and other impurities (mostly NaCl), PAMs were purified by the serial steps of dissolution, acidification, and precipitation in water-methanol mixtures (Francois *et al.*, 1979). Commercial PAM powders were firstly dissolved in distilled deionized water (DDW) and gently stirred on a Thermolyne® Bigger Bill orbital shaker (Thermo Fisher Scientific Inc., PA) for one or two days. After complete dissolution, PAM solutions were acidified to pH 3 with hydrochloric acid to protonate all carboxyl groups and simultaneously dissociate metal cations on PAM molecules. Then, PAM solids were collected by precipitation induced by the addition of methanol and preservation in a 4^{o}C cold room. The serial steps of dissolution, acidification, and placement were done repeated four to five times to collect pure PAM solids without salts or other contaminants on PAM molecules. Finally, purified PAM solids were lyophilized with a VirTis® bench top freeze dryer (SP Industries Inc., NY) and preserved as powder forms for the uses in the subsequent experiments.

Molecular weights (MW) of PAMs were estimated in a simple intrinsic viscosity measurement tests with a capillary viscometer (Sperling, 2006). A series of PAM solutions with different concentrations of 0.025, 0.05, 0.075, and 0.1 g/dL were prepared at 0.2 M Na_2SO_4 background salt concentration and at pH 9. Then, the intrinsic viscosity ($[\eta]$) of a certain PAM sample was estimated with the specific and relative viscosities of the serial PAM solutions, which were measured with #50 Cannon-Fenske routine viscometer (Cannon Instrument Company Inc., PA) at 25 ^{o}C in a constant temperature water bath (PolyScience, IL). Finally, Mark-Houwink-Sakurada equation (MHS equation, $[\eta] = K \cdot MW^{a}$) was used to determine MW of a PAM with a measured intrinsic viscosity (Wu *et al.*, 1991). Wu *et al.*'s MHS equation which has the continuous functions to obtain the model constants (K and a) with respect to ionizable site density (ISD) of a anionic PAM was used as a unique equation to estimate MWs of anionic PAMs having various ISDs. In our previous research, the intrinsic viscosity technique were found to have the ability to estimate the relative magnitude of MWs between various anionic PAM samples, even though the absoluteness of estimated MWs is still questionable due to the consistent deviation between the coupled MWs estimated with an intrinsic viscosity measurement and with a light scattering analysis technique. Thus, it should be acknowledged that the provided MWs of anionic PAMs are not the absolute values but rather the relative magnitudes of MWs.

Ionizable site densities (ISD) of anionic PAMs were estimated with the data from potentiometric titration experiments (see the next section). Ionizable site density (ISD) of a PAM sample was estimated with the maximum specific charge density found at the upper plateau of the *S*-shaped potentiometric titration curve, where the entire PAM molecules become fully ionized. Table 3.1 represents the summarized MWs and ISDs of anionic PAMs which were used in this research.

Table 3.1. Measured molecular weights (MW) and ionizable site densities (ISD) of the pre-cleaned Kimera® PAMs used in electrostatic interaction model applications.

Group	Generic Number	Manufacturer Provided		Measured	
		MW	CD	MW† (10^6 g/mol)	ISD* (%)
ISD 10%	ISD10-1	Medium	10	2.88 ± 0.02	9.9 ± 0.09
ISD 18%	ISD18-1	Medium	10	2.08 ± 0.01	18.3 ± 0.13
ISD 20%	ISD20-1	Ultra-High	15	2.12 ± 0.01	20.3 ± 0.11
ISD 25%	ISD25-1	Medium	20	1.46 ± 0.02	25.2 ± 0.07
	ISD25-2	High	20	1.86 ± 0.02	25.0 ± 0.05
	ISD25-3	Ultra-High	25	3.27 ± 0.01	25.7 ± 0.32
ISD 35%	ISD35-1	Medium	30	1.31 ± 0.01	35.1 ± 0.13
	ISD35-2	High	30	2.18 ± 0.02	34.8 ± 0.18

† MW represents Mean ± Difference between MWs estimated with Huggins and Kreamer plots.
* ISD represents Mean ± Standard Error between measurements in different salt concentrations.

3.3.2 Potentiometric Titration Test and Model-Data Fitting Procedure

In potentiometric titration tests, 50 mL solutions with 1 g/L PAM concentration were prepared at 0.001 M NaCl background salt concentration. For the prepared PAM solution, titration was performed upward with 0.5 M NaOH dose and then downward with 0.5 M HCl dose and pH was monitored continuously with Orion 420A pH meter (Thermo Scientific Inc., PA). After each cycle of the forward and backward titrations at pH 3, the concentrated NaCl solution was injected to increase ionic strengths to the level of 0.01 or 0.1M NaCl, to identify the effect of ionic strengths on electrostatic interaction acid-base chemistry. Also, the ionic strength and PAM concentration changes by adding acid or base titrant were recorded in the entire titration experiment. During titration, PAM solution was continuously purged with pure nitrogen gas (National Welders Supply Co., NC) to prevent CO_2 dissolution. For all the experimental results, differences between pHs at the equivalent acid or base doses measured with forward and backward titrations were estimated as 0.083 ± 0.009, 0.035 ± 0.003, and 0.059 ± 0.007 (mean ± standard error), for 0.001 M, 0.01 M, and 0.1 M NaCl solution conditions, respectively. Thus, the coupled potentiometric titration curves obtained with forward and backward titrations were proven to be close enough to prove the credibility of our experimental methodology. Finally, the *S*-shaped titration curves (pH *versus* specific charge density) were plotted after processing measured data (pH and the titrated volume of acid/base) and they were adjusted with subtracting background acid or base consumptions by water self-ionization (see Figure 3.2 and Appendix D).

In the model-data fitting procedure between experimental and simulated potentiometric titration curves, the method of least squares was applied with employing polyelectrolyte's sizes as fitting parameters (S in IS model or V_D in DN model) (Berthouex and Brown, 1994). The best fit curve and parameter was found at the minimum sum of residual errors (SRE) (see Equation (3.7)). Figure 3.2 shows an example of potentiometric titration curves, measured with potentiometric titration test and simulated with electrostatic interaction model (IS model). In contrast to IS and DN models, CY model was found to have constant model parameters for polyelectrolyte's cylindrical radius (a) and segment length (L_{seg}), which are applicable to all the experimental conditions without iterative model-data fitting procedures. This observation will be discussed again in the later section of this paper.

$$SRE = \sum_{i=1}^{n} \left(error_i \right)^2 = \sum_{i=1}^{n} \left(y_{exp,i} - y_{model,i} \right)^2 \tag{3.7}$$

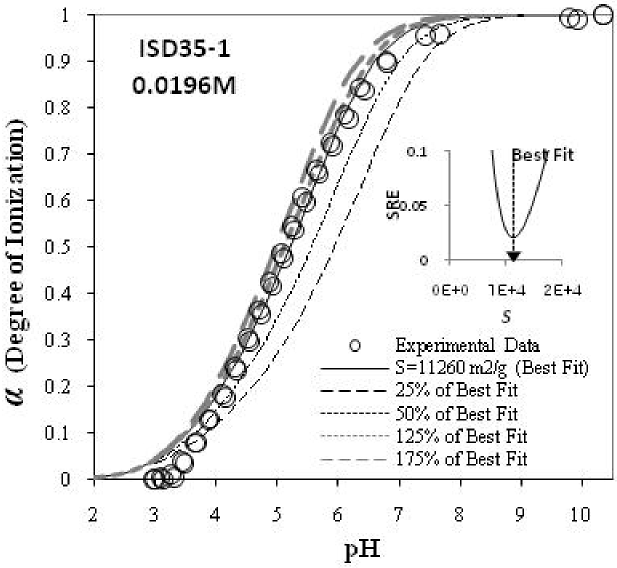

Figure 3.2. Experimental and simulated potentiometric titration curve with IS model application for ISD35-1 PAM (MW_v = 2.18 × 10^6 g/mol, ISD = 35%) at 0.0196M ionic strength. Degree of ionization (α) represents the normalized ionized site density of a polyelectrolyte by assuming the maximum ionized density as one. The inner plot represents SRE *versus S* plot in the model-data fitting procedure.

3.3.3 Specific Viscosity Measurement

The traveling time of the pure solvent and PAM solutions through a capillary tube (t_s and t_c) was measured with #50 Cannon-Fenske routine viscometer (Cannon Instrument Company Inc., PA) and then were used to estimate specific viscosity ($\eta_{sp} = t_c/t_s - 1$). According to Einstein viscosity theorem, specific viscosity is proportional to the volume of the hydrodynamic sphere of a polymeric molecule (Equation (3.8)) (Sperling, 2006). Thus, measured specific viscosity was used as a relative size index to find out its correlation with polyelectrolyte's hypothetical size estimated in the model-data fitting procedure (Avena *et al.*, 1999). In Equation (3.8), η_{sp} represents the specific viscosity, η is the viscosity of polyelectrolyte solution, η_0 is the viscosity of pure solvent, n_2/V is the number of molecules per unit volume, and V_H is the hydrodynamic volume (L/g; m^3/kg).

$$\eta_{sp} = \frac{\eta - \eta_0}{\eta_0} = \frac{t_c - t_s}{t_s} = 2.5\left(\frac{n_2}{V}\right)V_H \quad \Rightarrow \quad \therefore \eta_{sp} \propto V_H \tag{3.8}$$

3.4 Results and Discussion

First and foremost, to identify the characteristic trends of potentiometric titration curves, we carried out examinations on the sample potentiometric titration curves which were measured and simulated with ISD35-1 PAM at two different ionic strengths (0.0043 M and 0.1124 M) (see Figure 3.3). In addition, three different simplified electrostatic interaction models (IS, DN, and CY models) were applied in simulation, to identify how they make effects on the curvature and trend of simulated potentiometric titration curves. In general, potentiometric titration curves slant forward from a steep titration curve of a monomeric acid, due to electrostatic interaction potential which holds protons on or near the polyelectrolyte's surface and thus makes a lag of deprotonation of polyelectrolytes with increasing pH. The slants of titration curves become more severe with lower ionic strengths and with higher polyelectrolyte's ionizable site density due to increasing electrostatic interaction potential (see Figure 3.3, 3.7 and Appendix D).

Also, in Figure 3.3, the different curvatures of simulated potentiometric titration curves were observed with the applications of IS, DN, and CY models at the lower ionic strength (0.0043 M). In detail, with increasing pH in the bulk solution and degree of ionization (α) of polyelectrolyte molecules, the curves with CY and IS models become more oblique forward due to higher electrostatic interaction potential than the curve with DN model. Considering the geometry of polyelectrolyte's hypothetical shapes in different electrostatic interaction models, we could speculate that the same amount of charged sites of a PAM molecule should be distributed in a more compacted manner on the cylindrical surface (CY) or on the spherical surface (IS) than in the spherical volume (DN). In turn, the higher density of charged sites in IS and CY models induces higher electrostatic interaction potential and generates more oblique potentiometric titration curves than the lower density of charged sites in DN model. Especially, CY model generates better predictions with smaller residuals in the region of pH 5 to 10 than DN and IS models, because of its oblique curve (see Figure 3.3 (b) and (c)) Thus, polyelectrolyte's hypothetical shapes of different models were proven to play a significant role in determining electrostatic interaction chemistry and potentiometric titration curve.

With respect to the accuracy of the models in Figure 3.3, IS and CY models produced better fit curves on the experimental data and thus generated lower residuals between simulated and experimental data than DN model, especially for the low ionic strength condition. However, noteworthily, in CY model application, the fixed dimensional parameters for polyelectrolyte's hypothetical cylinder were found to be compatible for all the experimental conditions and thus used in simulation without the iterative model-data fitting procedure. The compatibility of the constant model parameters in CY model will be discussed again in the later part of this paper.

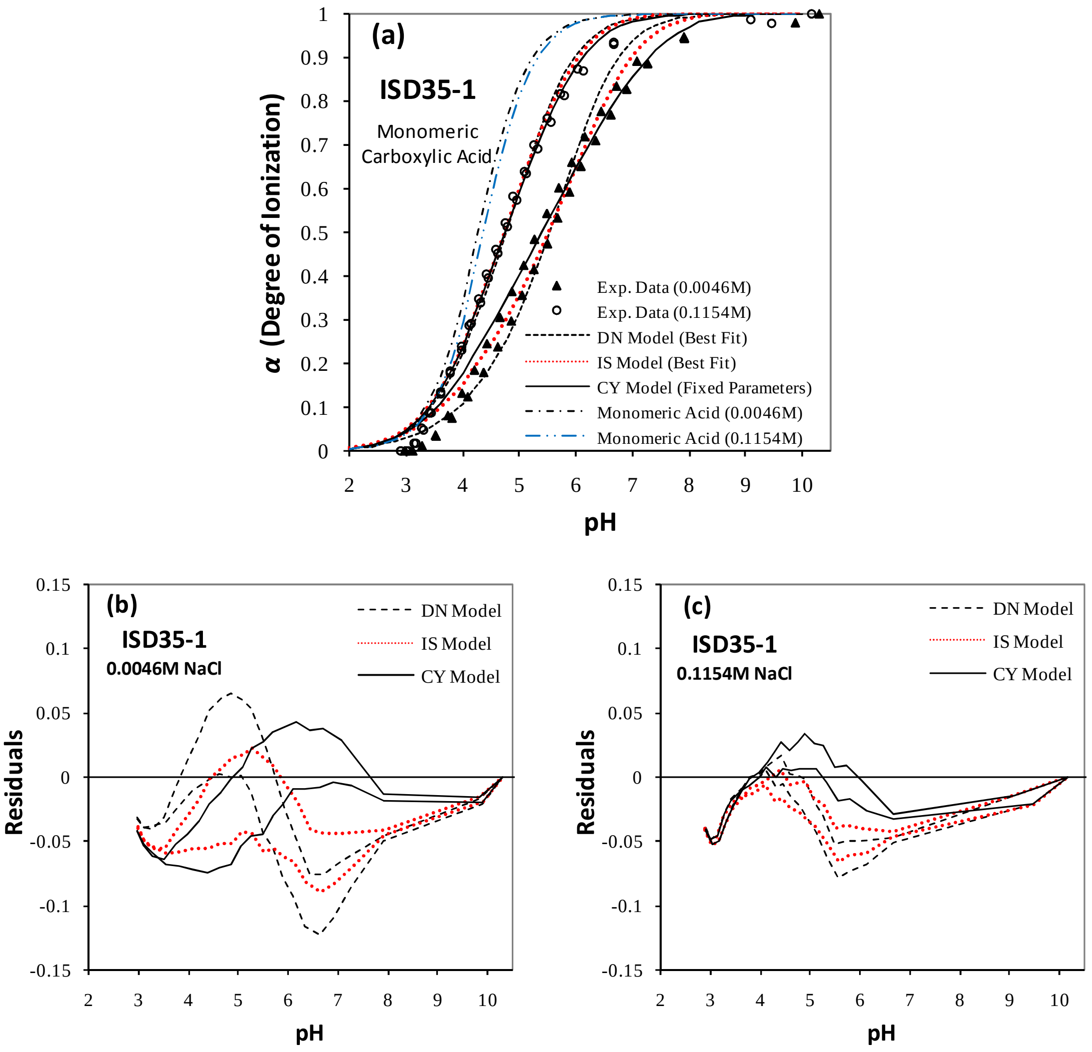

Figure 3.3. (a) typical experimental and simulated potentiometric titration curves with application of three different electrostatic interaction models. (b) and (c) represent

residual plots between experimental and simulated data. ISD35-1 PAM (MW_v = 2.18 × 10^6 g/mol, *ISD* = 35%) was used. (See Appendix D for all the other PAMs)

As mentioned in the experimental section, the measured specific viscosity (η_{sp}) was treated as the relative size index for polyelectrolyte molecules and used to find its correlation with the estimated polyelectrolyte's size in the model-data fitting procedures (*S* in IS model and V_D in DN model), according to Einstein viscosity theorem (Equation (3.8)). However, two remarkable inconsistencies between measured and estimated sizes were identified in this comparative study.

Firstly, the measured specific viscosities were found to increase with increasing pH due to polyelectrolyte's size expansion, while the hypothetical sizes in the framework of IS and DN models are assumed to be constant in the whole pH range (Avena *et al.*, 1999; Saito *et al.*, 2005). In Figure 3.4, the measured specific viscosities for ISD25-3 PAM solutions increase with increasing pH and interestingly the trends of the specific viscosity plots resemble those of *S*-shaped potentiometric titration curves. In other words, the specific viscosity change *i.e.* the expansion or contraction of polyelectrolytes was governed by pH in the bulk solution and degree of ionization (α) of polyelectrolytes. Thus, the model assumption that the size of polyelectrolytes should remain constant with changing pH clearly conflicts with the observed changes of the measured specific viscosities.

In contrast to our observation, Pohlmeier and Haber-Pohlmeier (2004) reported that the size change of polyelectrolyte were marginal in changing pH. However, considering that MWs or chain lengths of polyelectrolytes used in this research are tens or hundreds times bigger and hence inducing the chain coiling more severely than those used in Pohlmeier and Haber-Pohlmeier's research, the observed expansion or contraction of anionic PAMs with changing pH may be reasonable. Also, the dimensional or conformational alterations with changing pH have been reported numerously in the previous researches (Rice and Nagasawa, 1961; Nagasawa *et al.*, 1965; Olander and Holtzer, 1968; Kawaguchi and Nagasawa, 1969; Oosawa, 1971; Muroga *et al.*, 1972; Cleland, 1984; Ullner and Jonsson, 1996; Matijevic, 2001). Thus, the constant size parameter covering the whole pH range in the framework of IS and DN models may be irrational for very large linear polyelectrolytes such as anionic PAM used in this research.

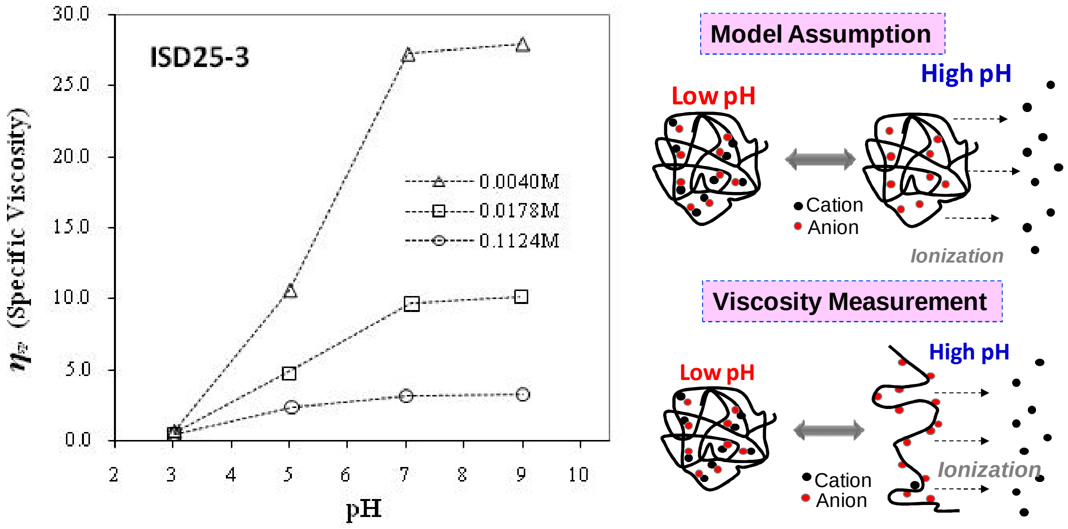

(a) (b)

Figure 3.4. (a) specific viscosities (η_{sp}) measured at different ionic strengths and pHs for ISD25-3 PAM ($MW_v = 2.18 \times 10^6$ g/mol, ISD = 35%) (See Appendix E for all the other

PAMs) and (b) schematic diagrams of the polymer conformation assumed in DN and IS model and the one measured in specific viscosity tests with increasing pH.

Secondly, the measured size indices of polyelectrolytes such as MWs or specific viscosities were not correlated with the estimated size parameters obtained in model-data fitting procedures. In IS and DN models, the sizes of polyelectrolyte's hypothetical sphere (V_D or S) are key factors in determining the curvature of potentiometric titration curves and thus used as model-data fitting parameters (see Equation (3.2) and (3.4)). Contrarily to the model theory, measured specific viscosities, which can be used as polyelectrolyte's size indices according to Equation (3.8), were not correlated to the estimated sizes of polyelectrolyte's hypothetical sphere (V_D or S). For example, a series of ISD25 PAM solutions were used to identify the correlations between measured specific viscosities and estimated spherical sizes with changing salt concentrations and MWs. In Figure 3.5, positive correlations between measured specific viscosities (η_{sp}, line-symbol plots) and estimated spherical sizes (S, bar plots) were observed with changing salt concentrations for a single MW. Generally, both measured specific viscosities and estimated spherical sizes decreased simultaneously with increasing salt concentrations, due to the compaction of electrostatic repulsion layers in a high salt concentration. However, those correlations between specific viscosities and spherical sizes were not observed with increasing MWs for a fixed salt concentration. Instead, estimated spherical sizes were constant irrespective of PAM MWs. Considering that potentionmetric titration curves with PAMs having different MWs were found to be very similar each other as long as PAMs have the same PAM ISD and solution condition, the observed similarity of estimated spherical sizes is no doubt. This issue on the negligible MW effects will be discussed closely in the later section. Similarly, for all the other PAM samples, the correlations between measured specific viscosities and estimated sizes were hardly identified, even though they were valid only for a single PAM with changing salt concentrations (see Figure 3.6). Thus, considering the observed disagreement between the model hypothesis and the real experiments, the polyelectrolyte's hypothetical sizes in IS and DN models (V_D and S) seem to be nothing more than fitting parameters which do not represent any substantial meanings for polyelectrolyte's sizes.

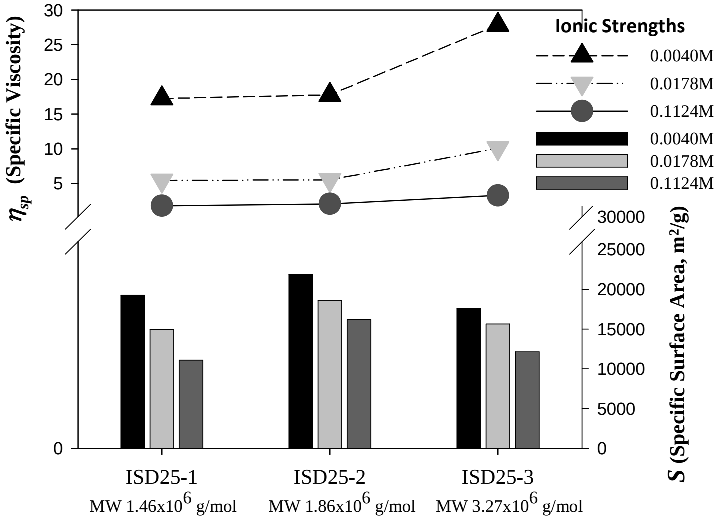

Figure 3.5. Comparison between measured specific viscosities at pH 9 and estimated specific surface areas for ISD25 group PAMs which have different MWs.

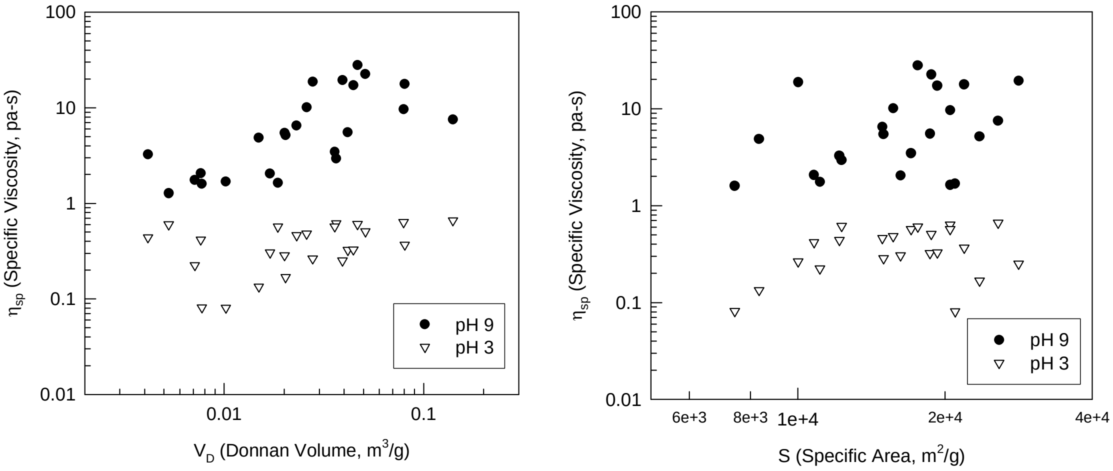

(a) (b)

Figure 3.6. (a) comparison between measured specific viscosities (pa-s) and estimated specific volume (m^3/g) with DN model and (b) comparison between measured specific viscosities (pa-s) and estimated specific viscosities (m^2/g) with IS model.

In contrast to IS and DN models which are simulated with macro-scale hypothetical sizes of polyelectrolytes (S and V_D) as model-data fitting parameters, CY model is simulated with constant micro-scale dimensions of cylindrical segments (cylindrical radius: a and length of a repeating segment: L_{seg}, see Equation (3.5)), which were found to be compatible for all the experimental conditions and thus not to require iterative model-data fitting procedures. Thus, the inconsistencies between measured and estimated sizes found in IS and DN model are not problematic in CY model. However, the fundamental assumption of CY model that polyelectrolytes are linear or coiled with enough void spaces between neighbor segments for counter-balancing ions to travel freely inside coiled structure without the effects of site-site interactions should be validated. This assumption will be discussed later in detail with simulation results.

Previous researchers had already applied the microscopic cylindrical models to predict electrostatic interaction chemistry of various linear anionic polyelectrolytes such as polysaccharides, polypeptides, polymethacrylic acid, polyacrylic acid, *etc.* (Kotin and Nagasawa, 1962; Nagasawa and Holtzer, 1964; Nagasawa *et al.*, 1965; Olander and Holtzer, 1968; Kawaguchi and Nagasawa, 1969; Cleland *et al.*, 1982; Cleland, 1984; Ullner and Jonsson, 1996; Deserno *et al.*, 2000). Specifically, we used the most simplified version among various cylindrical models and applied the cylindrical dimensions of polyacrylic acid, whose radius (a) and segment length (L_{seg}) were set as 0.66 nm and 0.2 nm due to the structural similarity of polyacrylic acid to anionic PAM (Ullner and Jonsson, 1996). However, anionic PAM differs from polyacrylic acid because a part of the repeating segments has ionizable sites on their backbone chain. For example, ISD25 PAM sample (25 % ISA) has 25 ionizable sites out of 100 repeating segments on its backbone chain, while polyacrylic acid contains entire 100 ionizable sites. The mathematical treatment for the reduced ionizable site density (ISD) of anionic PAMs was done by decreasing the concentration of ionizable sites ($\{L\text{-}\}_{TOT}$) in Equation (3.1). Various PAMs with different ISDs and MWs in Table 3.1 were tested in CY model applications to estimate the model validity for a broad range of polyelectrolyte's characteristics.

Figures 3.7 to 3.11 show potentiometric titration curves, which were measured with titration experiments and also simulated with CY model, and residual plots between experimental and simulated data. Two influencing factors on electrostatic interaction chemistry, ISD of PAMs and ionic strength of solutions, were chosen as the key variables in experiments and simulations. Thus, in Figures 3.7(a) to 3.11(a), potentionmetric titration curves are plotted for different PAM groups having different ionizable site densities and each figure contains three experimental and simulated plots at different ionic strengths. All the measured and simulated potentiometric titration curves slant forward from the curve of monomeric acrylic acid. The slant of the curves enhances with increasing ionizable site density of a PAM and decreasing ionic strength of an aqueous solution due to the increment of electrostatic interaction potential.

In Figures 3.7 to 3.11, consistencies between experimental and simulated potentiometric titration curves are commonly observed in all the experimental conditions and residuals between experimental and simulated results are generally below 0.5. Thus, the validity of CY model was proven for a broad range of PAM and solution characteristics. Furthermore, even though all the simulation results were obtained by applying constant cylindrical dimensions (a and L_{seg}) instead of adjusting fitting parameters, they were well fit onto experimental results. Thus, considering the observed validity of CY model, the answer of the debatable question on polyelectrolyte’s structures should be rather the microscopic cylinder than the macroscopic impermeable or permeable sphere of IS and DN models. Even though linear polyelctrolytes such as anionic PAMs can be assumed as large spheres in the macroscopic view due to their coiled structure, in electrostatic interaction model application, they are better to be treated as long rod-like cylinders with the assumption that void spaces are large enough for counter-balancing ions to travel freely inside polyelectrolyte’s structure without the effects of site-site interactions.

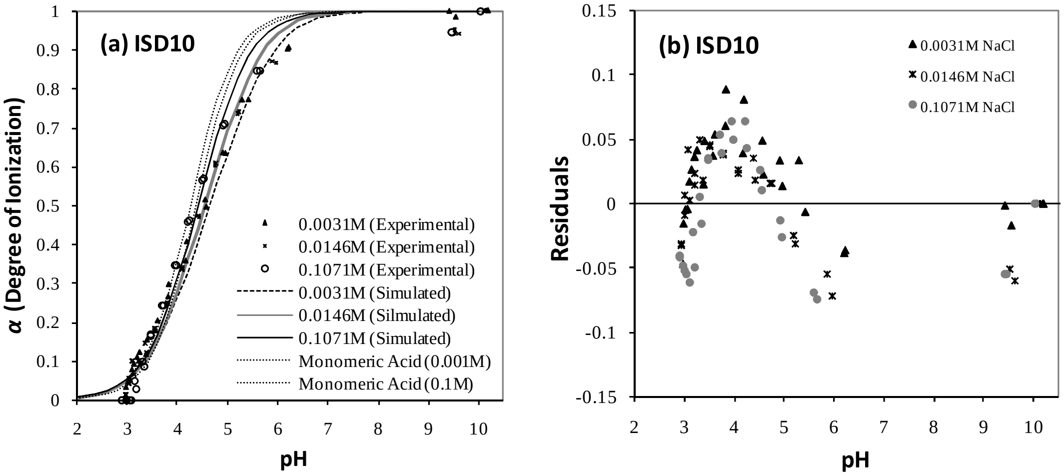

Figure 3.7. (a) experimental and simulated potentiometric titration curves and (b) residual plots between experimental data and best-fit curves for ISD10 PAM in different ionic strengths. All the simulated curves were obtained in application of CY model with constant model parameters (L_{seg} = 0.2 nm and a = 0.66 nm) (Ullner and Jonsson, 1996).

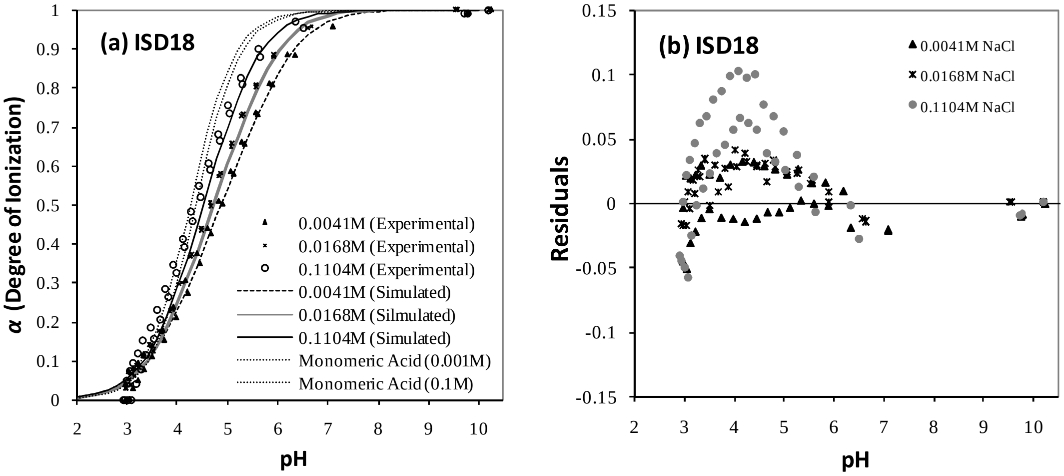

Figure 3.8. (a) Experimental and simulated potentiometric titration curves and (b) residual plots between experimental data and best-fit curves for ISD18 PAM in different ionic strengths. All the simulated curves were obtained in application of CY model with constant model parameters (L_{seg} = 0.2 nm and a = 0.66 nm) (Ullner and Jonsson, 1996).

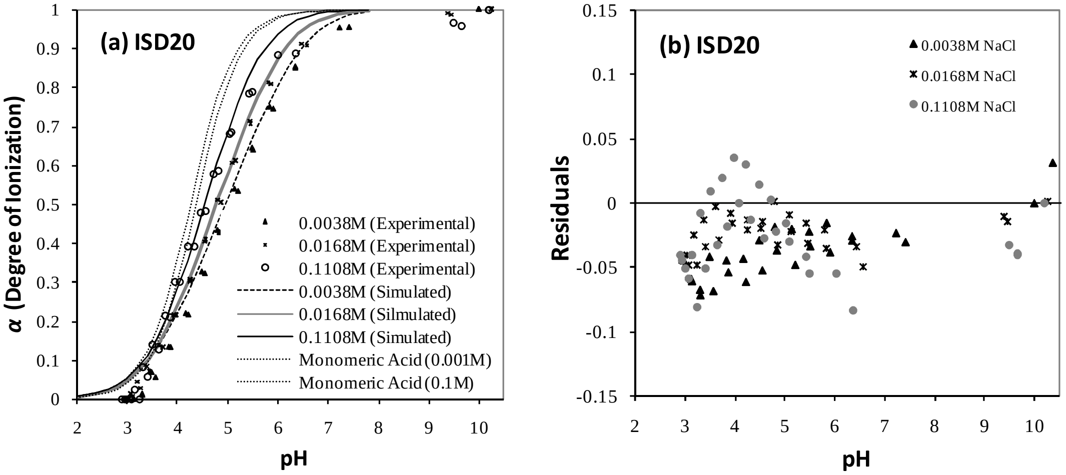

Figure 3.9. (a) Experimental and simulated potentiometric titration curves and (b) residual plots between experimental data and best-fit curves for ISD20 PAM in different ionic strengths. All the simulated curves were obtained in application of CY model with constant model parameters (L_{seg} = 0.2 nm and a = 0.66 nm) (Ullner and Jonsson, 1996).

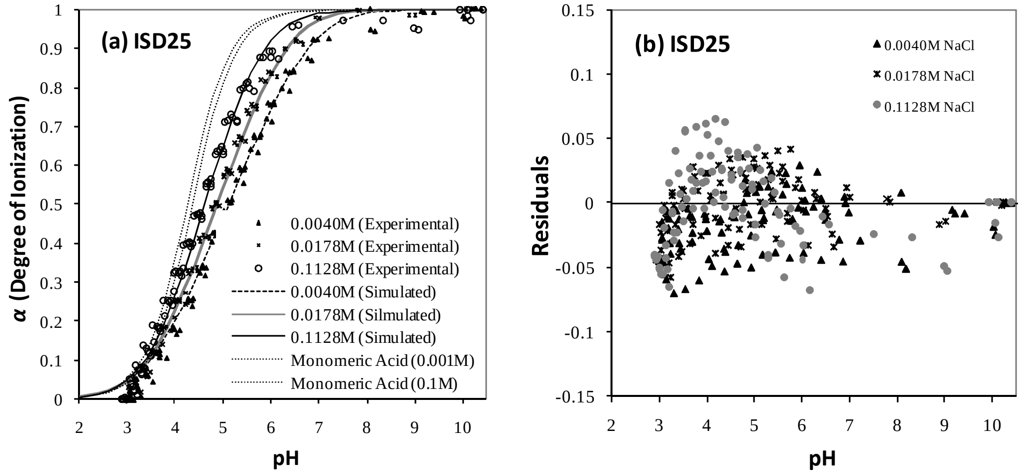

Figure 3.10. (a) Experimental and simulated potentiometric titration curves and (b) (b) residual plots between experimental data and best-fit curves for ISD25 PAM in different ionic strengths. All the simulated curves were obtained in application of CY model with constant model parameters (L_{seg} = 0.2 nm and a = 0.66 nm) (Ullner and Jonsson, 1996).

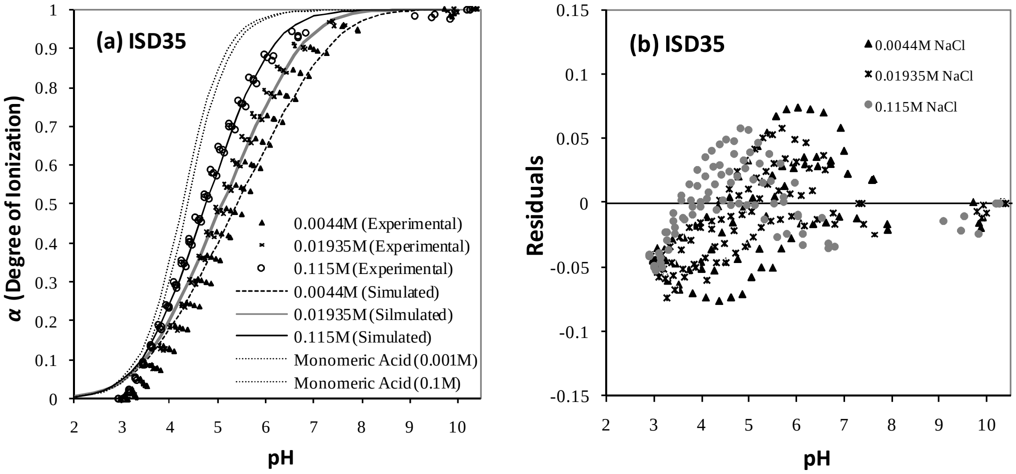

Figure 3.11. (a) Experimental and simulated potentiometric titration curves and (b) residual plots between experimental data and best-fit curves for ISD35 PAM in different ionic strengths. All the simulated curves were obtained in application of CY model with constant model parameters (L_{seg} = 0.2 nm and a = 0.66 nm) (Ullner and Jonsson, 1996).

In Figures 3.7(a) ~ 3.11(a), the other important finding is the disagreement between experimental and simulated results in the low pH range (2.5~3.5) near the zero degree of ionization ($\alpha = 0$), which are commonly observed for all the plots. The observed disagreement might be influenced by the conformational transition of polyelectrolytes between linear stretched and coiled contracted structures with changing pH and degree of ionization (α), which was proven partly in intrinsic viscosity measurements (see Figure 3.4). Thus, we hypothesized that in the low pH range the structures of polyelectrolytes become too coiled and contracted for counter-balancing ions to move freely inside polyelectrolyte structures. In turn, the limited ion mobility might prevent access or escape of protons on ionizable sites of polyelectrolytes and stop protonation and deprotonation of ionizable sites. Thus, in this low pH range, added protons or hydroxide ions in titration are used to form or ionize water molecules rather than to protonate or deprotonate the ionizable sites of polyelectrolyte molecules and consequently those measured potentiometric titration curves approach to the background level of the water self-ionization reaction (see Figures 3.7(a) ~ 3.11(a)). This conformational transition of polyelectrolytes near the zero degree of ionization (α) has been reported in many previous researches (Rice and Nagasawa, 1961; Nagasawa *et al.*, 1965; Olander and Holtzer, 1968; Kawaguchi and Nagasawa, 1969; Oosawa, 1971; Muroga *et al.*, 1972; Cleland, 1984; Ullner and Jonsson, 1996; Matijevic, 2001). Moreover, elaborate electrostatic interaction models had been developed to predict the conformational changes and transitions of polyelectrolytes, by incorporating the thermodynamics of polymeric chains (Olander and Holtzer, 1968; Cleland, 1984; Ullner and Jonsson, 1996). Needless to say, the better predictions of potentiometric titration curves would be achieved in the application of the elaborate electrostatic interaction models with their thermodynamic sub-models. However, considering that the observed deviations between experimental and simulated potentiometric titration curves were very small or even negligible, the simplicity and easiness of CY model may be advantageous enough to balance out the small or negligible deviations occurring in model applications.

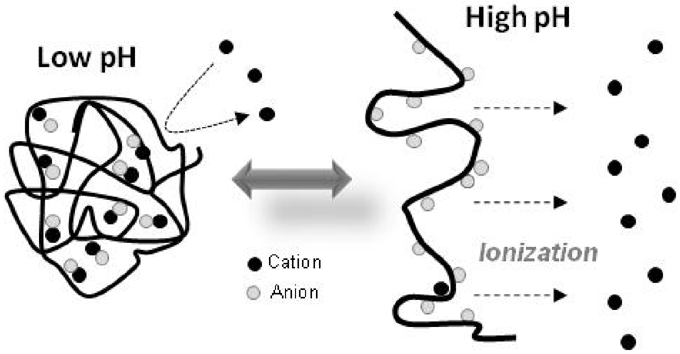

Figure 3.12. Schmatic diagram of conformational transition of polyelectrolytes with increasing degree of ionization (α) and pH.

3.5 Conclusion and Recommendation

In this research, a series of experimental and simulation studies proved the superiority of rod-like cylinders (CY model) to impermeable or permeable spheres (IS and DN models) in predicting electrostatic interaction chemistry of linear polyelectrolytes. The shapes of polyelectrolytes can be treated as coiled spheres in the macroscopic view of outside observers, while they can be also viewed as huge cylindrical structures in the microscopic view of reaction-participating ions. In other words, both conformational assumptions on polyelectrolytes' shapes, coiled sphere and linear cylinder, can be rational in different perspectives or applications. However, in the domain of electrostatic interaction chemistry, microscopic cylindrical shapes of polyelectrolytes were found to be more realistic than spherical shapes because molecular-sized ions are the main participants in electrostatic interaction chemistry. The enforcement of the macroscopic perspective onto molecular-sized ions may be nonsense, considering the minute scope of ions inside polyelectrolyte structures.

Unfortunately, the argument on the superiority of CY model was proven indirectly with the comparative study between experiments and simulations in this research. Thus, in the later researches, a straightforward method may be required to prove directly the validity of CY model and its hypothetical cylinder for linear polyelectrolyte molecules.

3.6 References

Avena, M. J., L. Koopal, and W. H. v. Riemsdijk, 1999, Proton binding to humic acids: electrostatic and intrinsic interactions, *Journal of Colloid and Interface Science*, **217**, 37-48

Berthouex, P. M., and L. C. Brown, 1994, *Statistics for Environmental Engineers*, Lewis Publishers, Boca Raton, FL

Cleland, R. L., 1984, Theory of potentiometric titration of polyelectrolytes: a discrete-site model for Hyaluronic acid, *Macromolecules*, **17**, 634-645

Cleland, R. L., J. L. Wang, and D. M. Detweiler, 1982, Polyelectrolyte properties of Sodium Hyaluronate. 2. Pontentiometric titration of Hyaluronic acid, *Macromolecules*, **15**, 386-395

Deserno, M., C. Holm, and S. May, 2000, Fraction of condensed counterions around a charged rod: comparison of Poisson-Boltzmann theory and computer simulations, *Macromolecules*, **33**, 199-206

Francois, J., D. Sarazin, T. Schwartz, and G. Weill, 1979, Polyacrylamide in water: molecular weight dependence of $<R^2>$ and $[\eta]$ and the problem of the excluded volume exponent, *Polymer*, **20**, 969-975

Hansen, J., and H. Lowen, 2000, Effective interactions between electric double layers, *Annu. Rev. Phys. Chem.*, **51**, 209-242

Hill, T. L., 1955, Approximate calculation of the electrostatic free energy of nucleic acids and other cylindrical macromolecules, *Arch. Biochem. Biophys.*, **57**, 229-239

Kawaguchi, Y., and M. Nagasawa, 1969, Potentiometric titration of stereoregular poly(acrylic acids), *The Journal of Physical Chemistry*, **73**(12), 4382-4384

Koopal, L. K., T. Saito, J. P. Pinheiro, and W. H. v. Riemsdijk, 2005, Ion binding to natural organic matter: general considerations and the NICA-Donnan model, *Colloids and Surfaces A: Physicochem. Eng. Aspects*, **265**, 40-54

Kotin, L., and M. Nagasawa, 1962, Chain model for polyelectrolytes. VII. potentiometric titration and ion binding in solutions of linear polyelectrolytes, *The Journal of Chemical Physics*, **36**(4), 873-880

Matijevic, E., 2001, *Surface and colloid science, Volume 16*, Kluwer Academic/Plenum Publishers, New York, NY

Molyneux, P., 1983, *Water-soluble synthetic polymers: Properties and behavior, Volume II*, CRC Press Inc., Boca Raton, Florida

Muroga, Y., K. Suzuki, Y. Kawaguchi, and M. Nagasawa, 1972, Potentiometric titration of polyelectrolytes having stiff backbones, *Biopolymers*, **11**, 137-144

Nagasawa, M., and A. Holtzer, 1964, The use of the Debye-Huckel approximation in the analysis of protein potentionmetric titration data, *Journal of the American Chemical Society*, **86**(4), 531-538

Nagasawa, M., T. Murase, and K. Kondo, 1965, Potentiometric titration of stereoregular polyelectrolytes, *J. Phys. Chem.*, **69**, 4005-4012

Olander, D. S., and A. Holtzer, 1968, The stability of the polygulutamic acid α helix, *Journal of the American Chemical Society*, **90**(17), 4549-4560

Oosawa, F., 1971, *Polyelectrolytes*, Mercel Dekker, New York

Pohlmeier, A., and S. Haber-Pohlmeier, 2004, Ionization of short polymethacrylic acid: titration, DLS, and model calculations, *Journal of Colloid and Interface Science*, **273**, 369-380

Rice, S. A., and M. Nagasawa, 1961, *Molecular biology, Volume 2: Polyelectrolyte solutions*, Academic Press Inc., New York, NY

Saito, T., S. Nagasaki, S. Tanaka, and L. Koopal, 2005, Electrostatic interaction models for ion binding to humic substances, *Colloids and Surfaces A: Physicochem. Eng. Aspects*, **265**, 104-113

Sperling, L. H., 2006, *Introduction to physical polymer science, 4th Edition*, John Wiley & Sons, Inc., Hoboken, NJ

Stumm, W., and J.J. Morgan, 1996, *Aquatic chemistry: Chemical equilibria and rates in natural waters, 3rd Ed.*, John Wiley & Sons, Inc., New York, NY

Tipping, E., 2002, *Cation biniding by humic substances*, Cambridge University Press, Cambridge, UK

Ullner, M., and B. Jonsson, 1996, A Monte Carlo study of titrating polyelectrolytes in the presence of salt, *Macromolecules*, **29**, 6645-6655

Wu, X. Y., D. Hunkeler, A. E. Hamielec, R. H. Pelton, and D. R. Woods, 1991, Molecular weight characterization of poly(acrylamide-co-sodium acrylate). I. Viscometry, *Journal of Applied Polymer Science*, **42**, 2081-2093

CHAPTER 4. INVESTIGATION ON THE EFFECTS OF POLYACRYLAMIDES' MOLECULAR WEIGHTS ON ADSORPTION AND FLOCCULATION PROCESSES IN KAOLINITE AND POLYACRYLAMIDE-CONTAINING SUSPENSIONS

4.0 Abstract

Polyacrylamides (PAMs) have long been used as soil stabilizers or flocculants due to their high adsorption capacity and flocculation efficiency. In this research, a series of nonionic PAMs have been tested to identify the effects of their MWs on adsorption and flocculation occurring in PAM- and kaolinite-containing suspensions. In adsorption tests, PAMs having different MWs of 1,500 (1.5 K), 10,000 (10 K), 600,000~1,000,000 (0.6~1 M), 5,000,000~6,000,000 (5~6 M), and 18,000,000 (18 M) g/mol were tested in PAM- and kaolinite-containing suspensions, to identify the effects of MWs on the adsorption capacity. The adsorption capacities of PAMs on kaolinite were found to increase with increasing MW up to a point. However, the adsorption capacity of the largest PAM (MW = 18 M) was twenty times smaller than the capacities of the other smaller 0.6~1 M and 5~6 M PAMs. This abnormal adsorption behavior of the largest PAM is hypothesized to be caused by the entanglements between polymeric chains, which were proven in the steady-shear viscosity measurements. In flocculation tests, after discarding 1.5 K, 10 K, and 18 M PAMs due to their negligible flocculation abilities, 0.6~1 M and 5~6 M PAMs were further tested to estimate the effects of PAM MW on the flocculation efficiency. The flocculation efficiency of the larger 5~6 M PAM

was found to be higher than the one of the smaller 0.6~1 M PAM, due to its higher susceptibility to the nonequilibrium flocculation, in which the transient and elongated chains of the adsorbed PAMs enhance the inter-particle bridging before collapsing down on kaolinite surfaces. In conclusion, the larger PAMs with high MWs are recommendable as soil stabilizers and flocculants because of the higher adsorption capacity and flocculation efficiency. However, the upper limit of MW should be set to avoid the poor adsorption capacity and flocculation efficiency and the handling difficulty caused by the polymeric chain entanglements.

4.1 Introduction

Soil erosion occurs in both urban and rural areas during storm events. In general, the problem increases with increasing land disturbance (*e.g.*, tillage, mining, road grading and rural to urban land conversion). The most problematic sediment particles typically are of colloidal-size clay, and if not controlled they can end up in various receiving water bodies, where the materials they carry (nutrients, toxicants, pathogens, etc.) can contribute to the coating of bottom sediments, algae blooms, oxygen depletion, and food-chain problem (Stumm and Morgan, 1996; Chapra, 1997; Schwarzenbach *et al.*, 2003). To counteract soil erosion and colloid proliferation in the water environment, polyacrylamides (PAMs) have long been used as soil stabilizers or flocculants with their characteristics of high solubility, viscosity and molecular weight. Especially, nonionic or anionic PAMs with their charged functional groups have been mostly used in the application onto the water environment because cationic PAMs are toxic on various aquatic lives by blocking the bodily membranes (McCollister *et al.*, 1965; Wallace and Wallace, 1986; Myagchenkov and Kurenkov, 1991; Stephens, 1991; Barvenik, 1994).

For the optimum use of PAMs as soil stabilizers and flocculants, many researchers have explored various physicochemical processes occurring in PAM- and clay-containing suspensions and tried to identify and optimize the controlling factors of those physicochemical processes. In polyacrylamide- and clay-containing suspensions, adsorption and flocculation are the representative physicochemical processes, which are driven by various microscale PAM-clay interaction mechanisms. In general, the adsorption of polymeric molecules on clay surfaces occurs very quickly after dosing PAM flocculants into clay suspensions. Then, the reconformation of the adsorbed polymeric chains follows and finally the flocculation between clay particles is induced by the adsorbed and reconformed polymeric bridges (Gregory, 1988; Pelssers *et al.*, 1989; Pelssers *et al.*, 1990; Adachi, 1995; Lu and Pelton, 2001). In detail, the adsorption of PAMs (or other polyelectrolytes) on negatively charged clay surfaces have been reported to occur with various physicochemical interaction mechanisms, such as covalent bonding, hydrogen bonding, hydrophobic interaction, electrostatic attraction, or divalent cationic bridging. Noteworthily, the adsorption process is not only driven by a specific mechanism but also by the combined effects of various interaction mechanisms (Jones *et al.*, 1998; Heller and Keren, 2002; Morris *et al.*, 2002; Heller and Keren, 2003; Torn *et al.*, 2003; Mpofu *et al.*, 2003a; Mpofu *et al.*, 2003b). After the adsorption and reconformation of PAMs on clay surfaces, the subsequent flocculation is triggered by the adsorbed polymeric chains. Considering that charge neutralization of anionic clay surfaces does not occur by adding nonionic or negatively-charged anionic PAMs, bridging flocculation, in which adsorbed polymer chains reach other clay surfaces out of the electric repulsion layer and make bridges between colloidal particles, should be the major flocculation mechanism in PAM- and clay-containing suspensions.

Adsorption and flocculation processes in PAM- and clay-containing suspensions are known to be affected by various PAM and solution characteristics, such as molecular weight (MW) and charge density (CD) of a PAM and the pH, ionic strength, and salt species of an aqueous solution. However, among various factors affecting on adsorption and flocculation, MW has been reported as one of the most decisive factors. For example, the adsorption capacity and the flocculation efficiency of PAMs have been reported to increase with increasing PAM MWs (Levy and Agassi, 1995; Green *et al.*, 2000; Heller and Keren, 2002). Considering that the longer polymeric chains of high-MW PAMs are able to form the thicker adsorption layer on kaolinite surfaces, the higher adsorption capacity and flocculation efficiency of high-MW PAMs are undoubted (Fleer *et al.*, 1993). Also, in bridging flocculation, the longer chains of high-MW PAMs are more susceptible to the beneficial nonequilibrium flocculation, in which the adsorbed polymeric molecules maintain the transient and elongated conformation for a longer time before collapsing down on clay surfaces (Pelssers *et al.*, 1989; Pelssers *et al.*, 1990; Lu and Pelton, 2001). Furthermore, MWs of PAMs can be customized in the manufacturing process and thus practically be used as the controlling factor in the field applications as soil stabilizers or flocculants.

In this research, a series of nonionic PAMs with various MWs have been used to identify the effects of PAM MWs on adsorption and flocculation occurring in PAM- and clay-containing suspensions. Firstly, in the adsorption test, the reported hypothesis that the adsorption capacity of a PAM increases with increasing PAM MW was tested again. Secondly, in the flocculation test, the nonequilibrium flocculation was investigated with PAMs having different MWs at various fluid shear conditions. We initially hypothesized that the nonequilibrium flocculation is enhanced with increasing MWs and fluid shear rates. In other words, the high-MW PAM and the strong fluid shear rate were hypothesized to give rise to the transient and elongated conformation of the adsorbed polymeric chains and consequently to enhance the flocculation efficiency. In this research article, the conformity to and the deviation from the above hypotheses will be discussed closely with the observed experimental results from the adsorption and the flocculation tests.

4.2 Materials and Methods

4.2.1 Materials

A series of PAMs having different MWs of 1,500 (1.5 K), 10,000 (10 K), 600,000~1,000,000 (0.6~1 M), 5,000,000~6,000,000 (5~6 M), and 18,000,000 (18 M) g/mol (Polyscience Inc.) were tested as adsorbates and flocculants in the adsorption and the flocculation tests. Polyacrylamide stock solutions were prepared at 1 g/L by dissolving Polyscience PAMs into distilled deionized water and adjusted at pH 7 and 0.01 M NaCl as the background salt concentration. They were gently stirred for several days for the complete dissolution and then stored in the dark during the adsorption and the flocculation tests. Kaolinite was chosen as the experimental clay in the adsorption and the flocculation tests because of its abundance in soils of the southeastern United States (Hurst and Pickering, 1997). Kaolinite suspensions were prepared by dissolving the commercial kaolinite powders into distilled deionized water and adjusted at pH 7 and 0.01 M NaCl. They were stirred for about two days to achieve the complete hydration of kaolinite surfaces and the equilibration with the atmosphere. In this research, two different kaolinites were used for the adsorption and the flocculation tests, respectively. Sigma kaolinite (Sigma-Aldrich, USA) was used in the adsorption tests. However, in the flocculation tests, Kaofil (Thiele Kaolin Company, USA) was used, because of the massive requirement of kaolinite powder in the Jar-test experiments. The size range of Sigma kaolin was reported as 0.1 ~ 4 µm by the manufacturer. The mean size of Kaofil was measured as 1.4 µm in the previous research (Ren and Packman, 2004).

4.2.2 Adsorption Test

Bottle point technique was applied to make the adsorption isotherms for five different PAMs (1.5 K, 10 K, 0.6~1 M, 5~6 M, and 18 M PAMs). A series of 225 mL polypropylene bottles (VWR, USA) were filled up with 200 ml of 10 g/L kaolinte suspension and the known amounts of the 1 g/L PAM stock solutions were injected into the kaolinite suspensions. All of the PAM stock solutions and the kaolinite suspensions were prepared at pH 7 and 0.01 M NaCl. For each experimental condition, the test bottles were triplicated for the quality control and assurance. Also, a set of control systems was prepared without kaolinite addition, to check the PAM loss in the aqueous phase by physicochemical processes other than the kaolinite-mediated adsorption process. Thus, to generate 8 points in an adsorption isotherm curve, 24 experimental bottles and 8 control bottles were prepared. These adsorption-testing bottles containing the kaolinite suspension and the PAM stock solution were stirred on Thermolyne® Bigger Bill orbital shaker (Thermo Fisher Scientific Inc., PA) at 20 ^{o}C for 48 hours, to reach the complete equilibrium state. After the reaction time, the aliquot samples were centrifuged at 10,000 g for 20 minutes with the super-speed centrifuge, Sorvall Evolution RC (Thermo Fisher Scientific Inc., USA), to separate solids from the solution phase. Then, polyacrylamide concentrations in the solution phase were measured with TOC-V_{CSH} TOC/TN analyzer (Shimadzu Corp., Japan). Instead of total organic carbon (TOC), total nitrogen (TN) was selected as the PAM measuring index because TOC measurements were exposed to the errors caused by inorganic carbons such as CO^{2-} and HCO^{-}. The adsorbed amounts of PAMs were estimated by subtracting the remaining amounts of PAMs in the solution phase from the dosed amounts. Adsorption capacities were expressed by adsorbed mass per kaolinite mass (mgPAM/gKaolinite) and used to plot the adsorption isotherm curves. Finally, the PAM adsorption isotherms on kaolinite surfaces were evaluated by the nonlinear data fitting on the Langmuir isotherm equation with SigmaPlot software (SPSS Inc., USA).

4.2.3 Viscosity Measurement

The steady-shear viscosities of a series of PAM solutions containing different PAM concentrations were measured to estimate the critical entanglement concentration of a PAM (Milas *et al.*, 1990; Bozzi *et al.*, 1996; Ndjouenkeu *et al.*, 1996; Tuinier *et al.*, 1999; Sperling, 2006). Firstly, polyacrylamide solutions in the concentration range from 0.02 to 1 g/L were prepared by dissolving different amounts of a PAM sample into distilled deionized water. They were gently stirred for several days to reach the complete dissolution and adjusted at pH 7 and 0.01 M NaCl, which are the same solution properties as those of the adsorption test. Then, the steady-shear viscosities for a series of PAM solutions in the concentration range from 0.02 to 1 g/L were measured with Rheometric Scientific ARES Rheometer with a Couttee cup (TA Instruments, USA). In the steady-shear measurements, the unidirectional shear rates, which range from 0.1 to 500 /s, were applied and the obtained steady-shear viscosities were plotted against the shear rates (see Figure 4.1). At a certain PAM concentration, the zero-shear specific viscosity was found at the plateau of the steady-shear viscosity plots, which is placed at the lower end of the applied shear rates (shear rate → 0) (see Figure 4.1(b)). Eventually, the zero-shear specific viscosities of a series of PAM solutions were plotted against PAM concentrations and the critical entanglement concentration was found at the inflexion point of the zero-shear specific viscosity curve (see Figure 4.1(c)).

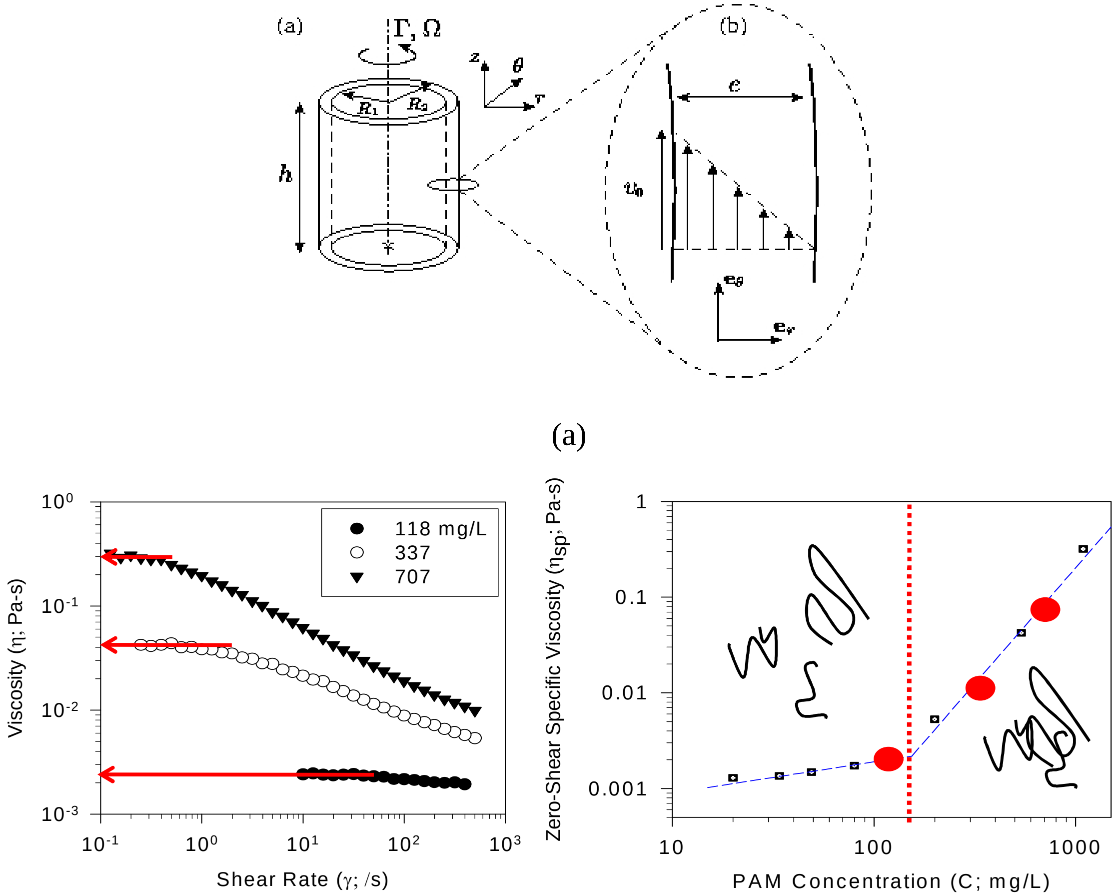

(a)

(b) (c)

Figure 4.1. (a) schematic digram of Couttee-type viscometer, (b) an example plot of steady-shear viscosity *versus* shear rate at different PAM concentrations, and (c) an example plot of zero-shear specific viscosity versus PAM concentration

4.2.4 Flocculation (Jar) Test

In jar tests, both the adsorption capacity and the flocculation efficiency were monitored as the representative experimental indices. At the beginning of Jar tests, different amounts of 1 g/L 0.6~1 M PAM or 5~6 M PAM stock solution, which range from 0 to 35 mgPAM/L as PAM dose concentrations, were injected into 2 L jars containing 2 g/L kaolinite suspensions. All the PAM stock solutions and the kaolinite suspensions were prepared at pH 7 and 0.01 M NaCl. With PB-700^{TM} Jar-tester (Phipps & Bird, Inc., USA), PAM- and kaolinite-containing suspensions were stirred at 50, 100, 200, or 300 rpm, equivalent to 42, 95, 220, or 360 /s as the shear rate, for 2 or 4 minutes, to evaluate the effect of shear rates and contact time on adsorption and flocculation. After 2 or 4 minutes stirring time, the suspensions were settled for 60 minutes and then the aliquots were taken at 1 cm below water surface, for the further analyses such as turbidity and PAM concentration. The turbidity of the aliquots was measured with Hach 2100N Turbidimeter (Hach, Inc., USA). For the PAM concentration measurement, aliquots were firstly centrifuged at 10,000 g for 20 minutes with the super-speed centrifuge, Sorvall Evolution RC (Thermo Fisher Scientific Inc., USA) and finally the PAM concentration of the centrifuged supernatants was measured with TOC/TN analyzer (Shimadzu TOC-V_{CSH}, Shimadzu Corporation, Japan). Again, the adsorbed amounts of PAMs were estimated by subtracting the remaining amounts of PAMs in the solution phase from the dosed amounts, and the adsorption capacities were expressed by adsorbed mass per kaolinite mass (mgPAM/gKaolinite).

4.3 Results and Discussion

4.3.1 Adsorption Test

In Figure 4.2(a), all of the adsorption isotherms were shown to rise steeply at the initial part of the isotherm and reach a (pseudo) plateau. Therefore, they follow the high-affinity adsorption behavior occurring at the polymer-surface interfaces (Parfitt and Rochester, 1983; Feast and Munro, 1987; Fleer *et al.*, 1993). However, the rounded parts of the adsorption isotherms between the initial steep rise and the plateau were deviated from the typical high-affinity adsorption behavior. This rounded part might be caused by the polydispersity effects of the experimental PAMs, which have a wide MW range of the constituent PAM molecules (Fleer *et al.*, 1993). The rounded high-affinity adsorption isotherms were reasonably fit onto the well-known Langmuir isotherm (see Table 4.1 and Figure 4.2(a)). However, the adsorption isotherm of the smallest 1.5 K PAM is deviated from the high-affinity adsorption behavior but rather increases continuously without developing a steep rise and an apparent plateau. Considering the lowest MW of 1.5 K PAM, the unique adsorption isotherm might follow the isotherm of the small-size molecules (Fleer *et al.*, 1993).

The maximum adsorption capacities of the experimental PAMs on kaolinite surfaces increased with increasing MWs, except one of the largest 18 M PAM (see Table 4.1 and Figure 4.2). This increasing trend of the polymer adsorption capacity with respect to MW has already been reported in many previous researches, (Fleer *et al.*, 1993; Green *et al.*, 2000; Heller and Keren, 2002; Yuang and Shen, 2005). Especially, 0.6~1 M and 5~6 M PAMs showed the highest maximum adsorption capacity among the experimental PAMs. However, the maximum adsorption capacity of the largest 18 M PAM was decreased down to the level of the smaller 1.5 K and 10K PAMs (see Table 4.1 and Figure 4.2 (b)). From the observed high viscosity, the 1 g/L stock solution of 18 M PAM was suspected to exceed the critical entanglement concentration, above which polymer chains are not suspended independently (dilute) but rather entangled each other (semi-dilute) (Fleer *et al.*, 1993; Sperling, 2006). The entanglement between polymeric chains might make polymeric molecules hard to approach and attach on adsorbent surfaces out of the semi-dilute solution phase. This critical entanglement concentration were identified with the steady-shear viscosity measurement and found at the transient concentration, where the viscosity of a polymer solution starts increasing steeply due to the development of the entanglement between polymeric chains.

Table 4.1. Nonlinear data fitting results onto the Langmuir isotherm ($q_e = q_{,max} \times C_e/(K_s+C_e)$) for 1.5K, 10K, 0.6~1M, 5~6M, and 18M PAMs

MW (g/mol)	$q_{,max}$ (mgPAM/gKaolinite)	K_s (mgPAM/L)	R^2
1.5K†	0.7753	12.542	0.9280
10K	0.9951	3.8749	0.9078
0.6~1M‡	17.941	1.0811	0.9851
5~6M	26.796	3.3032	0.9730
18M	0.8718	1.2365	0.9128

† K represents 10^3. ‡ M represents 10^6.

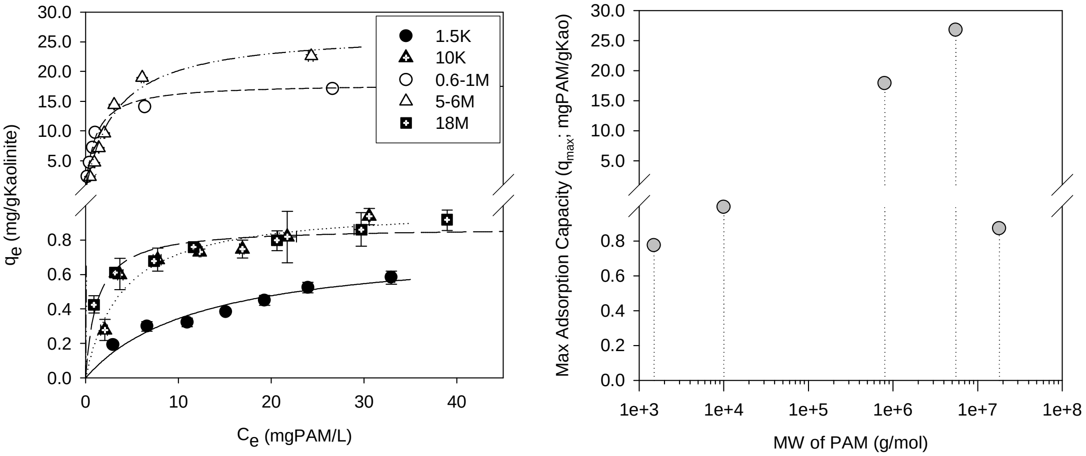

(a) (b)

Figure 4.2. Experimental results of the adsorption tests. (a) Adsorption isotherm curves of 1.5 K, 10 K, 0.6~1 M, 5~6 M, and 18 M PAMs and (b) Maximum adsorption capacity (mgPAM/gKaolite) *versus* PAM MW.

4.3.2 Steady-Shear Viscosity

In general, the steady-shear viscosity curve of a PAM solution at a fixed PAM concentration increases and then reaches a plateau, as it approaches the zero shear rate (shear rate → 0). Also, the magnitudes of these steady-shear viscosity curves increase with increasing PAM concentrations. Figure 4.3(a) shows the typical steady-shear viscosity curves, which were measured with a series of 18 M PAM solutions containing different PAM concentrations, from 0.02 to 1 g/L. However, the steady-shear viscosity curves of 1.5 K, 10 K, 0.6~1 M, and 5~6 M PAMs were constant at the level of pure water (≈ 0.001 Pa-s at 20 ^{o}C), irrespective of shear rates as well as PAM concentrations, and thus were not necessarily illustrated in the figure. The zero-shear specific viscosities, which were found at the zero shear rates (shear rate → 0) *i.e.* at the plateaus of the steady-shear viscosity curves, were plotted against PAM concentrations and used to identify the critical entanglement concentration separating dilute and semi-dilute regions (see Figure 4.3(b)) (Sperling, 2006) (Milas *et al.*, 1990; Bozzi *et al.*, 1996; Ndjouenkeu *et al.*, 1996; Tuinier *et al.*, 1999). In Figure 4.3(b), the zero-shear specific viscosities of 1.5 K, 10 K, 0.6~1 M, and 5~6 M PAMs were shown to be constant at the viscosity of pure water (≈ 0.001 Pa-s at 20 ^{o}C), irrespective of PAM concentrations. Thus, these PAM solutions were proven to be in the dilute region without serious polymeric entanglements.

In contrast to the other small PAMs, the zero-shear specific viscosity plot of the largest 18 M PAM increased with increasing PAM concentrations. Furthermore, in the zero-shear specific viscosity plot of 18 M PAM, the inflexion point was clearly found at about 155 mg/L with two different linear lines (see Figure 4.3(b)). The previous researchers defined this inflexion point as the critical entanglement concentration, which separate two solution regimes, the dilute and the semi-dilute regions (Milas *et al.,* 1990; Bozzi *et al.*, 1996; Ndjouenkeu *et al.*, 1996; Tuinier *et al.*, 1999; Sperling, 2006). Thus, above 155 mg/L of the PAM concentration, polymeric molecules of 18 M PAM are in the semi-dilute region and develop the entanglements between polymeric chains. Considering that the PAM concentration of the working stock solutions was prepared at 1 g/L in all the adsorption tests, far above the critical entanglement concentration, the observed small adsorption capacity of 18 M PAM might be caused by the thermodynamic disadvantage, which requires the additional energy or time for PAM molecules to disentangle out of the polymeric solution and to approach onto kaolinite surfaces. Even if a PAM concentration in a solution phase becomes below 155 mg/L after mixing PAM stock solution and kaolinite suspension, the entangled polymeric agglomerates still require the additional energy or time to be disentangled.

Therefore, in the field application of excessively high-MW PAMs as soil stabilizers and flocculants, the concentration of the working solutions should remain very low below the critical entanglement concentration. However, the low concentration of the PAM working solutions, for example the concentration below 155 mg/L for 18 M PAM, may not be practical because engineers or operators should prepare a large volume of a PAM working solution. Even though the selection among various PAMs is dependent on field conditions or engineer's selections, excessively high-MW PAMs may not be recommendable as soil stabilizers and flocculants, due to the polymeric entanglement problem as well as the handling difficulty (Levy and Agassi, 1995).

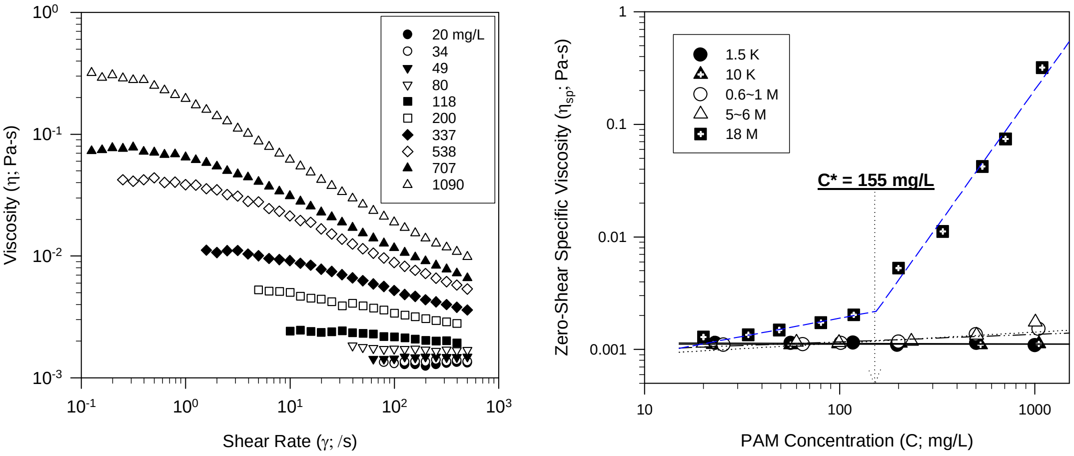

(a) (b)

Figure 4.3. Experimental results of the steady-shear viscosity measurements. (a) Steady-shear viscosity *versus* shear rate at different PAM concentrations for 18 M PAM and (b) zero-shear specific viscosity versus PAM concentration for 1.5 K, 10 K, 0.6~1 M, 5~6 M, and 18 M PAMs.

4.3.3 Flocculation Test

0.6~1 M and 5~6 M PAMs were shown to have the highest adsorption capacities and also their flocculation abilities were apparently observed in the previous adsorption tests. However, flocculation was hardly observed with 1.5 K, 10 K, and 18 M PAMs. In general, the polymer-induced flocculation occurring in polymer- (or polyelectrolyte-) and clay-containing suspensions is driven by the bridging flocculation mechanism, in which the elongated adsorbed polymer chains reach the other clay surfaces out of the electrostatic repulsion layer. Thus, in thinking of the bridging flocculation, the shorter polymeric chains of 1.5 K and 10 K PAMs may be confined within the electrostatic repulsion layer of colloidal clays, and thus their flocculation abilities are necessarily negligible. However, the small flocculation efficiency of 18 M PAM might be caused by the polymeric chain entanglement in the semi-dilute solution phase and the resultant small adsorption capacity. After discarding 1.5 K, 10 K, and 18 M PAMs due to their negligible flocculation abilities, 0.6~1 M and 5~6 M PAMs were selected as the experimental PAMs in the following flocculation tests, which were proposed to research the effects of PAM MW on the flocculation efficiency.

In addition to MW, the fluid shear rate (G; /s) was used as the controlling factor in our flocculation tests in order to identify the nonequilibrium flocculation mechanism (Gregory, 1988; Pelssers *et al.*, 1989; Pelssers *et al.*, 1990; Adachi, 1995; Lu and Pelton, 2001). The typical flocculation occurs with the consecutive processes of polymer adsorption, adsorbed chain reconformation, and inter-particle collision (Gregory, 1988; Adachi, 1995). However, in the nonequilibrium flocculation, inter-particle collision and aggregation occur without completing the reconformation process of the adsorbed chains and thus the transient and elongated conformation of the adsorbed polymeric chains enhances the flocculation efficiency. Considering the kinetic aspect of the chain reconformation process, the nonequilibrium flocculation can be enhanced at the higher shear rate, where the vigorous fluid and particle movement and the turbulence induce the fast inter-particle collisions to occur before completing the polymeric chain reconformation. Thus, the shear rate, *i.e.* the inter-particle collision frequency was selected as the controlling factor to limit or enhance the nonequilibrium flocculation.

Flocculation as well as adsorption were investigated in the flocculation tests with 0.6~1 M and 5~6 M PAMs at various shear rates and contact time (see Figure 4.4). Firstly, Figures 4.4 (a) and (b) show the adsorption capacities of 0.6~1 M and 5~6 M

PAMs with increasing PAM dose at different shear conditions. The adsorption capacity curves again resemble the high-affinity adsorption behavior, as shown in the previous section. However, their values are about an order of magnitude lower than those measured in the previous adsorption test, because of the short reaction time in the current flocculation tests. Interestingly, the adsorption capacity curves of the larger 5~6 M PAM changed significantly with increasing shear rates, while those of the smaller 0.6~1 M PAM remained constant (see Figures 4.4 (a) and (b)). The inconsistent adsorption of the larger PAM (5~6 M PAM) at different shear conditions might be caused by the thermodynamic disadvantage, in which the longer polymeric chains require the higher energy and the longer time in reconforming the adsorbed chains and reaching the equilibrium state. Especially, with increasing shear rates, the adsorption capacities of the larger PAM were found to decrease gradually. At the higher shear rate, the fast collision and aggregation might occur before completing the chain reconformation and consequently reduce the adsorption capacity with preventing the further adsorption of PAM molecules on kaolinite surfaces. In contrast, the smaller PAM (0.6~1 M) might reconform or settle down on kaolinite surfaces very quickly before the inter-particle collision and so produce the consistent adsorption capacity, even at the higher shear rates.

In addition to the kinetic aspect of the reconformation process of the adsorbed polymers, the mechanical aspect may be the reason of the inconsistent adsorption of the larger PAM. The mechanical force of the fluid (*i.e.* shear rate) has been reported to make a critical effect in determining the adsorbed polymers' conformation in the previous researches (Gramain and Myard, 1981; Cohen and Metzner, 1982; Lee and Fuller, 1984;

van Eijk and Stuart, 1997). Considering the conceptual picture of the long threads for the polymeric chains in a shear field, the larger polymeric chains should be necessarily more susceptible to the mechanical forces than the smaller ones. Therefore, the higher susceptibility of 5~6 M PAM to the mechanical forces as well as the longer chain reconformation time might be the plausible reason of the observed inconsistent adsorption capacity at different shear conditions. Now, the question of how the inconsistent adsorption affects on the flocculation efficiency will be discussed in the following paragraphs.

In Figures 4.4 (c) and (d), the relative turbidity ($\frac{Final\ Turbidity\ after\ Flocculation}{Intial\ Turbidity\ of\ Raw\ Sample}$) was used as the representative value of the flocculation efficiency in PAM- and kaolinite-containing suspensions and was plotted against PAM concentrations at different shear conditions. The turbidity removal of 5~6 M PAM were much more enhanced with increasing shear rates and contact time than those of 0.6~1 M PAM. For example, for 5~6 M PAM, the U-shaped relative turbidity curves were changed to the L-shaped curves with increasing shear rates, while those of 0.6~1 M PAM maintained the U-shaped curves irrespective of shear conditions. In the typical polymer-induced flocculation, the particle restabilization occurs in the polymer over-dose conditions because the highly covered adsorbent surfaces do not have enough free spaces to accommodate polymeric bridges, and the dense structure of adsorbed layers generate an additional repulsion (Pelssers *et al.*, 1989; Pelssers *et al.*, 1990; Lu and Pelton, 2001). However, the L-shaped relative turbidity curve of 5~6 M PAM at the higher shear rates showed the exception from the typical restabilization. For 5~6 M PAM, along with the observed inconsistent adsorption behaviors, the deviation from the typical restabilization and the consequent improvement of the flocculation efficiency might be caused by the nonequilibrium flocculation, in which the transient and elongated chains of the adsorbed PAMs enhance the inter-particle collision and aggregation before collapsing down on kaolinite surfaces (see Figure 4.5). As mentioned before, in the thermodynamic view of the nonequilibrium flocculation, a larger PAM should have the higher chance of the nonequilibrium flocculation than a smaller PAM, due to the higher susceptibility to the mechanical forces and the higher requirement of the reconformation energy or time.

From a series of experimental results in the adsorption and the flocculation tests, the higher shear rates and the larger PAMs were found to be beneficial in the field applications as soil stabilizers and flocculants, to avoid the steric stabilization and to induce the beneficial nonequilibrium flocculation. However, if the MW of a PAM is beyond a certain limit, such as 18 M PAM in this research, PAM molecules start entangling in the solution phase and eventually deteriorate the adsorption capacity and the flocculation efficiency.

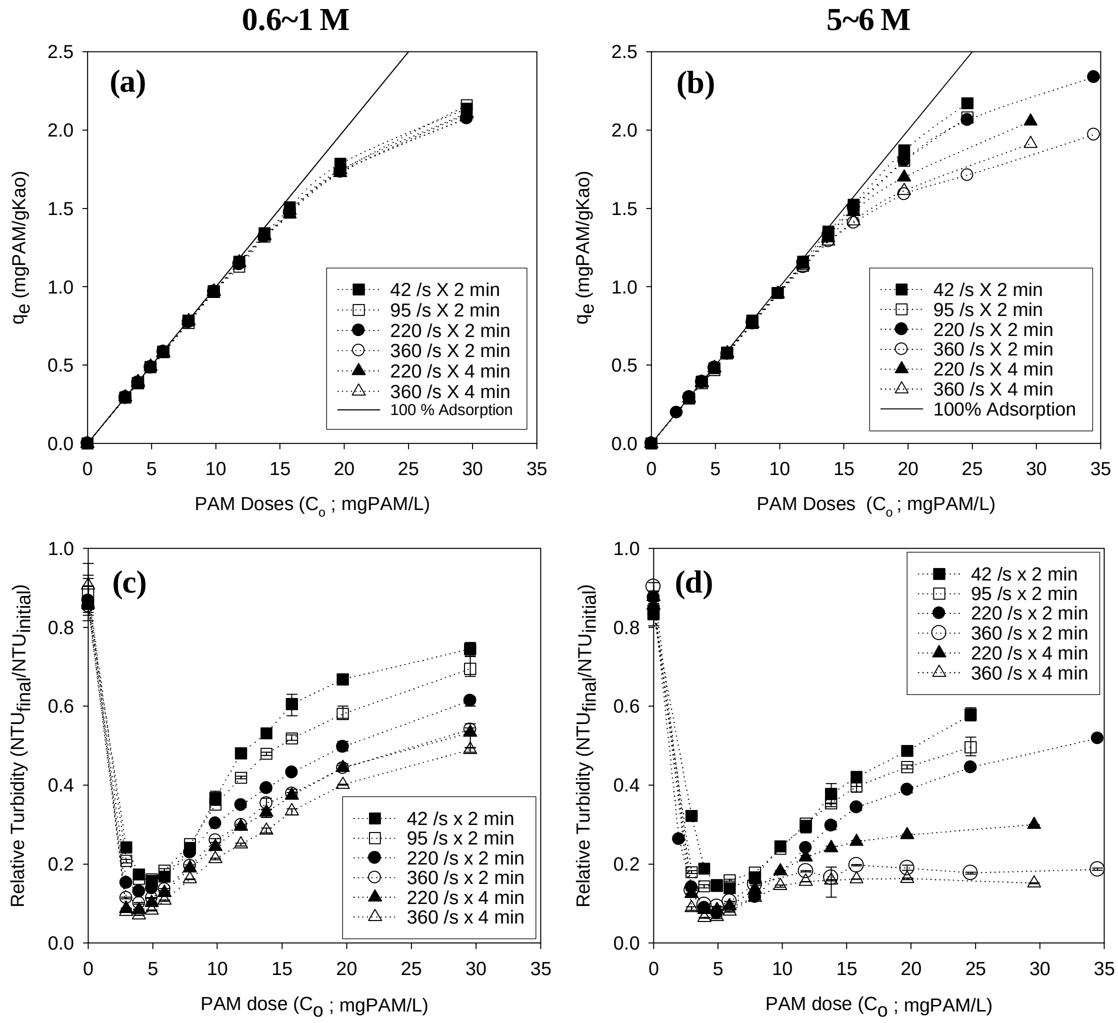

Figure 4.4. Experimental results of the flocculation tests with 0.6~1 M and 5~6 M PAMs at different shear conditions. Figures (a) and (b) represent the plots of adsorption capacities *versus* PAM dose concentrations for 0.6~1 M and 5~6 M, respectively. Figures (c) and (d) represent the plots of relative turbidities *versus* PAM dose concentrations (mg/L), for 0.6~1 M and 5~6 M, respectively.

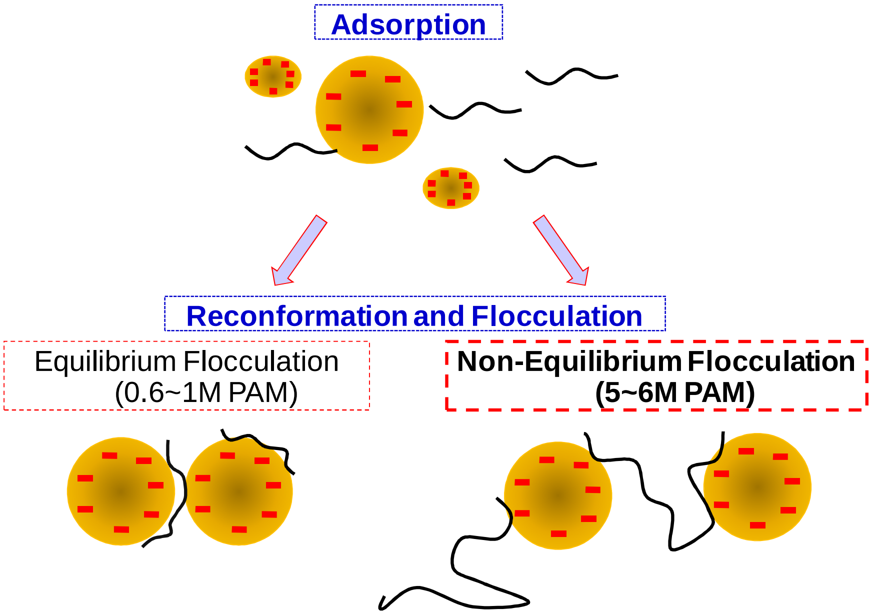

Figure 4.5. Schematic diagram of equilibrium and nonequilibrium flocculation mechanisms occurring in PAM- and kaolinite-containing suspensions.

4.4 Conclusion and Recommendation

In this research, the effects of PAM MW on adsorption and flocculation were investigated. Firstly, the adsorption capacities of nonionic PAMs on kaolinite surfaces increased with increasing their MW, except the one of the largest 18 M PAM. The maximum adsorption capacities of 0.6~1 M and 5~6 M PAMs were estimated at 17.9 and 26.8 mgPAM/gKaolinite, respectively, while those of 1.5 K, 10 K, and 18 M PAMs were below 1 mgPAM/gKaolinite. For the largest 18 M PAM, the 1 g/L stock solution of the adsorption tests was found to be in the semi-dilute region with developing polymeric chain entanglements and eventually to reduce the adsorption capacity.

Secondly, in the flocculation tests, compared to the smaller 0.6~1 M PAM, the larger 5~6 M PAM was shown to enhance the flocculation efficiency in PAM- and kaolinite-containing suspensions, due to the higher susceptibility to the nonequilibrium flocculation. Also, by means of the nonequilibrium flocculation, the large 5~6 M PAM was able to avoid the particle restabilization in the PAM over-dose conditions. In summary, the higher PAM MW was found to guarantee both the higher adsorption capacity and flocculation efficiency. However, if the MW of a PAM is beyond a certain limit, PAM molecules start entangling in the semi-dilute solution phase and eventually decrease the adsorption capacity and the flocculation efficiency.

In future studies, the other controlling factors of a PAM or a solution are required to be estimated for their effects on adsorption and flocculation. Especially, the charge density (CD) of anionic PAMs has been reported to make substantial effects on the adsorption capacity and the flocculation efficiency (Green *et al.*, 2000; Heller and Keren, 2002; Heller and Keren, 2003; McLaughlin and Bartholomew, 2007; Orts *et al.*, 2007). Therefore, the effects of PAM CD and MW and their synergetic effects on adsorption and flocculation will be investigated in the different solution properties, such as pH, ionic strength, and salt species.

4.5 References

Adachi, Y., 1995, Dynamic aspects of coagulation and flocculation, *Advances in Colloid and Interface Science*, **56**, 1-31

Barvenik, F. W., 1994, Polyacrylamide characteristics related to soil applications, *Soil Science*, **158**(4), 235-243

Bozzi, L., M. Milas, and M. Rinaudo, 1996, Solution and gel rheology of a new polysaccharide excreted by the bacterium *Alteromonas sp.* strain 1644, *International Jounal of Biological Macromolecules*, **18**, 83-91

Chapra, S. C., 1997, *Surface quality modeling*, McGraw-Hill,

Cohen, Y., and A. B. Metzner, 1982, Adsorption effects in the flow of polymer solutions through capillaries, *Macromolecules*, **15**, 1425-1429

Feast, W. J., and H. S. Munro, 1987, *Polymer surfaces and interfaces*, John Wiley & Sons, Chichester, UK

Fleer, G. J., M.A. Cohen Stuart, J.M.H.M. Scheutjens, T. Cosgrove, and B. Vincent, 1993, *Polymers at interfaces*, Chapman & Hall, London, UK

Gramain, P., and P. Myard, 1981, Elongational deformation by shear flow of flexible polymers adsorbed in porous media, *Macromolecules*, **14**, 180-184

Green, V. S., D. E. Stott, L. D. Norton, and J. G. Graveel, 2000, Polyacrylamide Molecular Weight and Charge Effects on Infiltration under Simulated Rainfall, *Soil Sci. Soc. Am. J.*, **64**, 1786-1791

Gregory, J., 1988, Polymer adsorption and flocculation in sheared suspensions, *Colloids and Surfaces*, **31**, 231-253

Heller, H., and R. Keren, 2002, Anionic Polyacrylamide Polymers Effect on Rheological Behavior of Sodium-Montmorillonite Suspensions, *Soil Sci. Soc. Am. J.*, **66**, 19-25

Heller, H., and R. Keren, 2003, Anionic polyacrylaide polymer adsorption by pyrophyllite and montmorillonite, *Clays and Clay Minerals*, **51**(3), 334-330

Hurst, V. J., and S. M. Pickering, 1997, Origin and classification of coastal plain kaolins, southeastern USA, and the role of groundwater and microbial action, *Clays and Clay Minerals*, **45**(2), 274-285

Jones, F., J.B. Farrow, and W. v. Bronswijk, 1998, An infrared study of a polyacrylate flocculant adsorbed on hematite, *Langmuir*, **14**, 6512-6517

Lee, J., and G. G. Fuller, 1984, Ellipsometry studies of adsorbed polymer chains subjected to flow, *Macromolecules*, **17**, 375-380

Levy, G. J., and M. Agassi, 1995, Polymer molecular weight and degree of drying effects on infiltration and erosion of three differen soils, *Aust. J. Soil Res.*, **33**, 1007-1018

Lu, C., and R. Pelton, 2001, PEO Flocculation of polystyrene-core poly(vinylphenol)-shell latex: an example of ideal bridging, *Langmuir*, **17**, 7770-7776

McCollister, D. D., C. L. Hake, S. E. Sadek, and V. K. Rowe, 1965, Toxicologic investigations of polyacrylamides, *Toxicol. Appl. Pharmacol.*, **7**, 639-651

McLaughlin, R. A., and N. Bartholomew, 2007, Soil factors influencing suspended sediment flocculation by polyacrylamide, *Soil Sci. Soc. Am. J.*, **71**, 537-544

Milas, M., M. Rinaudo, M. Knipper, and J. L. Schuppiser, 1990, Flow and viscoelastic properties of Xanthan Gum solution, *Macromolecules*, **23**, 2506-2511

Morris, G. E., D. Fornasiero, and J. Ralston, 2002, Polymer depressants at the talc-water interface: adsorption isotherm, microflotation and electrokinetic studies, *Int. J. Miner. Process*, **67**, 211-227

Mpofu, P., J. Addai-Mensah, and J. Ralston, 2003a, Influence of hydrolyzable metal ions on the interfacial chemistry, particle interactions, and dewatering behavior of kaolinite dispersion, *Journal of Colloid and Interface Science*, **261**, 349-359

Mpofu, P., J. Addai-Mensah, and J. Ralston, 2003b, Investigation of the effect of polymer structure type on flocculation, rheology and dewatering behaviour of kaolinite dispersions, *Int. J. Miner. Process*, **71**, 247-268

Myagchenkov, V. A., and V. F. Kurenkov, 1991, Applications of acrylamide polymers and copolymers: a review, *Polym.-Plast. Technol. Eng.*, **30**(2-3), 109-135

Ndjouenkeu, R., F. M. Goycoolea, E. R. Morris, and J. O. Akingbala, 1996, Rheology of okra (*Hibiscus esculentus* L.) and dika nut (*Irvingia gabonensis*) polysaccharides, *Carbohyrate Polymers*, **29**, 263-269

Orts, W. J., A. Roa-Espinosa, R.E. Sojka, G.M. Glenn, S.H. Imam, K. Erlacher, and J. S. Pederson, 2007, Use of synthetic polymers and biopolymers for soil stabilization in agricultural, construction, and military application, *Journal of Materials in Civil Engineering*, **19**(1), 58-66

Parfitt, G. D., and C. H. Rochester, 1983, *Adsorption from solution at the solid/liquid interface*, Academic Press, New York, USA

Pelssers, E. G. M., M.A. Cohen Stuart, and G. J. Fleer, 1989, Kinetic aspects of polymer bridging: equilibrium flocculation and nonequilibrium flocculation, *Colloids and Surfaces*, **38**, 15-25

Pelssers, E. G. M., M.A. Cohen Stuart, and G. J. Fleer, 1990, Kinetics of bridging flocculation, *J. CHEM. SOC. FARADAY TRANS.*, **86**(9), 1355-1361

Ren, J., and A. I. Packman, 2004, Stream-subsurface exchange of zinc in the presence of silica and kaolinite colloids, *Environ. Sci. Technol.*, **38**, 6571-6581

Schwarzenbach, R. P., P.M.Gschwend, and D. M. Imboden, 2003, *Environmental organic chemistry, 2nd ed*, Johns Wiley & Sons, Inc., Hoboken, New Jersey.

Sperling, L. H., 2006, *Introduction to physical polymer science, 4th Edition*, John Wiley & Sons, Inc., Hoboken, NJ

Stephens, S. H., 1991, Final report on the safety assessment of polyacrylamide, *J. Am. Coll. Toxicol.*, **10**, 193-202

Stumm, W., and J. J. Morgan, 1996, *Aquatic chemistry, 3rd ed*, Johns Wiley & Sons, Inc., Canada.

Torn, L. H., A. de Keizer, L.K. Koopal, and J. Lyklema, 2003, Mixed adsorption of poly(vinylpyrrolidone) and sodium dodecylbenzenesulfonate on kaolinte, *Journal of Colloid and Interface Science*, **260**, 1-8

Tuinier, R., P. Zoon, M. A. C. Stuart, and C. G. d. Kruif, 1999, Concentration and shear-rate dependence of the viscosity of an exocellular polysaccharide, *Biopolymers*, **50**, 641-646

van Eijk, M. C. P., and M. A. C. Stuart, 1997, Polymer adsorption kinetics: Effects of supply rate, *Macromolecules*, **13**(5447-5450),

Wallace, A., and G. A. Wallace, 1986, Effects of soil conditioners on emergence and growth of tomato, cotton, and lettuce seedlings, *Soil Science*, **141**, 313-316

Yuang, P., and Y. Shen, 2005, Determination of the surface area of smectite in water by ethylene oxide chain adsorption, *Journal of Colloid and Interface Sciences*, **285**, 443-447

CHAPTER 5. INVESTIGATION ON THE EFFECTS OF PAM AND SOLUTION CHARACTERISTICS ON ADSORPTION AND FLOCCULATION OCCURING IN SIMILARLY CHARGED ANIONIC PAM- AND KAOLINITE-CONTAINING SUSPENSIONS

5.0 Abstract

Anionic polyacrylamides (PAMs) have long been used as soil stabilizers or flocculants due to their high adsorption capacity and flocculation efficiency as well as non-toxicity on the aquatic ecosystem. However, the physicochemical processes in similarly changed anionic PAM- and clay-containing suspensions and their controlling characteristics are still unclear and thus investigated in the elaborate steady-state adsorption and flocculation tests. Above all, molecular weight (MW) and charge density (CD) were proven as the decisive PAM characteristics in determining adsorption capacity and flocculation efficiency. Adsorption capacities were found to be inversely proportional to PAM CDs, while flocculation efficiencies were directly proportional to PAM MWs. Along with PAM characteristics, cation species in the solution were found to be the key solution characteristics. Divalent cations in the solution, such as Ca^{2+} and Mg^{2+}, enhanced adsorption and flocculation processes with the cationic bridging between PAM and kaolinite (PAM^{-}–$^{+}M^{+}$–$^{-}$Kaolinite). However, concurring steric stabilization was also found to counteract flocculation due to the conformational changes of adsorbed PAMs by the cationic bridging between pre-adsorbed PAM molecules (PAM^{-}–$^{+}M^{+}$–$^{-}$

PAM). In addition, the polydispersity effect of polymer adsorption, which induces the competitive adsorption between the constituent low-MW and high-MW polymers, was found to be governed by PAM CD. Low-CD PAM showed the competitive adsorption with the polydispersity effect, while high-CD PAM represented the non-competitive high-affinity adsorption without the polydispersity effect. Thus, polyacrylamide and solution characteristics, CD and MW of PAM, and cation species in the solution were found to make critical effects on adsorption and flocculation processes and thus to be the controlling parameters in optimizing anionic PAM applications as soil stabilizer or flocculant.

5.1 Introduction

Soil erosion occurs in both urban and rural areas during storm events. In general, the problem increases with increasing land disturbance (e.g., tillage, mining, road grading and rural to urban land conversion). The most problematic sediment particles typically are of colloidal-size, and if not controlled they can end up in various receiving water bodies, where the materials they carry (nutrients, toxicants, pathogens, etc.) can contribute to the coating of bottom sediments, algae blooms, oxygen depletion and food-chain problem (Stumm and Morgan, 1996; Chapra, 1997; Schwarzenbach *et al.*, 2003).

To counteract soil erosion and colloid proliferation in water bodies, polyacrylamides (PAMs) have long been used as soil stabilizers or flocculants because of their characteristics of high solubility, viscosity and molecular weight (McCollister *et al.*, 1965; Wallace and Wallace, 1986; Stephens, 1991; Myagchenkov and Kurenkov, 1991;

Seybold, 1994). Generally, nonionic, anionic, and cationic PAMs, which are classified with their functional groups along backbone chains, are applicable for different purposes. However, in applications on the ecosystem as soil stabilizer or flocculant, anionic PAMs have been mostly used because cationic PAMs are reported to be toxic on aquatic lives by blocking bodily membranes (McCollister *et al.*, 1965; Wallace and Wallace, 1986; Stephens, 1991; Barvenik, 1994).

Similar to anionic PAMs, most colloids are anionic in the aquatic environment (Stumm and Morgan, 1996). For example, clays, the major constituents of aqueous colloids, are negatively charged above pH 4 ~ 5 due to isomorphic substitution and broken edge (Das, 1995; Sylvia *et al.*, 2003). Thus, considering the electrostatic repulsion between similarly charged surfaces of anionic PAM and clay in the ambient aquatic system, the physicochemical interactions in anionic PAM- and clay-containing suspensions are hardly anticipated. However, even in the electrostatic repulsion dominant conditions, physicochemical interaction processes, such as adsorption and flocculation, have been reported in many laboratory or field experiments (Entry *et al.*, 2002; McLaughlin and Bartholomew, 2007; Orts *et al.*, 2007; Mpofu *et al.*, 2003a; Ben-Hur *et al.*, 1992; Levy and Miller, 1999; Green *et al.*, 2000). Thus, the minute-scale interfacial interaction mechanisms to overcome the electrostatic repulsion and eventually to induce adsorption and flocculation were set as the research targets and explored in this research.

Adsorption and flocculation are rather integrated physicochemical processes containing various minute-scale interfacial interaction mechanisms in PAM- and clay-containing suspensions. In general, adsorption of polymeric molecules on clays occurs very quickly after dosing polymeric flocculant into clay suspensions and then flocculation of clay particles is driven by adsorbed polymeric molecules (Pelssers *et al.*, 1989; Pelssers *et al.*, 1990; Lu and Pelton, 2001).

Above all, to induce adsorption of anionic PAMs on clay surfaces, the steadfast binding mechanisms with enough binding energy should be guaranteed to overcome the electrostatic repulsion between anionic PAMs and clays. These binding mechanisms in anionic PAM- and clay-containing suspensions are very different with and without divalent cations. Firstly, in absence of divalent cations, various adsorption-driving mechanisms between anionic PAMs (or other anionic polyelectrolytes) and anionic mineral surfaces have been reported, such as covalent bonding, hydrogen bonding, hydrophobic interactions, or electrostatic attraction induced by the heterogeneous charge distribution on clay surfaces. Noteworthily, adsorption processes are not only driven by a specific mechanism but also by the combined effects of various mechanisms (Jones *et al.*, 1998; Heller and Keren, 2002; Morris *et al.*, 2002; Heller and Keren, 2003; Torn *et al.*, 2003; Mpofu *et al.*, 2003a; Mpofu *et al.*, 2003b). Secondly, in presence of divalent cations, the entirely different interaction mechanism has been reported to induce adsorption between similarly charged anionic surfaces and furthermore known to enhance adsorption capacities up to several-order higher than the capacities in absence of divalent cations. For this phenomenon, the researchers have proposed cationic bridging mechanism induced by divalent cations such as Ca^{2+} and Mg^{2+}, which mitigate the electrostatic repulsion between similarly charged surfaces and make bridges between anionic functional groups of polyelectrolytes and mineral surfaces (Jones *et al.*, 1998; Vermohlen *et al.*, 2000; Abraham *et al.*, 2001; Entry *et al.*, 2002; Mpofu *et al.*, 2003a; Claesson *et al.*, 2005; Feng *et al.*, 2005; Sabah and Erkan, 2006; Orts *et al.*, 2007; Lu and Letey, 2002; Mpofu *et al.*, 2004; Sander *et al.*, 2004; Mpofu *et al.*, 2005). In conclusion, whichever binding mechanisms occur individually or simultaneously in anionic PAM- and clay-containing suspensions, adsorption occurs apparently with sufficient binding energy to overcome electrostatic repulsion between similarly charged surfaces.

After adsorption of PAMs on clay surfaces, the subsequent flocculation is triggered by adsorbed polymers. Two flocculation mechanisms, charge neutralization and bridging flocculation, have been proposed as the most plausible polymer-induced flocculation mechanisms (Gregory, 1988; Pelssers *et al.*, 1989; Pelssers *et al.*, 1990; Adachi, 1995; Elimelech *et al.*, 1995; Zhang and Buffle, 1995; Ferretti *et al.*, 1997; Adachi and Wada, 2000; Lu and Pelton, 2001). However, considering that most clay species such as kaolinite, smectite, and montmoriorlite are negatively charged in ambient aquatic systems due to their lower pH_{pzc} values, charge neutralization by adding anionic PAMs should not be the major destabilization mechanism in anionic PAM- and clay-containing solutions. Thus, bridging flocculation, in which adsorbed polymer chains protruding out of the electric repulsion layer on clay surfaces make bridges between colloidal particles and eventually form large flocs, should be the major flocculation mechanism in anionic PAM- and clay-containing suspensions.

Even though various adsorption- and flocculation-driving interfacial interaction mechanisms in anionic PAM- and clay-containing suspensions have been identified in many previous researches, the decisive parameters and their effects on these adsorption- and flocculation-driving mechanisms are still under investigation. Thus, firstly, the characteristics of anionic PAMs, molecular weight (MW) and charge density (CD, $\frac{\text{No. of Charged Units}}{\text{No. of Repeating Units}}$ %) were chosen as the experimental parameters in our adsorption and flocculation tests (Levy and Miller, 1999; Green *et al.*, 2000; Heller and Keren, 2002; Heller and Keren, 2003). Secondly, the effects of the solution properties on adsorption and flocculation, such as the constituent cation species, were investigated in presence of different monovalent or divalent cations (Na^+, Ca^{2+}, and Mg^{2+}). All the adsorption and flocculation experiments were done in constant shear conditions to mimic the shear-induced conditions occurring on top soils and in flocculant-aided sediment retention ponds. At the end of this research, the interfacial interaction mechanisms in PAM- and kaolinite-containing suspensions and the effects of PAM and solution properties on those mechanisms were identified.

5.2 Materials and Methods

5.2.1 Polyacrylamide Purification and Characterization with respect to MW and CD

A series of PAMs with different MWs and CDs were provided from Kemira Water Solutions Inc. (Lakeland, FL). To remove salts and other impurities (mostly NaCl), PAMs were purified by the serial steps of dissolution, acidification, and precipitation in water-methanol mixtures (Francois *et al.*, 1979). Commercial PAM powders were firstly dissolved into distilled deionized water (DDW) and gently stirred on a Thermolyne® Bigger Bill orbital shaker (Thermo Fisher Scientific Inc., PA) for one to two days. After complete dissolution, PAM solutions were acidified to pH 3 with hydrochloric acid to protonate all carboxyl groups and simultaneously dissociate metal cations from the PAM molecules. Polyacrylamide solids were collected by precipitation which is induced by addition of methanol and placement in a 4^{o}C cold room. The serial steps of dissolution, acidification, and precipitation were repeated four to five times to collect pure PAM solids without salts or other contaminants on PAM molecules. Finally, purified PAM solids were lyophilized with a VirTis® bench top freeze dryer (SP Industries Inc., NY) and preserved as powder forms for uses in the subsequent experiments. Before adsorption and flocculation tests, 2 g/L aqueous stock solutions were prepared by dissolving purified PAM powders in DDW and then stored in the dark during the experiments.

Molecular weights (MW) of PAMs were estimated with simple intrinsic viscosity measurement tests with a capillary viscometer (Sperling, 2006). For a certain PAM sample, a series of PAM solutions with different concentrations of 0.025, 0.05, 0.075, and 0.1 g/dL were prepared in 0.2 M Na_2SO_4 aqueous solution at pH 9. Specific and relative viscosities for the serial PAM solutions having different concentrations were measured at 25 ^{o}C with #50 Cannon-Fenske routine viscometer (Cannon Instrument Company Inc., PA). Then, the intrinsic viscosity ($[\eta]$) was found at the y-intercept of the linear curve of specific or relative viscosity *versus* PAM concentration. Finally, Mark-Houwink-Sakurada equation (MHS equation, $[\eta] = K \cdot MW^{a}$) was used to determine MW of a PAM with a measured intrinsic viscosity (Wu *et al.*, 1991). Wu’s MHS equation, which has the empirical equations to obtain the model constants (*K* and *a*) with respect to the charge density (CD) of an anionic PAM, was used as the unique equation to estimate MWs of anionic PAMs having various CDs. In our previous research, an intrinsic viscosity measurement technique was found to have the ability to estimate the relative magnitudes of MWs for various anionic PAM samples. However, the intrinsic viscosity technique could not evaluate the absolute values of MWs because the consistent gap between MWs estimated with an intrinsic viscosity measurement and with a light scattering analysis techniques was observed (Lee *et al.*, 2008). Thus, it should be acknowledged that the provided MWs of anionic PAMs are not the absolute values but rather the relative magnitudes of MWs.

Charge densities of PAMs were measured with acid-base titration methods. Triplicate 50 mL PAM solutions with 1 g/L PAM concentration were prepared at 0.001, 0.01, and 0.1 M NaCl background salt concentrations by dissolving pre-cleaned PAM powders in the salt solutions. Titration was done upward with 0.5 M NaOH and then downward with 0.5 M HCl and pH was monitored continuously with Orion 420A pH meter (Thermo Scientific Inc., PA). During titration, PAM solution was continuously purged with pure nitrogen gas (National Welders Supply Co., NC) to prevent CO_2 dissolution. All the titration experiments produced identical results for both forward and backward titrations, which consequently endowed the credibility on our experimental method. The *S*-shaped titration curves (pH *versus* specific charge density) were plotted after processing the measured data such as acid or base doses and pHs and they were adjusted with subtracting background acid or base consumptions by the pure solvent.

Eventually, CD of a PAM sample was estimated at the maximum specific charge density on the upper plateau of the *S*-shaped titration curve, where the entire PAM molecules become fully hydrolyzed *i.e.* ionized.

Table 5.1. Measured molecular weights (MW) and charge density (CD) of the pre-cleaned Kimera® PAMs used in adsorption and flocculation tests. Errors of MWs represent the lowest and highest values calculated in the data fitting procedures. Errors of CDs represent the standard deviations of the triplicate samples.

PAMs	MW* (10^6 g/mol)	CD** (%)
N300	3.81 ± 0.178	-
A100H	2.73 ± 0.069	11.4 ± 0.06
A120	1.86 ± 0.058	25.5 ± 0.26
A120H	3.27 ± 0.098	25.2 ± 0.07
A150L	1.97 ± 0.051	51.1 ± 0.10
A150	2.49 ± 0.072	45.8 ± 0.47

5.2.2 Jar Test – Adsorption and Flocculation Test

PB-700™ Standard JarTester (Phips & Bird, Inc., VA) was used to investigate adsorption and flocculation processes in anionic PAM- and clay-containing suspensions. Kaolinite powder (Sigma-Aldrich, MO) was chosen as the representative clay because of its abundance in soils of the southeastern United States (Hurst and Pickering, 1997). In this research, finding the optimal doses of flocculants which is the general purpose of jar tests was not our interest but investigating physicochemical behaviors in a relatively long-term steady state condition was set as the main purpose of the research. Thus, to mimic steady state adsorption and flocculation processes occurring on top soils and in sediment retention ponds, the constant stirring condition at 150 rpm was applied to PAM- and kaolinite-containing suspensions for 6 hours, which are enough to reach the equilibrium between PAMs and kaolinite surfaces (Morris *et al.*, 2002). Also, considering the difficulty in controlling the injection of PAM stabilizers or flocculants in field applications onto top soils or sediment retention ponds, the wide range of dose conditions, from under- to over-dose, can be expected. Thus, adsorption and flocculation tests were designed to explore steady state adsorption and flocculation processes occurring in the wide range of PAM dose concentrations, up to 80 mgPAM/L.

For all the jar tests, kaolinite suspensions and PAM solutions were prepared in advance. Kaolinite suspensions were prepared at 20 g/L of suspended solid concentration and stirred continuously for two days to reach the equilibrium with the atmospheric carbonaceous system. pH of kaolinite suspensions were adjusted at 7 by adding sodium hydroxide or hydrochloric acid. Polyacrylamide solutions with various PAM concentrations were prepared by diluting PAM stock solutions with prepared carbonaceous water that is also equilibrated with the atmosphere and adjusted at pH 7. At the beginning of jar tests, 250 mL of kaolinite suspension and the same volume of serial PAM solutions containing different PAM dose concentrations were mixed and placed into 6 jars of the jar tester and stirred for 6 hours at 150 rpm stirring speed. Background salt concentration of PAM- and kaolinite-containing suspensions were adjusted at 3 mM NaCl, 1 mM $CaCl_2$, or 1 mM $MgCl_2$, by injecting salt stock solutions at the beginning of jar tests. Even though these background salt concentrations have the same ionic strengths, NaCl were used for the control system, while $CaCl_2$ or $MgCl_2$ for the experimental systems, to investigate cationic bridging effects of divalent cations. At the end of the jar test, suspended flocs were carefully taken from 6 jars respectively and fixed in agar plates for floc size analysis (Zahid and Ganczarczyk, 1990; Ganczarczyk *et al.*, 1992; Gorczyca B. and Ganczarczyk, 1996). Then, after additional 1 hour settling time without stirring, aliquots were taken to measure PAM concentrations, to quantify residual suspended solid concentrations, and to measure zeta potential. This jar test was triplicated for a certain experimental condition for the quality assurance and control. Thus, the error bar in the experimental results represents the standard deviations of three independent experiments having the same experimental conditions.

5.2.3 Measurements of Experimental Indices

To estimate PAM adsorption capacity on kaolinite surfaces, first, the collected aliquots from the jar tests were centrifuged at 10,000 g for 20 minutes to separate all the kaolinites from the solution phase with the superspeed centrifuge, Sorvall Evolution RC (Thermo Fisher Scientific Inc., USA). Then, PAM concentrations in the solution phase were measured with TOC-V_{CSH} TOC/TN analyzer (Shimadzu Corp., Japan). Instead of total organic carbon (TOC), total nitrogen (TN) was taken as the PAM measuring index because TOC was affected by inorganic carbons such as CO^{2-} and HCO^{-}. The adsorbed amounts of PAMs were estimated by differentiating the amounts in the solution phase from the dosed amounts of PAMs. Finally, adsorption capacities were expressed by adsorbed mass per kaolinite mass (mgPAM/gKaolinite) and used to plot adsorption isotherm curves.

Residual suspended solid concentrations were measured with following the Standard Methods 2540D, total suspended solids dried at 103 -105 ^{o}C (APHA, 1998). The aliquots taken from the experimental jars after 1 hour settling time were filtered through pre-weighed 0.1 μm Supor® membrane filter disks (Pall Corp., US). Then, the filter papers holding residual suspended solids were dried at 105 °C and weighed with MX5 microbalance (Mettler-Toledo Inc., OH, USA). Finally, residual suspended solid concentrations were estimated by differentiating the weight of the blank filter paper from the weight of the paper holding residual solids.

The microscopic image-processing technique in association with the particle/floc fixation method in agar plates was used to measure the size and morphology of flocs. The fixation method with agar plate was purposed to prevent further mobilization and flocculation of flocs (Zahid and Ganczarczyk, 1990; Ganczarczyk *et al.*, 1992; Gorczyca B. and Ganczarczyk, 1996). At the end of jar tests, suspended flocs were taken and fixed immediately in agar plates, which were prepared in the liquefied state on a hot plate before the floc sampling. Microscopic images of the fixed flocs in solidified agar plates were taken with Sanyo VPC-HD2 Digital Media Camera (10× optical zoom, 3072× 2404 resolution, Sanyo Electric Co., Japan), which was equipped with Tiffen close up lens (The Tiffen Company, NY, USA). Then, the raw images were converted to processed images with the public domain image processing software, Image J (National Institutes of Health, Bethesda, MD) (see Figure 5.1). Also, with aid of Image J software, the volume-averaged floc diameter for a fixed floc sample was automatically calculated in association with some handworks, such as adjusting image contrast or brightness, deleting unclear floc images, *etc.* (see Figure 5.1 (b)). These serial steps of floc sampling, fixation, and measurements were triplicated for a single sample *i.e.* for a certain data point, for quality assurance and control. Unfortunately, due to the resolution limit of the camera, the minimum measurable floc size was set at 50 μm *i.e.* flocs below 50 μm were discarded in calculating volume-averaged floc sizes. Thus, the measured volume-averaged floc diameter does not mean the absolute value, which covers the entire floc/particle size ranges from the primary particle size (about 0.4~2 μm) to the maximum floc size (up to 1000 μm). Instead, the measured volume-averaged floc diameters were used as the relative magnitude of floc sizes, which represent the binding strength or flocculation efficiency between constituent kaolinite particles.

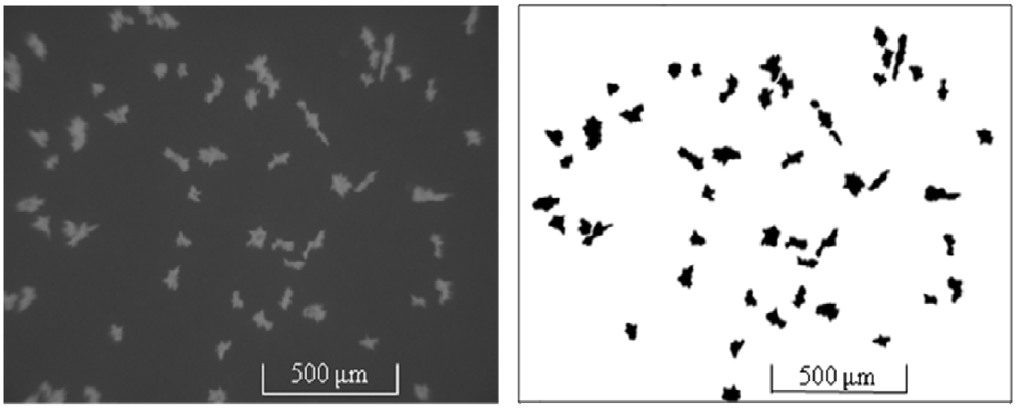

(a) (b)

Figure 5.1. (a) a raw image and (b) a processed image of a fixed floc sample in an agar plates.

To identify electrostatic characteristics of suspended particles or floc, zeta potentials were measured with Brookhaven ZetaPlus zeta potential analyzer (Brookhaven Instruments Corp., NY, USA) for the aliquots taken after one hour settling time. Even though zeta potentials of the aliquots do not mean the electrostatic properties of the entire PAM- and kaolinite-containing suspensions including the properties of settled flocs, they are rather used as the indirect and representative values of the electrostatic characteristics of the experimental systems. In zeta potential measurements, to make the particle concentrations to fall within the measurable concentration range without the overlapping problem, the raw samples were diluted with the buffer solutions which have the same solution characteristics, *e.g.* the same pH, ionic strength, ionic species, as those of the experimental system. For a certain sample, the averaged value of 10 replicated zeta potential measurements was taken for further analyses because of the fluctuating nature of the electrostatic measurement technique. Also, to identify the effects of Ca^{2+} and Mg^{2+} adsorption on zeta potentials, the adsorbed amounts of Ca^{2+} and Mg^{2+} on kaolinite surfaces were measured with the Standard Methods 2340C, EDTA titrimetric method (APHA, 1998). After adding 1~2 mL of the prepared buffer solution to raise pH at about 10 and 1~2 drops of Calmagite indicator (0.1 w/v aqueous, VWR, USA) to develop the end-point color into 50 mL filtered aliquot samples, 0.01 M standard EDTA (VWR, USA) was titrated to reach the end-point. The titrated volume of 0.01 M EDTA until the end-point was finally converted to Ca^{2+} and Mg^{2+} concentrations in the solution. The adsorbed amounts of Ca^{2+} and Mg^{2+} were estimated by subtracting the amounts in the solution phase from the injected amounts of Ca^{2+} and Mg^{2+}. Adsorption capacities were expressed by adsorbed Ca^{2+} or Mg^{2+} mass per kaolinite mass (mgPAM/gKaolinite).

5.3 Results and Discussion

5.3.1 Adsorption and Flocculation Behaviors

In this research, to explore adsorption and flocculation behaviors in anionic PAM- and kaolinite-containing suspensions, PAM adsorption capacity (mgPAM/gkaolinite), residual suspended solid concentration (mgSolid/L), and volume-averaged floc diameter (μm) were measured and the trend curves were plotted with increasing PAM dose concentrations (see Figure 5.2). These measured trend curves were used to identify the effects of PAM and solution characteristics on adsorption and flocculation, such as MWs and CDs of PAMs and salt species in the solution. Also, from the observed trend curves, various minute-scale interfacial interaction mechanisms, such as bridging flocculation, cationic bridging, and steric stabilization, were examined to identify their effects on adsorption and flocculation.

The first column of Figure 5.2 shows the adsorption isotherm curves obtained in PAM- and kaolinite-containing suspensions with different PAMs and salt species. Generally, the adsorption isotherm curves were found to proceed along the line of 100% adsorption *i.e.* all the dosed PAM molecules adsorb on kaolinite surfaces. Then, they come off from the 100% adsorption line *i.e.* the dosed PAM molecules start remaining in the solution phase. This adsorption behavior resembles the reported high-affinity adsorption at polymer-surface interfaces, in which the adsorbed amount rises steeply in the initial part of the isotherm and reaches a (pseudo) plateau (Parfitt and Rochester, 1983; Feast and Munro, 1987; Fleer *et al.*, 1993). However, in a close investigation, the adsorption isotherm curves after the initial steep rises were found to have different curvatures with respect to the electrostatic characteristics of PAMs and solutions. For example, PAMs with low CDs (*e.g.* A100H) have the continuous increase of the adsorption isotherm curves, while PAMs with high CDs (*e.g.* A150) show rather the flat plateau, after the initial steep increases. According to findings from the previous researchers, the continuous increase of the adsorption isotherm curves after the initial steep increase occurs due to the polydispersity effects of the constituent low- and high-MW polymers in the solution. Considering the thermodynamics of the adsorption process in polydisperse polymer-containing aqueous solutions (including polyelectrolytes), high-MW polymers adsorb preferentially due to their lower solubility over low-MW polymers. However, in the solution conditions with low PAM dose concentrations, low-MW polymers are prevalent in adsorption process because their high accessibility competes against the thermodynamic preference of high-MW polymers. Then, with increasing PAM dose concentrations, high-MW polymers start replacing the adsorbed low-MW polymers gradually because their thermodynamic preference starts predominating over the high accessibility of low-MW polymers (Fleer *et al.*, 1993). This step-wise substitution behavior of polydisperse polymers eventually generates the continuous increase of adsorption isotherms after the initial steep rise. However, with low ionic strengths of the solution (*i.e.* good solvents) or with high CDs of polyelectrolytes, the substitution process of the polydisperse polymers hardly occurs because high-MW polymers are still inclined to stay in the solution phase but not to approach and replace the adsorbed low-MW polymers even at the high polymer dose concentrations. Thus, this adsorption behavior generates rather the flat plateaus of isotherm curves after the initial steep rise (Robb and Smith, 1977; Parfitt and Rochester, 1983; Feast and Munro, 1987; Fleer *et al.*, 1993). Considering the high polydispersity of the commercial PAMs used in this research, the continuous increasing trends after the initial steep rises of adsorption isotherm curves are expected. However, due to the higher

CDs of the tested PAMs, except A100H, adsorption isotherm curves had rather flat plateaus without the significant substitution process of attached PAM molecules.

Also, as one of the unique behaviors in the adsorption tests, PAM adsorption capacities on kaolinites were an approximate order of magnitude higher in presence of divalent cations (in the experimental systems with 1 mM $CaCl_2$ or 1 mM $MgCl_2$) than those in presence of monovalent ions (in the control system with 3 mM NaCl). Divalent cations have been reported to enhance PAM adsorption on mineral surfaces, due to cationic bridging mechanism in which divalent cations make bridges between the similarly charged anionic surfaces and overcome the electrostatic repulsion forces (Jones *et al.*, 1998; Vermohlen *et al.*, 2000; Abraham *et al.*, 2001; Entry *et al.*, 2002; Mpofu *et al.*, 2003a; Claesson *et al.*, 2005; Feng *et al.*, 2005; Sabah and Erkan, 2006; Orts *et al.*, 2007; Lu and Letey, 2002; Mpofu *et al.*, 2004; Sander *et al.*, 2004; Mpofu *et al.*, 2005). Thus, cationic bridging is proven again in this research. In comparing the effects of different divalent cations, Ca^{2+} was more efficient to enhance cationic bridging and resultant adsorption capacities than Mg^{2+}. Considering the difference of the hydrated sizes of divalent cations, Ca^{2+} with a small hydrated size should have higher accessibility and affinity on PAM molecules or kaolinite surfaces and thus larger PAM adsorption capacities (Sabbagh and Delsanti, 2000; Abraham *et al.*, 2001; Lu and Letey, 2002).

The second and third columns in Figure 5.2 show residual suspended solid concentrations (mgKaolinite/L) and volume-averaged floc diameters (μm) with increasing PAM dose concentrations. These experimental indices were used as the representative parameters of flocculation efficiencies in PAM- and kaolinite-containing suspensions. Generally, cationic bridging mechanism was again found to enhance flocculation as well as adsorption, in presence of divalent cations, Ca^{2+} and Mg^{2+}. In the closer look on the individual trend curves, firstly, in the presence of Na^+, the marginal increase of residual suspended solid concentrations and the apparent decrease of floc sizes were observed with increasing PAM dose concentrations, except the opposite behaviors of A100H. Thus, additional PAM doses seem to deteriorate inter-particle flocculation efficiencies, probably due to steric stabilization with conformational changes of adsorbed PAM molecules on kaolinite surfaces (Gregory, 1988; Pelssers *et al.*, 1989; Pelssers *et al.*, 1990; Lu and Pelton, 2001; Santore, 2005). Contrarily, in case of A100H, flocculation efficiencies were enhanced with increasing PAM dose concentrations. This unique flocculation behavior with A100H may be related to the polydispersity effects (Parfitt and Rochester, 1983; Fleer *et al.*, 1993).

Secondly, in presence of Ca^{2+} or Mg^{2+}, enhanced flocculation efficiencies by cationic bridging effects were proven with smaller residual solid concentrations and bigger floc sizes than those in presence of Na^+. However, in the close investigation on individual curves of residual solid concentrations and floc sizes, two contradictory flocculation behaviors, detrimental increase of residual solid concentrations and beneficial growth of floc sizes, were found to occur simultaneously with increasing PAM dose concentrations. In other words, two adverse processes, particle restabilization (or breakup) and flocculation, were found to occur at the same time. Considering the concurrence of restabilization and flocculation, some of adsorbed PAM molecules seem to become active for flocculation with binding colloidal particles but at the same time the others to be inactive with restabilizing colloidal particles by steric stabilization (Pelssers *et al.*, 1989; Pelssers *et al.*, 1990; Lu and Pelton, 2001). Thus, in the cationic bridging process, divalent cations seemingly make two types of bridges, the one between PAM and kaolinite ($\mathrm{PAM^{-}}$–$\mathrm{^{+}M^{+}}$–$^{-}$kaolinite) enhancing flocculation and the other between PAMs ($\mathrm{PAM^{-}}$–$\mathrm{^{+}M^{+}}$–$\mathrm{^{-}PAM}$) aggravating steric stabilization. Especially, the cationic bridges between PAM molecules ($\mathrm{PAM^{-}}$–$\mathrm{^{+}M^{+}}$–$\mathrm{^{-}PAM}$) might change the floppy and sticky conformation of the adsorbed PAM molecules to the dense and bouncing one, which are more vulnerable to steric stabilization. This hypothesis was somewhat proven with the steep increase of residual solid concentration with increasing PAM dose concentrations in presence of divalent cations, compared to the marginal increase in presence of monovalent cations (see the second column of Figure 5.2). Considering the hydrated sizes of cations, divalent cations with small hydrated size may reside inside adsorbed PAM matrices, alter the polymeric structures, and eventually induce steric stabilization, whereas monovalent ions with large hydrated size reside outside of adsorbed PAM layers and make marginal effects on the polymeric structures and steric stabilization. This observation on the steric stabilization enhanced by the cationic bridges between PAM molecules ($\mathrm{PAM^{-}}$–$\mathrm{^{+}M^{+}}$–$\mathrm{^{-}PAM}$) will be discussed again in the later section with the experimental results of zeta potential and $\mathrm{Ca^{2+}}$/$\mathrm{Mg^{2+}}$ adsorption capacity. After the competing region between restabilization and flocculation, with further increases of PAM dose concentrations, restabilization eventually was proven to be dominant against flocculation with observation of increasing residual solid concentration and decreasing floc sizes. Floc sizes were found to be maximized at a certain PAM dose concentration, which are noteworthily matched to the inflection points in the adsorption isotherm curves. For example, with A120 dose in 1 mM $CaCl_2$, floc sizes clearly decrease after the inflection point of the PAM adsorption isotherm curve (the second row in Figure 5.2). This trend of the measured floc sizes was commonly observed for all the other PAMs with some small variations. Thus, flocculation efficiencies seems to increase rapidly until the full coverage of high-affinity adsorption sites and then decrease gradually with the prevalence of steric stabilization against flocculation, due to the conformational alteration of adsorbed PAM molecules.

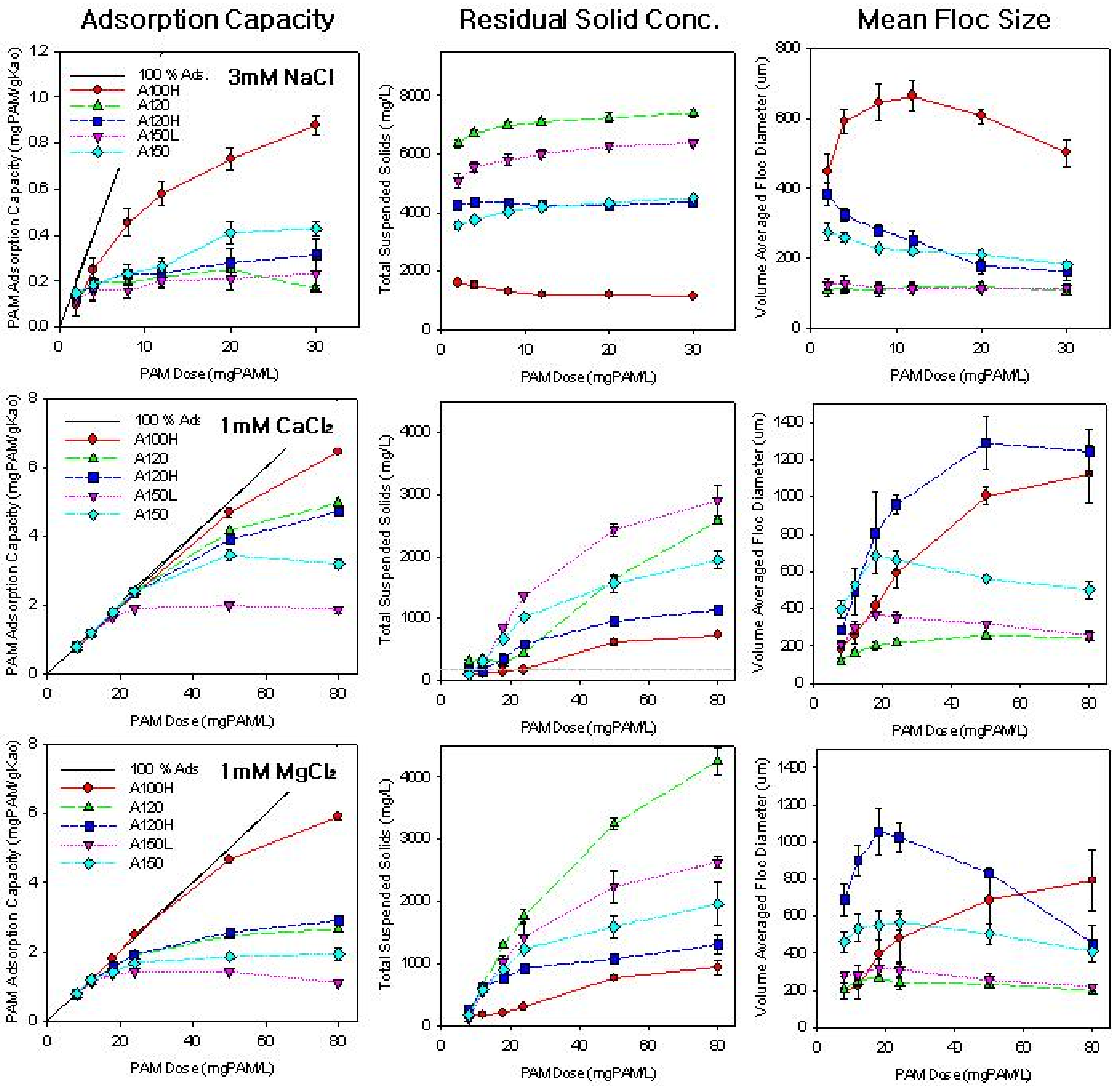

Figure 5.2. PAM adsorption isotherm (mgPAM/gKaolinite), residual suspended solid concentration (mgKaolinite/L), and volume-averaged floc diameter (μm) with increasing PAM dose concentrations for different PAM species and solution chemistries.

From the plots of PAM adsorption capacities and volume-averaged floc diameters shown in the first and third columns of Figure 5.2, maximum values were obtained and presented in bar graphs, to identify briefly how PAM and solution characteristics make effects on adsorption capacities and flocculation efficiencies (see Figure 5.3). Above all, the solution chemistries *i.e.* the salt species, was proven to be a key factor in determining adsorption capacities and flocculation efficiencies. For example, maximum adsorption capacities and maximum floc sizes increased about five to twenty and two to three times, respectively, in presence of divalent cations, compared to those in presence of monovalent cations. These enhancements of adsorption capacities and flocculation efficiencies might be caused by cationic bridging effects of divalent ions. In Figure 5.3, with respect to the effects of PAM characteristics, maximum PAM adsorption capacities were seemingly governed by PAM CDs, while maximum floc sizes by MWs. These correlations of adsorption capacity *versus* CD and flocculation efficiency *versus* MW will be discussed closely in the later section with Figure 5.5.

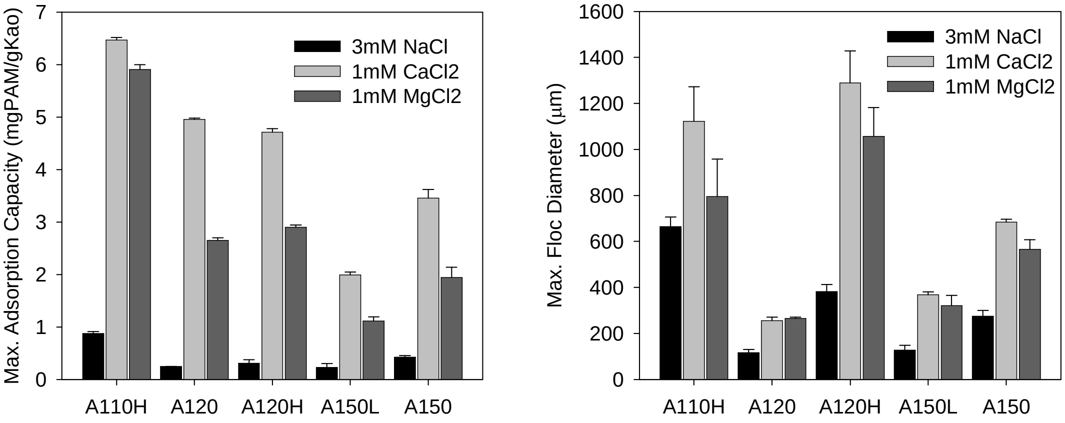

(a) (b)

Figure 5.3. (a) maximum adsorption capacity (mgPAM/gKaolinite) and (b) maximum volume-averaged floc size (μm) in the range of applied PAM dose concentrations for different PAM species and solution conditions.

In this research, the PAM with the smallest charge, A100H, repeatedly showed abnormal behaviors which deviated from the general trends of other PAMs in adsorption and flocculation tests. As mentioned in the previous section, A100H seems not to follow the adsorption and flocculation behaviors of other anionic PAMs but rather to follow those of nonionic PAMs. Figure 5.4 shows the adsorption isotherms measured in the supporting adsorption experiments with nonionic N300 in 1 mM NaCl, anionic A100H in 1 mM NaCl, and A100H in 3 mM NaCl. Firstly, in 1 mM NaCl solution, the adsorption isotherm curve of A100H increases steeply along 100% adsorption line and forms a plateau. Thus, the adsorption isotherm of A100H in 1 mM NaCl resembles those of highly charged PAMs in 3 mM NaCl. In these cases, the strong electrostatic charge conditions seem to prevent the polydispersity effects of polymeric adsorbates (Parfitt and Rochester, 1983; Fleer *et al.*, 1993). However, with increasing background salt concentrations from 1 mM NaCl to 3 mM NaCl, the adsorption isotherm of A100H was shown to resemble the one of nonionic PAMs, in which the adsorption isotherm curve increases continuously with the known polydispersity effect (see the adsorption isotherm of nonionic N300 in Figure 5.4). This might be caused by lowering electrostatic repulsion with increasing the ionic strength of the solution. Thus, the abnormal behavior of A100H and its resemblance to nonionic PAMs was concluded to be caused by the reduction of the electrostatic repulsion with lowering CD of PAM or increasing ionic strength of the solution (Robb and Smith, 1977; Parfitt and Rochester, 1983; Feast and Munro, 1987; Fleer *et al.*, 1993).

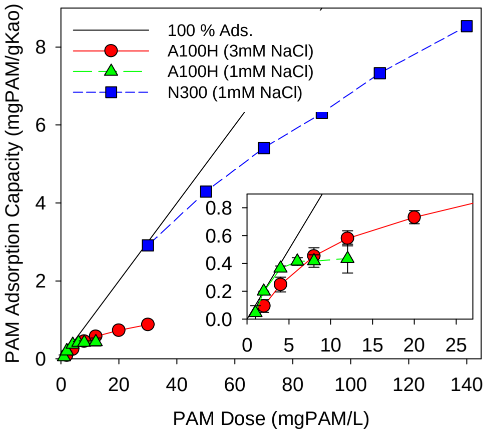

Figure 5.4. Adsorption isotherm curves for different PAM species and solution conditions, A100H in 1 mM NaCl, A100H in 3 mM NaCl, and N300 in 1 mM NaCl.

5.3.2 Effect of Molecular Weight and Charge Density on Adsorption and Flocculation

Figure 5.5 shows the correlations of PAM CD *versus* maximum PAM adsorption capacity and MW *versus* maximum volume-averaged floc diameter. Except A100H, of which abnormal adsorption and flocculation behaviors were shown in the previous discussion, the other PAMs produced reasonable correlations between CD and adsorption capacity as well as MW and floc size. Firstly, with respect to the effect of PAM CD, maximum adsorption capacities were found to be inversely proportional to CDs, especially in presence of divalent ions (see Figure 5.5 (a)). From this observation, we concluded that adsorption capacity is rather governed by the electrostatic property among various physicochemical characteristics. For instance, MWs of different PAMs had been hypothesized to make critical effects on PAM adsorption but eventually turned out to be insignificant within the MW range of the tested PAMs. In Figure 5.5 (a), divalent cations in the solution phase are again proven to increase adsorption capacities several times higher than monovalent ions, because of cationic bridging effects (Lu and Letey, 2002; Mpofu *et al.*, 2003a). Also, the adsorption capacity in presence of Ca^{2+} is shown to be higher than the one of Mg^{2+}, due to the smaller hydrated size and higher accessibility of Ca^{2+} which in turn induce the higher cationic bridging effect (Sabbagh and Delsanti, 2000; Abraham *et al.*, 2001; Lu and Pelton, 2001). Secondly, with respect to the effect of PAM MW, flocculation efficiencies, which are represented by maximum volume-averaged floc diameters, were directly proportional to PAM MWs in presence of either monovalent or divalent cations, again except the unique flocculation behavior of A100H (see Figure 5.5 (b)). Similar to the trend of adsorption capacity, flocculation efficiencies increased much more in presence of divalent cations than those in presence of monovalent cations, by cationic bridging.

Considering the independency of the two separate correlations of adsorption capacity *versus* CD and flocculation efficiency *versus* MW, the higher adsorption capacity does not seem to guarantee the higher flocculation efficiency but sometimes deteriorate flocculation efficiency with steric stabilization. For example, even if both A120 and A120H have similar adsorption capacities because of their similar CDs at about 25%, the floc sizes with application of low-MW A120 are several-order smaller than the floc sizes with high-MW A120H. In polymer-induced bridging flocculation, some parts of adsorbed polymeric chains protrude and make bridges between colloids for flocculation, while the other parts remain flat on clay surfaces (Gregory, 1988; Pelssers *et al.*, 1989; Pelssers *et al.*, 1990; Lu and Pelton, 2001; Santore, 2005). By imagining this conceptual picture of polymer-induced adsorption and flocculation, PAMs with high

MWs (*e.g.* A120H) would have a higher chance to protrude out of the electrostatic repulsion layers as the active conformations for flocculation, while PAMs with low MWs (*e.g.* A120) would be rather retained inside the electrostatic repulsion layer as the flat and inactive conformations. In short, irrespective of PAM CD, PAM with high MWs may be able to form the large amounts of active polymeric segments on kaolinite surfaces and eventually enhance the flocculation efficiency.

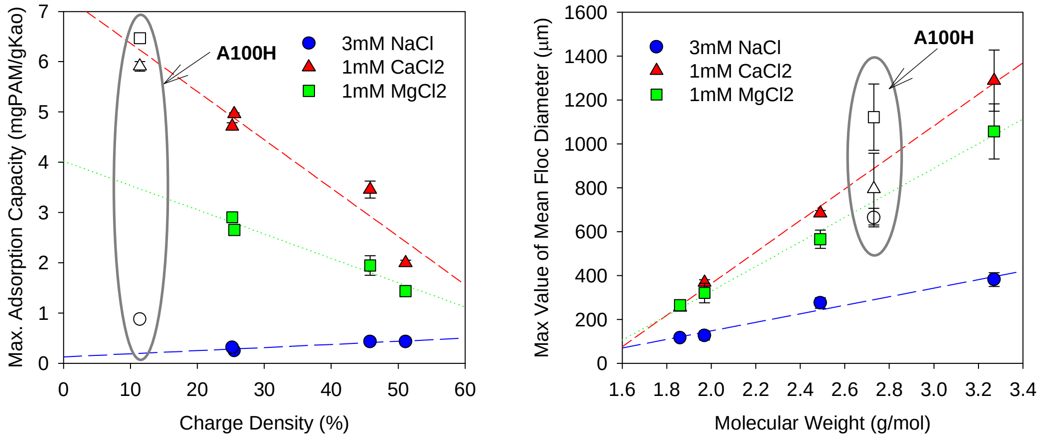

(a) (b)

Figure 5.5. Trend curves of (a) CD *versus* maximum adsorption capacity and (b) MW *versus* maximum volume-averaged floc size for different solution chemistries, 3 mM NaCl, 1 mM $CaCl_2$, and 1 mM $MgCl_2$.

5.3.3 Zeta Potential and Ca^{2+}/Mg^{2+} Adsorption

In Figure 5.2, severe steric restabilization was observed with increasing PAM dose concentrations in presence of divalent ions and was hypothesized to occur due to cationic bridges between adsorbed PAM molecules (PAM^{-}–$^{+}M^{+}$–^{-}PAM) and related conformational changes. With measuring zeta potentials of PAM- and kaolinite-containing suspensions and adsorbed amounts of Ca^{2+} or Mg^{2+} on kaolinite surfaces, we tried to verify the hypothesis for the observed steric stabilization.

Firstly, in presence of monovalent ions *i.e.* without cationic bridging effects, measured zeta potentials for all the PAMs except A100H were constant at about -60 mV, irrespective of PAM dose concentrations (see Figure 5.6). Probably, the unchangeability of the measured zeta potentials with increasing PAM dose concentrations proves the indifference of Na^{+} on kaolinite surfaces or PAM molecules. However, in case of A100H, zeta potential decreased from -60 mV to -40 mV with increasing PAM doses and the generated the clear correlation between zeta potentials and PAM adsorption capacities. In this case, the continuous replacement and adsorption of PAM molecules by the polydispersity effect seem to shield charged sites of kaolinite surfaces and thus decrease zeta potentials with increasing PAM dose concentrations.

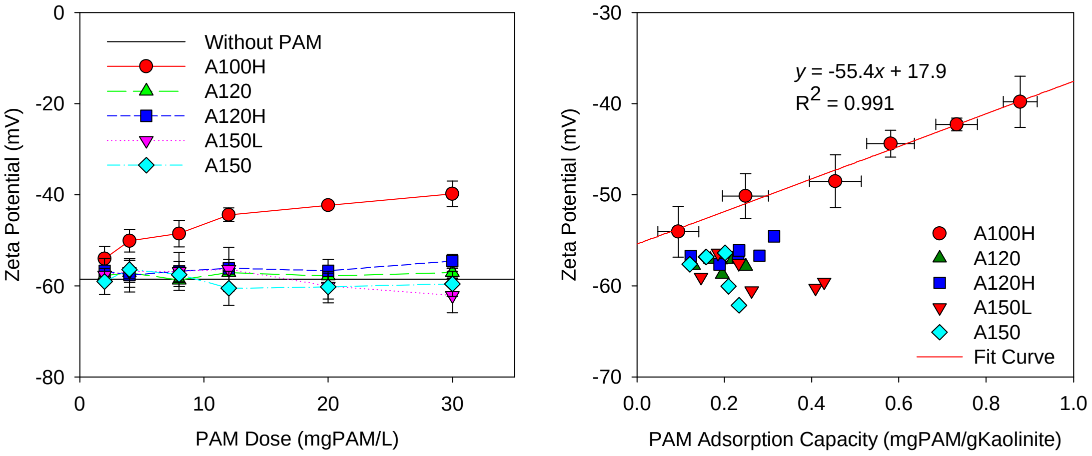

(a) (b)

Figure 5.6. (a) measured zeta potentials with increasing PAM dose concentration and (b) zeta potentials with increasing PAM adsorption capacity for different PAM species in 3 mM NaCl aqueous solution.

Secondly, Figures 5.7 (a) and (c) shows measured zeta potentials and adsorbed amounts of Ca^{2+} or Mg^{2+} on kaolinite surfaces with increasing PAM doses, in presence of divalent ions *i.e.* with cationic bridging effects. In Figures 5.7 (a) and (c), irrespective of PAM dose, zeta potentials were estimated at a constant level about -19 ~ -24 mV, which is roughly one-third of those measured in presence of monovalent ions (see also Figure 5.6). The reduction of zeta potential with divalent ions might be caused by the higher charge and the smaller hydrated radius of divalent cations, which in turn induce the higher affinity and accessibility of divalent cations on kaolinite surfaces. Also, in Figure 5.7 (b) anc (d), Ca^{2+} or Mg^{2+} adsorption capacities were found to increase with increasing PAM adsorption capacities beyond Ca^{2+} or Mg^{2+} adsorption capacities on bare kaolinites. Thus, additionally adsorbed amounts of Ca^{2+} or Mg^{2+} above the amounts on bare kaolinites were proven to be associated with adsorbed PAM molecules on kaolinites and they were estimated up to about 30 % and 25 % out of total adsorbed amounts of Ca^{2+} or Mg^{2+} (including the amounts on bare kaolinite surfaces and on absorbed PAM molecules). However, zeta potentials remained almost constant, irrespective of additional Ca^{2+} or Mg^{2+} amounts on adsorbed PAM molecules. Initially, we had expected that the measured zeta potentials could be reduced by additional positive charges of absorbed divalent cations. However, in contrast to our expectation, additional adsorption of divalent cations on adsorbed PAM molecules was found to make marginal changes of zeta potentials. The additional cationic charges induced by Ca^{2+} or Mg^{2+} in adsorbed PAM matrices might be balanced with the additional anionic charges of adsorbed PAMs and thus the combined charges seem to remain at the constant level, irrespective of PAM doses. By the way, considering the constant zeta potentials, the observed restabilization in presence of divalent ions was proven not to be caused by the electric factors but to be governed by the nonelectric factors, such as conformational alteration and consequent steric stabilization.

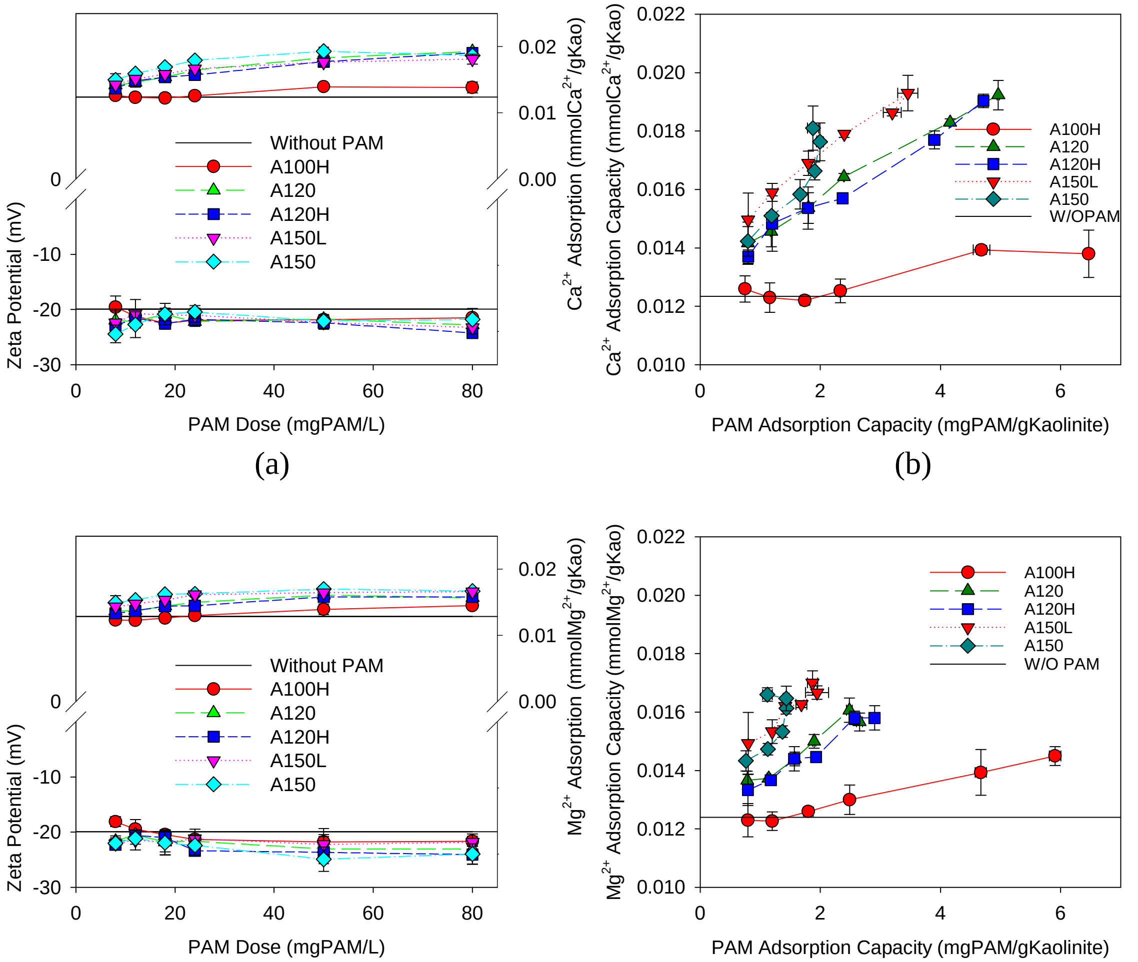

(a) (b)

(c) (d)

Figure 5.7. (a) zeta potential and Ca^{2+} adsorption capacity *versus* PAM dose and (b) Ca^{2+} adsorption capacity *versus* PAM adsorption capacity in 1 mM $CaCl_2$ aqueous solution. (c) zeta potential and Mg^{2+} adsorption capacity *versus* PAM dose and (d) Mg^{2+} adsorption capacity *versus* PAM adsorption capacity in 1 mM $MgCl_2$ aqueous solution

Considering the observed adsorption, flocculation, and electrostatic behaviors, the cationic bridging mechanism seems to occur in a stepwise manner in PAM- and kaolinite-containing suspensions. For example, firstly, divalent ions adsorb immediately on bare kaolinite surfaces and shield or reduce the electrostatic repulsion between similarly charged surfaces. Then, PAM molecules approach and attach easily on the neutralized kaolinite surfaces and eventually enhance flocculation process by cationic bridges between PAM molecules and kaolinite surfaces (PAM^{-}–$^{+}$M^{+}–$^{-}$kaolinite). However, the further association of divalent cations seems not to make the cationic bridges between PAM molecules and kaolinite surfaces (PAM^{-}–$^{+}$M^{+}–$^{-}$kaolinite) but rather to make the bridges between pre-adsorbed PAM molecules (PAM^{-}–$^{+}$M^{+}–$^{-}$PAM), which finally make vulnerable structures of adsorbed PAMs to steric stabilization (see Figure 5.8).

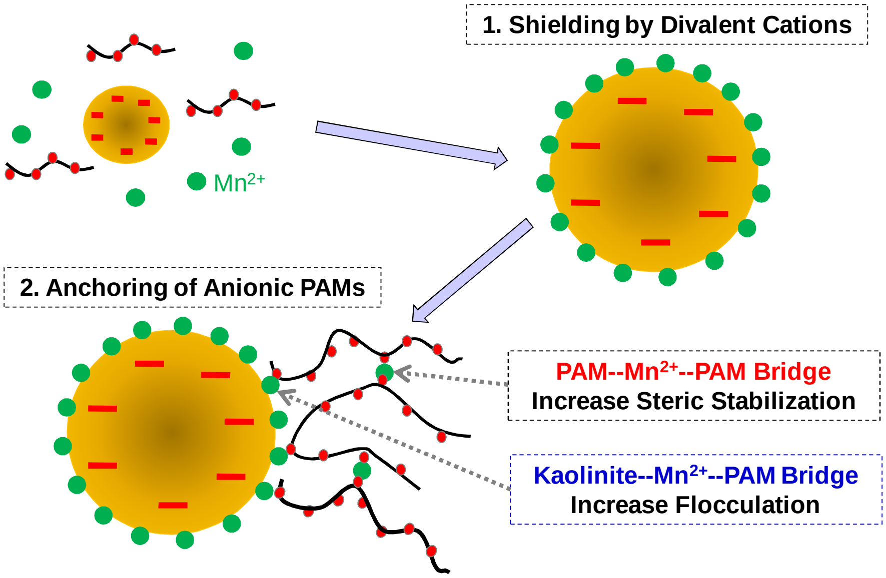

Figure 5.8. Schematic diagram of cationic bridging adsorption and flocculation mechanisms in mixed suspensions of divalent cations, PAM, and kaolinites.

5.4 Conclusion and Recommendation

In the series of adsorption and flocculation tests, interfacial interaction mechanisms, such as polydispersity effect, divalent cationic bridging, polymer-induced bridging flocculation, and steric stabilization, were investigated in similarly charged anionic PAM- and kaolinite-containing suspensions. From the experimental results, three physicochemical characteristics of PAMs and solutions were identified as the key controlling parameters for these interfacial interaction mechanisms and also adsorption and flocculation processes.

Firstly, PAM CD was found to be a key parameter in determining the characteristic behaviors and the capacities of PAM adsorption on kaolinite surfaces. For example, the adsorption behaviors of low-CD anionic PAM were more governed by the polydispersity effects than those of high-CD PAM. In addition to the dependency of the adsorption behaviors on PAM CD, adsorption capacities of PAM on kaolinite surfaces were found to be inversely proportional to PAM CD *i.e.* the lower PAM CD guarantees the higher adsorption capacity. Secondly, PAM MW was critical in determining the flocculation efficiencies in PAM- and kaolinite-containing suspensions. The higher MW of PAM represented the higher flocculation efficiency because they have the higher chance to extend their adsorbed polymer chains out of the electric repulsion layers. Thirdly, the salt species, monovalent or divalent ions, were important in determining both adsorption capacity and flocculation efficiency. In presence of divalent ions, adsorption capacity and flocculation efficiency were enhanced with the well-known cationic bridging effect.

From the findings and theories with respect to these three controlling parameters, we are able to set the guidelines in application of anionic PAMs as soil stabilizer or flocculant. In the future research, the empirical and continuous equations, which are able to quantify in detail the effects of these known decisive factors on adsorption and flocculation, need to be developed for better understanding and application of anionic PAMs.

5.5 Reference

Abraham, T., A.K. Kumpulainen, Z. Xu, M. Rutland, P.M. Claesson, and J. Masliyah, 2001, Polyelectrolyte-mediated interaction between similarly charged surfaced: role of divalent counter ions in tuning surface forces, *Langmuir*, **17**, 8321-8327

Adachi, Y., 1995, Dynamic aspects of coagulation and flocculation, *Advances in Colloid and Interface Science*, **56**, 1-31

Adachi, Y., and T. Wada, 2000, Initial stage dynamics of bridging flocculation of polystyrene latex spheres with polyethylene oxide, *Journal of Colloid and Interface Science*, **229**, 148-154

APHA, 1998, *Standard methods for the examination of water and wastewater, 20th ed.*, American Public Health Association, USA

Barvenik, F. W., 1994, Polyacrylamide characteristics related to soil applications, *Soil Science*, **158**(4), 235-243

Ben-Hur, M., M. Malik, J. Letey, and U. Mingelgrin, 1992, Adsorption of polymers on clays as affected by clay charge and structure, polymer properties, and water quality, *Soil Science*, **153**(5), 349-356

Chapra, S. C., 1997, *Surface quality modeling*, McGraw-Hill,

Claesson, P. M., E. Poptoshev, E. Blomberg, and A. Dedinaite, 2005, Polyelectrolyte-mediated surface interactions, *Advances in Colloid and Interface Science*, **114-115**, 173-187

Das, B. M., 1995, *Principles of geotechnical engineering, 3rd ed*, PWS Publishing Company, Boston, USA

Elimelech, M., X. J. J. Gregory, and R. A. Williams, 1995, *Particle deposition and aggregation: measurement, modelling and simulation,* Butterworth-Heinemann, Woburn, MA, USA

Entry, J. A., R.E. Sojka, M. Watwood, and C. Ross, 2002, Polyacrylamide preparations for protection of water quality threatened by agricultural runoff contaminants, *Environmental Pollution*, **120**, 191-200

Feast, W. J., and H. S. Munro, 1987, *Polymer surfaces and interfaces*, John Wiley & Sons, Chichester, UK

Feng, X., A.J. Simpson, and M. J. Simpson, 2005, Chemical and mineralogical controls on humic acid sorption to clay mineral surfaces, *Organic Geochemistry*, **36**, 1553-1566

Ferretti, R., J. Zhang, and J. Buffle, 1997, Kinetivs of hematite aggregation by polyacrylic acid: effect of polymer molecular weights, *Colloids and Surfaces A: Physicochem. Eng. Aspects*, **121**, 203-215

Fleer, G. J., M.A. Cohen Stuart, J.M.H.M. Scheutjens, T. Cosgrove, and B. Vincent, 1993, *Polymers at interfaces,* Chapman & Hall, London, UK

Francois, J., D. Sarazin, T. Schwartz, and G. Weill, 1979, Polyacrylamide in water: molecular weight dependence of $\langle R^2 \rangle$ and $[\eta]$ and the problem of the excluded volume exponent, *Polymer*, **20**, 969-975

Ganczarczyk, J. J., W. M. Zahid, and D. Li, 1992, Physical stabilization and embedding of microbial aggregates for light microscopy studies, *Water Research*, **26**(12), 1695-1699

Gorczyca B., and J. Ganczarczyk, 1996, Image analysis of alum coagulated mineral suspensions, *Environmental Technology*, **17**, 1361-1369

Green, V. S., D. E. Stott, L. D. Norton, and J. G. Graveel, 2000, Polyacrylamide Molecular Weight and Charge Effects on Infiltration under Simulated Rainfall, *Soil Sci. Soc. Am. J.*, **64**, 1786-1791

Gregory, J., 1988, Polymer adsorption and flocculation in sheared suspensions, *Colloids and Surfaces*, **31**, 231-253

Heller, H., and R. Keren, 2002, Anionic Polyacrylamide Polymers Effect on Rheological Behavior of Sodium-Montmorillonite Suspensions, *Soil Sci. Soc. Am. J.*, **66**, 19-25

Heller, H., and R. Keren, 2003, Anionic polyacrylaide polymer adsorption by pyrophyllite and montmorillonite, *Clays and Clay Minerals*, **51**(3), 334-330

Hurst, V. J., and S. M. Pickering, 1997, Origin and classification of coastal plain kaolins, southeastern USA, and the role of groundwater and microbial action, *Clays and Clay Minerals*, **45**(2), 274-285

Jones, F., J.B. Farrow, and W. v. Bronswijk, 1998, An infrared study of a polyacrylate flocculant adsorbed on hematite, *Langmuir*, **14**, 6512-6517

Lee, B. J., I.A. Luzinov, and M. A. Schlautman, 2008, Investigation on applicability of easy measurement techniques in estimating molecular weights and charge densities of polyacrylamide soil stabilizers or flocculants, In Preparation

Levy, G. J., and W. P. Miller, 1999, Polyacrylamide adsorption and aggregate stability, *Soil & Tillage Research*, **51**, 121-128

Lu, C., and R. Pelton, 2001, PEO Flocculation of polystyrene-core poly(vinylphenol)-shell latex: an example of ideal bridging, *Langmuir*, **17**, 7770-7776

Lu, J. H., and J. Letey, 2002, Effects of soil and water properties on anionic polyacrylamide sorption, *Soil Sci. Soc. Am. J.*, **66**, 578-584

McCollister, D. D., C. L. Hake, S. E. Sadek, and V. K. Rowe, 1965, Toxicologic investigations of polyacrylamides, *Toxicol. Appl. Pharmacol.*, **7**, 639-651

McLaughlin, R. A., and N. Bartholomew, 2007, Soil factors influencing suspended sediment flocculation by polyacrylamide, *Soil Sci. Soc. Am. J.*, **71**, 537-544

Morris, G. E., D. Fornasiero, and J. Ralston, 2002, Polymer depressants at the talc-water interface: adsorption isotherm, microflotation and electrokinetic studies, *Int. J. Miner. Process*, **67**, 211-227

Mpofu, P., J. Addai-Mensah, and J. Ralston, 2003a, Influence of hydrolyzable metal ions on the interfacial chemistry, particle interactions, and dewatering behavior of kaolinite dispersion, *Journal of Colloid and Interface Science*, **261**, 349-359

Mpofu, P., J. Addai-Mensah, and J. Ralston, 2003b, Investigation of the effect of polymer structure type on flocculation, rheology and dewatering behaviour of kaolinite dispersions, *Int. J. Miner. Process*, **71**, 247-268

Mpofu, P., J. Addai-Mensah, and J. Ralston, 2004, Flocculation and dewatering behavior of smectite dispersion effect of polymer structure type, *Mineral Engineering*, **17**, 411-423

Mpofu, P., J. Addai-Mensah, and J. Ralston, 2005, Interfacial chemistry, particle interactions and improved dewatering behavior of smectite clay dispersions, *Int. J. Miner. Process*, **75**, 155-171

Myagchenkov, V. A., and V. F. Kurenkov, 1991, Applications of acrylamide polymers and copolymers: a review, *Polym.-Plast. Technol. Eng.*, **30**(2-3), 109-135

Orts, W. J., A. Roa-Espinosa, R.E. Sojka, G.M. Glenn, S.H. Imam, K. Erlacher, and J. S. Pederson, 2007, Use of synthetic polymers and biopolymers for soil stabilization in agricultural, construction, and military application, *Journal of Materials in Civil Engineering*, **19**(1), 58-66

Parfitt, G. D., and C. H. Rochester, 1983, *Adsorption from solution at the solid/liquid interface*, Academic Press, New York, USA

Pelssers, E. G. M., M.A. Cohen Stuart, and G. J. Fleer, 1989, Kinetic aspects of polymer bridging: equilibrium flocculation and nonequilibrium flocculation, *Colloids and Surfaces*, **38**, 15-25

Pelssers, E. G. M., M.A. Cohen Stuart, and G. J. Fleer, 1990, Kinetics of bridging flocculation, *J. CHEM. SOC. FARADAY TRANS.*, **86**(9), 1355-1361

Robb, I. D., and R. Smith, 1977, Adsorption of polymers at the solid-liquid interface: a comparison of the e.p.r. and i.r. techniques, *Polymer*, **18**, 500-504

Sabah, E., and Z. E. Erkan, 2006, Interaction mechanism of flocculants with coal waste slurry, *Fuel*, **85**, 350-359

Sabbagh, I., and M. Delsanti, 2000, Solubility of highly charged anionic polyelectrolytes in presence of multivalent cations: Specific interaction effect, *Eur. Phys. J. E.*, **1**, 75-86

Sander, S., L.M. Mosley, and K. A. Hunter, 2004, Investigation of interparticle forces in natural waters: effects of adsorbed humic acids on iron oxide and alumina surface properties, *Environ. Sci. Technol.*, **38**, 4791-4796

Santore, M. M., 2005, Dynamics in adsorbed homopolymer layers: understanding complexity from simple starting points, *Current Opinion in Colloid & Interface Science*, **10**, 176-183

Schwarzenbach, R. P., P.M.Gschwend, and D. M. Imboden, 2003, *Environmental organic chemistry, 2nd ed*, Johns Wiley & Sons, Inc., Hoboken, New Jersey.

Seybold, C. A., 1994, Polyacylamide review: soil conditioning and environmental fate, *Commun. Soil Sci. Plant Anal.*, **25**(11-12), 2171-2185

Sperling, L. H., 2006, *Introduction to physical polymer science, 4th Edition*, John Wiley & Sons, Inc., Hoboken, NJ

Stephens, S. H., 1991, Final report on the safety assessment of polyacrylamide, *J. Am. Coll. Toxicol.*, **10**, 193-202

Stumm, W., and J. J. Morgan, 1996, *Aquatic chemistry, 3rd ed*, Johns Wiley & Sons, Inc., Canada.

Sylvia, D. M., J. J. Fuhrmann, P. G. Hartel, and D. A. Zuberer, 2003, *Principles and applications of soil microbiology, 2nd ed*. Pearson Education Inc., NJ, USA

Torn, L. H., A. de Keizer, L.K. Koopal, and J. Lyklema, 2003, Mixed adsorption of poly(vinylpyrrolidone) and sodium dodecylbenzenesulfonate on kaolinte, *Journal of Colloid and Interface Science*, **260**, 1-8

Vermohlen, K., H. Lewandowski, H. D. Narres, and M. J. Schwuger, 2000, Adsorption of polyelectrolytes onto oxide - the influence of ionic strength, molar mass, and Ca^{2+} ions, *Colloids and Surfaces A: Physicochem. Eng. Aspects*, **163**, 45-53

Wallace, A., and G. A. Wallace, 1986, Effects of soil conditioners on emergence and growth of tomato, cotton, and lettuce seedlings, *Soil Science*, **141**, 313-316

Wu, X. Y., D. Hunkeler, A.E. Hamielec, R.H. Pelton, and D. R. Woods, 1991, Molecular weight characterization of poly(acrylamide-co-sodium acrylate). I. Viscometry, *Journal of Applied Polymer Science*, **42**, 2081-2093

Zahid, W. M., and J. J. Ganczarczyk, 1990, Suspended solids in biological filter effluents, *Water Research*, **24**(2), 215-220

Zhang, J., and J. Buffle, 1995, Kinetics of hematite aggragation by polyacrylic acid: Importance of charge neutralization, *Journal of Colloid and Interface Science*, **174**, 500-509

CHAPTER 6. SIMULATION OF TURBULENT FLOCCULATION AND SEDIMENTATION IN FLOCCULANT-AIDED SEDIMENT RETENTION PONDS

6.0 Abstract

A model combining Multi-dimensional Discretized Population Balance Equations with a Computational Fluid Dynamics simulation (CFD-DPBE model) was developed and applied to simulate turbulent flocculation and sedimentation processes in sediment retention basins. Computation fluid dynamics and the discretized population balance equations were solved to generate steady state flow field data and to simulate flocculation and sedimentation processes in a sequential manner. Up-to-date numerical algorithms such as operator splitting and Leveque's flux-corrected upwind schemes were applied to cope with the computational demands caused by complexity and nonlinearity of the population balance equations and the instability caused by advection-dominated transport. In a modeling and simulation study with a 2-dimensional simplified pond system, the applicability of the CFD-DPBE model was demonstrated by tracking mass balances and floc size evolutions and by examining particle/floc size and solid concentration distributions. Thus, the CFD-DPBE model may be used as a valuable simulation tool for natural and engineered flocculation and sedimentation systems as well as flocculant-aided sediment retention ponds.

6.1 Introduction

In recent years, various Best Management Practices (BMPs) have been developed that relate to the control of sediments during storm events (USDOT, 2002; EERC, 2003). Among these BMPs, several suggest that removal of clay and other colloidal-sized particles by retention or detention ponds may be enhanced by the addition of flocculating agents. A few operators are now experimenting with the addition of such agents to sediment inflow, which can greatly improve the retention properties of the ponds in some cases. Reading contemporary literature and talking to sediment pond operators supports the conclusion that flocculant-aided sediment retention ponds are going to become increasingly important in future years as a means to minimize the detrimental effects of erosion and non-point-source water pollution (Gowdy and Iwinski, 2007; Harper, 2007; Kang *et al.*, 2007; Sojka *et al.*, 2007). To date, use has been driven more by practicing engineers than by academics. However, the operation of such ponds is complicated, involving turbulent flow of variable intensity, different pond geometries, particle growth due to flocculation, sedimentation of particle size classes at different rates and various schemes for time-dependent flocculant additions. Most existing pond systems are not designed in a consistent manner based on fundamental principles. For example, many designs are based simply on an *ad hoc* rule such as a set pond volume per hectare of drained area (Akan and Houghtalen, 2003). So the entire field would benefit from a better understanding of the flocculation and sedimentation processes and the availability of a realistic, physically-based model for designing and optimizing the automated operation of sediment retention ponds. What is needed is a realistic theory describing flocculation and non-homogeneous turbulent sedimentation in retention ponds, a practical method for solving the rather complex governing equations and the performance of the required small-scale and large-scale experiments necessary to characterize the parameters and functions that the theory contains. This paper deals primarily with the mathematical formulation and computation underlying flocculation and sedimentation processes in flocculant-aided sediment retention ponds.

One of the most realistic ways to simulate flocculation and non-homogeneous turbulent sedimentation in retention ponds is by applying Population Balance Equations (PBE) within a Computational Fluid Dynamics (CFD) framework for solving the Navier-Stokes equations (mass and momentum conservation equations). Population balance equations have been used to simulate particle/floc aggregation phenomena for many scientific and engineering applications. Most PBEs derive from the famous Smoluchowski equation describing a simple particle/floc aggregation process. They are now generalized by incorporating various additional processes such as particle/floc breakage models, shaping and growth strategies, chemical interaction models and more (Smoluchowski, 1917; Lawler and Wilkes, 1984; Hounslow *et al.*, 1988; Spicer and Pratsinis, 1996a; Spicer and Pratsinis, 1996b; McGraw, 1997; Lee *et al.*, 2000; Somasundaran and Runkana, 2003; Marchisio *et al.*, 2003a; Rahmani *et al.*, 2004; Ding *et al.*, 2006; Prat and Ducoste, 2006; Runkana *et al.*, 2006). The application of PBEs, ranging from fundamental scientific research to advanced engineering applications, has become more practical as computational speed and capacity has increased. However, such applications are still at the forefront of engineering research.

In multi-dimensional simulation, such as simulation of retention pond dynamics, conventional PBEs are still computationally demanding even with modern computer technologies. For example, in conventional PBEs, particles/flocs are aggregating in a sequential manner from singlet to doublet, then to triplet, and so on. Thus, conventional PBEs require thousands to millions of particle/floc size classes and associated differential transport-reaction equations to simulate the particle/floc growth from nano- or micro-sized constituent monomers to milli-sized aggregates that settle due to gravity. To overcome this computational difficulty in multi-dimensional simulations, the discretized PBE (DPBE) and the Quadrature Method of Moments (QMOM) have been proposed.

In the QMOM approach, moments of the particle/floc size distribution instead of the number concentrations of particles/flocs are used as dependent variables in differential transport-reaction equations, in order to reduce computational overloads occurring in multi-dimensional applications. The lower-order moments then yield the key monitoring indices such as particle/floc sizes and solid concentrations indirectly through the use of Product-Difference (PD) algorithms (McGraw, 1997; Fox, 2003; Marchisio *et al.*, 2003a; Marchisio *et al.*, 2003b; Wang *et al.*, 2005; Prat and Ducoste, 2006). Thus, QMOM provides computational advantages but imposes difficulties for scientists or engineers to understand results due to the more abstract formulation and resulting algorithms.

In DPBE methodology, the particle/floc number concentrations can be tracked as dependent variables in differential transport-reaction equations, similar to conventional PBEs. However, the DPBE formulation differs from conventional PBEs because particles/flocs of DBPE are assumed to double their sizes from singlet to doublet and then to quadruplet, *etc.*, in a flocculation process. Thus, with only dozens of defined particle/floc size classes, particles/flocs can grow to sizes susceptible to gravity-induced settling, which are thousands to millions of times larger than the size of monomers (Hounslow *et al.*, 1988; Kumar and Ramkrishna, 1996; Ramkrishna and Mahoney, 2002; Marchisio *et al.*, 2003a). Contrast to QMOM, the DPBE tracks directly the key indices, such as particle/floc sizes and solid concentrations, simply by integration of differential equations without additional data processing steps. Thus, viewed with respect to clearness of results, the DPBE approach may be more intuitive and advantageous than QMOM. Therefore, in this research the discretized particle transport-reaction model combined with a fluid dynamics model (CFD-DPBE model) was set up, and its applicability was tested in a model pond system. The mathematical formulation and application strategy of the CFD-DPBE model were studied in a 2-dimension computational domain representing the vertical and flow-parallel cross-section of a flocculant-aided sediment retention pond.

6.2 Background and Mathematical Models

The CFD-DPBE model consists of (1) CFD software to obtain the Reynolds-averaged turbulent flow field, and (2) multi-dimensional DPBE software, containing particle/floc aggregation and break-up kinetics, to simulate transport, flocculation and sedimentation within the pre-obtained flow field.

6.2.1 Computational Fluid Dynamics (CFD)

The Reynolds-Averaged continuity and Navier-Stokes (RANS) equations, containing a two-equation $k-\varepsilon$ turbulence model, were solved using FLOW3D software to simulate turbulent fluid motion within a retention pond. In the CFD-DPBE model, particles/flocs are assumed to travel *via* fluid motion and to aggregate or disintegrate due to impact and shear forces or effects (White, 1991; Fox, 2003; Prat and Ducoste, 2006).

The RANS equations consist of mass and momentum conservation equations in a differential form given by Equations (6.1) and (6.2), respectively. (We now use the summation convention in writing the 3-D equations, wherein sums over the 3 spatial coordinates are understood when an index is repeated.)

$$\frac{\partial \langle U_i \rangle}{\partial x_i} = 0 \qquad (6.1)$$

$$\frac{\partial \langle U_i \rangle}{\partial t} + \langle U_j \rangle \frac{\partial \langle U_i \rangle}{\partial x_j} + \frac{\partial \langle u_j u_i \rangle}{\partial x_j} = -\frac{1}{\rho}\frac{\partial \langle p \rangle}{\partial x_i} + \nu \nabla^2 \langle U_i \rangle \qquad (6.2)$$

$$\langle u_i u_j \rangle = \frac{2}{3} k \delta_{ij} - \nu_T \left(\frac{\partial \langle U_i \rangle}{\partial x_j} + \frac{\partial \langle U_i \rangle}{\partial x_i} \right) \qquad (6.3)$$

$$\nu_T = C_\mu \frac{k^2}{\varepsilon} \qquad (6.4)$$

In Equations (6.1) and (6.2), i and j are indices, x_i represents coordinate directions ($i = 1$ to 3 for x, y, z directions, respectively), $\langle U_i \rangle$ is the time averaged velocity component (m/s), t represents time (s), ρ is the fluid density (kg/m^3), p is the piezometric pressure (kg/m/s^2), and ν is the kinematic viscosity of the fluid (m^2/s). A symmetric second-order tensor $\langle u_i u_j \rangle$ represents Reynolds normal or shear stresses (m^2/s^2) and is modeled with Equation (6.3), ν_T, the turbulent viscosity (N·s/m^2) is specified by Equation (6.4). In Equations (6.3) and (6.4), δ_{ij} is Kroneker's delta, C_μ is 0.09, a model constant, k represents turbulent kinetic energy (m^2/s^2) and ε is the turbulent energy dissipation rate (m^2/s^3). These two energy terms are obtained from Equations (6.5) and (6.6), which together represent the so-called k-ε turbulence model. They are solved simultaneously with the RANS equations. The velocity gradient ($G=\sqrt{\varepsilon/\nu}$, /s), which is obtained from the two-equation $k-\varepsilon$ turbulence model, causes particle/floc aggregation or break-up kinetics in the DPBE and thus serves as a coupling term between the turbulent flow field (CDF problem) and the DPBE (Prat and Ducoste, 2006). In Equations (6.5) and (6.6), model fitting constants have been found as $\sigma_k = 1.0$, $\sigma_\varepsilon = 1.3$, $C_{\varepsilon 1} = 1.44$, and $C_{\varepsilon 2} = 1.92$ (Fox, 2003). **P** is the turbulent kinetic energy production term (m^2/s^3) specified by Equation (6.7).

$$\frac{\partial k}{\partial t} + \langle U \rangle \cdot \nabla k = \nabla \cdot \left(\frac{\nu_T}{\sigma_k} \right) + P - \varepsilon \qquad (6.5)$$

$$\frac{\partial \varepsilon}{\partial t} + \langle U \rangle \cdot \nabla \varepsilon = \nabla \cdot \left(\frac{\nu_T}{\sigma_e} \nabla \varepsilon \right) + \frac{\varepsilon}{k}\left(C_{\varepsilon 1}\mathbf{P} - C_{\varepsilon 2}\varepsilon \right) \qquad (6.6)$$

$$\mathbf{P} \equiv -\langle u_i u_j \rangle \frac{\partial \langle U_i \rangle}{\partial x_j} \tag{6.7}$$

6.2.2 Multi-dimensional Discretized Population Balance Equations (DPBE)

With a given flow field obtained from CFD software, the multi-dimensional DPBE is used to simulate particle/floc transport and flocculation in the ponds. Following Prat and Ducoste (2006), a generic mathematical model for the DPBE may be written as:

$$\begin{aligned}
&\left[\frac{\partial n_i}{\partial t}\right] && \text{(I)}\\
&+\left[\frac{\partial}{\partial x}(\langle U_x\rangle n_i)+\frac{\partial}{\partial y}(\langle U_y\rangle n_i)+\frac{\partial}{\partial z}(\langle U_z\rangle n_i)\right] && \text{(II)}\\
&-\left[\frac{\partial}{\partial x}\left(C_\mu\frac{k^2}{\varepsilon}\frac{\partial n_i}{\partial x}\right)+\frac{\partial}{\partial y}\left(C_\mu\frac{k^2}{\varepsilon}\frac{\partial n_i}{\partial y}\right)+\frac{\partial}{\partial z}\left(C_\mu\frac{k^2}{\varepsilon}\frac{\partial n_i}{\partial z}\right)\right] && \text{(III)}\\
&=(agg/break)_i - u_{gi}\frac{\partial n_i}{\partial z} && \text{(IV)}
\end{aligned} \tag{6.8}$$

In Equation (6.8), $n_i = n(x, y, z, D_i, t)$ = number concentration of flocs (/m^3) of linear class size D_i (m) ($i=1, 2, \ldots i_{max}$; $D_1 \leq D_i \leq D_{max}$; for all D_i, n_i is called the population density function), x, y, z, t = position and time, $\langle U_x \rangle$, $\langle U_y \rangle$, and $\langle U_z \rangle$ = mean fluid velocity components in the x, y and z directions (m/s), ρ = fluid density (kg/m^3), $k = k(x,y,z,t)$ = turbulent kinetic energy (m^2/s^2), $\varepsilon = \varepsilon(x,y,z,t)$ = turbulent energy dissipation rate (m^2/s^3), C_μ = 0.09 = standard value of a CFD model constant (see Equation (6.4)), and u_{gi} = settlement velocity (m/s) of the i-th floc class due to gravity.

On the left-hand side of Equation (6.8), the respective terms in brackets represent the storage change (I), particle/floc mean advection (II), and the turbulent dispersion of the particle/floc (III), while on the right-hand side, the source/sink terms (IV) represent the net effects of aggregation, breakup and settling due to gravity (Prat and Ducoste, 2006). The coefficients or functions in these later terms are largely empirical and must be determined by experiment. The quantities depending on turbulent fluid variables ($\langle U_x \rangle, \langle U_y \rangle, \langle U_z \rangle, k,$ and ε) couple the DPBE equations (Equations (6.8)) to the CFD equations (Equations (6.1) ~ (6.7)). However, as currently formulated the CDF equations are solved independent of the DPBE.

To track particle/floc fates with the DPBE, both Eulerian and Lagrangian tracking methods are applicable. However, in this research the Eulerian method was applied to observe the distribution of scalars within the entire computational domain rather than the Lagrangian method which tracks individual particles or flocs. (Eulerian: (Heath and Koh, 2003; Marchisio *et al.*, 2003a; Marchisio *et al.*, 2003b; Wang *et al.*, 2005; Lian *et al.*, 2006; Prat and Ducoste, 2006) and Lagrangian: (Schwarzer *et al.*, 2006)

To obtain the particle/floc settling velocity in Equation (6.8), Stoke's equation was used in the context of fractal theory, which represents the structural characteristics of aggregating particles/flocs. Even though many complex and elaborate particle/floc settling equations have been developed, including those involving interaction or drag coefficients with ambient flow, the standard Stoke's equation was applied as a prototype in this research (Stokes, 1880; Brown and Lawler, 2003). Fractal theory describes particle/floc packing or growth structure with constituent monomers in which particle/floc size follows a power law function with respect to the number of monomers in a given floc size (Equation (6.10)) (Jiang and Logan, 1991; Johnson *et al.*, 1996; Spicer *et al.*, 1998; Flesch *et al.*, 1999; Chakraborti *et al.*, 2000; Chakraborti *et al.*, 2003). Stoke's equation combined with fractal theory is given by Equation (6.9) (Adachi and Tanaka, 1997; Lee *et al.*, 2000; Miyahara *et al.*, 2002; Sterling *et al.*, 2005). In Equations (6.9) and (6.10), D_i represents floc diameter of size class i (m), D_0 is monomer diameter (m), D_f is fractal dimension, k is lacunarity (generally set as 1, which implies no lacunarity), ρ_s is particle density (kg/m^3), ρ_w is fluid density (kg/m^3), g is gravitational acceleration (9.81 m/s^2), and η is fluid viscosity (kg/m/s). In Equation (6.10), 2^{i-1} represents the number of monomers forming an i-th particle/floc by following the discretized size classification strategy of the DPBE, which will be described in the following section.

$$u_{gi}=\frac{g}{18\eta}\left(\rho_s-\rho_w\right)D_0^{3-D_f}D_i^{D_f-1} \tag{6.9}$$

$$D_i=D_0\left(\frac{2^{i-1}}{k}\right)^{1/D_f} \tag{6.10}$$

6.2.3 Kinetics of Particle/Floc Aggregation and Breakage

The core part of a multi-dimensional DPBE (Equation (6.8)) is the sink and source terms which characterize the aggregation and break-up kinetics ($(agg/break)_i$). These terms are written as a series of differential equations in Equation (6.11). The particle/floc number concentration in a certain discrete size range (n_i) is used as a dependent variable of a partial differential equation. Following the discretization scheme of the DPBE, each mean particle size class contains two times the number of constituent monomers in the previous smaller class. Thus if "δ" is the beginning (irreducible) particle size, class 1 would contain particles of size "δ" , class 2 would contain particles of size "2δ", class 3 would contain sizes "3δ" and "4δ", class 4 would contain "5δ" through "8δ", class 5 would contain "9δ" through "16δ", and so on. Since the maximum particle size in class "*i*" increases as $2^{(i-2)}$, 30 classes will contain particles sizes varying from "δ" to "2^{28}δ", which represents a growth factor of more than 268 million. Ignoring transport and settling for notational convenience, the partial differential equations with discrete particle/floc size sets may be written as:

$$
\begin{aligned}
\frac{\partial n_i}{\partial t} = \left(agg/break\right)_i = {} & \underbrace{n_{i-1}\sum_{j=1}^{i-2} 2^{j-i+1}\alpha(i-1,j)\beta(i-1,j)n_j}_{(I)} + \underbrace{\frac{1}{2}\alpha(i-1,i-1)\beta(i-1,i-1)n_{i-1}^2}_{(II)} \\
& \underbrace{-\,n_i\sum_{j=1}^{i-1} 2^{j-i}\alpha(i,j)\beta(i,j)n_j}_{(III)} \underbrace{-\,n_i\sum_{j=i}^{(max\ i)}\alpha(i,j)\beta(i,j)n_j}_{(IV)} \underbrace{-\,a(i)n_i}_{(V)} + \underbrace{\sum_{j=i+1}^{(max\ i)+2} b(i,j)a(j)n_j}_{(VI)}
\end{aligned}
\qquad (6.11)
$$

In Equation (6.11), the processes indicated by the various Roman numerals are (I) *i*-sized particle/floc generation by collision with other smaller particle/floc classes, (II) generation by collision within the *i-1* class, (III) disappearance by collision with smaller classes, (IV) disappearance by collision with equal or larger classes, (V) disappearance by fragmentation of the *i* class, and (VI) generation by fragmentation of larger classes. These mechanisms are illustrated in Figure 6.1.

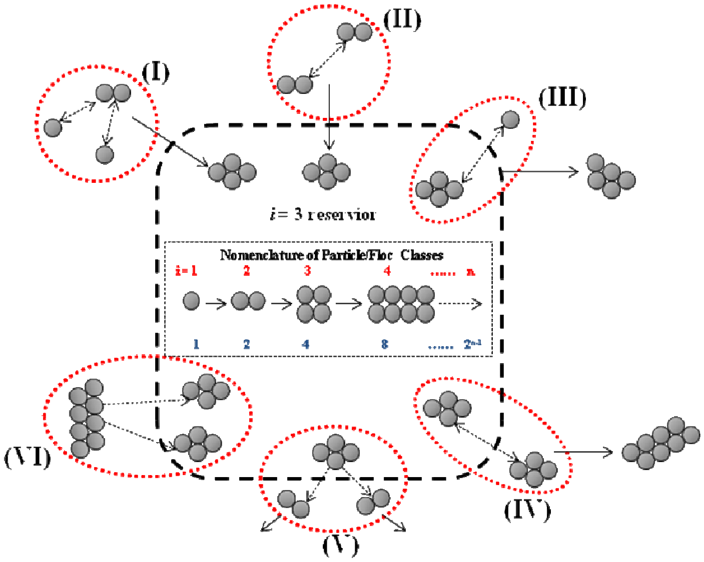

Figure 6.1. Diagram of aggregation and break-up processes for the *i* = 3 particle/floc size class in the DPBE.

Several empirical or theoretical factors or functions (α, β, *a*, and *b*) are incorporated into the aggregation and break-up kinetics. The collision efficiency factor (α) represents the physicochemical properties of solid and liquid to cause inter-particle attachments (aggregation), while the collision frequency factor (β) represents the mechanical properties of fluids to induce inter-particle collisions. In experimental and modeling applications, the collision efficiency factor (α) is generally used as an application-specific fitting parameter and the collision frequency factor (β) is generally applied as a fixed theoretical function correlated with shear rate ($\beta(i,j)=\left(G/6\right)\cdot\left(D_i+D_j\right)^3$) (Spicer and Pratsinis, 1996a). Based on experiments, Ding *et* *al.* (2006) recently modified these collision efficiency and frequency factors by incorporating the concept of the critical size (D_c) which subdivides two different aggregation kinetic regions which are the fast and slow aggregation regions with respect to particle/floc sizes. In our preliminary modeling and simulation study, the application of the critical size concept was found to prevent particle/floc overgrowth beyond the highest particle/floc size and consequently to minimize unexpected mass losses caused by mass escaping out of the defined size range. Thus, in this research, Ding's critical size (D_c) was used as a limiter to prevent unrealistic particle/floc overgrowth in aggregation and break-up kinetics. Equations (6.12) and (6.13) represent collision efficiency and frequency functions, respectively. D_i is the diameter of the *i*-th class particle/floc and D_c is the critical diameter at which 50% of the collisions are successful in forming aggregates (Ding *et al.*, 2006).

$$\alpha(i,j)=\frac{1}{1+\left(\left(D_i+D_j\right)/\left(2D_c\right)\right)^3} \tag{6.12}$$

$$\begin{aligned} \beta(i,j)&=\frac{1}{6}\left(\frac{\varepsilon}{\nu}\right)^{1/2}\left(D_i+D_j\right)^3 \qquad if\ \ D_i,D_j\le D_c \\ \beta(i,j)&=\frac{1}{6}\left(\frac{\varepsilon}{\nu}\right)^{1/2} 8\left(D_c\right)^3 \qquad if\ \ D_i,D_j\ge D_c \end{aligned} \tag{6.13}$$

With respect to particle/floc breakage kinetics, the size-dependent kinetic function shown in Equation (6.14) has been commonly applied in previous studies (Parker DS *et al.*, 1972; Spicer and Pratsinis, 1996a; Flesch *et al.*, 1999; Ding *et al.*, 2006). To simulate the fate of the broken fragments, among various break-up distribution functions, the binary break-up distribution function was applied in our pond simulations due to its simplicity and robustness in computation. In the discretized PBE scheme, the binary break-up distribution function becomes 2, because one parent particle/floc is assumed to produce two equally sized daughter fragments in the break-up process (Equation (6.15)) (Flesch *et al.*, 1999; Ding *et al.*, 2006). In Equations (6.14) and (6.15), a_0 is the selection rate constant, and V_i is volume of the *i*–th class particle/floc size.

$$a(i)=a_0 V_i^{1/3} \tag{6.14}$$

$$b(i,i\text{-}1)=\frac{V_i}{V_{i-1}}=2 \tag{6.15}$$

6.3 Numerical Simulation

At the first step of the CFD-DPBE simulation procedure, the commercial CFD code (FLOW-3D®) was used to generate a steady state flow field in the model pond. Among various model options built into FLOW-3D®, RANS and the two equation k- ε turbulence models were selected to simulate flow velocities and turbulence. This resulted in nodal values for ($\langle Ux\rangle, \langle Uy\rangle, \langle Uz\rangle, k,$ and ε) (Equations (6.1) ~(6.7)). Three different flow conditions that represent low, moderate, and high turbulent conditions were simulated with FLOW-3D®, and thus data resulting from three steady state flow fields were obtained and saved for the following multi-dimensional DPBE simulation.

After the CFD simulation, the multi-dimensional DPBE was solved with an in-house program based on the finite-difference method and codified with MATLAB®. In these simulations, two significant numerical obstacles were identified and overcome in our preliminary research. Firstly, the complexity and nonlinearity of a large number of coupled partial differential (DBPE) equations in an advection-dominated application resulted in a computational overload. To increase computational efficiency, we applied an operator splitting algorithm, in which particle/floc advection was split from particle/floc dispersion-reaction (Table 6.1) (Langseth *et al.*, 1996; Aro *et al.*, 1999; Badrot-Nico *et al.*, 2007). Thus, the advection terms and the dispersion-reaction terms were applied sequentially at each time step. Secondly, a standard central-differencing Finite Difference Method (FDM) was not optimal for simulating advection-dominated flow conditions with high Peclet numbers. Previous studies have shown that upwind-differencing methods produce much improved results for a given node separation (Durran, 1998; Rogers and Kwak, 1998; Alhumaizi, 2004; Timin and Esmail, 2005). Among various upwind-differencing schemes, Leveque's flux-corrected upwind algorithm was applied to solve scalar transport equations in advection-dominaned conditions (Leveque, 1996; Durran, 1998). In this algorithm, particle/floc concentration (n_i) of a computational cell was updated at each time step with the inflow and outflow, which are determined by velocities through cell interfaces and concentrations of neighbor computational cells at each time step. Outlined in Table 6.1 is the numerical scheme used to solve the multi-dimension DPBE with operator splitting and flux-corrected upwind algorithms. At each time step, particle/floc advection equations were solved with

Leveque's flux-corrected upwind scheme and stepwise particle/floc dispersion-reaction equations were calculated implicitly with the Gauss-Siedel iterative method.

Table 6.1. The simplified numerical algorithm for solving the CFD-DPBE model.

- **INITIALIZATION**
  - Supporting data (flow field data from CFD, solid and liquid properties)
  - Computational system layout (Dimensions, Mesh)
- **DPBE CALCULATION (Operator Splitting Algorithm)**

↓

Leveque's flux-corrected upwind scheme (Advection)

$$\frac{\partial n_i}{\partial t}+\frac{\partial}{\partial x}\left(\left\langle U_x\right\rangle n_i\right)+\frac{\partial}{\partial y}\left(\left\langle U_y\right\rangle n_i\right)+\frac{\partial}{\partial z}\left(\left\langle U_z\right\rangle n_i\right)+u_{gi}\frac{\partial n_i}{\partial z}=0$$

t+Δt

FDM calculated with Gauss-Siedel iteration (Dispersion and Reaction)

$$\frac{\partial n_i}{\partial t}-\frac{\partial}{\partial x}\left(C_\mu\frac{k^2}{\varepsilon}\frac{\partial n_i}{\partial x}\right)+\frac{\partial}{\partial y}\left(C_\mu\frac{k^2}{\varepsilon}\frac{\partial n_i}{\partial y}\right)+\frac{\partial}{\partial z}\left(C_\mu\frac{k^2}{\varepsilon}\frac{\partial n_i}{\partial z}\right)-(agg/break)_i=0$$

↑

- **POST PROCESSING**
  - Mass balance, Particle/floc diameters, Solid concentrations, etc.

Shown in Figure 6.2 are schematic diagrams of a flocculant-aided sediment retention pond which consists of a turbulent mixing zone at the inlet and a subsequent sedimentation basin. This turbulent mixing zone may function as an effective flocculation basin with high fluid turbulence. Chemical flocculant is assumed to be injected at the inlet of the pond, so particles/flocs will start aggregating immediately after entering the basin.

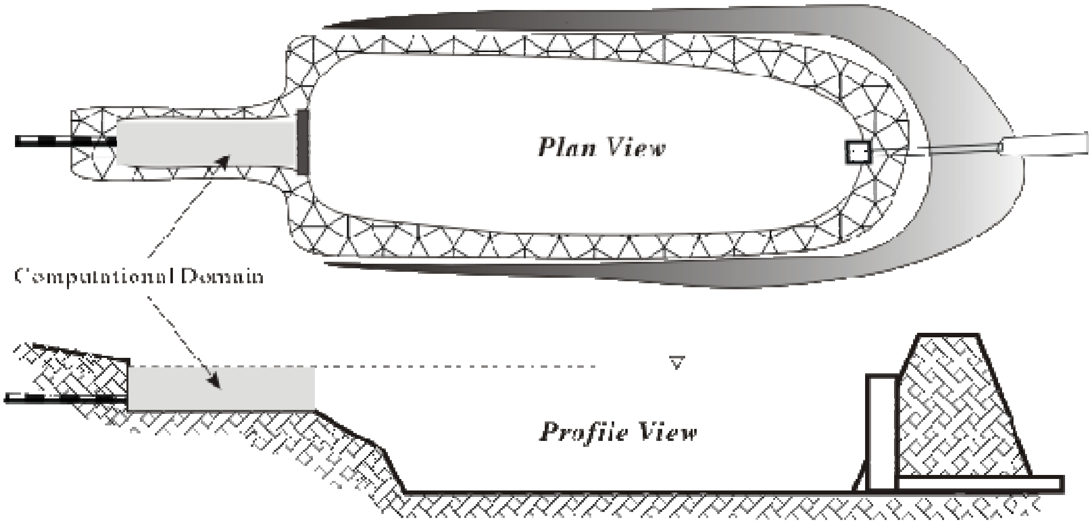

Figure 6.2. Schematic diagram of a flocculant-aided sediment retention pond with a turbulent mixing zone, sedimentation basin and discharge drain.

Figure 6.3 shows the 2-dimensional computational domain representing a simplified turbulent mixing zone with dimensions of 2 m (height) × 10 m (length). The size of each computational cell was set as 0.2 m × 0.2 m. Both inlet and outlet were treated as continuous boundaries ($Flux_{in} = Flux_{out}$), while the water surface was treated as a closed boundary ($Flux_{out} = 0$). The bottom layer of the mixing zone was set as a closed boundary for fluid but an open boundary for settling particles/flocs. In other words, for simplication of the model pond system, settling particle/floc was allowed to move through the bottom layer of the zone, thereby leaving the domain, while fluid remained in the computational domain. Volumetric influent flow rate was set initially at a fixed value of 8 m^3/m/min, which is equivalent to 2.5 minutes of mean hydraulic residence time ($t_{mean} = Volume / FlowRate$) within the model mixing zone. However, to create different levels of fluid turbulence, and to compare the effects of turbulent intensity on flocculation efficiency, influent flow velocities were set at three different values (0.222, 0.334, and 0.667 m/s) by adjusting inlet width. Influent clay particles (monomers) were assumed as spheres with 1 μm diameter and 2.65 g/L density. Influent solid concentration was set as 2 g/L, which is equivalent to a particle number concentration of 1.47×10^{15} /m^3.

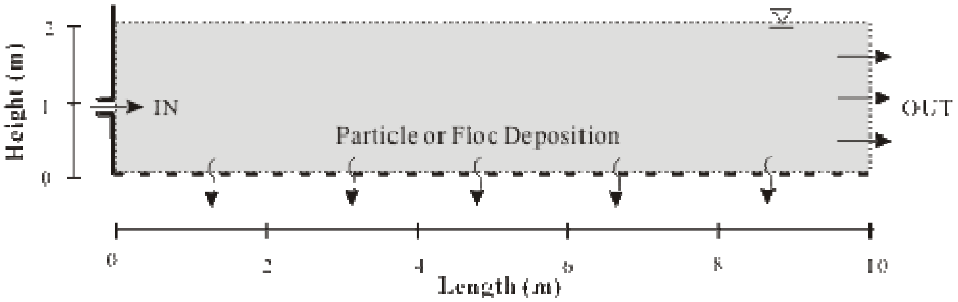

Figure 6.3. Schematic diagram of the computational domain representing a simplified turbulent mixing zone in a sediment retention pond.

In a CFD-DPBE simulation, three empirical model constants (D_f, D_c, and a_0) were used for aggregation and break-up kinetics. The fractal dimension (D_f) was selected as 2.5, which is an intermediate value in the data set obtained from previous studies (Adachi and Tanaka, 1997; Bushell *et al.*, 2001; Turchiuli and Fargues, 2004; Sterling *et al.*, 2005). A critical diameter (D_c) and breakage kinetic constant (a_0) were rather arbitrarily chosen as 100 μm and 10/s following Ding's recent flocculation theory (Ding *et al.*, 2006). However, these constants are previous site-specific values, so it is recommended ultimately that more applicable constants be measured with settling and kinetic experiments appropriate for retention pond applications.

6.4 Results and Discussion

In CFD simulation with the commercial FLOW-3D® code, three steady state flow fields were obtained for the model mixing zone. These flow fields are shown in Figure 6.4, with (a) Case 1: low, (b) Case 2: moderate, and (c) Case 3: high turbulence conditions, which were induced by the different influent flow velocities of 0.222, 0.334, and 0.667 m/min. Arrows and contours in Figure 6.4 represent mean flow velocity vectors ($\langle U \rangle$) and shear rate distributions ($G = (\varepsilon / \nu)^{1/2}$), respectively. In the low turbulence condition (Case 1), velocity vectors were uniformly directed from the inlet to the outlet and shear rates were limited by a low level with a maximum shear rate of 13.5 /s (Figure 6.4(a)). However, in the high turbulence condition (Case 3), a swirling zone above the inlet was identified and high shear rates near the inlet were observed with a maximum shear rate of 79.3 /s (Figure 6.4(c)). Moderate turbulent flow conditions (Case 2) showed flow characteristics between the two extreme cases (Figure 6.4(b)). Later in this paper, we will illustrate the theoretical effects of velocity and shear rate distributions on flocculation efficiencies.

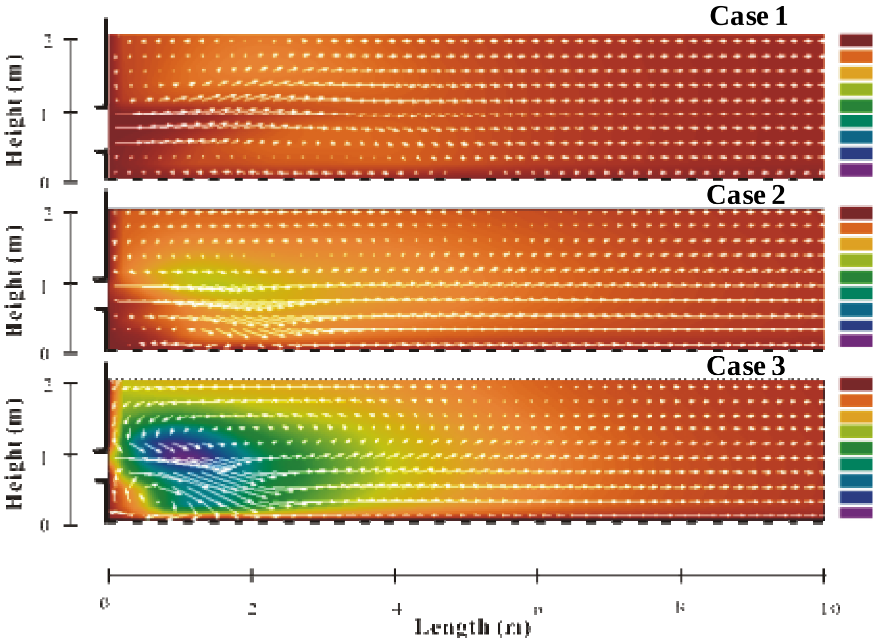

Figure 6.4. Steady state flow field profiles from CFD simulation for (a) Case 1 : low turbulence, (b) Case 2 : moderate turbulence, and (c) Case 3 : high turbulence. Arrows and colors represent flow velocities and shear rates, respectively.

With steady state flow field data obtained from the CFD simulation, solutions to the multi-dimensional DPBE were obtained with an in-house program. At the beginning, the consistency and stability of the developed numerical algorithms were tested by monitoring solid mass balances and particle/floc size evolution.

Mass balances were calculated with Equation (6.16) and monitored as shown in Figure 6.5(a). In Equation (6.16), $Mass_{in,acc}$, $Mass_{out,acc}$, $Mass_{deposit,acc}$, and $Mass_{retained}$ represent time-integrated masses caused by influx at the inlet, outflux at the outlet, deposition on the bottom, and retention in the pond, respectively, with time progression. Theoretically, $Mass_{in,acc}$ should be equal to the sum of $Mass_{out,acc}$, $Mass_{deposit,acc}$, and $Mass_{retained}$ *i.e.* the mass balance calculated from Equation (6.16) should be 100 %. In contrast to our expectation, mass balances for low, moderate, and high turbulent conditions were all below, or slightly below, 100 % at steady state conditions (99.7, 97.8, and 96.1 %, respectively). However, these balances were in an acceptable error range considering the approximating nature and complexity of the numerical methods. In Figure 6.5(a), the mass fractions by particle/floc deposition on the bottom ($Mass_{deposit,acc}$ / $Mass_{in,acc}$) are also shown for three different turbulence conditions. The mass fraction by deposition in high turbulence conditions (Case 3) was found to be much higher than the one in low turbulence conditions (Case 1), because high turbulence enhanced flocculation and subsequent sedimentation processes. These mass fractions and balances became stabilized as the mixing zone systems approached steady state conditions.

$$Mass\,Balance(\%) = \frac{Mass_{out,acc} + Mass_{deposit,acc} + Mass_{retained}}{Mass_{in,acc}} \tag{6.16}$$

Similarly, mass weighted, mean particle/floc diameter (D_{mm}), defined by Equation (6.17) (Hinds, 1999), flowing through the outlet was tracked with time progression to check numerical stability. In Equation (6.17), m_i represents the mass of all particles in the i-th particle/floc size class and M represents the total mass for all particle/floc size classes.

$$D_{mm} = \frac{\sum m_i D_i}{M} = \left(\frac{m_1}{M} D_1 + \frac{m_2}{M} D_2 + \cdots + \frac{m_i}{M} D_i \right) \tag{6.17}$$

In Figure 6.5(b), after the fastest growing phase, mass mean particle/floc diameters (D_{mm}) oscillated and then appeared to stabilize gradually. As mentioned in the previous section, the CFD-DPBE model consists of highly coupled nonlinear equations, which may produce fluctuating results. Strogatz (1994) discussed the tendency of such nonlinear equations to produce oscillatory behavior in numerical simulations. A variety of phenomena can contribute to this, including “chaotic” behavior. Thus, the observed oscillatory behaviors shown in Figure 6.5(b) were ascribed to the nonlinear nature of the CFD-DPBE model. Such behavior should be examined closely in future experimental and modeling studies.

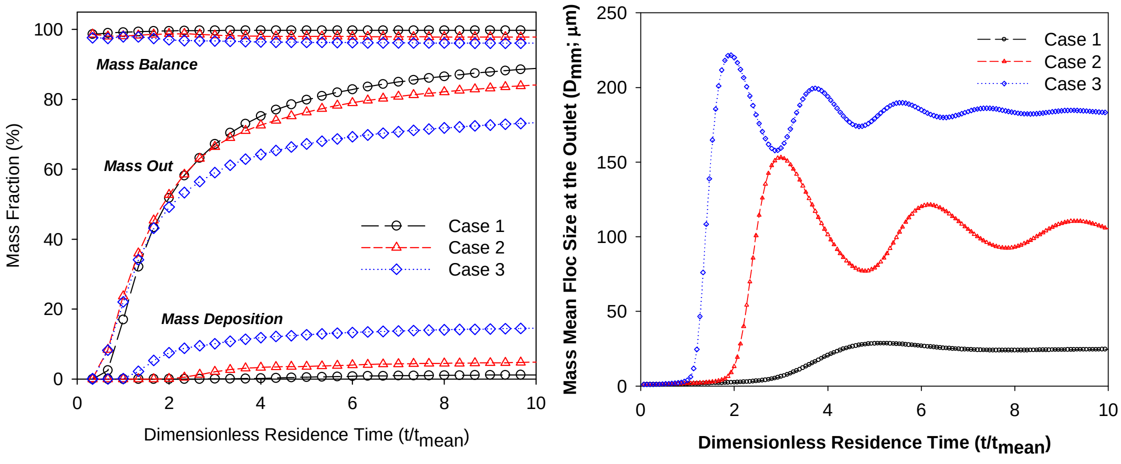

(a) (b)

Figure 6.5. (a) Mass fractions and balances and (b) mass weighted, mean floc diameter (D_{mm}) with respect to dimensionless residence time, which is normalized by dividing real fluid residence time with theoretical mean residence time.

After examining consistency and stability of the CFD-PBE model and mass weighted, mean particle/floc size (D_{mm}), solid concentration distributions at steady state conditions were investigated in the model mixing zone. Figures 6.6 and 6.7 show the distributions of mass-weighted mean particle/floc size and solid concentration, respectively, in three different turbulent flow fields. In Case 1 with low turbulence, mass mean particle/floc sizes were limited to below 27 μm, and solid concentrations were near-homogeneously distributed without particle/floc deposition. In case 3, however, with high turbulence, mass-weighted, mean particle/floc sizes grew up to 195 μm, which are of sufficient size to escape from the computational system by settling and depositing on the bottom. Thus, the longitudinal gradient of solid concentrations was observed in the computational domain due to particle/floc sedimentation. The moderate turbulent flow condition produced results approximately midway between the two extremes. The other interesting finding is that the swirling zones above the inlet in Cases 2 and 3 were found to work as small flocculation compartments. Particles/flocs traveling through these swirling zones are more exposed to flocculation and thus tend to grow larger than those passing through the other zones. For example, in case 3, particles/flocs in the swirling zone grew up to about 200 μm, while those right next to the swirling zone remained below 50 μm.

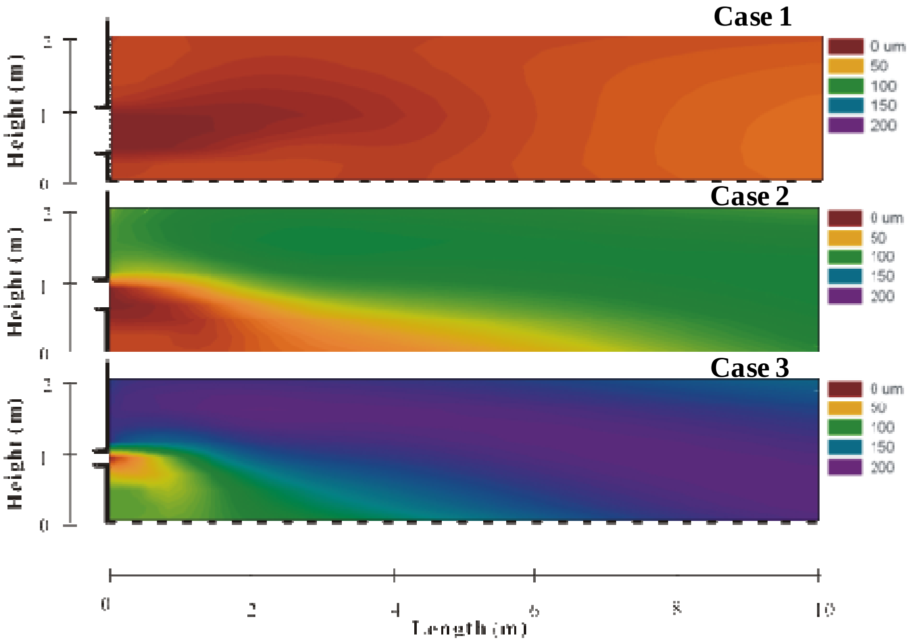

Figure 6.6. Mass weighted, mean floc diameter (D_{mm}) distributions in the computational domain. The distributions of Case 1, Case 2, and Case 3 are listed from the top.

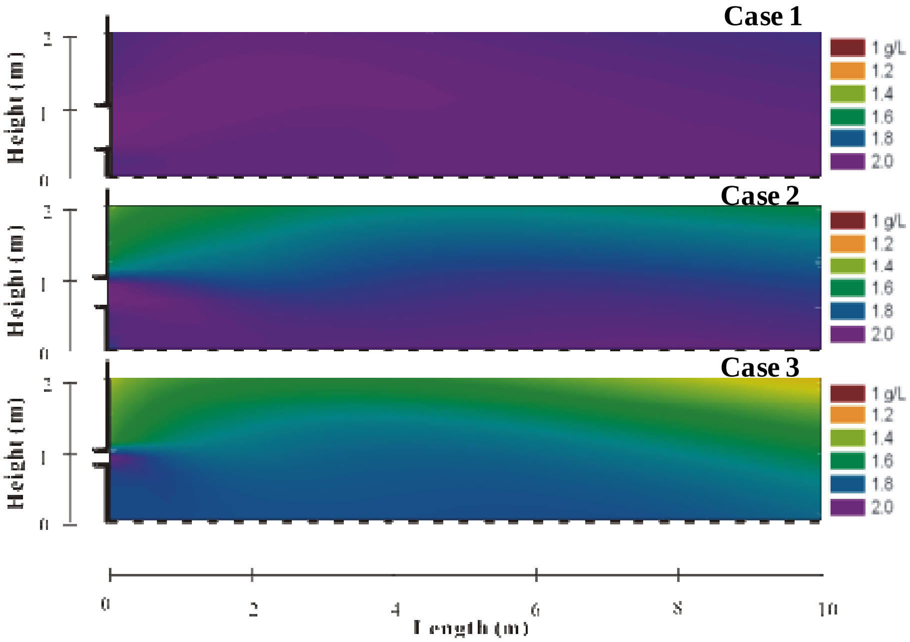

Figure 6.7. Solid concentration distributions in the computational domain. The distributions of Case 1, Case 2, and Case 3 are listed from the top.

Summarized in Table 6.2 are results from CFD-PBE simulations after reaching steady state. Mass-weighted, mean particle/floc size (D_{mm}) and deposited mass fraction ($Mass_{deposit,acc} / Mass_{in,acc}$) in Case 3, with the highest influent flow velocity and shear rate were up to 7.5 and 12.1 times higher than those in Case 1 with the lowest influent flow velocity and shear rate. As expected, turbulence in sediment retention ponds will enhance the flocculation efficiency in the mixing zone, at least up to a certain point. In Figure 6.8, the cumulative mass distributions of particles/flocs flowing through the outlet are shown for the three different turbulent conditions studied. As expected for the low turbulent condition (Case 1), the particle/floc size distribution in was more weighted in the small size range than those in the moderate and high turbulent conditions (Cases 2 and 3). Thus, in Case 1, raw clay particles coming through the inlet are not aggregated properly in the turbulent mixing zone, and thus a large fraction of particles/flocs may not settle appropriately in the subsequent sedimentation basin. In conclusion, considering the results in Table 6.2 and Figure 6.8 from the steady state CFD-DPBE simulations, turbulent conditions in a turbulent mixing zone were found to have important effects on both flocculation and subsequent sedimentation efficiencies. How to optimize this situation is an important topic for future study, both experimental and theoretical.

Table 6.2. Flow field characteristics and flocculation/sedimentation efficiencies for three different turbulent conditions in the mixing zone.

	Flow Field Characteristics		**Flocculation/Sedimentation Efficiencies**	
	v_{in} (m/s)	G* (/s)	D_{mm} **(μ m)	$\frac{Mass_{deposit,acc}}{Mass_{in,acc}}$ (%)
Case 1	0.222	13.5	24.59	1.204 %
Case 2	0.334	28.3	105.2	4.787 %
Case 3	0.667	79.3	183.2	14.54 %

* Maximum values in the computational domain
** Averaged values along the outlet

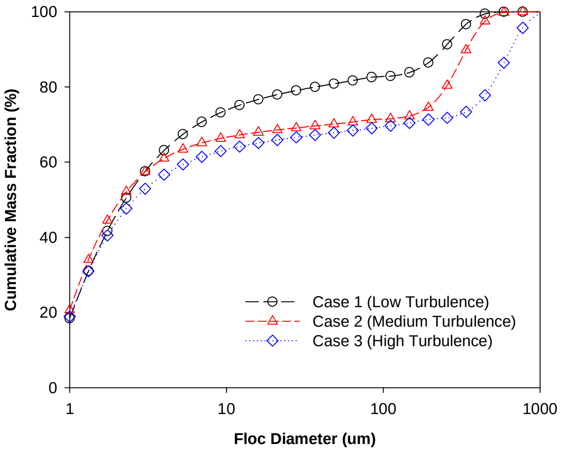

Figure 6.8. Cumulative mass distribution of particle/floc sizes at the outlet of the model basin.

6.5 Conclusions and Recommendations

The main purpose of this research was to estimate the applicability of a novel CFD-DPBE combined model to simulate flocculation and sedimentation processes in a turbulent mixing zone of a sediment retention pond. In this modeling and simulation study, several important findings were identified and discussed:

(1) The employed CFD software (FLOW-3D®) was a useful tool to generate steady state flow field data, such as flow velocities and shear rates, which were used in subsequent multi-dimensional DPBE simulations.

(2) As an alternative to QMOM, The DPBE formulation was applied to simulate a multi-dimensional flocculation/sedimentation process. Solution of the Multi-dimensional DPBE provided more readily understandable results for engineers and scientists with a bit more computations than QMOM but well within the capabilities of modern personal computers for two-dimensional flow fields.

(3) A standard, central-differencing, finite difference approach was judged as inadequate for simulating the flocculation and sedimentation processes in sediment retention ponds due to computational instability caused by nonlinearity, advection dominance and complexity of the DPBE model. Thus, operator splitting and Leveque's flux-corrected algorithms were applied to overcome the computational difficulties. The detailed numerical model is available from the authors upon request.

(4) In applications of the CFD-DPBE model, increased turbulence was found to enhance the flocculation and sedimentation efficiencies. However, methodology optimizing this effect requires further study.

Irrespective of the above findings, this research was limited to a pure simulation work without experimental validation. Thus, in future research, batch kinetic experiments and bench- or full-scale pond tests are required to calibrate, validate, and fully understand the CFD-DPBE model. In addition, the irregular behavior shown in Figure 6.5(b) requires further investigation.

In summary, the CFD-DPBE model was successfully applied to generate steady state flow field data and to simulate numerically flocculation and sedimentation processes in the turbulent mixing zone of sediment retention ponds. Thus, the CFD-DPBE model was shown to be a promising simulator of flocculant-aided sediment retention ponds. Furthermore, it may be applied to flocculation and sedimentation occurring in various natural and engineering systems such as water/wastewater treatment, nano-material synthesis, or sediment-depositing estuary systems (Lawler and Wilkes, 1984; Winterwerp, 2002; Bungartz and Wanner, 2004; Ding *et al.*, 2006; Schwarzer *et al.*, 2006; Maggi *et al.*, 2007). .

6.6 References

Adachi, Y., and Y. Tanaka, 1997, Settling velocity of an aluminium-kaolinite floc, *Water Research*, **31**(3), 449-454

Akan, A. O., and R. J. Houghtalen, 2003, *Urban Hydrology, Hydraulics and Stormwater Quality*, John Wiley & Sons, Hoboken, NJ

Alhumaizi, K., 2004, Comparison of finite difference methods for the numerical simulation of reacting flow, *Computer and Chemical Engineering*, **28**, 1759-1769

Aro, C. J., G.H. Rodrigue, and D. A. Rotman, 1999, A high performance chemical kinetics algorithm for 3-D atmospheric models, *The International Journal of High Performance Computing Applications*, **13**(1), 3-15

Badrot-Nico, F., F. Brissaud, and V. Guinot, 2007, A finite volume upwind scheme for the solution of the linear advection-diffusion equation with sharp gradients in multiple dimensions, *Advances in Water Resources*, **30**, 2002-2025

Brown, P. P., and D. F. Lawler, 2003, Sphere drag and settling velocity revisited, *Journal of Environmental Engineering - ASCE*, **129**(3), 222-231

Bungartz, H., and S. C. Wanner, 2004, Significance of particle interaction to the modelling of cohesive sediment transport in rivers, *Hydrological Processes*, **18**, 1685-1702

Bushell, G. C., Y.D. Yan, D. Woodfield, J. Raper, and R. Amal, 2001, On techniques for the measurement of the mass fractal dimension of aggregates, *Advances in Colloid and Interface Science*, **95**(1), 1-50

Chakraborti, R. K., J. F. Atkinson, and J. E. v. Benschoten, 2000, Characterization of alum floc by image analysis, *Environmental Science and Technology*, **34**,

Chakraborti, R. K., K. H. Gardner, J. F. Atkinson, and J. E. v. Benschoten, 2003, Changes in fractal dimension during aggregation, *Water Research*, **37**, 873-883

Ding, A., M.J. Hounslow, and C. A. Biggs, 2006, Population balance modelling of activated sludge flocculation: Investigating the size dependence of aggregation, breadkage and collision efficiency, *Chemical Engineering Science*, **61**, 63-74

Durran, D. R., 1998, *Numerical methods for wave equations in geophysical fluid dynamics*, Springer-Verlag, New York, U.S.

EERC, 2003, Stormwater BMP Selection Guide Manual for Tennessee, from *http://eerc.ra.utk.edu/divisions/wrrc/BMP/bmp.htm*

Flesch, J. C., P. T. Spicer, and S. E. Pratsinis, 1999, Laminar and turbulent shear-induced flocculation of fractal aggregation, *AIChE Journal*, **45**(5), 1114-1124

Fox, R. O., 2003, *Computational models for turbulent reacting flows*, Cambridge University Press, Cambridge UK

Gowdy, W., and S. R. Iwinski, 2007, Removal Efficiencies of Polymer Enhanced Dewatering Systems. *In Proceedings of the 9th Biennial Conference on Stormwater Research & Watershed Management*, Orlando, FL,May 2 - 3, 2007.

Harper, H. H., 2007, Current research and trends in alum treatment of stormwater runoff. *In Proceedings of the 9th Biennial Conference on Stormwater Research & Watershed Management*, Orlando, FL,May 2 - 3, 2007.

Heath, A. R., and P. T. L. Koh, 2003, Combined population balance and CFD modelling of particle aggregation by polymeric flocculant. *Third International Conference on CFD in the Minerals and Process Industries,* CSIRO, Melbourne, Australia,10-12 December 2003.

Hinds, W. C., 1999, *Aerosol technology: properties, behavior, and measurement of airborne particles, 2nd ed.*, John Wiley & Sons, Inc, New York, NY

Hounslow, M. J., R. L. Ryall, and V. R. Marshall, 1988, A discretized population balance for nucleation, growth, and aggregation, *AIChE Journal*, **34**(1), 1821-1832.

Jiang, Q., and B. E. Logan, 1991, Fractal dimensions of aggregates determined from steady-state size distributions, *Environmental Science and Technology*, **25**, 2031-2038

Johnson, C. P., X. Li, and B. E. Logan, 1996, Settling velocities of fractal aggregates, *Environmental Science and Technology*, **30**, 1911-1918

Kang, J. H., Y. X. Li, S. L. Lau, M. Kayhanian, and M. K. Stenstrom, 2007, Particle destabilization in highway runoff to optimize pollutant removal, *Journal of Environmental Engineering - ASCE*, **133**, 426-434

Kumar, S., and D. Ramkrishna, 1996, On the solution of population balance equations by discretization - A fixed pivot technique, *Chemical Engineering Science*, **51**(8), 1311-1332

Langseth, J. O., A. Tveito, and R. Winther, 1996, On the convergence of operator splitting applied to conservation laws with source terms, *SIAM J. Numer. Anal.*, **33**, 843-863

Lawler, D. F., and D. R. Wilkes, 1984, Flocculation model testing: particle sizes in a softening plant, *Journal AWWA*, **76**(7), 90-97

Lee, D. G., J.S. Bonner, L.S. Garton, A.N.S. Ernest, and R. L. Autenrieth, 2000, Modeling coagulation kinetics incorporating fractal theories: a fractal rectilinear approach, *Water Research*, **34**(7), 1987-2000

Leveque, R. J., 1996, High-resolution conservative algorithms for advection in incompressible flow, *SIAM J. Numer. Anal.*, **33**(2), 627-665

Lian, G. L., M. Steve, and L. Heeney, 2006, Population balance and computational fluid dynamics modelling of ice crystallisation in a scraped surface freezer, *Chemical Engineering Science*, **61**, 7819-7826

Maggi, F., F. Mietta, and J. C. Winterwerp, 2007, Effect of variable fractal dimension on the floc size distribution of suspended cohesive sediment, *J. of Hydrol.*, **343**, 43-55

Marchisio, D. L., J. T. Pikturna, R. O. Fox, R. D. Vigil, and A. A. Barresi, 2003a, Quadrature method of moments for population-balance equations, *AIChE Journal*, **49**(5), 1266-1276

Marchisio, D. L., R. D. Vigil, and R. O. Fox, 2003b, Implementation of the quadrature method of moments in CFD codes for aggregation-breakage problems, *Chemical Engineering Science*, **58**, 3337-3351

McGraw, R., 1997, Description of aerosol dynamics by the quadrature method of moments, *Aerosol Science and Technology*, **27**, 255-265

Miyahara, K., Y. Adachi, K. Nakaishi, and M. Ohtsubo, 2002, Settling velocity of a sodium montmorilloinite floc under high ionic strength, *Colloids and Surfaces A: Physicochemical and Engineering Aspects*, **196**, 87-91

Parker DS, ASCE Am, Kaufman WJ, and J. D, 1972, FLOC BREAKUP IN TURBULENT FLOCCULATION PROCESSES, *Journal of the Sanitary Engineering - ASCE*, **98**, 79

Prat, O. P., and J. J. Ducoste, 2006, Modeling spatial distribution of floc size in turbulent processes using the quadrature method of moment and computational fluid dynamics, *Chemical Engineering Science*, **61**, 75-86

Rahmani, N. H. G., T. Dabros, and J. H. Masliyah, 2004, Evolution of asphaltene floc size distribution in organic solvents under shear, *Chemical Engineering Science*, **59**, 685-697

Ramkrishna, D., and A. W. Mahoney, 2002, Population balance modeling. Promise for the future, *Chemical Engineering Science*, **57**, 595-606

Rogers, S. E., and D. Kwak, 1998, An upwind-differencing scheme for the incompressible Navier-Stokes equations, NASA TM-101051, NASA, Washington, DC, U.S.

Runkana, V., P. Somasundaran, and P. C. Kapur, 2006, A population balance model for flocculation of colloidal suspensions by polymer bridging, *Chemical Engineering Science*, **61**, 182-191

Schwarzer, H., F. Schwertfirm, M. Manhart, H. Schmid, and W. Peukert, 2006, Predictive simulation of nanoparticle precipitation based on the population balance equation, *Chemical Engineering Science*, **61**, 167-181

Smoluchowski, M., 1917, Versuch Einer Mathematischen Theorie der Koagulations - Kinetic Kolloider Losungen, *Zeitschrift fur Physikalische Chemie*, **92**(2), 129

Sojka, R. E., D. L. Bjorneberg, J. A. Entry, R. D. Lentz, and W. J. O. Orts, 2007, Polyacrylamide in agriculture and environmental land management, *Advances in Agronomy*, **92**, 75

Somasundaran, P., and V. Runkana, 2003, Modeling flocculation of colloidal mineral suspensions using population balances, *International Journal of Mineral Processing*, **72**, 33-55

Spicer, P. T., and S. E. Pratsinis, 1996a, Coagulation-fragmentation: universal steady state particle size distribution, *AIChE Journal*, **42**, 1612

Spicer, P. T., and S. E. Pratsinis, 1996b, Shear-induced flocculation: the evolution of floc structure and the shape of the size distribution at steady state, *Water Research*, **30**, 1049

Spicer, P. T., S.E. Pratsinis, J. Raper, R. Amal, G. Bushell, and G. Meesters, 1998, Effect of shear schedule on particle size, density, and structure during flocculation in stirred tanks, *Powder Technology*, **97**, 26-34

Sterling, M. C., J. Bonner, A.N.S Ernest, C.A. Page, and R. L. Autenrieth, 2005, Application of fractal flocculation and vertical transport model to aquatic sol-sediment systems, *Water Research*, **39**, 1818-1830

Stokes, G., 1880, *Mathematical and physical papers, Vol. 1*, Cambridge University Press, Cambridge, U.K.

Timin, T., and M. N. Esmail, 2005, A comparative study of central and upwind difference schemes using the primitive variables, *International Journal for Numerical Methods in Fluids*, **3**(3), 295-305

Turchiuli, C., and C. Fargues, 2004, Influence of structural properties of alum and ferric flocs on sludge dewaterability, *Chemical Engineering Journal*, **103**, 123-131

USDOT, 2002, *Stormwater Best Management Practices in an Ultra-Urban Setting: Selection and Monitoring*, from *http://www.fhwa.dot.gov/environment/ultraurb/index.htm*

Wang, L., D. L. Marchisio, and R. O. Fox, 2005, CFD simulation of aggregation and breakage processes in laminar Taylor-Couette flow, *Journal of Colloid and Interface Science*, **282**, 380-396

White, F. M., 1991, *Viscous Fluid Flow*, McGrow Hill, New York, U.S.

Winterwerp, J. C., 2002, On the flocculation and settling velocity of estuarine mud, *Continental Shelf Research*, **22**, 1339-1360

CHAPTER 7. SUMMARY, CONCLUSIONS AND RECOMMENDATIONS

7.1 Summary

The overall objective of the research was set as optimization of the flocculant-aided sediment retention ponds and was investigated with both experimental and modeling approaches, including characterization of PAMs, investigation on PAM-driven physicochemical processes, and simulation of flocculant-aided sediment retention ponds. At the beginning of this research, the simple measurement techniques were developed to estimate MW and CD of a PAM, which are the key characteristics in the subsequent optimization tasks of this research. The characteristic behaviors of PAM in the aqueous solution, such as acid-base chemistry and conformational layouts of PAMs, were investigated with application of the simplified electrostatic interaction models. After the above supportive experiments, the actual optimization of PAM-aided sediment retention ponds was performed with both experimental and modeling efforts. Firstly, in adsorption and flocculation experiments, the practical guides for the optimal use of PAM flocculants were provided with respect to the properties of a PAM and a solution. Secondly, in model formulation, the simulation tool for the optimal design and operation of PAM-aided sediment retention ponds was developed by combining the Discretized Population Balance Equations (DPBEs) with a Computational Fluid Dynamics (CFD) ,model that is available commercially. In the following section, the key findings are summarized from the individual research tasks.

7.2 Conclusions

(1) Both the intrinsic viscosity measurement technique and the acid-base titration method been shown as the simple alternative techniques for measuring MW and CD of a PAM. However, the intrinsic viscosity measurement technique had drawbacks in measuring MWs, because the technique consistently underestimated MW compared to measurements made with a state-of-the-art light scattering procedure.

(2) During the calibration experiments between acid-base titrations and electrostatic interaction chemistry models, cylindrical shapes were proven to be more realistic in describing PAM conformation in the aqueous phase than coiled or spherical shapes, because even spherical or coil-like polyelectrolytes have large void spaces for reaction-participating ions to travel freely inside the coiled structures and thus can be assumed to be very long cylinders.

(3) In adsorption and flocculation tests done with nonionic PAMs, adsorption capacities and flocculation efficiencies in PAM- on kaolinite-containing suspensions were found to increase with increasing PAM MWs. However, the adsorption capacity and flocculation efficiency of the largest PAM (MW = 18 M) decreased down under the capacities of the other smaller PAMs, due to the entanglements between polymeric chains.

(4) Both MW and CD were proven to be the key characteristics of anionic PAMs in determining adsorption capacity and flocculation efficiency. Adsorption capacities were found to be inversely proportional to PAM CDs, while flocculation efficiencies were directly proportional to PAM MWs. Along with PAM characteristics, the cation

species in the solution were found to be the decisive solution characteristics. Divalent cations in the solution, such as Ca^{2+} and Mg^{2+}, enhanced adsorption and flocculation processes with the cationic bridging between PAM and kaolinite (PAM^{-}–$^{+}\mathrm{M}^{+}$–$^{-}$Kaolinite). However, concurring steric stabilization was also found to counteract flocculation due to the conformational changes of adsorbed PAMs by the cationic bridging between pre-adsorbed PAM molecules (PAM^{-}–$^{+}\mathrm{M}^{+}$–$^{-}\mathrm{PAM}$).

(5) Multi-dimensional Discretized Population Balance Equations combined with a computational fluid dynamics model (CFD-DPBE model) was proven by tracking mass balances and floc size evolutions and by examining particle/floc size and solid concentration distributions. Thus, the CFD-DPBE model may be used as a valuable simulation tool for natural and engineered flocculation and sedimentation systems as well as flocculant-aided sediment retention ponds.

7.3 Recommendations

(1) Simple and reliable intrinsic viscosity measurement method :

In this research, MWs measured with the pre-developed intrinsic viscosity measurement technique were found to be consistently lower compared to those made with a state-of-the-art light scattering analysis. Thus, further investigation will be required to develop a new intrinsic viscosity measurement method with an adequate MHS equation and a standardized experimental protocol, to cope with the inhomogeneous and dynamic nature of high-MW PAM flocculants.

(2) Toxic Metal-binding capacity of anionic PAMs :

Storm-water has been reported to contain significant amounts of toxic metals, which are flushed from roads, industrial, residential, and other areas (Characklis and Wiesner, 1997; Lau and Stenstrom, 2005; Kayhanian *et al.*, 2008). Considering the protonation capacity, anionic PAMs may be used as the applicable adsorbent of toxic metal ions in non-point contaminant source management. Thus, future investigation is required to estimate the cationic binding capacity of anionic PAMs and the removal potential for toxic metal ions. The metal-binding capacity of anionic PAMs may be estimated with application of the CY model validated in this research.

(3) Other controlling factors in PAM-driven adsorption and flocculation :

In this research, MW and CD of a PAM, cationic species of a solution, and shear rates of the turbulent fluid were mainly investigated as the key factors for adsorption and flocculation processes in PAM- and kaolinite-containing suspensions. However, there are still many other controlling factors to be investigated in adsorption and flocculation tests. For example, the coating of iron or humic substances on clay surfaces is known to have significant effects on adsorption and flocculation (Gibbs, 1983; Arias *et al.*, 1995; Arias *et al.*, 1996; Tombacz *et al.*, 1998; Mosley *et al.*, 2003). Also, various anions or cations in the solution phase are able to enhance or reduce PAM-driven adsorption and flocculation. Thus, all these potential controlling factors should be investigated with respect to their effects on adsorption and flocculation.

(4) Natural polymers as alternative flocculants :

Even though nonionic and anionic PAMs are known as non-toxic flocculants, their long-term impacts on ecosystems are still unknown due to their synthetic and xenobiotic nature. Thus, several natural flocculants, which are totally free from toxicity concerns, need to be investigated as alternatives to PAMs. For example, chitosan from sea food processing, starches from staple food processing, mucilages from the seeds or roots of plants, and exudates from microorganisms are among the most applicable natural flocculants (Jahn, 1988; Jarnstrom *et al.*, 1995; Ndabigengesere *et al.*, 1995; Gomoiu and Catley, 1996; Divakaran and Pillai, 2001; Okuda *et al.*, 2001; Mishra *et al.*, 2004; Pal *et al.*, 2005; Taniguchi *et al.*, 2005).

(5) Experimental validation and extended application of the DPBE-CFD model :

The DPBE-CFD model developed in this research was limited to a pure simulation study without the experimental validation. Thus, in future research, batch kinetic experiments and flume- or full-scale pond tests are required to calibrate and validate the CFD-DPBE model. Eventually, the DPBE-CFD model may be applied to simulate flocculation and sedimentation occurring in various natural and engineered systems such as water/wastewater treatment, nano-material synthesis, or sediment-depositing estuary systems (Lawler and Wilkes, 1984; Winterwerp, 2002; Bungartz and Wanner, 2004; Ding *et al.*, 2006; Schwarzer *et al.*, 2006; Maggi *et al.*, 2007).

7.4 References

Arias, M., M. T. Barral, and F. Diaz-Fierros, 1996, Effects of associations between humic acids and iron or aluminium on the flocculation and aggregation of kaolin and quartz, *European Journal of Soil Science*, **47**, 335-343

Arias, M., T. Barral, and F. Diaz-Fierros, 1995, Effects of iron and aluminum oxides on the colloidal and surface properties of kaolin, *Clay and Clay Minerals*, **43**(4), 406-416

Bungartz, H., and S. C. Wanner, 2004, Significance of particle interaction to the modelling of cohesive sediment transport in rivers, *Hydrological Processes*, **18**, 1685-1702

Characklis, G. W., and M. R. Wiesner, 1997, Particles, metals, and water quality in runoff from a large urban watershed, *Journal of Environmnetal Engineering*, **123**(8), 753-759

Ding, A., M.J. Hounslow, and C. A. Biggs, 2006, Population balance modelling of activated sludge flocculation: Investigating the size dependence of aggregation, breakage and collision efficiency, *Chemical Engineering Science*, **61**, 63-74

Divakaran, R., and V. N. S. Pillai, 2001, Flocculation of kaolinite suspensions in water by chitosan, *Water Research*, **35**(16), 3904-3908

Gibbs, R. J., 1983, Effect of natural organic coatings on the coagulation of particles, *Environ. Sci. Technol.*, **17**, 237-240

Gomoiu, I., and B. J. Catley, 1996, Properties of a kaolin-flocculating polymer elaborated by *Byssochlamys nivea*, *Enzyme and Mirobial Technology*, **19**, 45-49

Jahn, S. A. A., 1988, Using *Moringa* seeds as coagulants in developing-countries, *Journal AWWA*, **80**(6), 43-50

Jarnstrom, L., L. Lason, and M. Rigdahl, 1995, Flocculation in kaolin suspensions induced by modified starches - 1. Cationically modified starch - effects of temperature and ionic strength, *Colloids and Surfaces A: Physicochem. Eng. Aspects*, **104**, 191-205

Kayhanian, M., C. Stransky, S. Bay, S. L. Lau, and M. K. Stenstrom, 2008, Toxicity of urban highway runoff with respect to storm duration, *Science of The Total Environment*, **389**(2-3), 386-406

Lau, S. L., and M. K. Stenstrom, 2005, Metals and PAHs adsorbed to street particles, *Water Research*, **39**(17), 4083-4092

Lawler, D. F., and D. R. Wilkes, 1984, Flocculation model testing: particle sizes in a softening plant, *Journal AWWA*, **76**(7), 90-97

Maggi, F., F. Mietta, and J. C. Winterwerp, 2007, Effect of variable fractal dimension on the floc size distribution of suspended cohesive sediment, *J. of Hydrol.*, **343**, 43-55

Mishra, A., A. Yadav, M. Agarwal, and M. Baipai, 2004, Fenugreek mucilage for solid removal from tannery effluent, *Reactive & Functional Polymer*, **59**, 99-104

Mosley, L. M., K. A. Hunter, and W. A. Ducker, 2003, Forces between colloid particles in natural waters, *Environ. Sci. Technol.*, **37**, 3303-3308

Ndabigengesere, A., K. S. Narashiah, and B. G. Talbot, 1995, Active agents and mechanism of coagulation of turbid waters using *Moringa oleifere*, *Water Research*, **29**(2), 703-710

Okuda, T., A. U. Baes, W. Nishijima, and M. Okada, 2001, Coagulation mechnism of salt solution-extracted active component in Moringa oleifera seeds, *Water Research*, **35**(3), 830-834

Pal, S., D. Mal, and R. P. Singh, 2005, Cationic starch: an effective flocculating agent, *Carbohydrate Polymers*, **59**, 417-423

Schwarzer, H., F. Schwertfirm, M. Manhart, H. Schmid, and W. Peukert, 2006, Predictive simulation of nanoparticle precipitation based on the population balance equation, *Chemical Engineering Science*, **61**, 167-181

Taniguchi, M., K. Kato, A. Shimauchi, X. Ping, K. Fujita, T. Tanaka, Y. Tarui, and E. Hirasawa, 2005, Physicochemical properties of cross-linked poly-gamma-glutamic acid and its flocculating activity against kaolin suspension, *Journal of Bioscience and Bioengineering*, **99**(2), 130-135

Tombacz, E., M. Szekeres, L. Baranyi, and E. Micheli, 1998, Surface modification of clay minerals by organic polyions, *Colloids and Surfaces A: Physicochem. Eng. Aspects*, **141**, 379-384

Winterwerp, J. C., 2002, On the flocculation and settling velocity of estuarine mud, *Continental Shelf Research*, **22**, 1339-1360

APPENDICES

Appendix A

Molecular Weight Measurement with Multi-Angle Light Scattering Analyzer : Zimm-Berry Plots

Zimm Plot - Polyscience_1MNaCl_1st

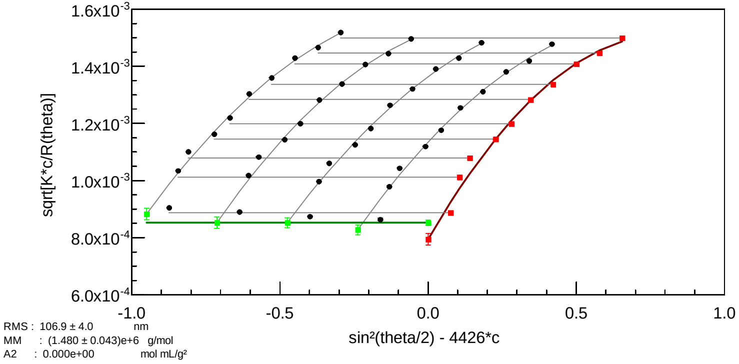

RMS : 106.9 ± 4.0 nm
MM : (1.480 ± 0.043)e+6 g/mol
A2 : 0.000e+00 mol mL/g^2

Zimm Plot - Polyscience_1MNaCl_2nd

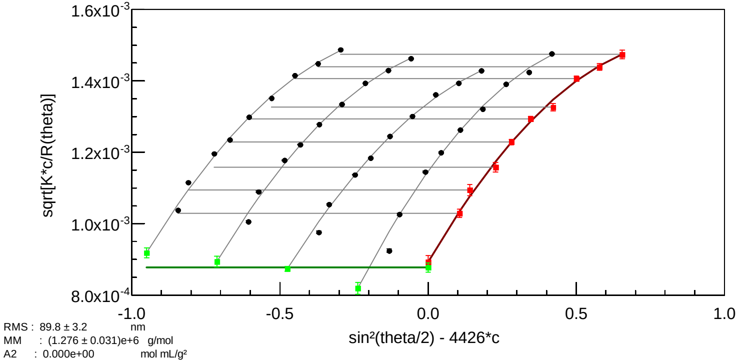

RMS : 89.8 ± 3.2 nm
MM : (1.276 ± 0.031)e+6 g/mol
A2 : 0.000e+00 mol mL/g^2

Zimm Plot - Polyscience_1MNaCl_3rd

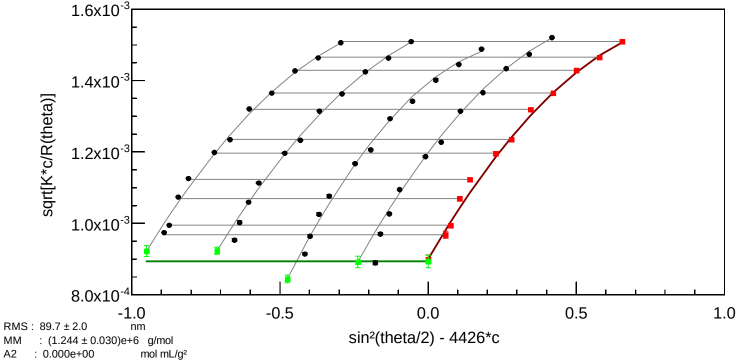

RMS : 89.7 ± 2.0 nm
MM : (1.244 ± 0.030)e+6 g/mol
A2 : 0.000e+00 mol mL/g^2

Figure A.1. Zimm-Berry plots for triplicate N1 PAM samples used to estimate molecular weights.

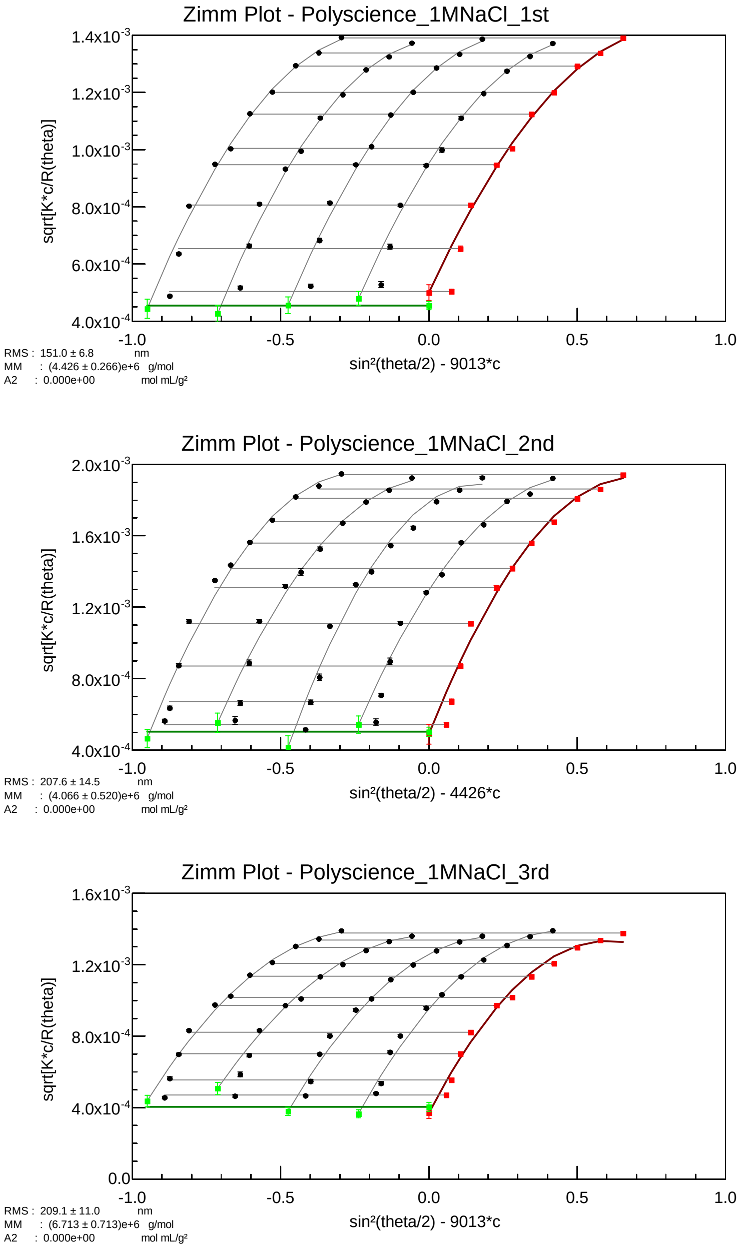

Figure A.2. Zimm-Berry plots for triplicate N2 PAM samples used to estimate molecular weights.

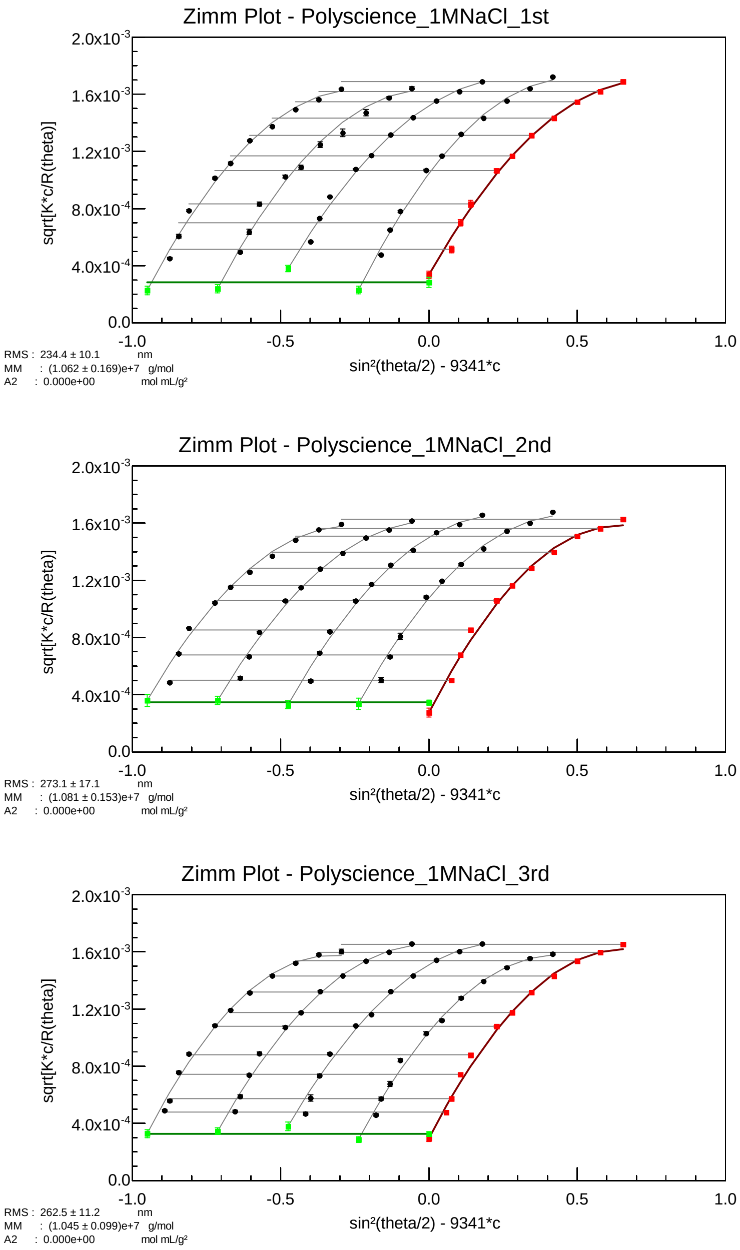

Zimm Plot - Polyscience_1MNaCl_1st

RMS : 234.4 ± 10.1 nm
MM : $(1.062 \pm 0.169)e+7$ g/mol
A2 : 0.000e+00 mol mL/g^2

Zimm Plot - Polyscience_1MNaCl_2nd

RMS : 273.1 ± 17.1 nm
MM : $(1.081 \pm 0.153)e+7$ g/mol
A2 : 0.000e+00 mol mL/g^2

Zimm Plot - Polyscience_1MNaCl_3rd

RMS : 262.5 ± 11.2 nm
MM : $(1.045 \pm 0.099)e+7$ g/mol
A2 : 0.000e+00 mol mL/g^2

Figure A.3. Zimm-Berry plots for triplicate N3 PAM samples used to estimate molecular weights.

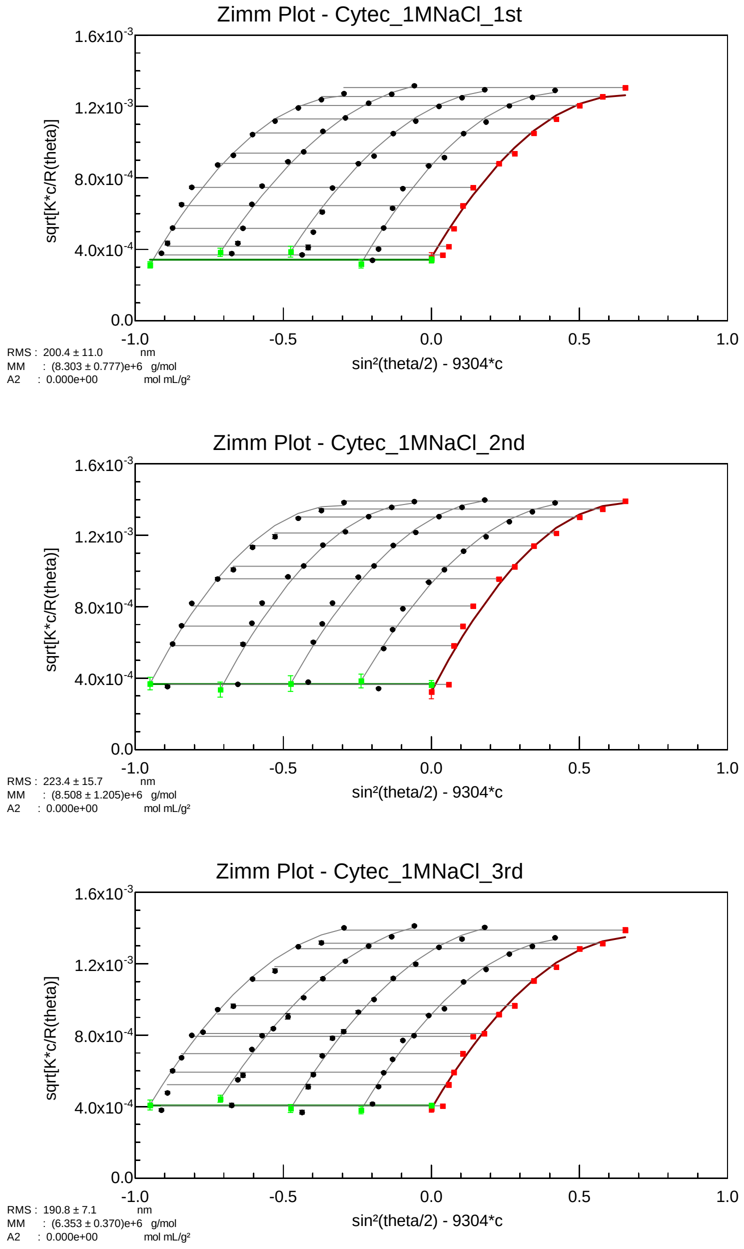

Figure A.4. Zimm-Berry plots for triplicate A1 PAM samples used to estimate molecular weights.

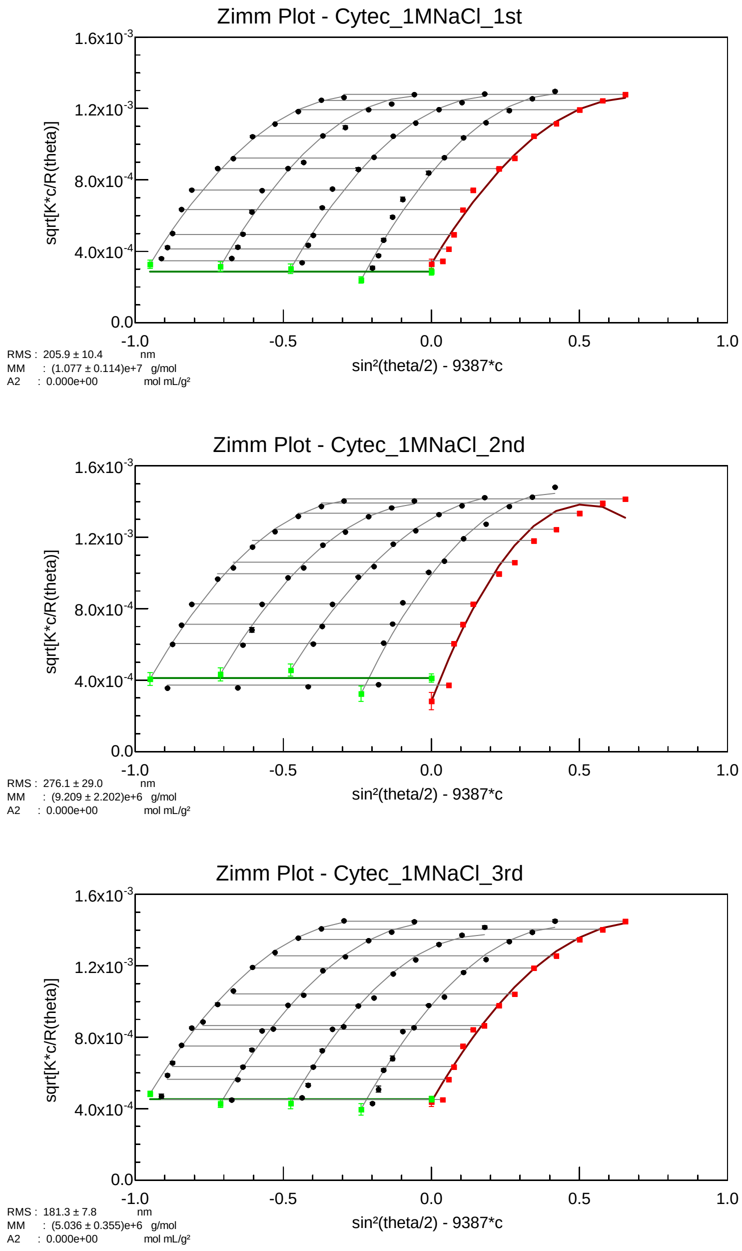

Figure A.5. Zimm-Berry plots for triplicate A2 PAM samples used to estimate molecular weights.

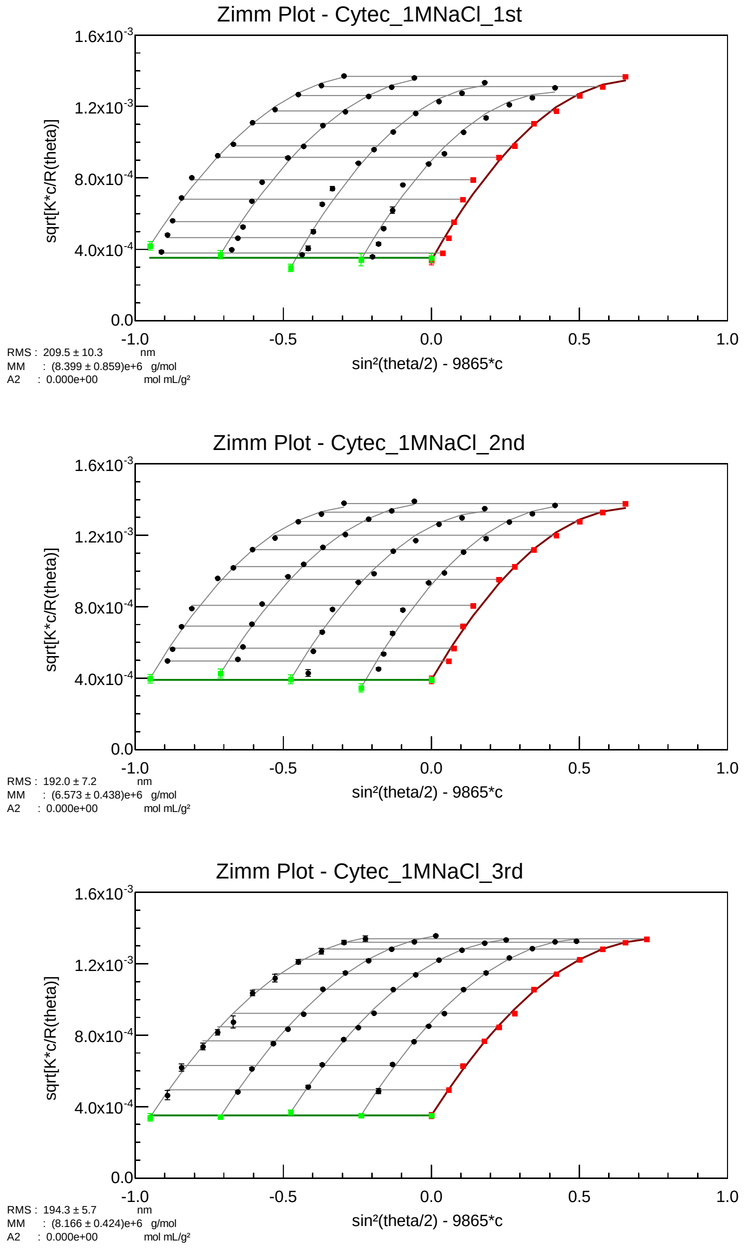

Figure A.6. Zimm-Berry plots for triplicate A3 PAM samples used to estimate molecular weights.

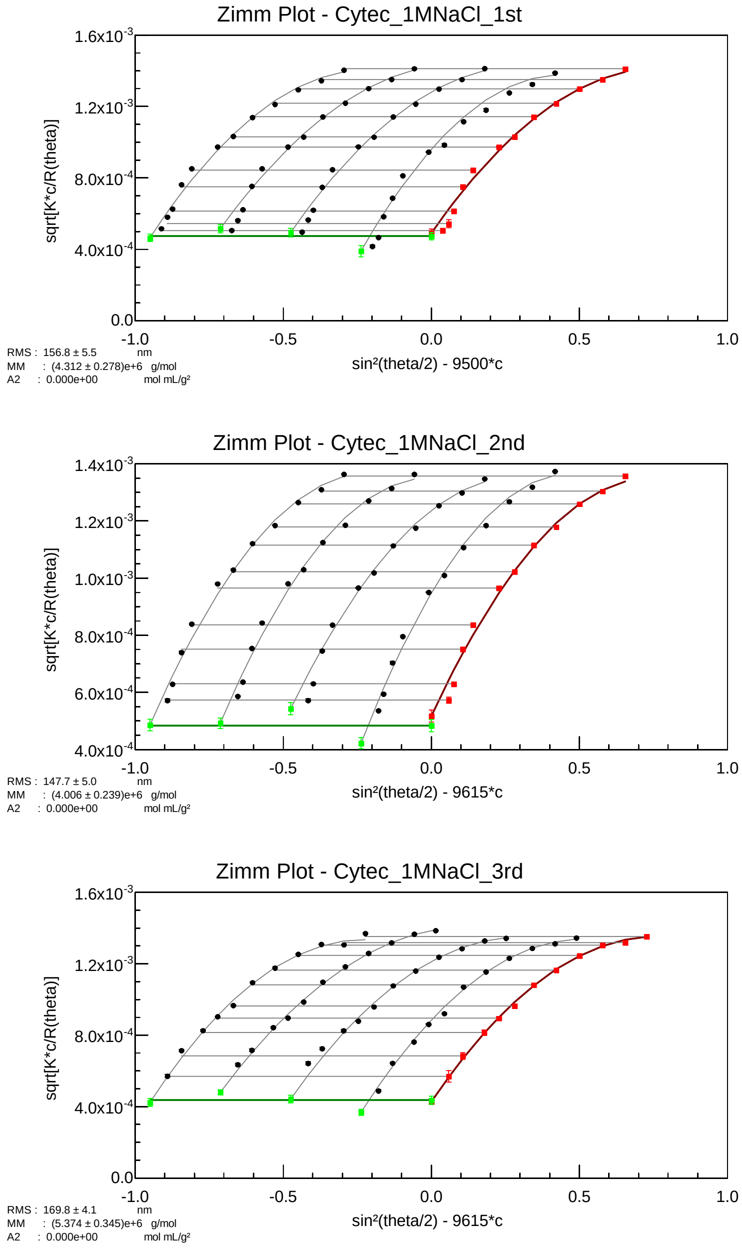

RMS : 156.8 ± 5.5 nm
MM : (4.312 ± 0.278)e+6 g/mol
A2 : 0.000e+00 mol mL/g²

RMS : 147.7 ± 5.0 nm
MM : (4.006 ± 0.239)e+6 g/mol
A2 : 0.000e+00 mol mL/g²

RMS : 169.8 ± 4.1 nm
MM : (5.374 ± 0.345)e+6 g/mol
A2 : 0.000e+00 mol mL/g²

Figure A.7. Zimm-Berry plots for triplicate A4 PAM samples used to estimate molecular weights.

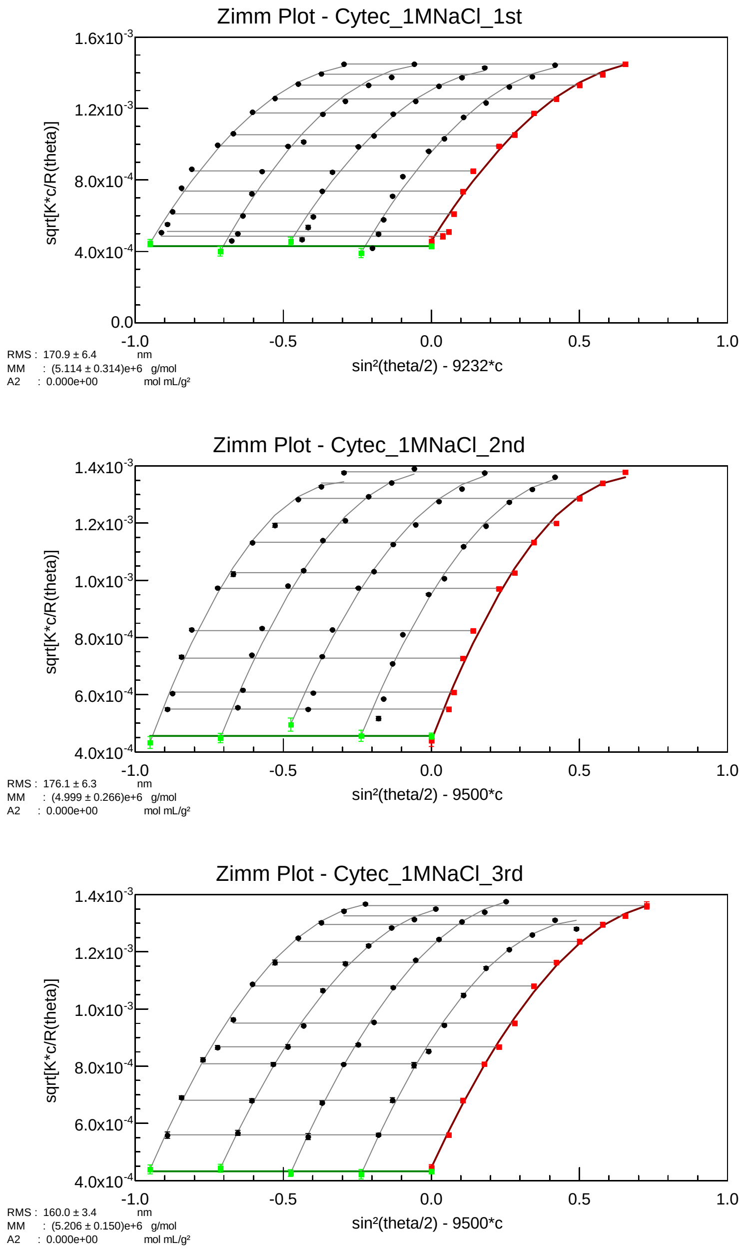

RMS : 170.9 ± 6.4 nm
MM : (5.114 ± 0.314)e+6 g/mol
A2 : 0.000e+00 mol mL/g²

RMS : 176.1 ± 6.3 nm
MM : (4.999 ± 0.266)e+6 g/mol
A2 : 0.000e+00 mol mL/g²

RMS : 160.0 ± 3.4 nm
MM : (5.206 ± 0.150)e+6 g/mol
A2 : 0.000e+00 mol mL/g²

Figure A.8. Zimm-Berry plots for triplicate A5 PAM samples used to estimate molecular weights.

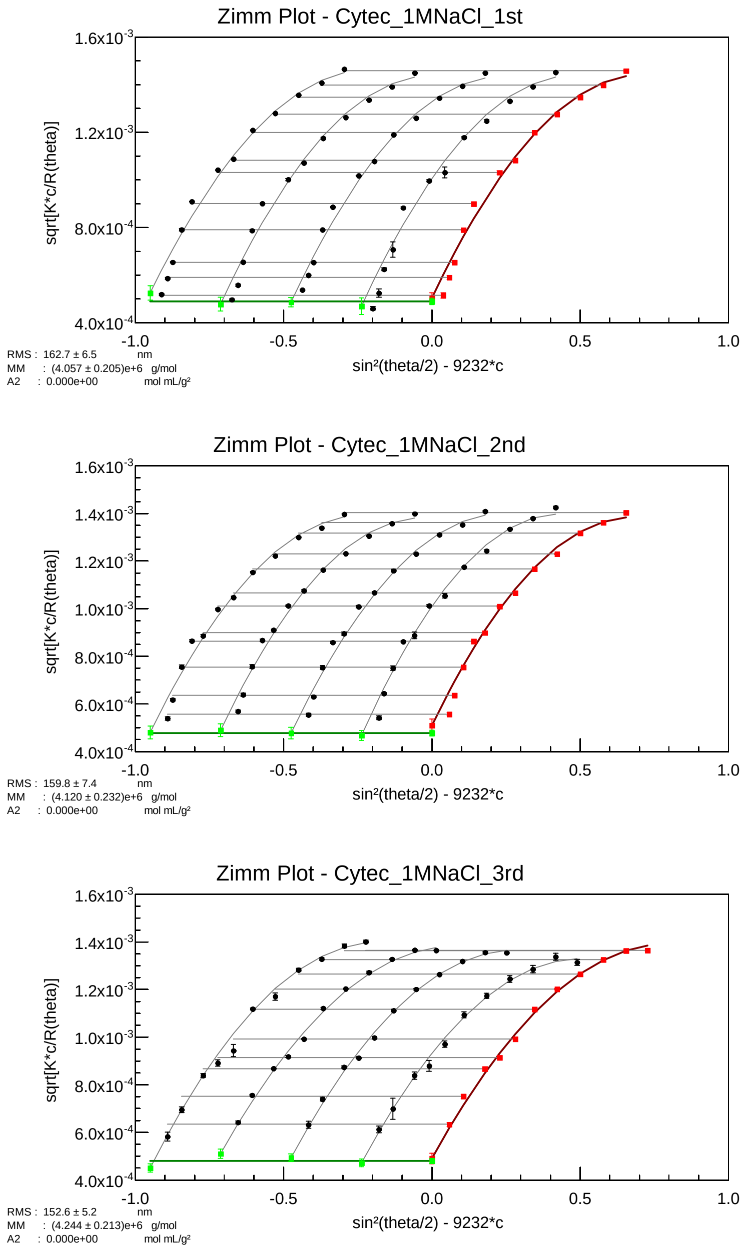

Figure A.9. Zimm-Berry plots for triplicate A6 PAM samples used to estimate molecular weights.

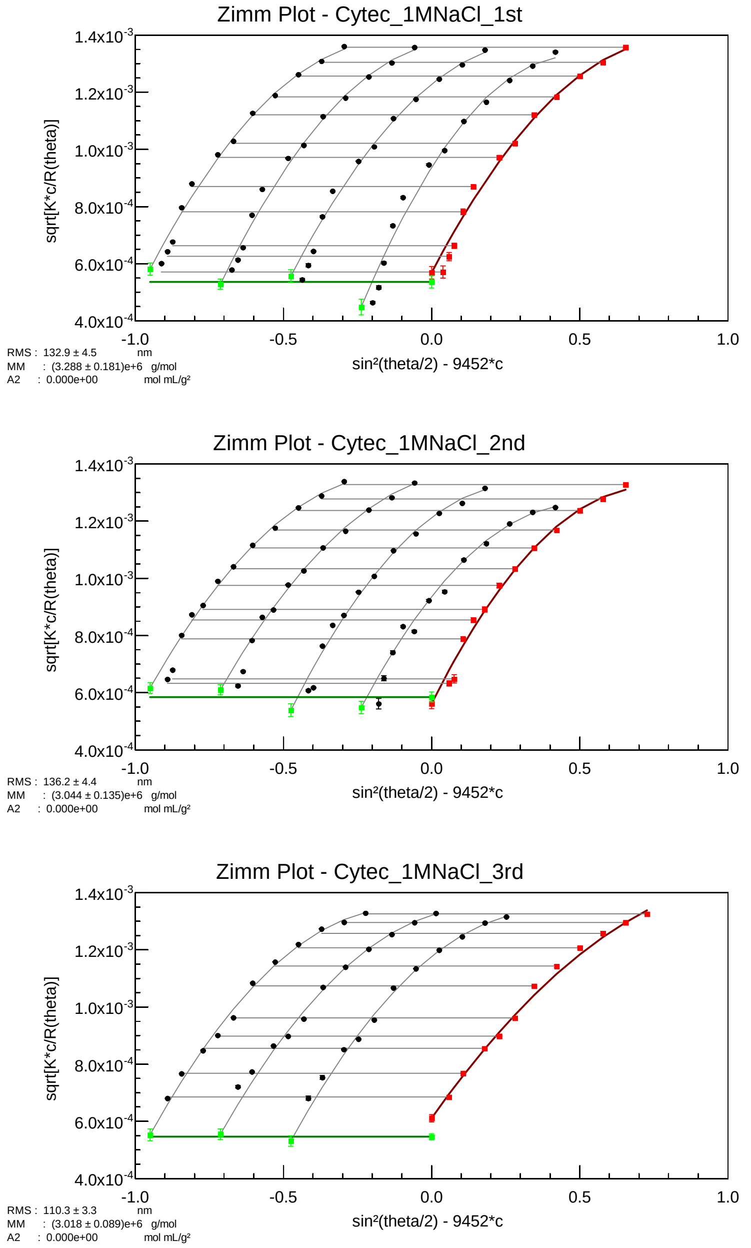

```
RMS :  132.9 ± 4.5            nm
MM      :  (3.288 ± 0.181)e+6   g/mol
A2      :  0.000e+00               mol mL/g²
```

```
RMS :  136.2 ± 4.4            nm
MM      :  (3.044 ± 0.135)e+6   g/mol
A2      :  0.000e+00               mol mL/g²
```

```
RMS :  110.3 ± 3.3            nm
MM      :  (3.018 ± 0.089)e+6   g/mol
A2      :  0.000e+00               mol mL/g²
```

Figure A.10. Zimm-Berry plots for triplicate A7 PAM samples used to estimate molecular weights.

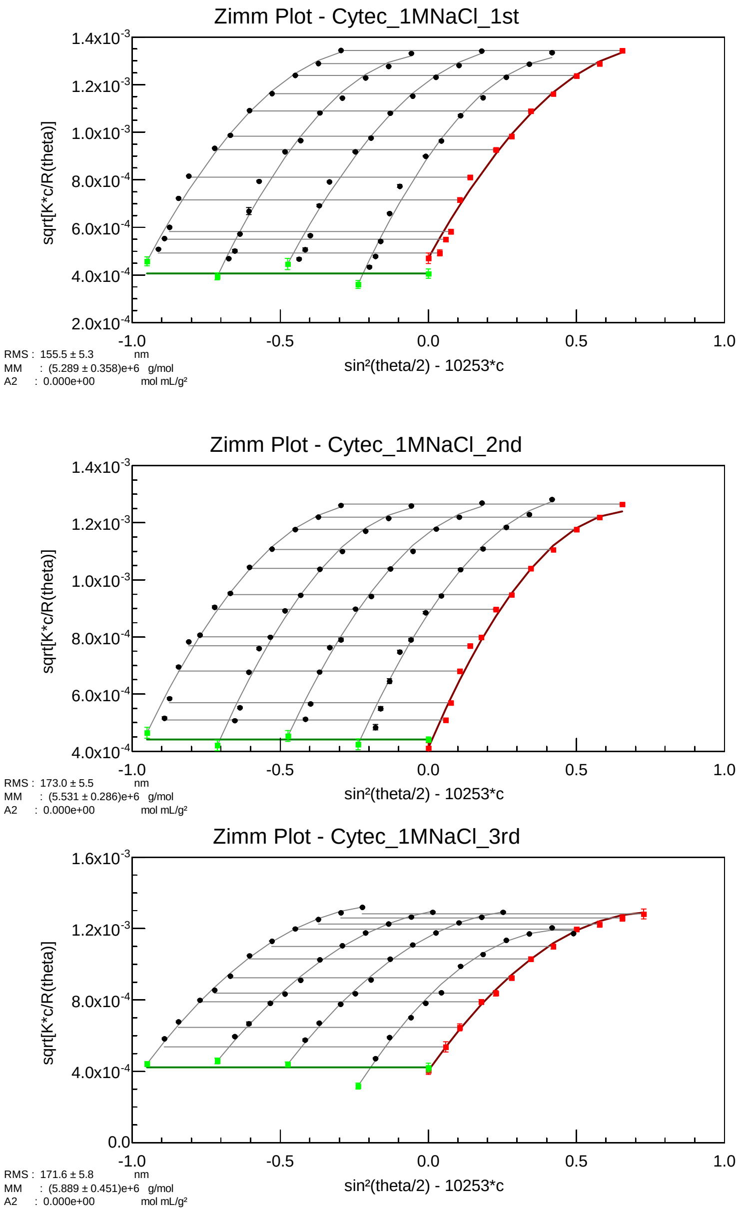

Figure A.11. Zimm-Berry plots for triplicate A8 PAM samples used to estimate molecular weights.

Appendix B

Molecular Weight Estimation with Intrinsic Viscosity Measurement Technique

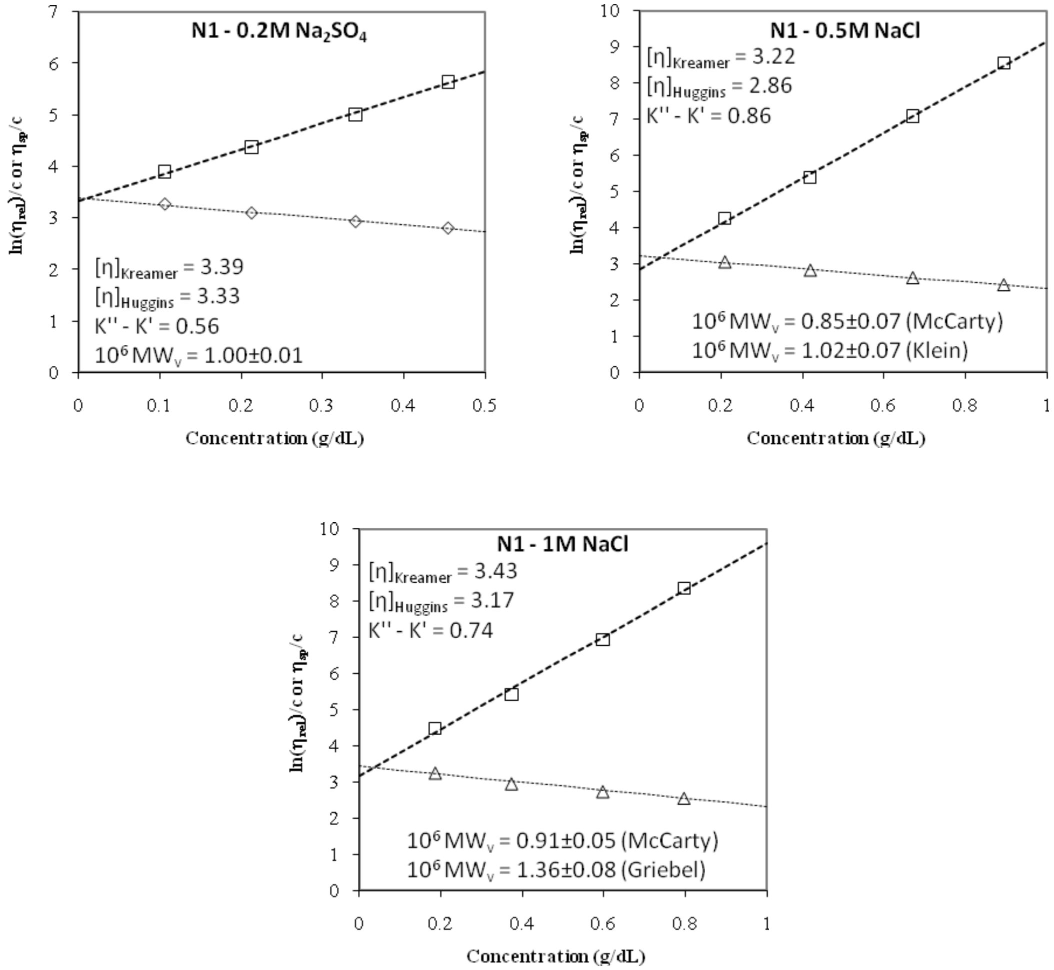

Figure B.1. Kreamer and Huggins plots of N1 PAM sample in different background salt species and concentrations, used to estimate molecular weights.

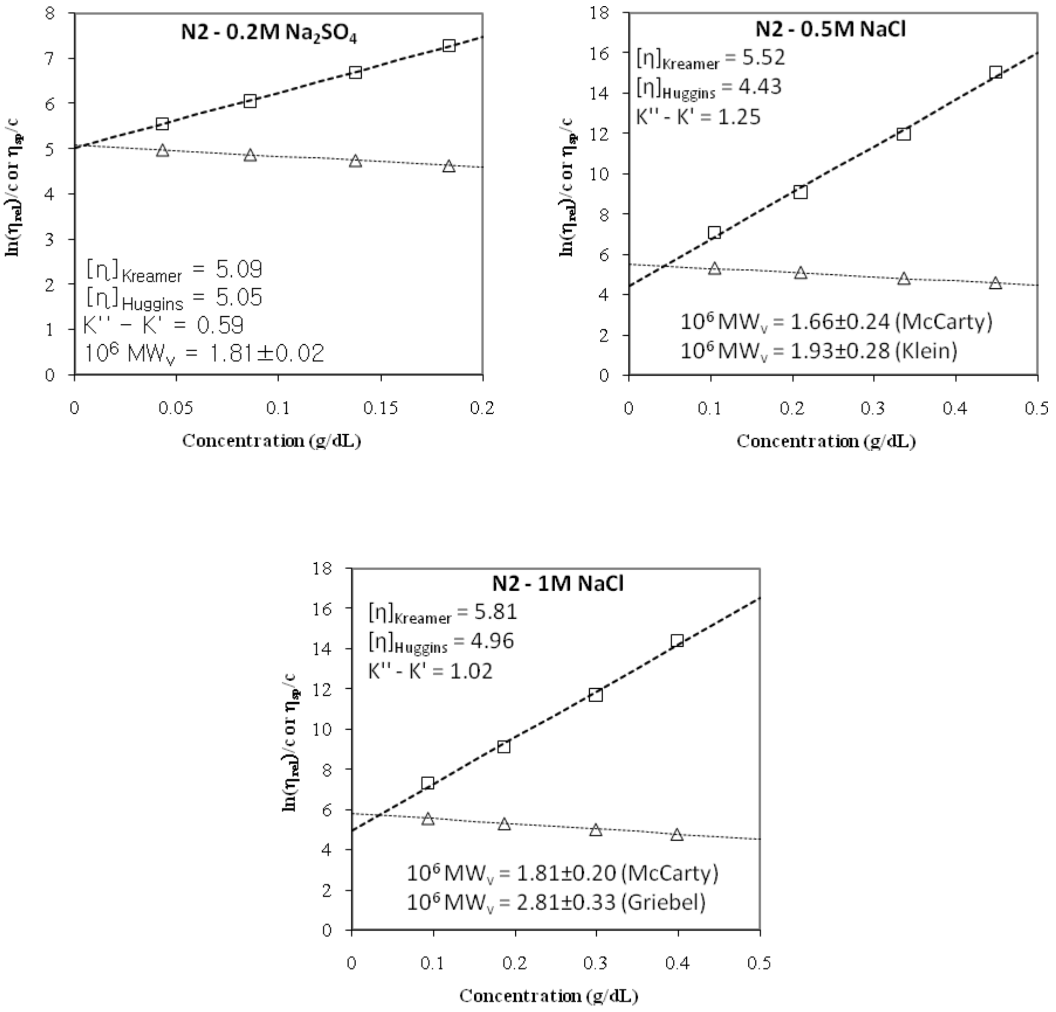

Figure B.2. Kreamer and Huggins plots of N2 PAM sample in different background salt species and concentrations, used to estimate molecular weights.

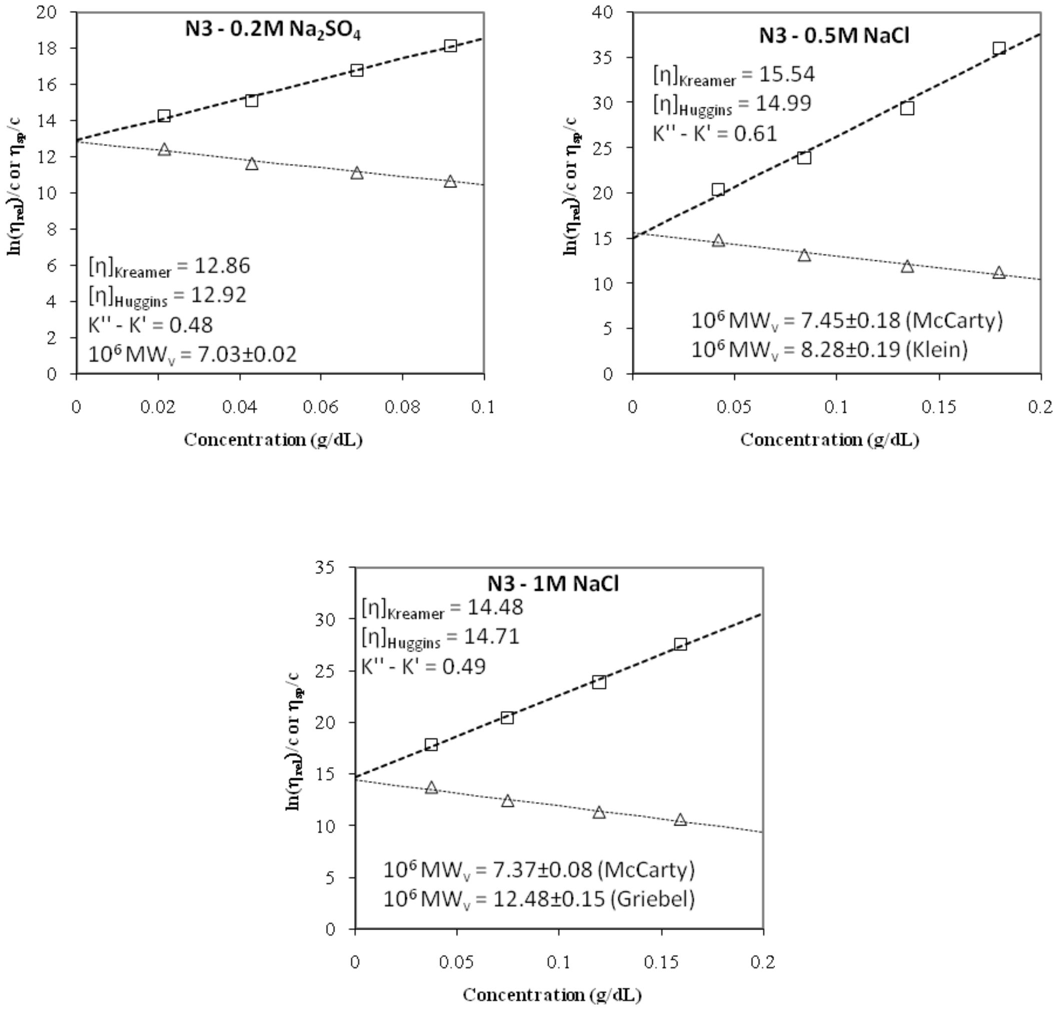

Figure B.3. Kreamer and Huggins plots of N3 PAM sample in different background salt species and concentrations, used to estimate molecular weights.

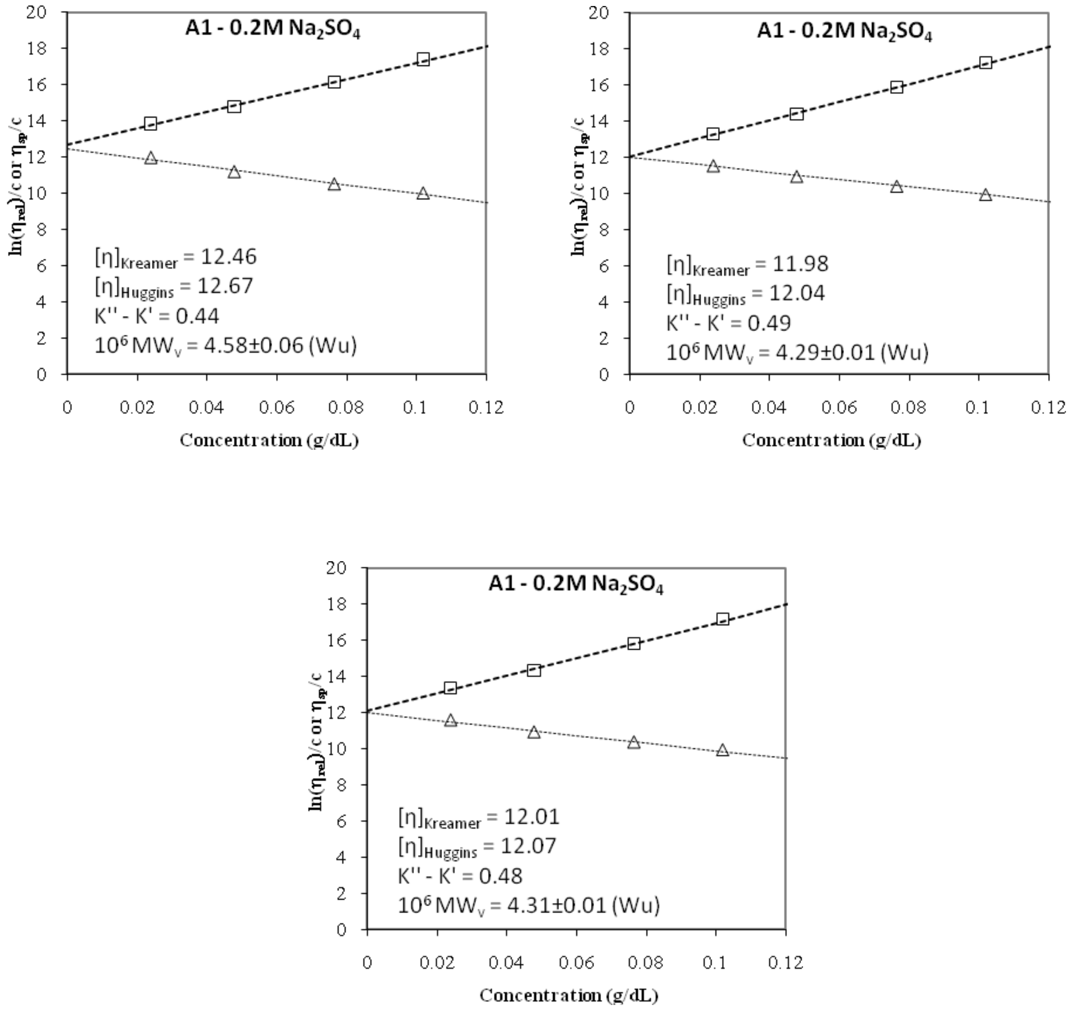

Figure B.4. Kreamer and Huggins plots for triplicate A1 PAM samples in 0.2 M Na_2SO_4, used to estimate molecular weights.

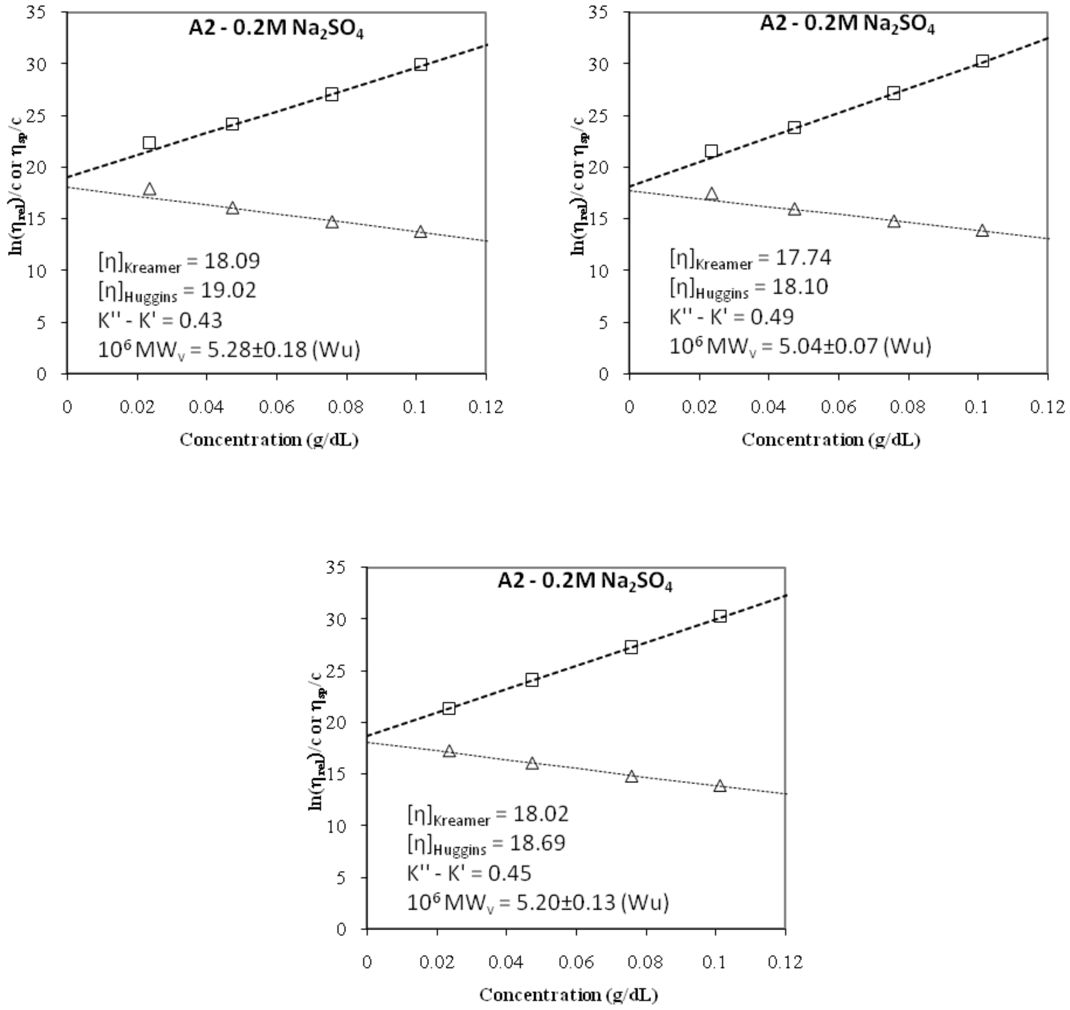

Figure B.5. Kreamer and Huggins plots for triplicate A2 PAM samples in 0.2 M Na_2SO_4, used to estimate molecular weights.

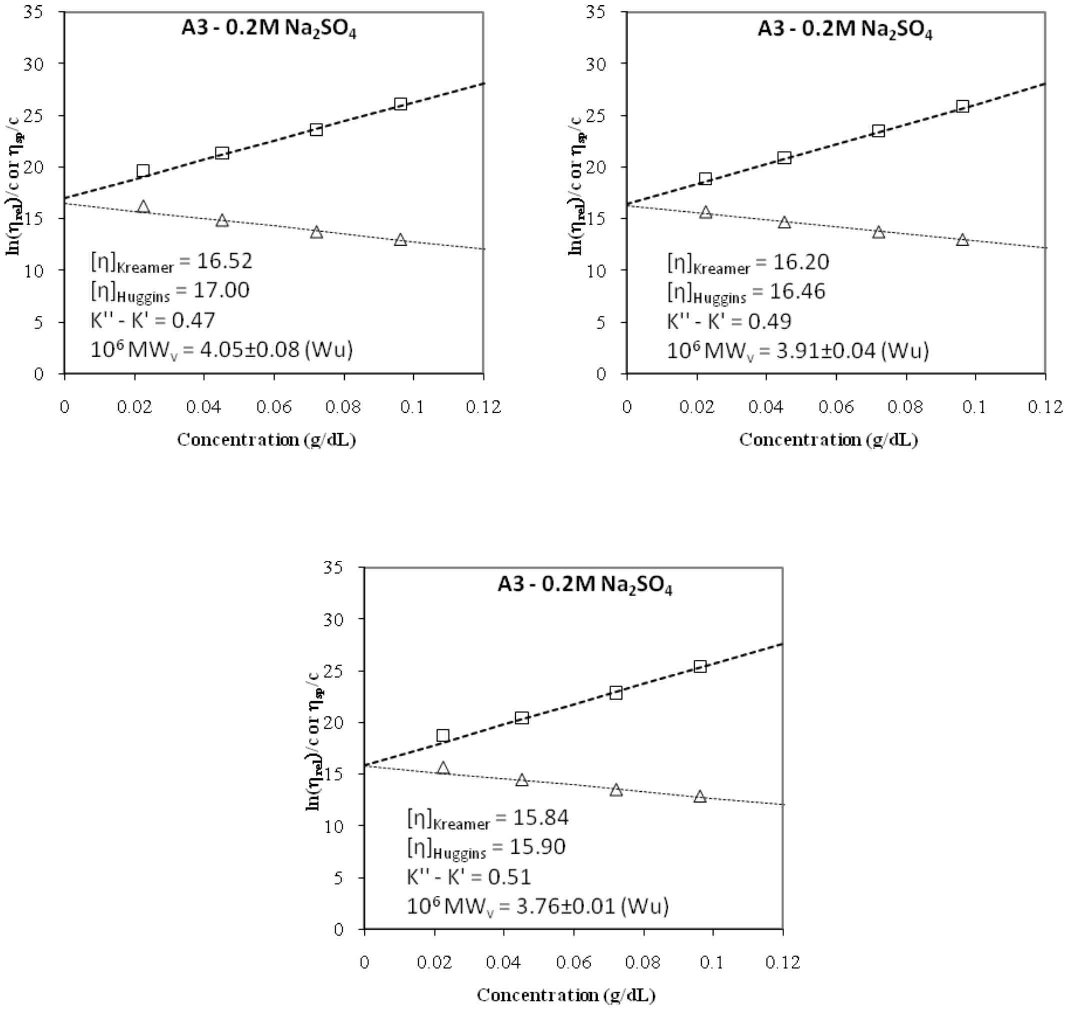

Figure B.6. Kreamer and Huggins plots for triplicate A3 PAM samples in 0.2 M Na_2SO_4, used to estimate molecular weights.

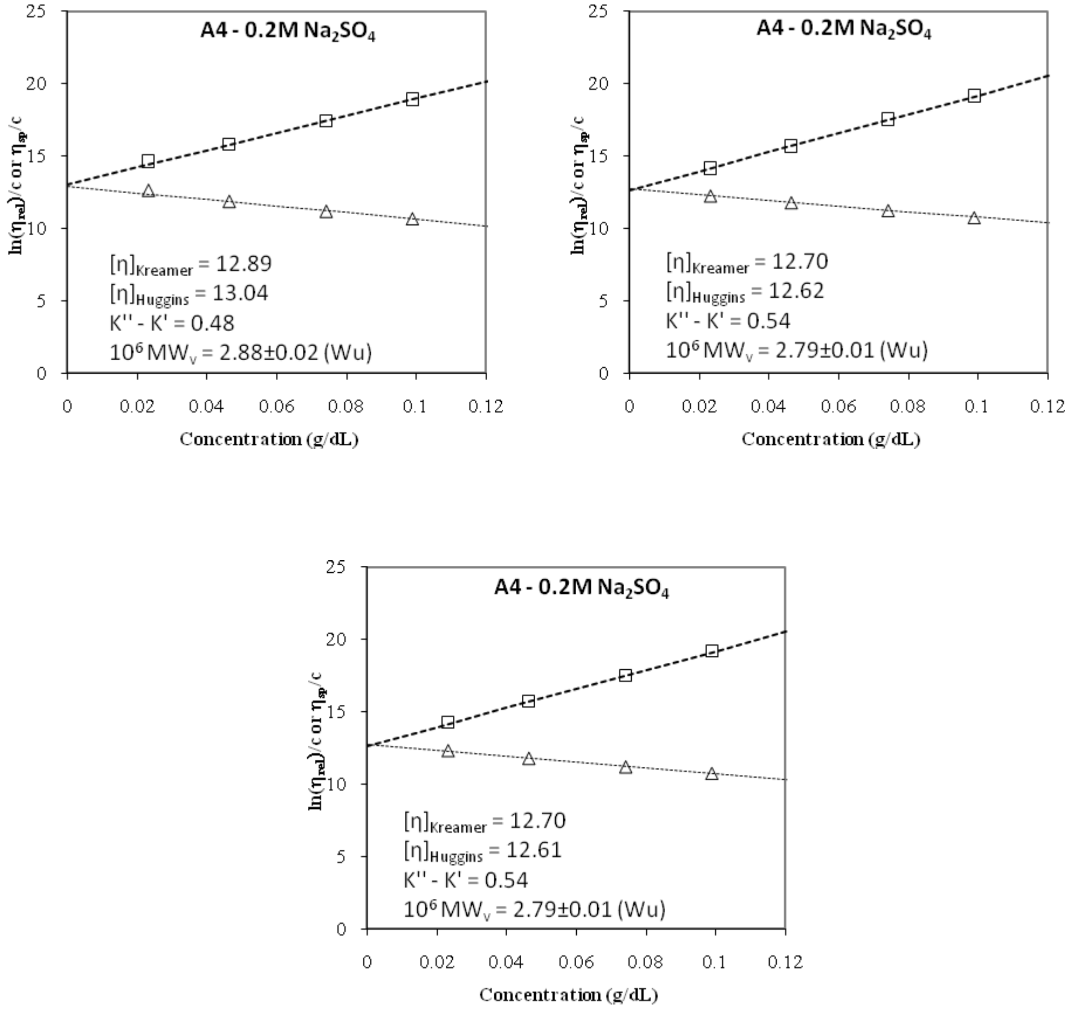

Figure B.7. Kreamer and Huggins plots for triplicate A4 PAM samples in 0.2 M Na_2SO_4, used to estimate molecular weights.

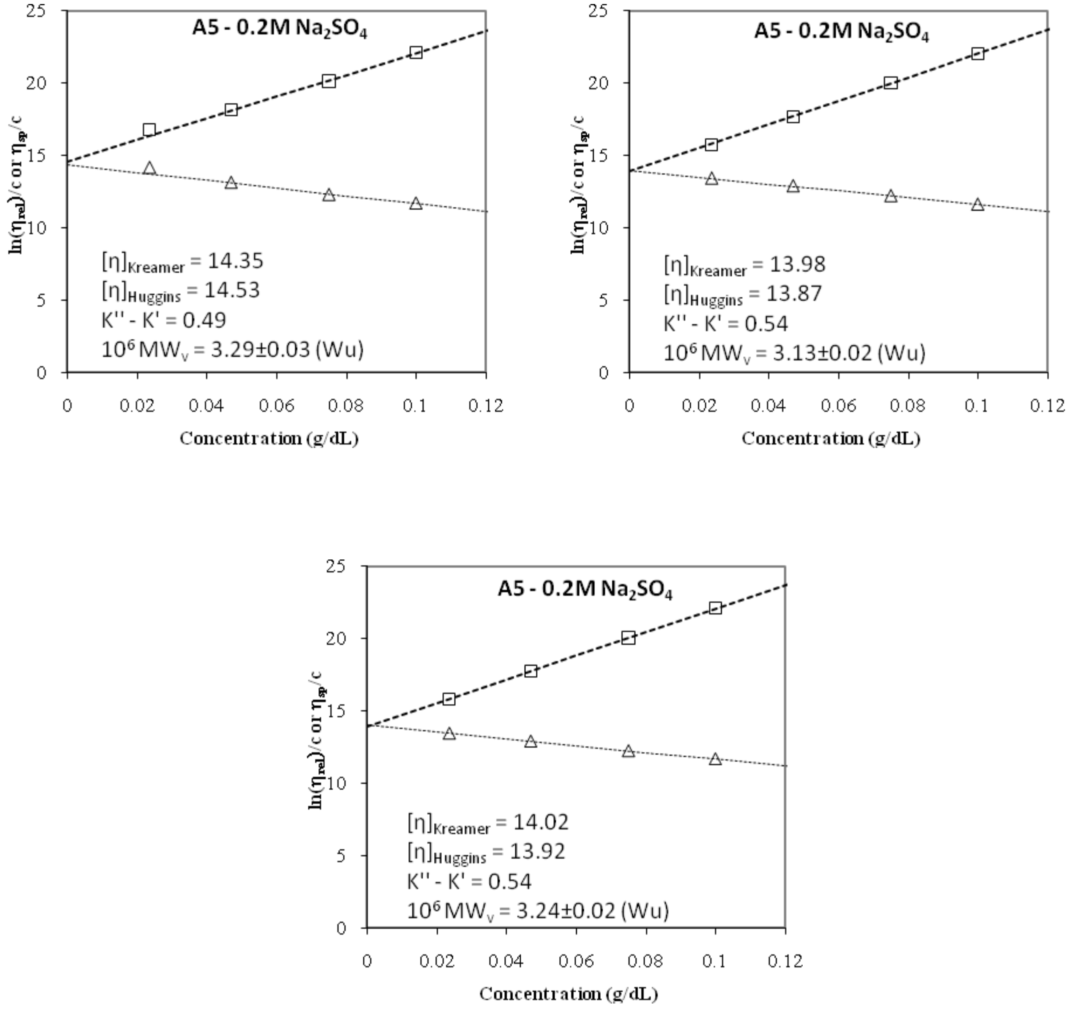

Figure B.8. Kreamer and Huggins plots for triplicate A5 PAM samples in 0.2 M Na_2SO_4, used to estimate molecular weights.

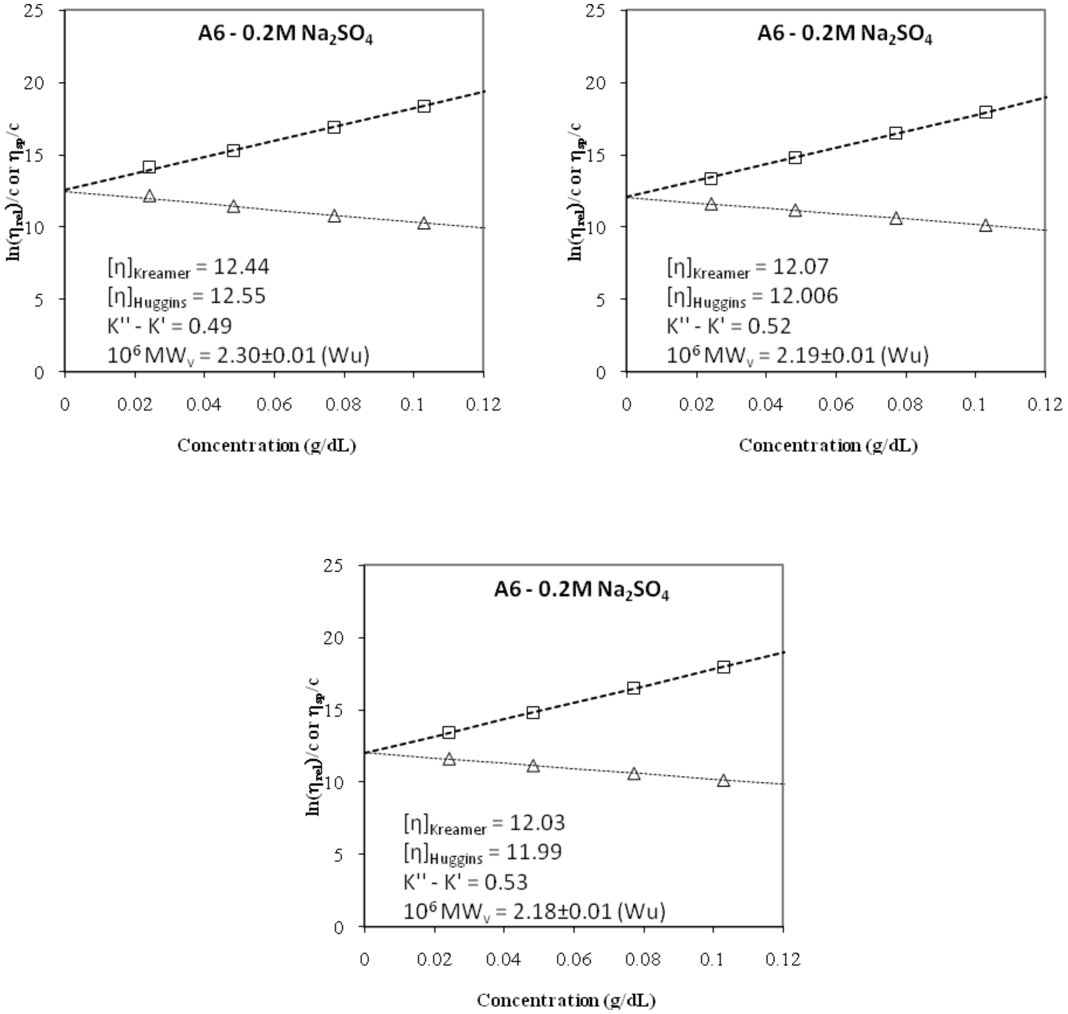

Figure B.9. Kreamer and Huggins plots for triplicate A6 PAM samples in 0.2 M Na_2SO_4, used to estimate molecular weights.

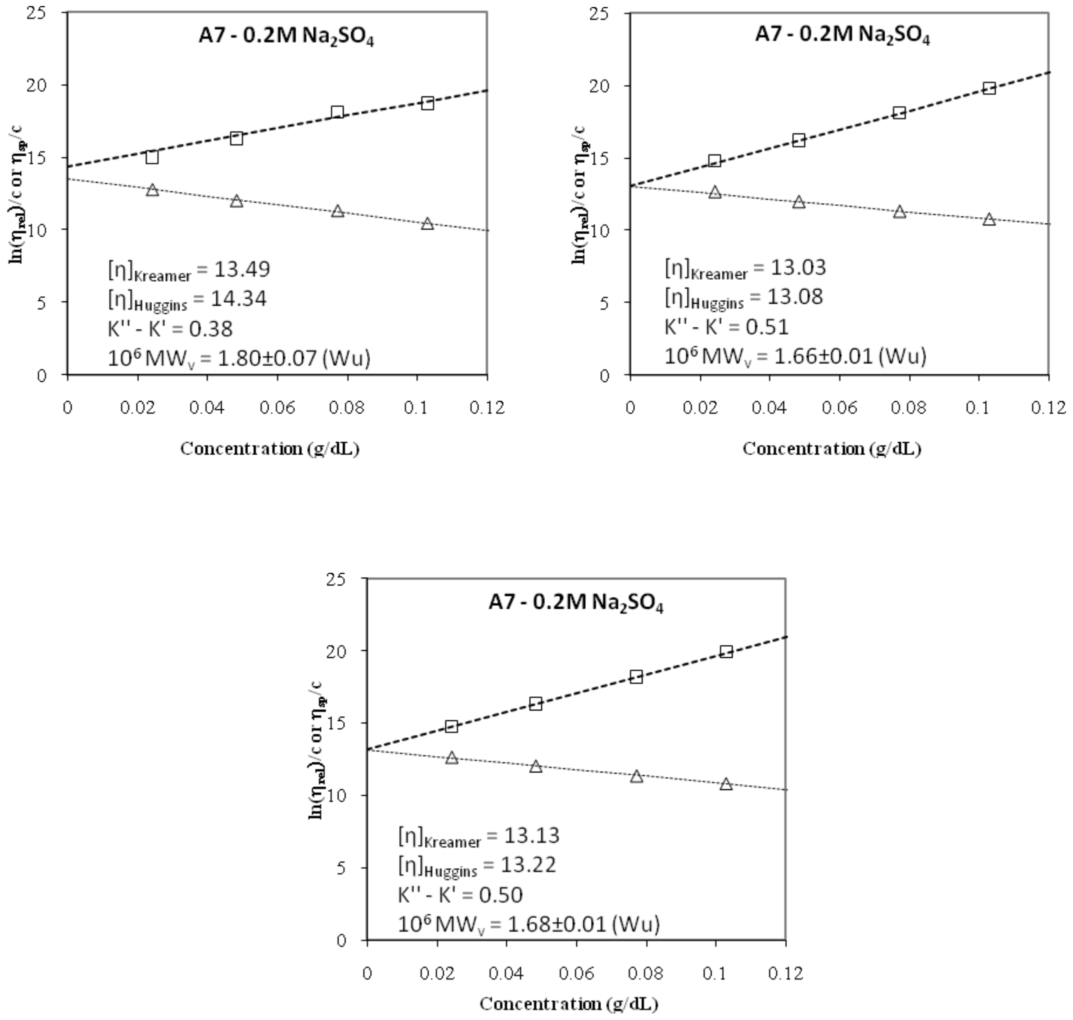

Figure B.10. Kreamer and Huggins plots for triplicate A7 PAM samples in 0.2 M Na_2SO_4, used to estimate molecular weights.

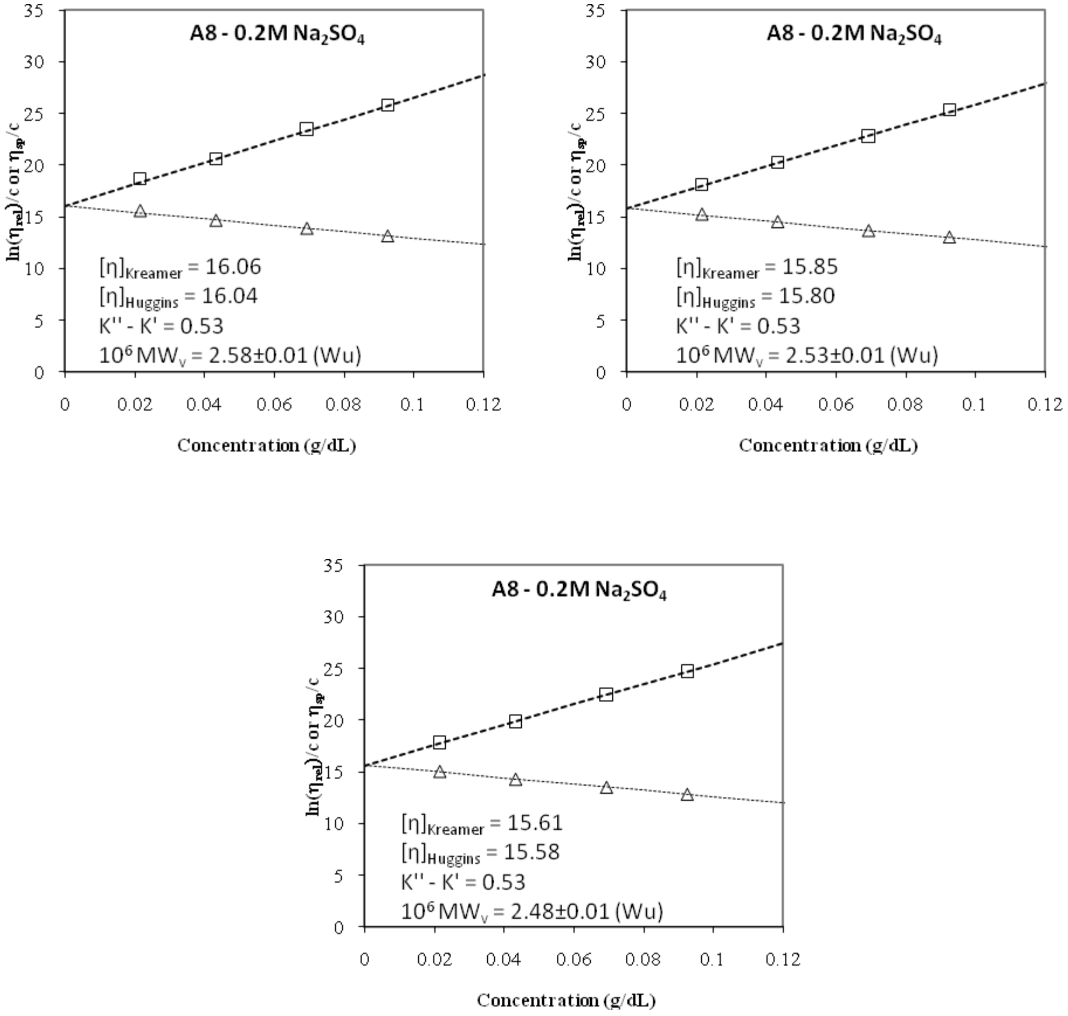

Figure B.11. Kreamer and Huggins plots for triplicate A8 PAM samples in 0.2 M Na_2SO_4, used to estimate molecular weights.

Appendix C

Charge Density Measurement with Potentiometric Acid-Base Titration

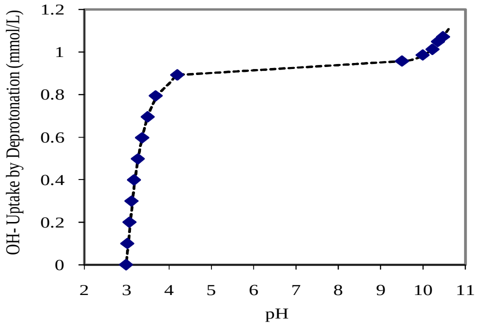

Fitting Equations (0.001M NaCl)

Upto pH4.2

y= -73.3376+159.7874*LN(pH)
-115.2477*(LN(pH))^2
+27.8359*(LN(pH))^3
R2= 0.9987

4.2<pH<9.6

Assume as Linear Increase

Above pH9.6

y= -45.0613+14.9344*(pH)
-1.6161*(pH)^2
+0.05831*(pH)^3
R2= 0.9929

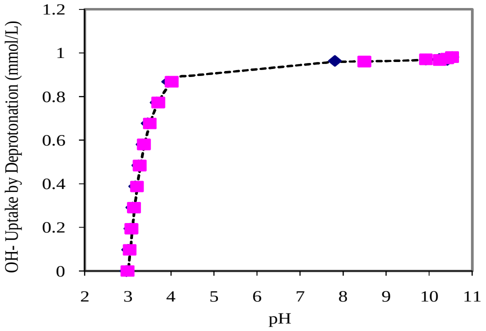

Fitting Equations (0.01M NaCl)

Upto pH4.1

y= -67.3277+145.8016*LN(pH)
-104.6555*(LN(pH))^2
+25.2213*(LN(pH))^3
R2= 0.9946

4.2<pH<7.8

Assume as Linear Increase

Above pH7.8

y= -0.9579+5.252E-6*EXP(0.7669*pH)
R2= 0.675

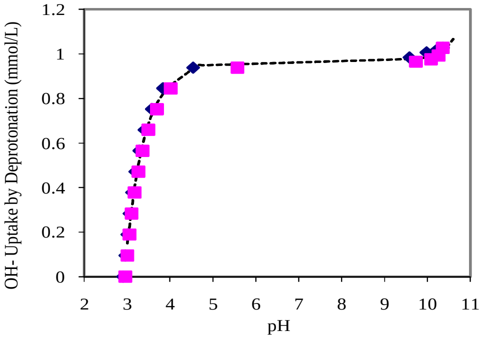

Fitting Equations (0.1M NaCl)

Upto pH4.6

y= -40.0929+84.1254*LN(pH)
-57.9533*(LN(pH))^2
+13.4005*(LN(pH))^3
R2= 0.9832

4.6<pH<9.6

Assume as Linear Increase

Above pH9.6

y= -0.9748+4.631E-19*EXP(3.757*pH)
R2= 0.6034

Figure C.1. Potentiometric titration curves and equations for background subtraction of the deprotonation capacity in 0.001 M, 0.01 M, and 0.1 M NaCl solutions.

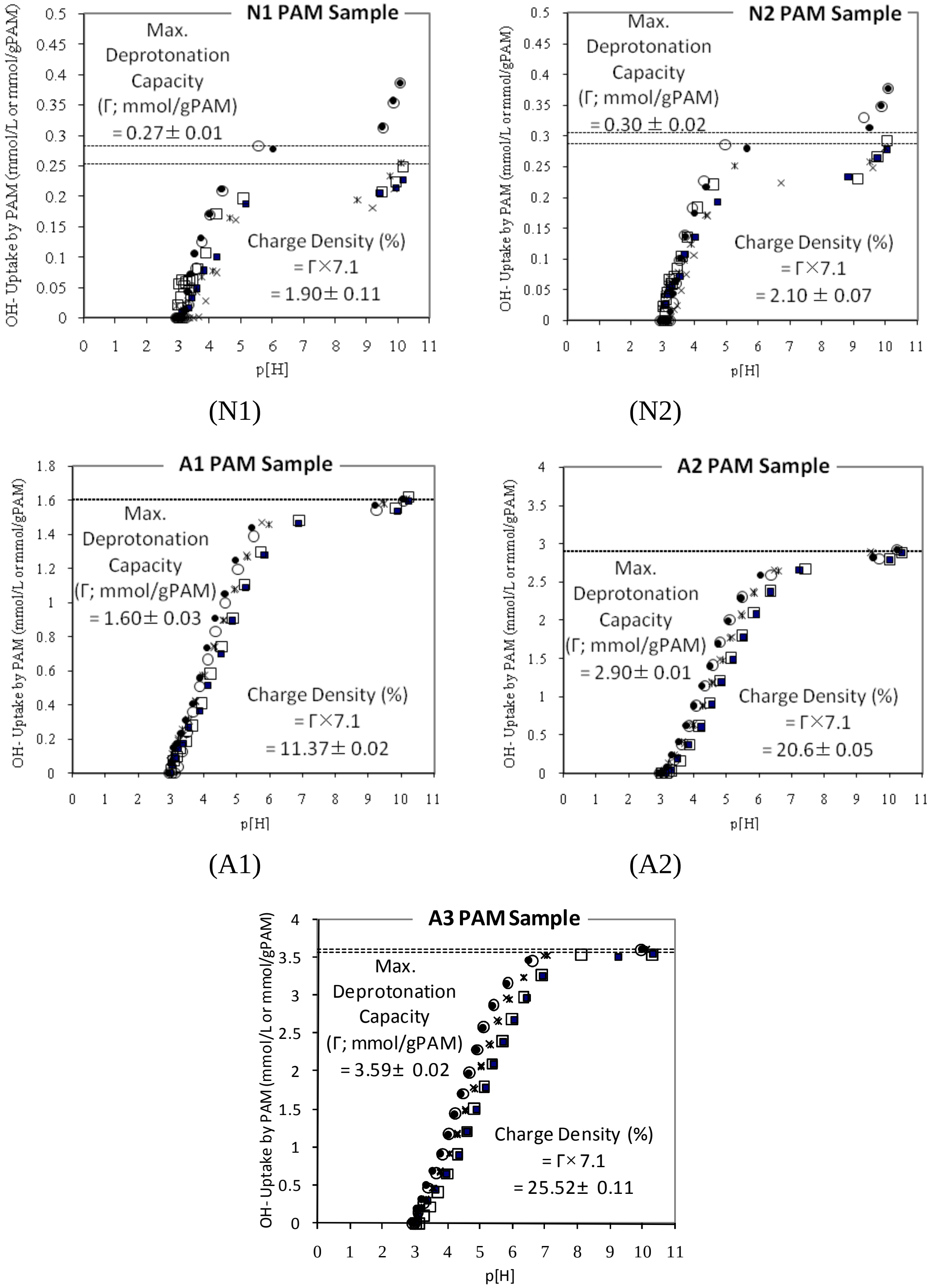

(N1) (N2)

(A1) (A2)

(A3)

Figure C.2. Potentiometric titration curves for N1, N2, A1, A2, and A3 PAM samples.

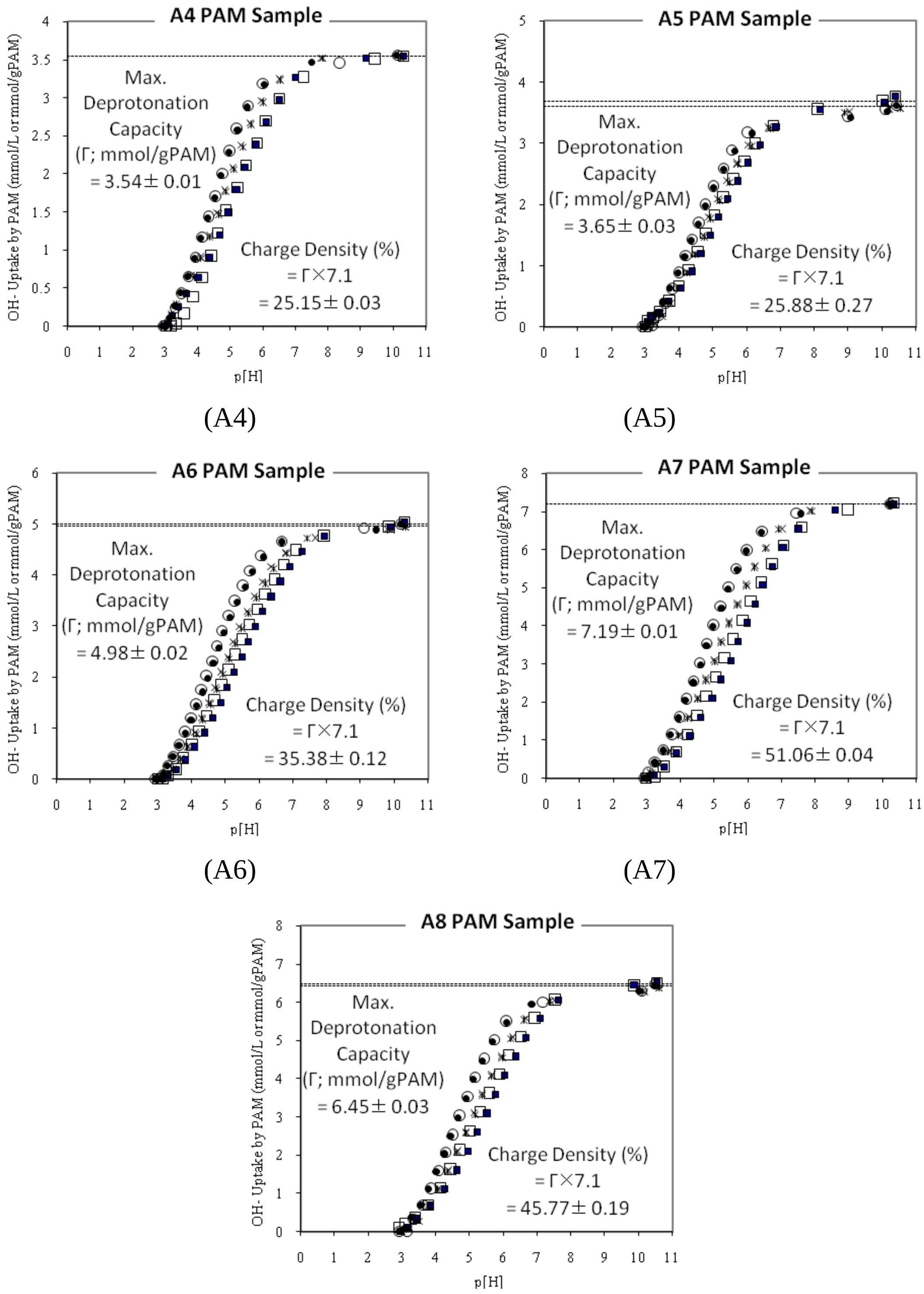

(A4) (A5)

(A6) (A7)

(A8)

Figure C.3. Potentiometric titration curves for A4, A5, A6, A7, and A8 PAM samples.

Appendix D

Potentiometric Titration Plots and Fitted Curves
with Donnan, Impermeable Sphere, and Cylindrical Models

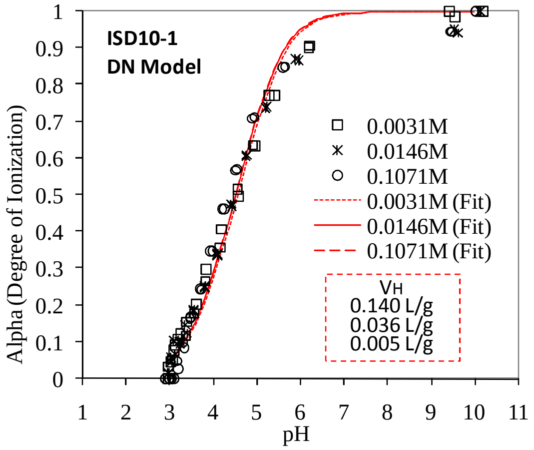

Figure D.1. Potentiometric titration plots for ISD10 PAM in different salt concentrations and fitted curves with DN model

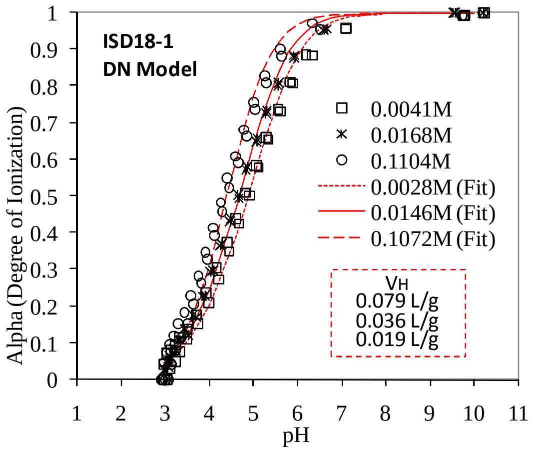

Figure D.2. Potentiometric titration plots for ISD18 PAM in different salt concentrations and fitted curves with DN model

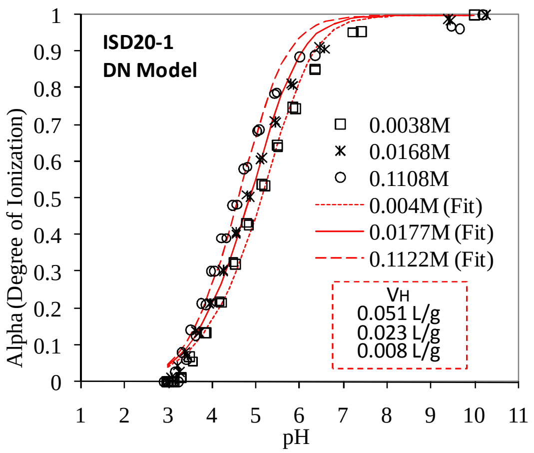

Figure D.3. Potentiometric titration plots for ISD20 PAM in different salt concentrations and fitted curves with DN model

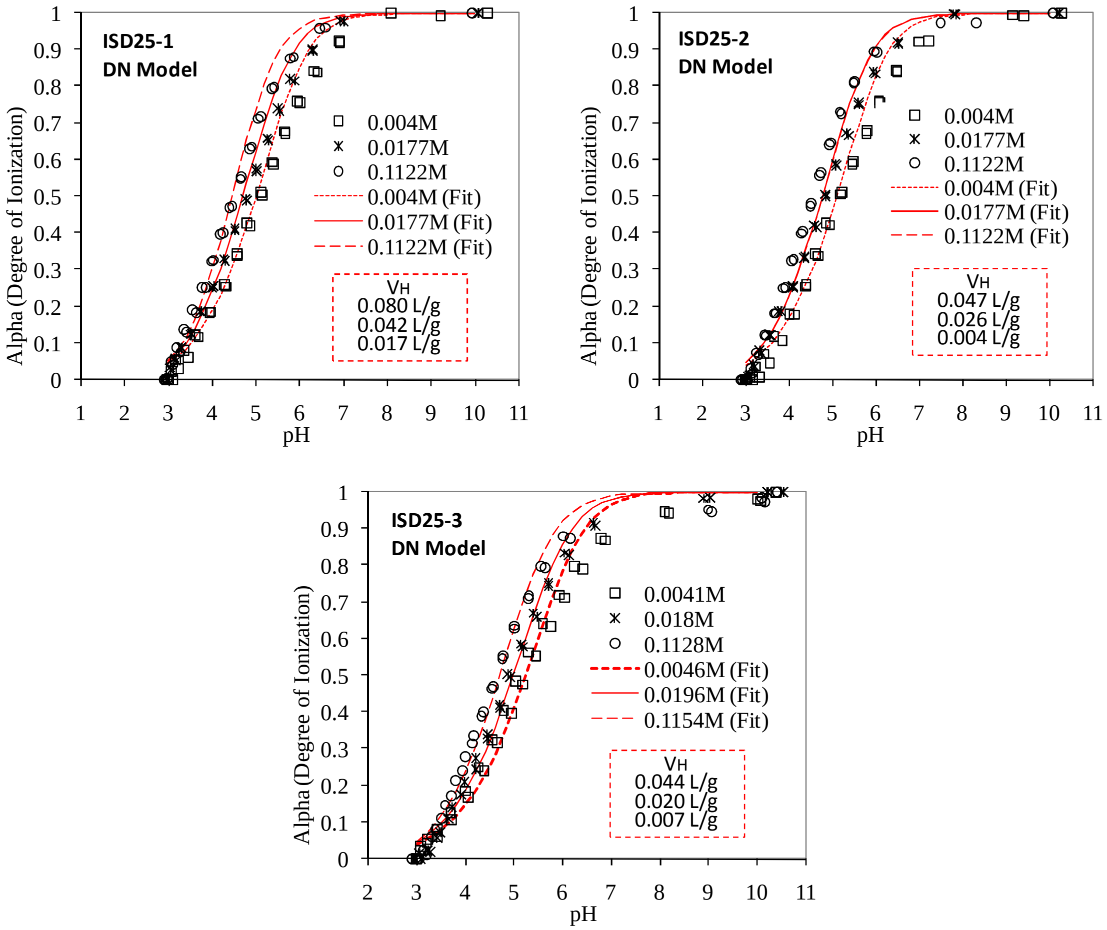

Figure D.4. Potentiometric titration plots for ISD25 PAMs in different salt concentrations and fitted curves with DN model

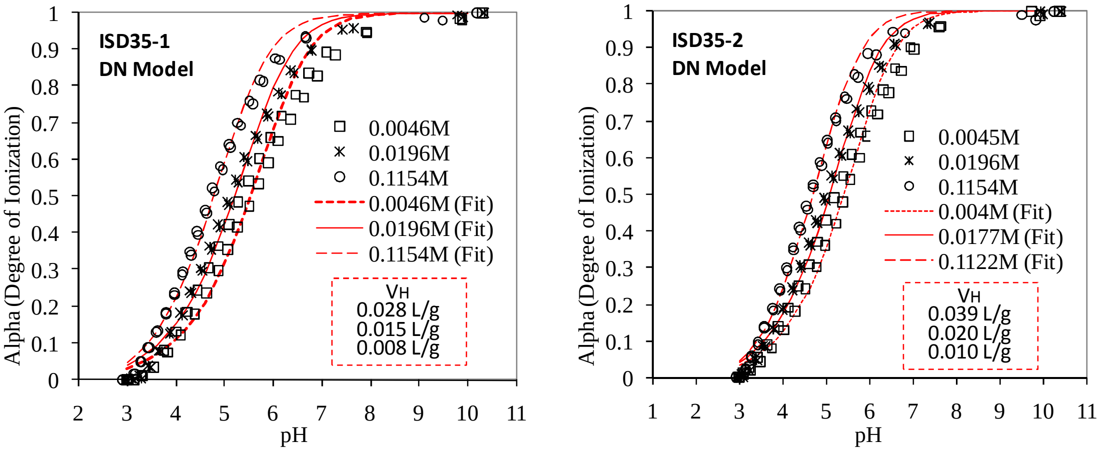

Figure D.5. Potentiometric titration plots for ISD35 PAMs in different salt concentrations and fitted curves with DN model

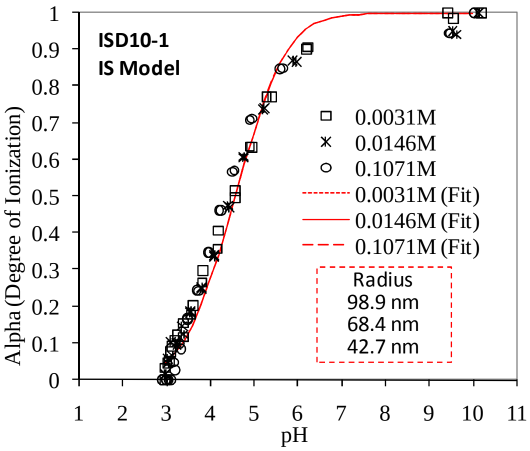

Figure D.6. Potentiometric titration plots for ISD10 PAM in different salt concentrations and fitted curves with IS model

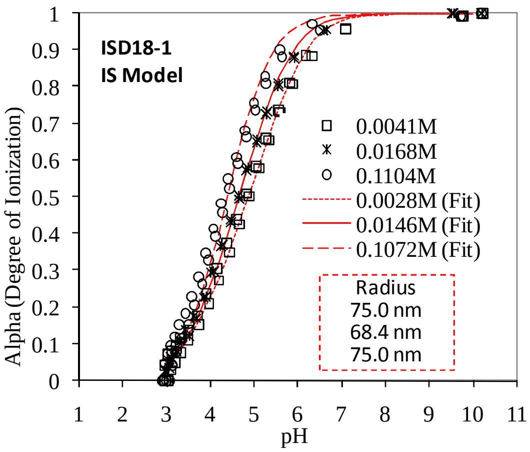

Figure D.7. Potentiometric titration plots for ISD18 PAM in different salt concentrations and fitted curves with IS model

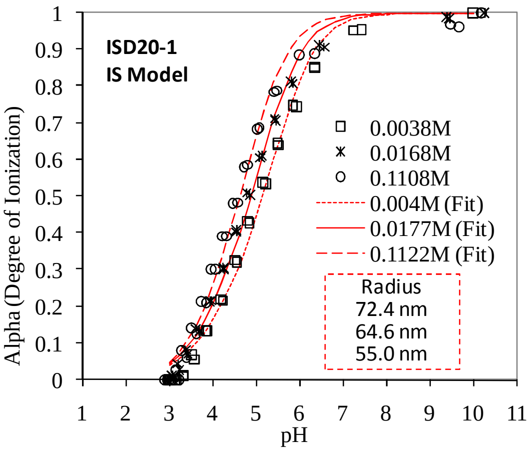

Figure D.8. Potentiometric titration plots for ISD20 PAM in different salt concentrations and fitted curves with IS model

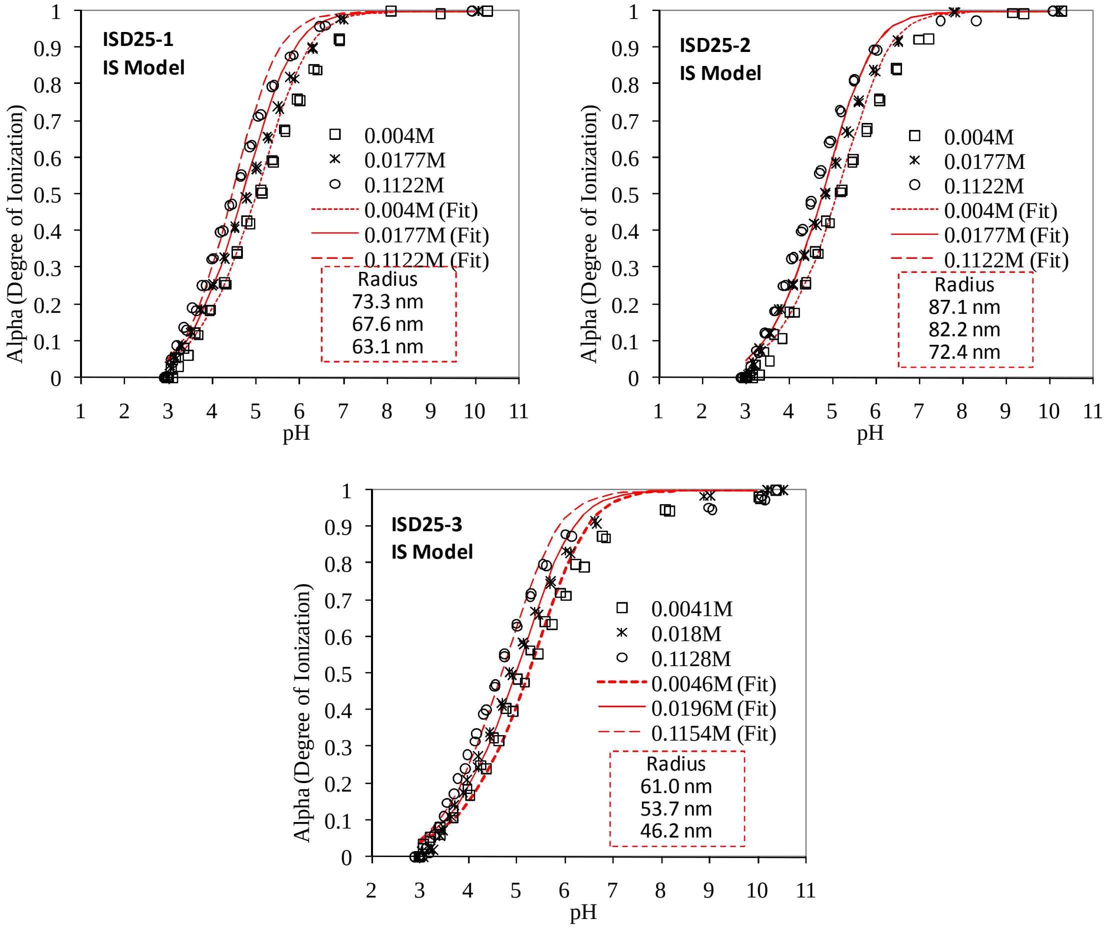

Figure D.9. Potentiometric titration plots for ISD25 PAMs in different salt concentrations and fitted curves with IS model

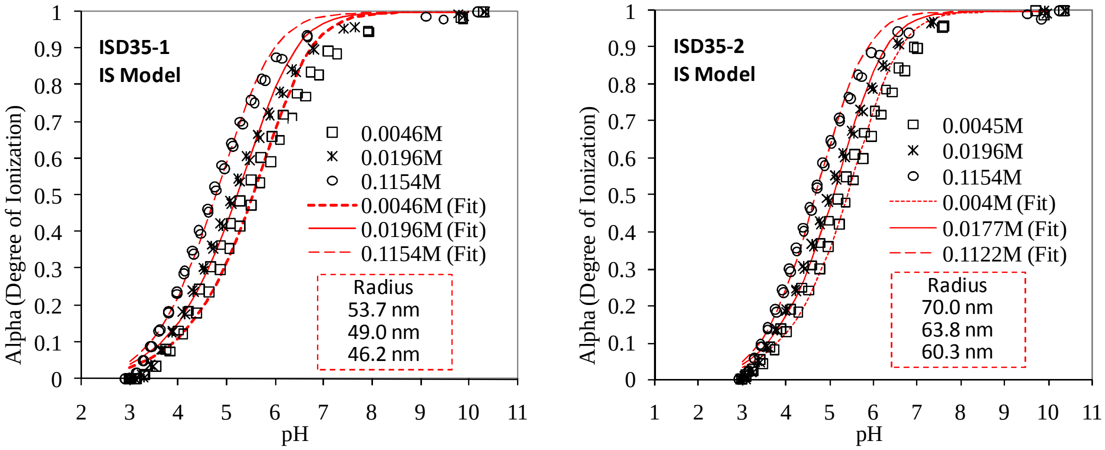

Figure D.10. Potentiometric titration plots for ISD35 PAMs in different salt concentrations and fitted curves with IS model

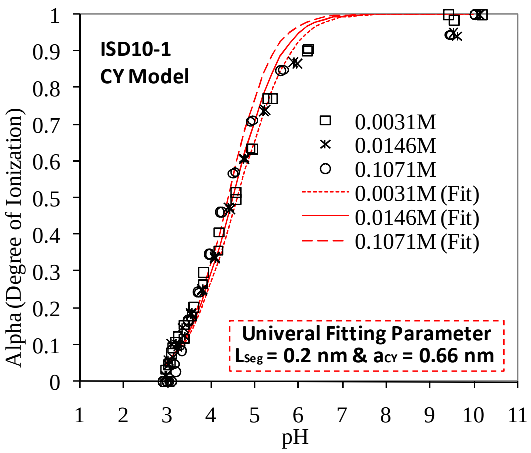

Figure D.11. Potentiometric titration plots for ISD10 PAM in different salt concentrations and fitted curves with CY model

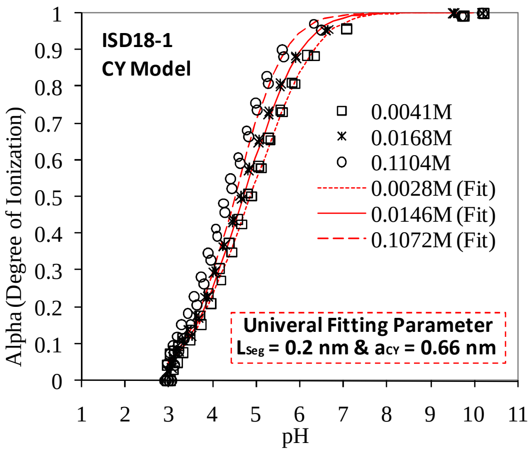

Figure D.12. Potentiometric titration plots for ISD18 PAM in different salt concentrations and fitted curves with CY model

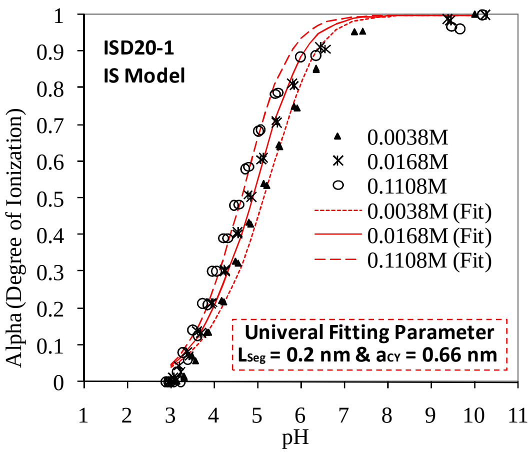

Figure D.13. Potentiometric titration plots for ISD20 PAM in different salt concentrations and fitted curves with CY model

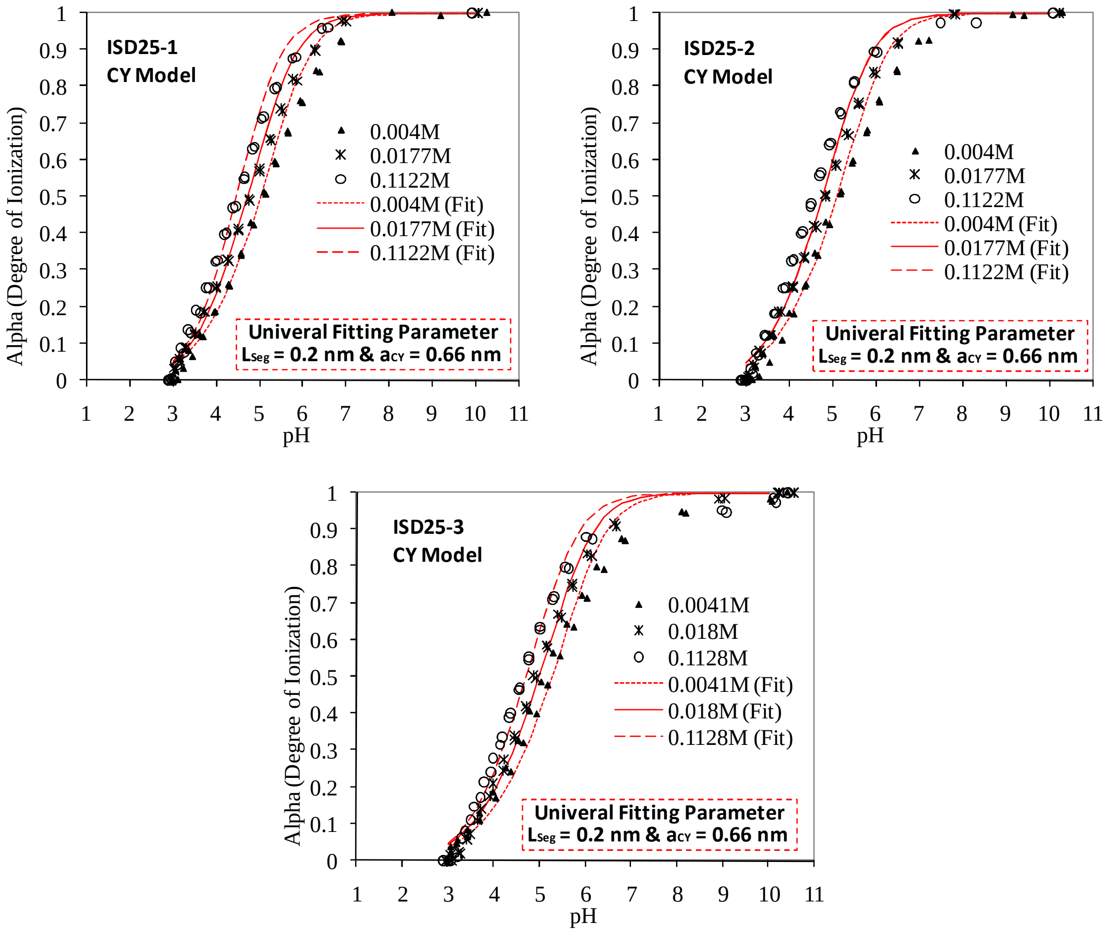

Figure D.14. Potentiometric titration plots for ISD25 PAMs in different salt concentrations and fitted curves with CY model

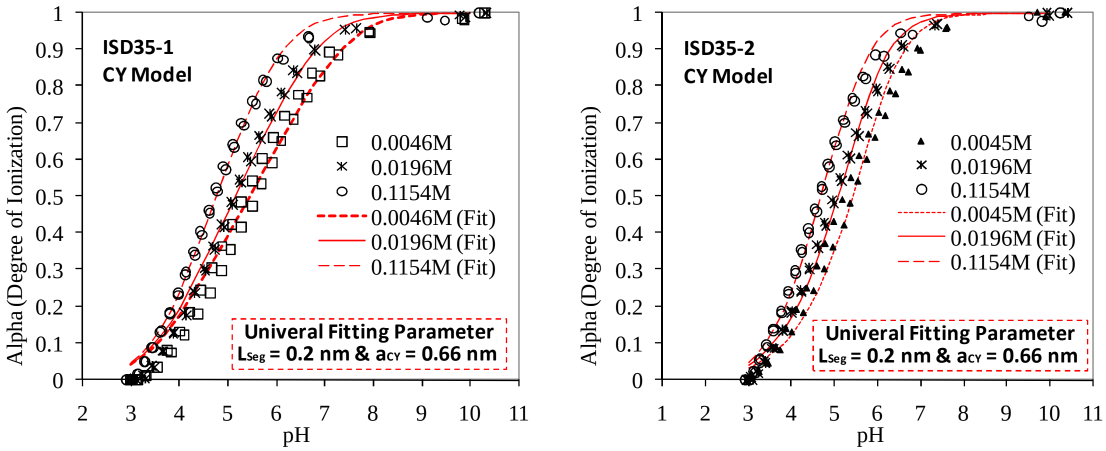

Figure D.15. Potentiometric titration plots for ISD35 PAMs in different salt concentrations and fitted curves with CY model

Appendix E

Specific Viscosity (η_{sp}) Plots with respect to pH for anionic PAMs

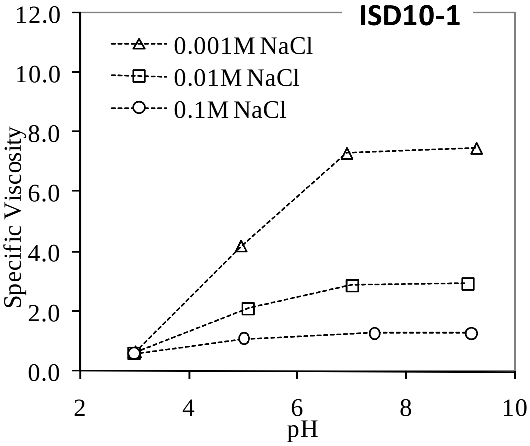

Figure E.1. Specific Viscosity (η_{sp}) Plots for ISD10 PAM in different salt concentrations

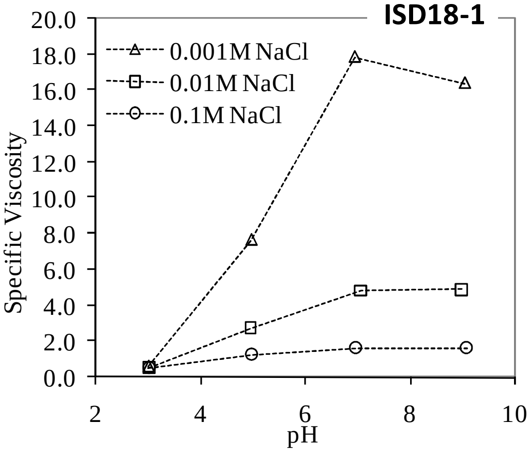

Figure E.2. Specific Viscosity (η_{sp}) Plots for ISD18 PAM in different salt concentrations

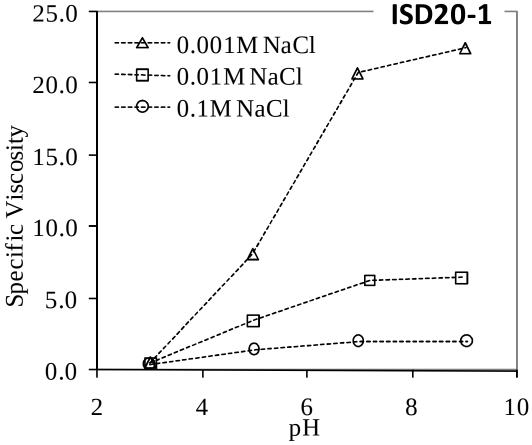

Figure E.3. Specific Viscosity (η_{sp}) Plots for ISD20 PAM in different salt concentrations

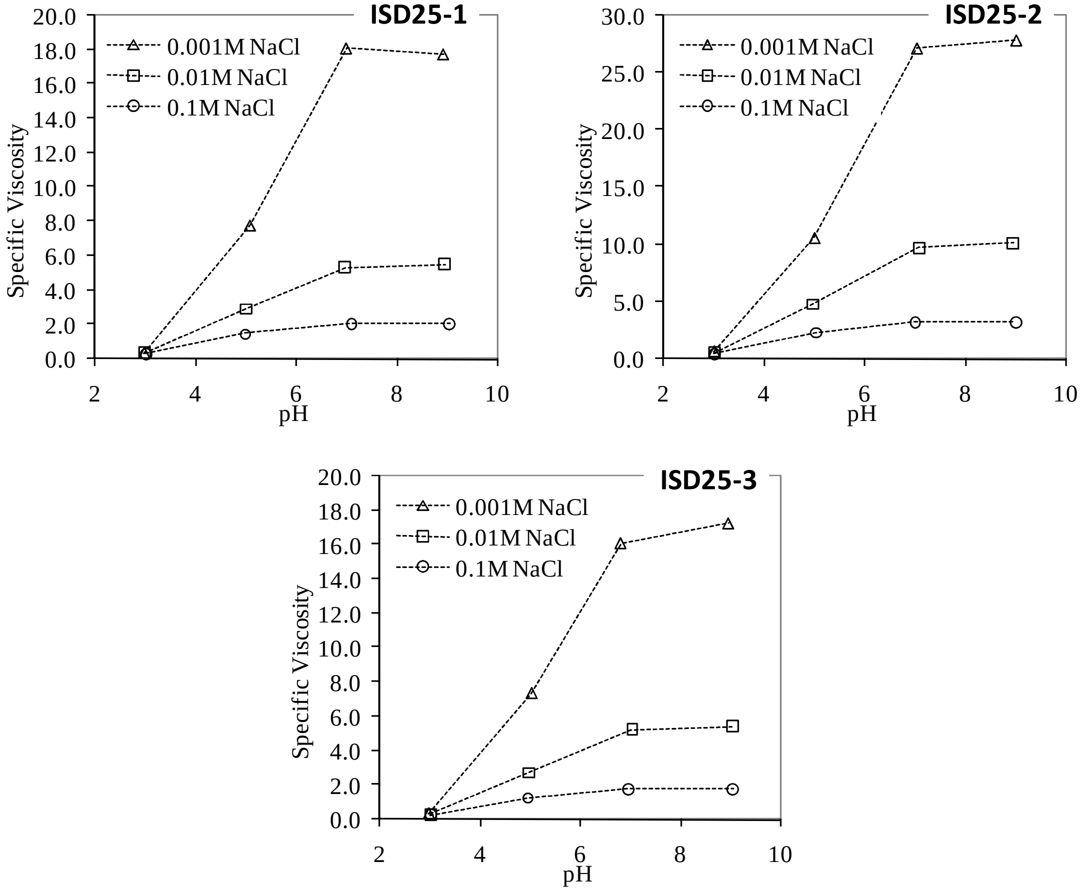

Figure E.4. Specific Viscosity (η_{sp}) Plots for ISD25 PAM in different salt concentrations

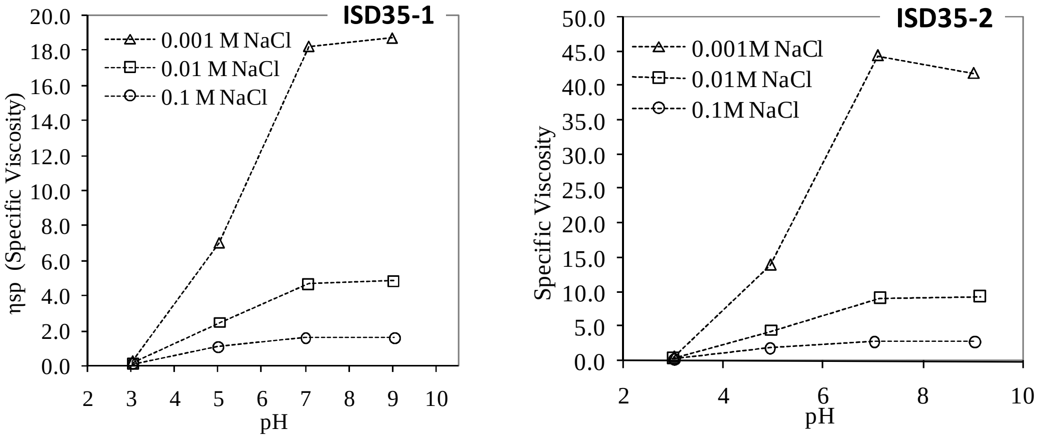

Figure E.5. Specific Viscosity (η_{sp}) Plots for ISD35 PAM in different salt concentrations

APENDIX F

Matlab® Code for Potentiometric Titration Data Fitting with DN, IS, and CY models

F.1 Code for data fitting with DN model

```
% Donnan Nonlinear Curve Fitting
global xdata pH Na_b_ini Cl_b_ini mass KH0 L_tot MW radius
avo F R T m_max

Na_b_ini=0.1197; % Ionic Strength (I or u)     *******
Cl_b_ini=0.1197; % Ionic Strength (I or u)     *******
mass=0.9259; % Mass of polyelectrolyte (gPAM/L)
*******
KH0=10^(4.25); % Acid Equilibrium Constant (Be careful
about sign!!!)
L_tot=0.006446835; % Maximum Deprotonating Capacity
=======
MW=2492155; % Molecular Weight of Polyelectrolyte (g/mol)
=======
avo=6.022*10^23; % Avogadro's Number (/mol)
F=96485; % Faraday Constant (C/mol)
R=8.314; % Ideal Gas Constant (J/mol/K)
T=298; % Temperature (K)

xdata = [“INPUT DATA”]; % pH data from experiments
ydata =[“INPUT DATA”]; % Alpha data from experiments
m_max=numel(xdata); % Number of experimental data
SRE=zeros(100,1); % Sum of Residual Error
radius=0; % Fitting Parameter!!! Donnan Volume of
polyelectrolyte

for i=1:100
    radius=10^(-8+i*0.005); % Unit m
    Fxdata = phiter;
    for m=1:m_max
        SRE(i)=SRE(i)+0.5*(Fxdata(m)-ydata(m))^2;
    end
end
```

```
% donnanzero Iteration with respect to pH
function ALPHA=phiter(VD, xdata)
global xdata pH Na_b_ini Cl_b_ini mass KH0 L_tot MW radius
avo F R T m_max
options = optimset('TolFun', 1e-16);
ALPHA=ones(m_max,1);
for k=1:m_max
    pH=xdata(k);
    chi_real=equilzero;
    ALPHA(k)=(L_tot*exp(-chi_real)/(KH0*pH+exp(-
chi_real))/mass)/L_tot*mass;
end
```

```
% Donnan Model Electrostatic Equilibration  elecequil.M
% Seeding Parameters
function y=elecequil(chi)
global xdata pH Na_b_ini Cl_b_ini mass KH0 L_tot MW radius
avo F R T
% Acid-Base Chemistry y value should be zero for
electrostatic equlibration
y=-2*1000*Na_b_ini*sinh(-chi)*(4*pi*(radius^3)*avo/3/MW)...
    -L_tot*exp(-chi)/(KH0*pH+exp(-chi))/mass; % Unit g/mol
```

```
% Find out zero of electrostatic equilibrium equilzero.m
function chi=equilzero(chi)
global xdata pH Na_b_ini Cl_b_ini mass KH0 L_tot MW radius
avo F R T
options = optimset('TolFun', 1e-16);
chi=fzero('elecequil', 0);
```

F.2 Code for data fitting with IS model

```
% Impermeable Sphere Nonlinear Curve Fitting
global xdata pH Na_b_ini Cl_b_ini mass KH0 L_tot MW radius
avo F R T debye  m_max

Na_b_ini=0.1212; % Background Salt Concentration (mol/L)
*******
Cl_b_ini=0.1212; % Background Salt Concentration (mol/L)
*******
mass=0.9217; % Mass of polyelectrolyte (gPAM/L)     *******
L_tot=0.007191383; % Maximum Deprotonating Capacity
=======
MW=1970321; % Molecular Weight of Polyelectrolyte (g/mol)
=======
KH0=10^(4.25); % Acid Equilibrium Constant (Be careful
about sign!!!)
avo=6.022*10^23; % Avogadro's Number (/mol)
F=96485; % Faraday Constant (C/mol)
R=8.314; % Ideal Gas Constant (J/mol/K)
T=298; % Temperature (K)
epslon0=8.854*10^(-12); % Permittivity of Free Space
(C/V/m)
epslon=78.5; % Relative Dielectric Constant of Water
debye=(2*F^2*Na_b_ini*1000/(R*T*epslon0*epslon))^(0.5); %
Debye Parameter (/m)

xdata = [“INPUT DATA”]; % pH data from experiments
ydata =[“INPUT DATA”]; % Alpha data from experiments
m_max=numel(xdata); % Number of experimental data
SRE=zeros(100,1); % Sum of Residual Error
radius=0; % Fitting Parameter!!!

for i=1:100
    radius=10^(-7.5+i*0.005);
    Fxdata = phiter;
    for m=1:m_max
        SRE(i)=SRE(i)+0.5*(Fxdata(m)-ydata(m))^2;
    end
end
```

```
% ISzero Iteration with respect to pH
function ALPHA=phiter(radius, xdata)
global xdata pH Na_b_ini Cl_b_ini mass KH0 L_tot MW radius
avo F R T debye  m_max
options = optimset('TolFun', 1e-16);
ALPHA=ones(m_max,1);
for k=1:m_max
    pH=xdata(k);
    chi_real=equilzero;
    ALPHA(k)=(L_tot*exp(-chi_real)/(KH0*pH+exp(-
chi_real))/mass)/L_tot*mass;
end
```

```
% Impermeable Sphere Model Electrostatic Equilibration
elecequil.M
% Seeding Parameters
function y=elecequil(chi)
global xdata pH Na_b_ini Cl_b_ini mass KH0 L_tot MW radius
avo F R T debye  m_max
% Acid-Base Chemistry y value should be zero for
electrostatic equlibration
y=-2*Na_b_ini/debye*1000*(2*sinh(-0.5*chi)...
    +4/(debye*radius)*tanh(-0.25*chi))...
    -(L_tot*exp(-chi)/(KH0*pH+exp(-chi))/mass)...
    *MW/(4*pi*(radius^2)*avo);
```

```
% Find out zero of electrostatic equilibrium equilzero.m
function chi=equilzero(chi)
global xdata pH Na_b_ini Cl_b_ini mass KH0 L_tot MW radius
avo F R T debye  m_max
options = optimset('TolFun', 1e-16);
chi=fzero('elecequil', 0);
```

F.3 Code for data fitting with IS model

```
% Cylindrical Nonlinear Curve Fitting
global xdata pH Na_b_ini Cl_b_ini mass KH0 L_tot epslon0
epslon debye MW radius avo F R T debye Lc Lsp m_max

Na_b_ini=0.0055; % Background Salt Concentration (mol/L)
*******
Cl_b_ini=0.0055; % Background Salt Concentration (mol/L)
*******
mass=0.9843; % Mass of polyelectrolyte (gPAM/L)     *******
L_tot=0.006446835; % Maximum Deprotonating Capacity)
=======
MW=2492155; % Molecular Weight of Polyelectrolyte (g/mol)
=======
KH0=10^(4.25); % Acid Equilibrium Constant (Be careful
about sign!!!)
avo=6.022*10^23; % Avogadro's Number (/mol)
F=96485; % Faraday Constant (C/mol)
R=8.314; % Ideal Gas Constant (J/mol/K)
T=298; % Temperature (K)
epslon0=8.854*10^(-12); % Permittivity of Free Space
(C/V/m)
epslon=78.5; % Relative Dielectric Constant of Water
debye=(2*F^2*Na_b_ini*1000/(R*T*epslon0*epslon))^(0.5); %
Debye Parameter (/m)
Lc=MW/71*0.252*10^-9; % Chain Length (m)
Lsp=Lc*avo/MW; % Specific Contour Length (m/gPAM)

xdata = [“INPUT DATA”]; % pH data from experiments
ydata =[“INPUT DATA”]; % Alpha data from experiments
m_max=numel(xdata); % Number of experimental data
SRE=zeros(100,1); % Sum of Residual Error
radius=0; % Fitting Parameter!!! Donnan Volume of
polyelectrolyte

for i=1:100
    radius=(0.4+0.005*i)*10^-9;
    Fxdata = phiter;
    for m=1:m_max
        SRE(i)=SRE(i)+0.5*(Fxdata(m)-ydata(m))^2;
    end
end
```

```
% CYzero Iteration with respect to pH
function ALPHA=phiter(radius, xdata)
global xdata pH Na_b_ini Cl_b_ini mass KH0 L_tot epslon0
epslon debye MW radius avo F R T debye Lc Lsp m_max
options = optimset('TolFun', 1e-16);
ALPHA=ones(m_max,1);
for k=1:m_max
    pH=xdata(k);
    chi_real=equilzero;
    ALPHA(k)=(L_tot*exp(-chi_real)/(KH0*pH+exp(-
chi_real))/mass)/L_tot*mass;
end
```

```
% CY Model Electrostatic Equilibration  elecequil.M
% Seeding Parameters
function y=elecequil(chi)
global xdata pH Na_b_ini Cl_b_ini mass KH0 L_tot epslon0
epslon debye MW radius avo F R T debye Lc Lsp m_max
% Acid-Base Chemistry y value should be zero for
electrostatic equlibration
y=-epslon0*epslon*debye*besselk(1, debye*radius)/besselk(0,
debye*radius)...
    *(-chi*R*T/F)*1*2*pi*radius*Lsp/F...
    -(L_tot*exp(-chi)/(KH0*pH+exp(-chi))/mass);
```

```
% Find out zero of electrostatic equilibrium equilzero.m
function chi=equilzero(chi)
global xdata pH Na_b_ini Cl_b_ini mass KH0 L_tot epslon0
epslon debye MW radius avo F R T debye Lc Lsp m_max
options = optimset('TolFun', 1e-16);
chi=fzero('elecequil', 0);
```

Appendix G

Finite Difference Approximation of Multi-Dimensional PBEs

G.1 PBE differential equations

$$\begin{aligned}&\left[\frac{\partial n_i}{\partial t}\right]+\left[\frac{\partial}{\partial x}(\langle U_x\rangle n_i)+\frac{\partial}{\partial y}(\langle U_y\rangle n_i)+\frac{\partial}{\partial z}(\langle U_z\rangle n_i)\right]+u_{gi}\frac{\partial n_i}{\partial z}\\&-\left[\frac{\partial}{\partial x}\left(C_\mu\frac{k^2}{\varepsilon}\frac{\partial n_i}{\partial x}\right)+\frac{\partial}{\partial y}\left(C_\mu\frac{k^2}{\varepsilon}\frac{\partial n_i}{\partial y}\right)+\frac{\partial}{\partial z}\left(C_\mu\frac{k^2}{\varepsilon}\frac{\partial n_i}{\partial z}\right)\right]=(agg/break)_i\end{aligned} \tag{A.1}$$

$$\begin{aligned}(agg/break)_i&=\frac{\partial n_i}{\partial t}=n_{i-1}\sum_{j=1}^{i-2}2^{j-i+1}\alpha_{i-1,j}\beta_{i-1,j}n_j+\frac{1}{2}\alpha_{i-1,i-1}\beta_{i-1,i-1}n_{i-1}^2\\&-n_i\sum_{j=1}^{i-1}2^{j-i}\alpha_{i,j}\beta_{i,j}n_j-n_i\sum_{j=i}^{(max\ i)}\alpha_{i,j}\beta_{i,j}n_j-a_in_i+\sum_{j=i+1}^{(max\ i)+2}b_{i,j}a_jn_j\end{aligned} \tag{A.2}$$

Equation (A.1), $n_i = n(x, y, z, D_i, t)$ = number concentration of flocs of linear class size D_i ($i=1, 2, \ldots i_{max}$; $D_1 \le D_i \le D_{max}$; for all D_i, n_i is called the population density function), x, y, z, t = position and time, $\langle U_x\rangle$, $\langle U_y\rangle$, and $\langle U_z\rangle$ = mean fluid velocity components in the x, y and z directions, ρ = fluid density, $k = k(x,y,z,t)$ = turbulent kinetic energy, $\varepsilon = \varepsilon(x,y,z,t)$ = turbulent energy dissipation rate, C_μ = 0.09 = standard value of a CFD model constant, and u_{gi} = settlement velocity of the i-th floc class due to gravity. In Equation (A.2), α = collision efficiency factor, β = collision frequency factor, a = particle/floc breakage kinetic function ($a(i)=a_0V_i^{1/3}$), and b = break-up distribution functions ($b(i,i-1)=V_i\,/V_{i-1}=2$).

G.2 Operator splitting algorithm

To increase computational efficiency, we applied an operator splitting algorithm, in which particle/floc advection was split from particle/floc dispersion-reaction (Langseth *et al.*, 1996; Aro *et al.*, 1999; Badrot-Nico *et al.*, 2007).

(1) Advection Operator :

$$\frac{\partial n_i}{\partial t}+\frac{\partial}{\partial x}\left(\left\langle U_x\right\rangle n_i\right)+\frac{\partial}{\partial y}\left(\left\langle U_y\right\rangle n_i\right)+\frac{\partial}{\partial z}\left(\left\langle U_z\right\rangle n_i\right)+u_{gi}\frac{\partial n_i}{\partial z}=0$$

(2) Dispersion-Reaction Operator :

$$\frac{\partial n_i}{\partial t}-\frac{\partial}{\partial x}\left(C_\mu\frac{k^2}{\varepsilon}\frac{\partial n_i}{\partial x}\right)+\frac{\partial}{\partial y}\left(C_\mu\frac{k^2}{\varepsilon}\frac{\partial n_i}{\partial y}\right)+\frac{\partial}{\partial z}\left(C_\mu\frac{k^2}{\varepsilon}\frac{\partial n_i}{\partial z}\right)-(agg\,/\,break)_i=0$$

G.3 Finite difference approximations

(1) Advection Based Finite Difference Equations :

To overcome the drawbacks of a standard central-differencing Finite Difference Method (FDM) for simulating pure advective transport, Leveque's flux-corrected upwind algorithm was applied to solve the advective operator (Leveque, 1996; Durran, 1998).

$$n_i(k,l)=pn_i(k,l)-\frac{\Delta t}{\Delta x}\left[\mathrm{F}_i(k,l)-\mathrm{F}_i(k-1,l)+\mathrm{G}_i(k,l)-\mathrm{G}_i(k,l-1)\right] \qquad \text{(A.3)}$$

$$\begin{aligned}\mathrm{F}_i(k-1,l)=\mathrm{F}_i(k-1/2,l)&\xrightarrow{If\ u(k-1/2,l)>0}=u(k-1/2,l)\cdot n_i(k-1,l)\\&\xrightarrow{If\ u(k-1/2,l)<0}=u(k-1/2,l)\cdot n_i(k,l)\end{aligned} \qquad \text{(A.4)}$$

$$
\begin{aligned}
\mathrm{G}_i(k,l-1)=\mathrm{G}_i(k,l-1/2) &\xrightarrow{If\ v_i(k,l-1/2)>0} = v_i(k,l-1/2)\cdot n_i(k,l-1) \\
&\xrightarrow{If\ v_i(k,l-1/2)<0} = v_i(k,l-1/2)\cdot n_i(k,l)
\end{aligned}
\tag{A.5}
$$

$$
v_i(k,l)=v(k,l)+u_{g,i} \tag{A.6}
$$

In Equations (A.3) ~ (A.6), $\mathrm{F}_i(k,l)$ and $\mathrm{G}_i(k,l)$ represent particle mass fluxes through vertical and horizontal interfaces of the computational cell (k,l), $pn_i(k,l)$ is the number concentration of i-th class particles at the previous time step. $u = \langle U_x \rangle$ and $\mathrm{v} = \langle U_y \rangle$ are obtained from the CFD simulation.

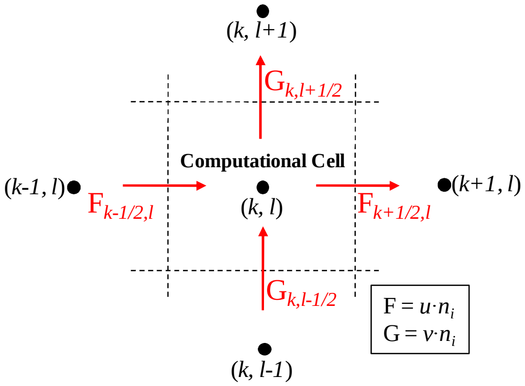

Figure G.1. A typical computation cell within the problem domain. F and G represent mass fluxes through the cell boundaries.

(2) Dispersion-Reaction Finite Difference Equations

The discretized equations of particle/floc dispersion-reaction equations were calculated implicitly with the Gauss-Siedel iteration method. $cn_i(k,l)$ represents the number concentration of i-th class particles at the previous iteration step.

$$n_i(k,l)=\frac{\begin{bmatrix}a_1(k,l)n_i(k+1,l)+a_2(k,l)n_i(k-1,l)+a_3(k,l)n_i(k,l+1)\\ +a_4(k,l)n_i(k,l-1)+\Delta t\cdot GEN_i(k,l)+cn_i(k,l)\end{bmatrix}}{\left[1+a_1(k,l)+a_2(k,l)+a_3(k,l)+a_4(k,l)+\Delta t\cdot DIS_i(k,l)\right]} \tag{A.7}$$

The following Equations (A.8) ~ (A.14) represent the constants used for simplifying dispersion-reaction equations.

$$a_1(k,l)=\frac{\Delta t}{2\left(\Delta x\right)^2}\left[Te(k+1,l)+Te(k,l)\right] \tag{A.8}$$

$$a_2(k,l)=\frac{\Delta t}{2\left(\Delta x\right)^2}\left[Te(k,l)+Te(k-1,l)\right] \tag{A.9}$$

$$a_3(k,l)=\frac{\Delta t}{2\left(\Delta y\right)^2}\left[Te(k,l+1)+Te(k,l)\right] \tag{A.10}$$

$$a_4(k,l)=\frac{\Delta t}{2\left(\Delta y\right)^2}\left[Te(k,l)+Te(k-1,l)\right] \tag{A.11}$$

$$Te(k,l)=\frac{0.09\rho\cdot k_e^2(k,l)}{\varepsilon(k,l)} \tag{A.12}$$

$$GEN_i(k,l)=\sum_{j=1}^{i-2}2^{j-i+1}\alpha\beta_{i-1,j}n_j(k,l)n_{i-1}(k,l)+\frac{1}{2}\alpha\beta_{i-1,i-1}n_{i-1}^2(k,l)+2a_{i+1}n_{i+1}(k,l) \tag{A.13}$$

$$DIS_i(k,l)=-\sum_{j=1}^{i-1}2^{j-i}\alpha\cdot\beta_{i,j}\cdot n_j(k,l)-n_i\sum_{j=i}^{(max\ i)}\alpha\cdot\beta_{i,j}\cdot n_j(k,l)-a_i \tag{A.14}$$

G.4 Numerical strategy for an operator splitting algrotithm

In solving DPBEs with an operator splitting algorithm, advection based finite difference equations and dispersion-reaction finite difference equations were solved sequentially at each time step (see Figure F.2). Firstly, Leveque's flux-corrected upwind algorithm was applied to solve advection based finite difference equations. Secondly, Gauss-Siedel iterative method was used to solve dispersion-reaction finite difference equations.

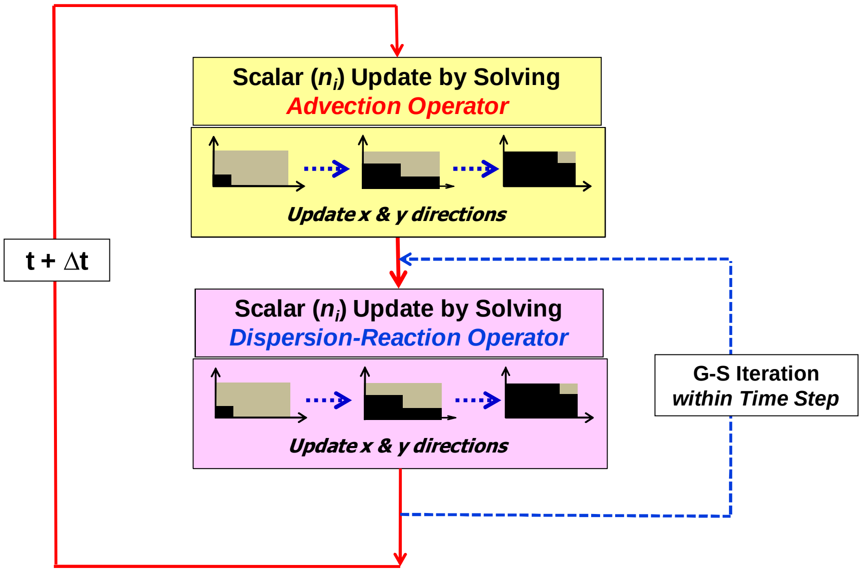

Figure G.2. Flowchart for solving DPBEs with operator splitting algorithm.

G.5 Boundary conditions

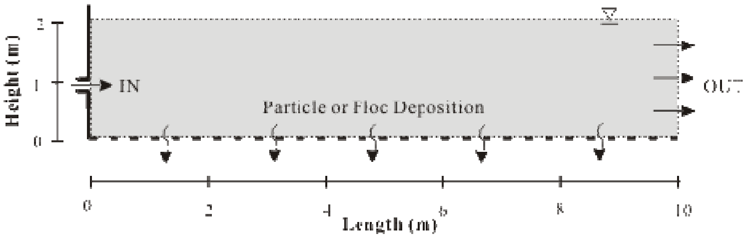

Figure G.3. Schematic diagram of the problem domain.

(a) Left Boundary (b) Right Domain

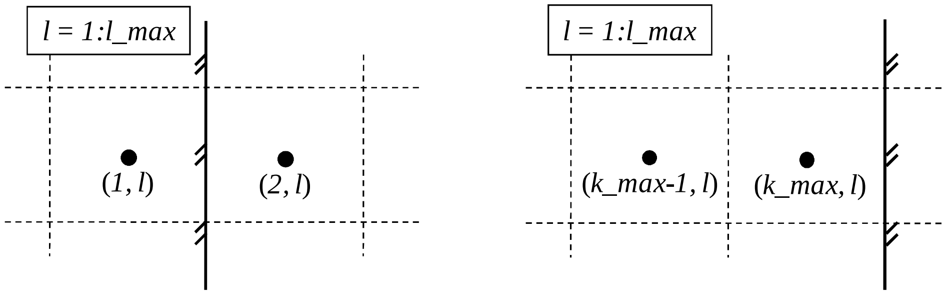

$$F(1,l) = 0 \quad \mathrm{Q}\, u(1,l) = 0 \qquad F(k\_max, l) = u(k\_max, l) \times n_i(k\_max, l)$$

(c) Bottom Boundary (d) Top Domain

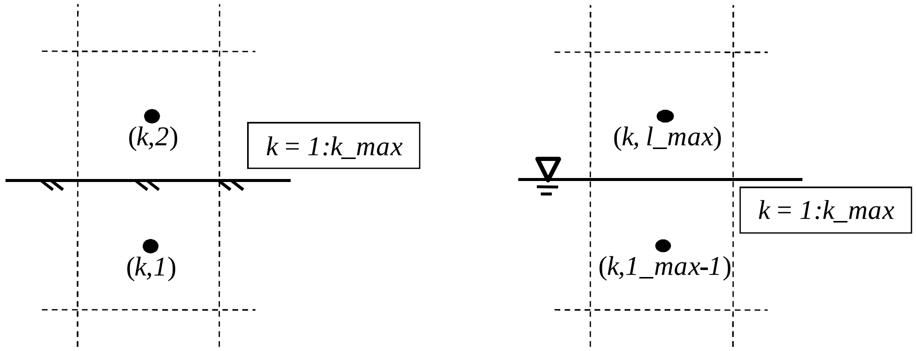

$$G_i(k,1) = v_i(k,1) \times n_i(k,1) = u_{g,i} \times n_i(k,1)$$

$$G_i(k, l\_max) = 0 \quad \mathrm{Q}\, v_i(k, l\_max) = 0$$
$$G_i(k, l\_max - 1) = 0 \quad \mathrm{Q}\, v_i(k, l\_max - 1) = 0$$

Figure G.4. Boundary conditions for advection based transport equations.

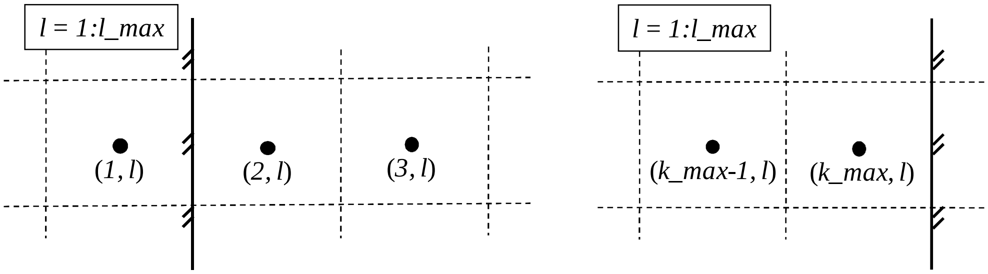

(a) Left Boundary

(b) Right Domain

$$n_i(1,l)=\frac{1}{3}\left[4n_i(2,1)-n_i(3,1)\right] \qquad n_i(k\_max,l)=n_i(k\_max-1,1)$$

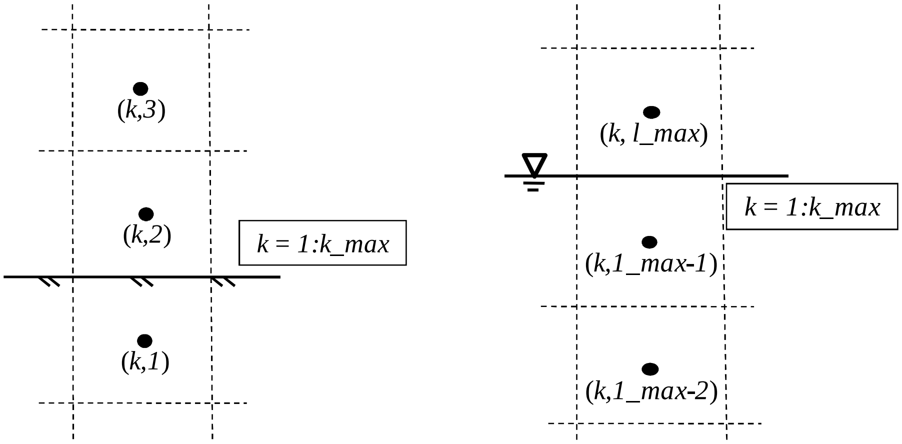

(c) Bottom Boundary

(d) Top Domain

$$n_i(k,1)=\frac{1}{3}\left[4n_i(k,2)-n_i(k,3)\right] \qquad n_i(k,1\_max)=\frac{1}{3}\left[4n_i(k,1\_max-1)-n_i(k,1\_max-2)\right]$$

Figure G.5. Boundary conditions for dispersion-reaction equations.

F.6 References

Aro, C. J., G.H. Rodrigue, and D. A. Rotman, 1999, A high performance chemical kinetics algorithm for 3-D atmospheric models, *The International Journal of High Performance Computing Applications*, **13**(1), 3-15

Badrot-Nico, F., F. Brissaud, and V. Guinot, 2007, A finite volume upwind scheme for the solution of the linear advection-diffusion equation with sharp gradients in multiple dimensions, *Advances in Water Resources*, **30**, 2002-2025

Durran, D. R., 1998, *Numerical methods for wave equations in geophysical fluid dynamics*, Springer-Verlag, New York, U.S.

Langseth, J. O., A. Tveito, and R. Winther, 1996, On the convergence of operator splitting applied to conservation laws with source terms, *SIAM J. Numer. Anal.*, **33**, 843-863

Leveque, R. J., 1996, High-resolution conservative algorithms for advection in incompressible flow, *SIAM J. Numer. Anal.*, **33**(2), 627-665

Appendix H

Matlab® Code for the DPBE-CFD Model

```
% Population Balance Equation 2D Simulation (MKS Units)
% ----------------------------------------------------------------------
% Node Information
distance=10;
height=2;
delx=0.2;
dely=0.2;
delt=0.1;
k_max=51;
l_max=12;
z=0;

% ----------------------------------------------------------------------
% Set constants and arrays required for Multi-Dimensional PBE
vol = zeros(30,1);                  % i-th Particle Apparent Volume
dia_micron = zeros(30,1);           % i-th Particle Radius
dia = zeros(30,1);                  % i-th Particle Diameter
floc_den = zeros(30,1);       % i-th Particle Diameter
floc_mass = zeros(30,1);            % i-th Particle Diameter
alpha_pbe=zeros(30,30);             % collision efficiency
beta_pbe = zeros(k_max,l_max,30,30); % collision frequency B/T i and j
s = zeros(30);                % breakage function
u_set=zeros(30,1);                  % Settling Velocity [m/s]
v=zeros(k_max,l_max,30);            % Y-axis flow Vel. + Set Vel. [m/s]

% ----------------------------------------------------------------------
% Flow field information
u=xlsread('C:\Pond_2.5MRTD_Case3\Joon_Thesis_case3_u.xls');
v_raw=xlsread('C:\Pond_2.5MRTD_Case3\Joon_Thesis_case3_v.xls');
Te=xlsread('C:\Pond_2.5MRTD_Case3\Joon_Thesis_case3_Te.xls');
shear=xlsread('C:\Pond_2.5MRTD_Case3\Joon_Thesis_case3_G.xls');

% ----------------------------------------------------------------------
% Physicochemical Properties of Solid and Liquid
par_den=2600;                 % [kg/m3]
liq_den=1000;                       % [kg/m3]
g=9.81;                       % [m/s2]
mu=0.001002;                        % [kg/m/s]
bolz=1.38*10^(-23);                 % [kg-m2/(s2-K)]
temp=293;                     % [k]

% ----------------------------------------------------------------------
% Constants (make 'MKS' units)- Check Spicer & Pratsinis (AICHE, 1996)
ini_dia=1*10^(-6);                  % Diameter of Primary Particle [m]
ini_vol=1/6*pi()*ini_dia^3;   % [m3]
ini_mass=ini_vol*par_den;           % [kg/m3]
dia_c=100*10^(-6);                  % Critical Diameter [m]
vol_c=1/6*pi()*dia_c^3;       % Critical Volume [m3]
```

```
% ----------------------------------------------------------------------
% Constant for Breakage Kinetics - (Ding et al., 2006, Chem. Eng. Sci.)
s_o=10;                      % [/m/s]

% ----------------------------------------------------------------------
% Constant for Fractal Theory - Check Flesch et al (AICHE, 1999)
frac_df=2.5;                       % If 3, Follow Eucledian Model
frac_k=1;

% ----------------------------------------------------------------------
% Particle classes and Radius
for i=1:30
   dia(i)=(2^(i-1))^(1/frac_df)*ini_dia;
   dia_micron(i)=(2^(i-1))^(1/frac_df)*ini_dia*1000000;
   vol(i)=pi()/6*(ini_dia^(3-frac_df))*(dia(i))^(frac_df);
   floc_den(i)=liq_den+(par_den-liq_den)*(dia(i)/ini_dia)^(frac_df-3);
   floc_mass(i)=ini_mass*2^(i-1);
end

% ----------------------------------------------------------------------
% Calculation of settling velocity of i-th particle
% Micale et al. (Trans IChemE, 2000)
% According to Fractal Theory
for i=1:30
    u_set(i)=-(dia(i)^2)*g*(par_den-liq_den)*...
        ((dia(i)/ini_dia)^(frac_df-3))/(18*mu);       % [m/s]
end
% Y-axis Flow Velocity + Settling Velocity
for k=1:k_max
    for l=1:l_max
        for i=1:30
            v(k,l,i)=v_raw(k,l)+u_set(i);
        end
    end
end
for l=1:l_max
    for i=1:30
        v(1,l,i)=0;
    end
end
for k=1:k_max
    for i=1:30
        v(k,l_max,i)=0;
        v(k,l_max-1,i)=0;
    end
end

% ----------------------------------------------------------------------
% Generate PBE Kinetic Constants (space variant)
gamma_pbe = zeros(30,30);          % breakage distribution function
for i=1:30
   for j=1:30
       for k=2:k_max-1
```

```
           for l=2:l_max-1
               if dia(i)<=dia_c && dia(j)<=dia_c
                   beta_pbe(k,l,i,j) =
1/6*shear(k,l)*(dia(i)+dia(j))^3;
               else
                   beta_pbe(k,l,i,j) = 8*1/6*shear(k,l)*dia_c^3;
               end
           end
       end
   end
end
for i=1:30
   for j=1:30
       alpha_pbe(i,j) = 1/(1+((vol(i)^(1/3)+vol(j)^(1/3))...
           /(2*vol_c^(1/3)))^3);
   end
end
for i=1:30
    s(i)=s_o*vol(i)^(1/3);              %[/s]
end

% ----------------------------------------------------------------------
% Coefficient Calculation for Diffusion in particle transport equations
ae5=zeros(k_max,l_max);
ae6=zeros(k_max,l_max);
ae7=zeros(k_max,l_max);
ae8=zeros(k_max,l_max);
for k=2:k_max-1
    for l=2:l_max-1
        ae5(k,l)=delt*(Te(k+1,l)+Te(k,l))/(2*(delx)^2);
    end
end
for k=2:k_max-1
    for l=2:l_max-1
        ae6(k,l)=delt*(Te(k,l)+Te(k-1,l))/(2*(delx)^2);
    end
end
for k=2:k_max-1
    for l=2:l_max-1
        ae7(k,l)=delt*(Te(k,l+1)+Te(k,l))/(2*(dely)^2);
    end
end
for k=2:k_max-1
    for l=2:l_max-1
        ae8(k,l)=delt*(Te(k,l)+Te(k,l-1))/(2*(dely)^2);
    end
end

% ----------------------------------------------------------------------
% Initial Condition (intial seeding)
n=zeros(k_max,l_max,30);
pn=zeros(k_max,l_max,30);
cn=zeros(k_max,l_max,30);
FG=zeros(k_max,l_max,i);
```

```
FF=zeros(k_max,l_max,i);
for k=1:k_max
    for l=1:l_max
        for i=1:30
            n(k,l,30)=0;
        end
    end
end

% ----------------------------------------------------------------------
% Advection Calcuation for nodes inside Boundaries
% Start Time Evolution
t=0;
w=1.6;    %SOR Factor
Flux_Bottom=0;
Flux_Right=0;
Flux_In=0;
Flux_Bottom_T=zeros(15000,1);
Flux_Right_T=zeros(15000,1);
Flux_In_T=zeros(15000,1);
Flux_Acc_T=zeros(15000,1);
Mass_Bal=zeros(15000,1);
n_out=zeros(15000,30);
n_out_dia=zeros(15000,1);

for p=1:15000
    t=t+delt;

% ----------------------------------------------------------------------
% Set the current values
    cn=n;

% ----------------------------------------------------------------------
% Left Domain (Inlet) - Caution in Node Spacing
    for i=1:30
        n(1,6,i)=0;
        n(1,5,i)=0;
        n(1,4,i)=0;
    end
        n(1,6,1)=1.47*10^15;
        n(1,5,1)=1.47*10^15;
        n(1,4,1)=1.47*10^15;

% ----------------------------------------------------------------------
% Diffusion Calculation at the end of time step
% Start Gauss-Siedel Iteration
    for q=1:3

% ----------------------------------------------------------------------
% Scalar Update by Diffution at the End of Time Step
% Boundary Conditions of Diffution
    for l=1:l_max
        for i=1:30;
            n(1,l,i)=1/3*(4*n(2,l,i)-n(3,l,i)); % Left Boundary
```

```
        end
    end
    for i=1:30
        n(1,6,i)=0;
        n(1,5,i)=0;
        n(1,4,i)=0;
    end
        n(1,6,1)=1.47*10^15;
        n(1,5,1)=1.47*10^15;
        n(1,4,1)=1.47*10^15;              % Inlet

    for k=1:k_max
        for i=1:30;
            n(k,1,i)=1/3*(4*n(k,2,i)-n(k,3,i)); % Bottom Boundary
        end
    end

    for k=1:k_max
        for i=1:30;
            n(k,l_max,i)=1/3*(4*n(k,l_max-1,i)-n(k,l_max-2,i)); % Top
        end
    end

    for l=1:l_max
        for i=1:30;
            n(k_max,l,i)=n(k_max-1,l,i);        % Right Boundary
        end
    end

% ----------------------------------------------------------------------
% Update GEN(i), DIS(i), and n(k,l,i) with Diffusion-Reaction Equation
        for k=2:k_max-1
            for l=2:l_max-1
                for i=1:30

% ----------------------------------------------------------------------
% Set intial values as zero
                    GEN=zeros(30,1);
                    DIS=zeros(30,1);
                    GEN_MC=zeros(30,1);
                    GEN_BC=zeros(30,1);
                    GEN_B=zeros(30,1);
                    DIS_CS=zeros(30,1);
                    DIS_CL=zeros(30,1);
                    DIS_B=zeros(30,1);

% ----------------------------------------------------------------------
% Update GEN(i)
                    if i==1
                        GEN_MC(1)=0;
                    elseif i==2
                        GEN_MC(2)=0;
                    else
                        for j=1:(i-2)
```

```
                            GEN_MC(i)=GEN_MC(i)+2^(j-i+1)...
                                *alpha_pbe(i-1,j)*beta_pbe(k,l,i-
1,j)...

                                *n(k,l,i-1)*n(k,l,j);
                        end
                    end

                    if i==1
                        GEN_BC(1)=0;
                    else
                        GEN_BC(i)=0.5*alpha_pbe(i-1,i-1)...
                            *beta_pbe(k,l,i-1,i-1)*n(k,l,i-1)^2;
                    end

                    if i==30
                        GEN_B(30)=0;
                    else
                        GEN_B(i)=2*s(i+1)*n(k,l,i+1);
                    end
                    GEN(i)=GEN_MC(i)+GEN_BC(i)+GEN_B(i);

% -----------------------------------------------------------------------
% Update DIS(i)
                    if i==1
                        DIS_CS(1)=0;
                    elseif n(k,l,i)==0;
                        DIS_CS(i)=0;
                    else
                        for j=1:(i-1)
                            DIS_CS(i)=DIS_CS(i)+2^(j-i)...
                                *alpha_pbe(i,j)*beta_pbe(k,l,i,j)...
                                *n(k,l,j);
                        end
                    end

                    for j=i:30
                        DIS_CL(i)=DIS_CL(i)+alpha_pbe(i,j)...
                            *beta_pbe(k,l,i,j)*n(k,l,j);
                    end

                    if i==1
                        DIS_B(1)=0;
                    elseif n(k,l,i)==0;
                        DIS_B(i)=0;
                    else
                        DIS_B(i)=s(i);
                    end
                    DIS(i)=DIS_CS(i)+DIS_CL(i)+DIS_B(i);

% -----------------------------------------------------------------------
% Node Calculation inside Boundary
                    n(k,l,i)=(1-w)*n(k,l,i)+w*(cn(k,l,i)+...
                        delt*GEN(i)+n(k-1,l,i)*ae6(k,l)+n(k+1,l,i)*...
                        ae5(k,l)+n(k,l-1,i)*ae8(k,l)+...
```

```
                        n(k,l+1,i)*ae7(k,l))/(1+ae5(k,l)+ae6(k,l)+...
                        ae7(k,l)+ae8(k,l)+delt*DIS(i));
                end
            end
        end

% -----------------------------------------------------------------------
% End of Gauss-Siedel Iteration
    end

% -----------------------------------------------------------------------
% Left Domain (Inlet) - Caution in Node Spacing
    for i=1:30
        n(1,6,i)=0;
        n(1,5,i)=0;
        n(1,4,i)=0;
    end
        n(1,6,1)=1.47*10^15;
        n(1,5,1)=1.47*10^15;
        n(1,4,1)=1.47*10^15;

% -----------------------------------------------------------------------
% Set the current values
    pn=n;

% -----------------------------------------------------------------------
% Flux Update
    for k=2:k_max
        for l=2:l_max-1
            for i=1:30;
                if u(k-1,l)>0
                    FF(k-1,l,i)=u(k-1,l)*n(k-1,l,i);
                elseif u(k-1,l)<=0
                    FF(k-1,l,i)=u(k-1,l)*n(k,l,i);
                end
                if v(k,l-1,i)>0
                    FG(k,l-1,i)=v(k,l-1,i)*n(k,l-1,i);
                elseif v(k,l-1,i)<=0
                    FG(k,l-1,i)=v(k,l-1,i)*n(k,l,i);
                end
            end
        end
    end

% -----------------------------------------------------------------------
% Right Domain (Insulation & Inflow)(Check for Free Boundary)
        for l=1:l_max
            for i=1:30
                FF(51,l,i)=u(51,l)*n(51,l,i);
            end
        end


% -----------------------------------------------------------------------
```

```
% Scalar Update
    for k=2:k_max
        for l=2:l_max-1
            for i=1:30;
                n(k,l,i)=pn(k,l,i)-delt/delx*(FF(k,l,i)...
                    -FF(k-1,l,i)+FG(k,l,i)-FG(k,l-1,i));
            end
        end
    end

% -----------------------------------------------------------------------
% Check Mass Blance
        for k=2:k_max-1
            for i=1:30
                Flux_Bottom=Flux_Bottom-FG(k,1,i)*...
                    floc_mass(i)*delt*(delx);
            end
        end
        Flux_Bottom_T(p,1)=Flux_Bottom;

        for l=2:l_max-1
            for i=1:30
                Flux_Right=Flux_Right+n(k_max,l,i)*u(k_max,l)...
                    *floc_mass(i)*delt*(delx);
            end
        end
        Flux_Right_T(p,1)=Flux_Right;

        Flux_Acc=0;
        for k=2:k_max-1
           for l=2:l_max-1
               for i=1:30
                   Flux_Acc=Flux_Acc+(n(k,l,i)*floc_mass(i)*delx^2);
               end
           end
        end
        Flux_Acc_T(p,1)=Flux_Acc;

    Flux_In=Flux_In+n(1,6,1)*3*u(1,6)*ini_mass*delt*(delx);
        Flux_In_T(p,1)=Flux_In;

    Mass_Bal(p,1)=(Flux_Bottom+Flux_Right+Flux_Acc)/(Flux_In);

% -----------------------------------------------------------------------
% Check Floc Size at the Outlet
    check_time=p/100-fix(p/100);
    if check_time==0
    n_out_dia(p,1)=0;
    mass_out=0;
    massbysize_out=0;
    for i=1:30
        for l=2:l_max-1
            n_out(p,i)=n_out(p,i)+n(k_max,l,i);
            mass_out=mass_out+floc_mass(i)*n(k_max,l,i);
```

```
                massbysize_out=massbysize_out+...
                    floc_mass(i)*n(k_max,l,i)*dia_micron(i);
            end
        end
        n_out_dia(p,1)=massbysize_out/mass_out;
        end

    % ----------------------------------------------------------------------
    % Post Processing at a fixed time step
        check_time=p/100-fix(p/100);
        if check_time==0
            z=z+1;
            for k=2:k_max-1
                for l=2:l_max-1
                    temp_mass_conc=0;
                    temp_mass_by_size=0;
                    temp_avg_size=0;
                    for i=1:30
                        temp_mass_conc=temp_mass_conc+...
                            floc_mass(i)*n(k,l,i);
                        temp_mass_by_size=temp_mass_by_size+...
                            floc_mass(i)*n(k,l,i)*(dia_micron(i));
                        if temp_mass_conc==0
                            temp_avg_size=0;
                        else
                            temp_avg_size=temp_mass_by_size/temp_mass_conc;
                        end
                    end
                    mass_conc(k,l)=temp_mass_conc;
                    mass_by_size(k,l)=temp_mass_by_size;
                    avg_size(k,l)=temp_avg_size;
                end
            end
            dlmwrite('C:\Results\mass.txt',mass_conc(:,:),...
                '-append', 'delimiter', '\t');
            dlmwrite('C:\Results\size.txt',avg_size(:,:),...
                '-append', 'delimiter', '\t');
        end

    % ----------------------------------------------------------------------
    % End of Time Step
    end
```